The Mars Shuttle

An investigation into the feasibility of a shuttle vehicle between the Martian surface and an orbital node to support the continued presence of humans on Mars

Eleonoor van Beers

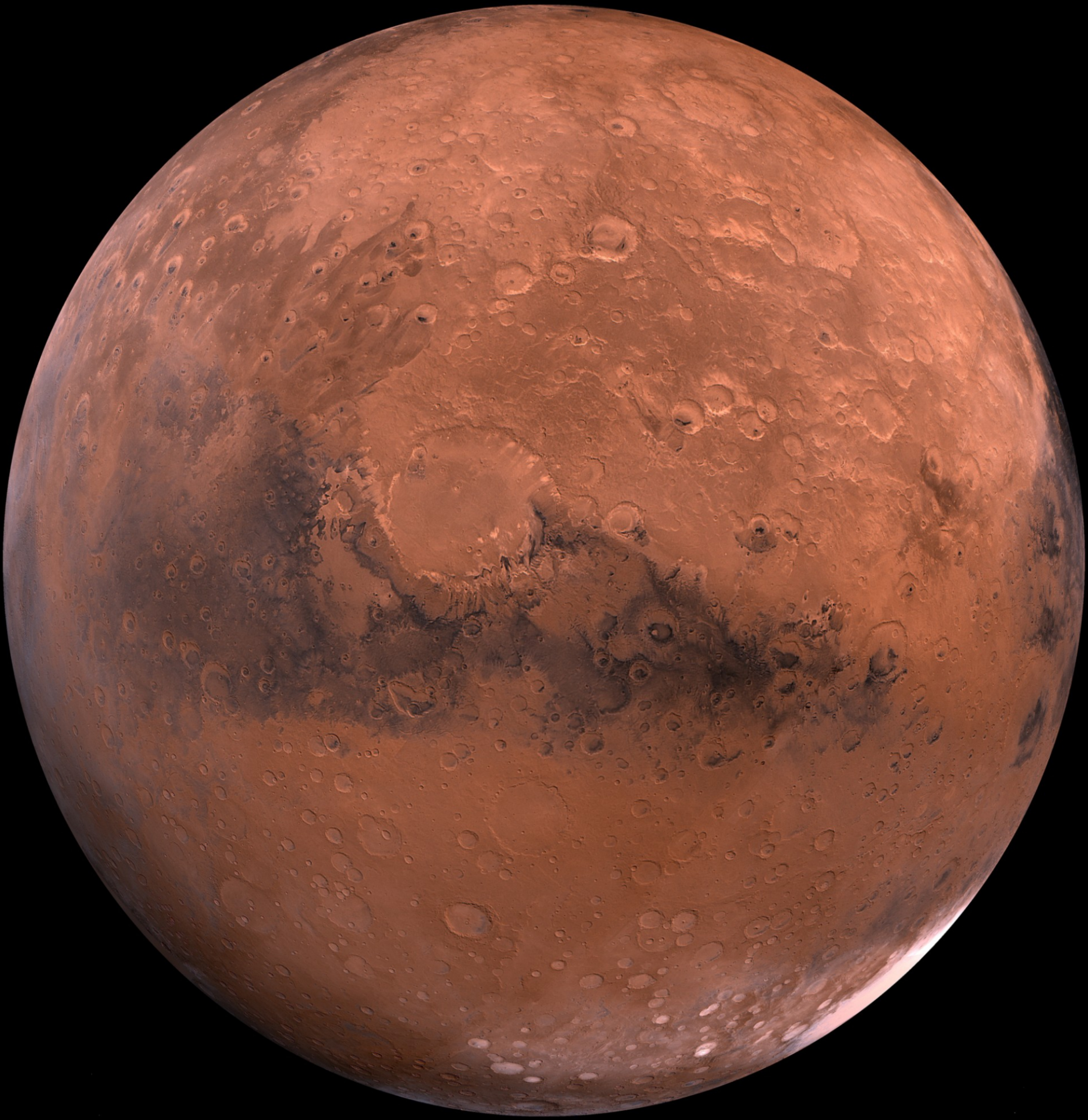

Delft University of Technology

The Mars Shuttle

An investigation into the feasibility of a shuttle vehicle between the Martian surface and an orbital node to support the continued presence of humans on Mars

by

Eleonoor van Beers

to obtain the degree of Master of Science
at the Delft University of Technology,
to be defended publicly on Tuesday August 24, 2021 at 10:00 AM

Student number:	4273427	
Project duration:	August 1, 2020 – August 1, 2021	
Thesis committee:	Assist. Prof. ir. M.C. Naeije,	TU Delft, supervisor
	Dr. Ir. W. van der Wal,	TU Delft, chair
	Ir. B.T.C. Zandbergen,	TU Delft

This thesis is confidential and cannot be made public until August 24, 2021.

TU Delft

Preface

The report you are about to read is culmination of my academic journey at the TU Delft. The last year has been a turbulent experience, as the appearance COVID-19 resulted in a rather unwelcome, and unforeseen, change of circumstances. Nonetheless, being able to delve into this research topic has most definitely been inspiring, not only as a research topic itself, but also as we are at the cusp of a very new phase of space exploration. My research consists of the investigation into a reusable single-stage-to-orbit vehicle, serving as a shuttle between a Martian base and an orbital node in lower-Martian orbit. Although this concept at this point in time still seems like a science fiction tale, the expansion of humankind from Earth into the solar system will most likely be a reality by the end of the decade.

First and foremost I want to thank my supervisor, Marc Naeije, for bearing with me throughout the chaos of this last year. Many aspects of the thesis ran smoothly, however others definitely did not, as is tradition. Although most meetings unfortunately had to be held via Zoom, I definitely had a lot of fun during the weekly catch ups, and very much appreciated their easygoing nature, as well as the guidance and enthusiasm for my project.

I next want to thank my friends, especially Rosan and Isabel, for enduring my endless complaining that I, once again, had turned on the wrong optimiser settings. A thesis is a long process, throughout which everyone who writes one encounters many ups and downs, so thank you for being there through it all.

I also want to thank my family- my mum, my dad, and my sister- for being my personal cheer leading squad throughout my academic journey. I have only ever felt your enthusiasm and patience for me throughout the years, and through that I am proud of what I have been able to achieve.

Lastly, I also want to thank my boyfriend Harry for making the last couple months of my thesis so much more manageable. Thank you for motivating me, as well as helping me take a step back sometimes, and of course thank for your delicious cooking. I hope I can provide as much support to you in the upcoming months as you provided me.

Eleonoor van Beers
Rotterdam, July 2021

Abstract

The last 20 years has brought with it a surge in efforts toward the Red Planet as the next frontier is human space exploration draws closer. Many concepts have been proposed for a sustained human settlement on Mars, with NASA's ISRU-to-the-wall campaign identifying the need for a shuttle vehicle between the Martian surface and a station in an orbit around the planet [4]. Two such vehicle concepts have been designed: the Charon by Gaffarel et. al. [22] and Hercules by Komar et. al. [38]. However a Multidisciplinary Design Optimisation (MDO) has thus far not been applied. In this research an MDO is employed for the same mission scenario as the Charon vehicle's. The vehicle must transport 1200 kg, including 6 crew, to a 607 km circular orbit at 44.96° inclination from the Martian base that is located at 42.5° North and 25.5° East. It must then return to the base, its entry beginning at 80 km altitude at a velocity of 3500 m/s.

The MDO in this research is performed by dividing the design of the vehicle and its trajectories into various disciplines, which are optimised in parallel. In reality cost commonly is the dominant factor that drives the design, in this case, the vehicle's Gross Take Off Weight (GTOW) is taken as the objective. Estimating the cost of the Martian shuttle vehicle within reasonable accuracy is exceedingly difficult, as not only is its realisation still decades away, costs such as the shuttle's transportation to Mars, its operational costs, and its maintenance costs are very hard to estimate. However, a vehicle's GTOW is directly influential on its cost, and its reduction is therefore the optimisation's goal.

The disciplines within the optimisation are the vehicle's geometry, mass, aerodynamics, and ascent and descent trajectories. Constraints are set for both the vehicle and its trajectories, to which the design must adhere, and the performance of the design is determined by a fitness function that ensures the reduction of the vehicle's GTOW. The optimiser itself is written using Tudat software, a set of C++ libraries developed by the TU Delft.

As the same mission scenario is taken for the vehicle in this research as that of the Charon vehicle, the Charon design can be directly compared to that of the optimiser. The MDO is able to significantly reduce the vehicle GTOW, obtaining an optimum solution of 146.2 tonnes, which is more than 20 tonnes lighter than Charon, at 168.1 tonnes. The greatest reduction in mass is found in the ascent propellant mass, which is the greatest contributor to the GTOW. This reduction is mostly due to the lower maximum Thrust to Weight (TW) ratio used in the MDO.

Other scenarios are also investigated and their effects observed. Two other target orbits and rendezvous strategies are tested, namely the same as the Hercules vehicle (108 km pericentre altitude and an eccentricity of 0.0178), and a direct ascent to the orbital node at a circular 500 km altitude orbit. The Hercules vehicle scenario proved to be by far the most GTOW-preferable, with a GTOW of only 103.0 tonnes. The GTOW of the MDO solution found for the Hercules scenario is also less than that of the Hercules vehicle design, which is 162.8 tonnes, however the Hercules vehicle transports a payload mass of 5750 kg as opposed to the MDO's 1200 kg, therefore the mass reductions cannot be solely attributed to the optimiser performance. It is clear from the results that the altitude of the initial target orbit is the greatest factor contributing to the GTOW, with a reduction in both payload mass and Martian base latitude also shown to reduce the GTOW. Neither an increase in the maximum acceleration constraint, nor a change in ascent thrust profile, were shown to have any benefit on the GTOW.

The sensitivity of the optimum design with respect to uncertainties is assessed. The final pericentre and final eccentricity are both most sensitive to the final pitch node value, especially when taking interference with other variables into account. The inclination, however, was almost solely influenced by the first pitch angle value. The latitude and longitude are also almost solely influenced by a single variable, namely the flight path angle, and the final velocity and final pitch angle are both highly volatile to all variables when interference effects are taken into account. The MDO model as a whole is found to be sensitive to changes in both aerodynamics coefficients and propulsive efficiency; an increase in aerodynamic coefficients adversely affects the GTOW, and an increase in propulsive efficiency benefits the GTOW, and vice versa.

List of Figures

List of Tables

List of Abbreviations

ATO Abort To Orbit.
ATS Abort To Surface.

CEA Chemical Equilibrium with Applications.

DA Direct Ascent.
DE Differential Evolution.

EDL Entry, Descent, and Landing.

GA Genetic Algorithm.
GTOW Gross Takeoff Weight.

HTA Hohmann Transfer Ascent.

ISRU In-Situ Resource Utilisation.
ITAR International Traffic in Arms Regulations.

LDRO Lunar Distance Retrograde Orbit.
LMO Lower Martian Orbit.

MCD Mars Climate Database.
MDF Multi Discipline Feasible.
MDO Multidisciplinary Design Optimisation.
MOEA/D Multi-Objective Evolutionary Algorithm on Decomposition.
MOI Mars Orbit Insertion.
MRP Modified Rodriquez Parameters.

NLP Non-Linear Programming.

O/F Oxygen-to-Fuel mixture ratio.

PaGMO Parallel Global Multiobjective Optimizer.
PSO Particle Swarm Optimisation.
PSOG Particle Swarm Optimisation Generational.

RKF Runge-Kutta-Fehlberg.

SSTO Single State To Orbit.

TW Thrust-to-Weight.

USM Unified State Model.

Nomenclature

Physical Constants

g_0	Gravitational acceleration on Earth at sea level	9.80665, $\mathrm{m/s^2}$
G	Gravitational constant	6.67408, $\times 10^{-11}$ $\mathrm{m^3/kg/s^2}$
k	Boltzmann constant	1.38064852 $\times 10^{-23}$ $\mathrm{m^2\ kg/s^2/K}$
R_A	Universal gas constant	8.314 J/mol/K

Greek Symbols

α	Angle of attack	deg
β	Angle of sideslip	deg
χ	Heading angle	deg
δ	Latitude	deg
δ_0	Initial latitude	deg
$\dot{v}_{max}$	Maximum acceleration	$\mathrm{m/s^2}$
$\dot{v}_{max}$	Maximum acceleration	$\mathrm{m/s^2}$
Γ	Vandenkerckhove parameter	-
γ	Flight path angle	deg
γ	Ratio of specific heats	-
$\mathbb{T}_{BA}$	Frame transformation matrix	-
μ	Bank angle	deg
Ω	Right ascension of the ascending node	deg
ω	Argument of pericentre	deg
ρ	Air density	$\mathrm{kg\,m^{-3}}$
ρ_p	Propellant density	$\mathrm{kg\,m^{-3}}$
ρ_t	Tank material density	$\mathrm{kg\,m^{-3}}$
σ_y	Yield stress	Pa
τ	Longitude	deg
τ_0	Initial longitude	deg
θ	Pitch angle	deg
θ	True anomaly	deg
θ_{eq}	Equivalence half-angle	deg
ε	Expansion ratio	-
ε_c	Contraction ratio	-
ξ_P	Propellant consumption quality factor	-
ξ_T	Thrust quality factor	-

Roman Symbols

a	Semi-major axis	km
A_e	Exhaust area	$\mathrm{m^2}$
a_g	Acceleration due to gravity	$\mathrm{m/s^2}$
A_t	Throat area	$\mathrm{m^2}$
a_{aero}	Acceleration due to aerodynamic forces	$\mathrm{m/s^2}$
A_c	Cross-sectional combustion chamber area	$\mathrm{m^2}$
$a_{T,max}$	Maximum acceleration due to thrust	$\mathrm{m/s^2}$
A_{tank}	Tank surface area	$\mathrm{m^2}$
b	Semi-minor axis	m
c^*	Characteristic velocity	m/s
C_D	Drag coefficient	-

C_F	Thrust coefficient	-
C_L	Lift coefficient	-
C_{nm}	Spherical harmonics coefficient of degree n and order m	-
D	Drag	N
D_c	Combustion chamber diameter	m
D_v	Vehicle diameter	m
e	Eccentricity	-
F	Thrust	N
F_m	Modelled thrust	N
F_r	Real thrust	N
F_{loc}	Landing location factor	-
F_{safe}	Landing safety factor	-
F_{tar}	Target orbit factor	-
F_T	Total thrust	N
g	Current gravitational acceleration	$\mathrm{m/s^2}$
$g(x,y,z)$	Inequality constraints	-
g_0	Surface gravitational acceleration	$\mathrm{m/s^2}$
$h(x,y,z)$	Equality constraints	-
h_{rb}	Retroburn altitude	km
i	Inclination	deg
$I_{sp,m}$	Modelled specific impulse	s
$I_{sp,r}$	Real specific impulse	s
I_{sp}	Specific impulse	s
K	Gain factor	-
k_{boil}	Propellant boil-off factor	-
k_{ull}	Tank ullage factor	-
k_{ull}	Ullage fraction	N
k_d	Load factor	-
k_m	Composite tank mounting factor	-
k_p	Unused propellant mass fraction	-
k_T	Engine throttle level	%
k_{boil}	Boil-off fraction	N
L	Lift	N
L^*	Characteristic length	m
L_c	Combustion chamber length	m
L_n	Nozzle length	m
L_t	Total vehicle length	m
L_{eng}	Engine length	m
L_f	Fuel tank length	m
L_{ox}	Oxidiser tank length	m
M	Mass	kg
$\dot{m}$	Mass flow rate	kg/s
M_c	Current vehicle mass	kg
M_f	Final mass	kg
M_i	Initial mass	kg
M_t	Total vehicle mass	kg
M_W	Molecular weight	kg/mol
M_{eng}	Engine mass	m
M_{ins}	Tank insulation mass	kg
$M_{P,a}$	Ascent propellant mass	kg
$M_{P,l}$	Landing propellant mass	kg
M_{ts}	Thrust structure mass	kg
M_{val}	Mass of the valves	N
n_{eng}	Engine number	-
n_{max}	Maximum g-load	-
O/F	Mixture ratio	-

P	Fitness penalty	-
P	Legendre polynomial	-
p	Pressure	Pa
p_a	Ambient pressure	Pa
p_c	Chamber pressure	Pa
p_e	Exhaust pressure	Pa
P_T	Trajectory fitness penalty	-
q_{max}	Maximum heat flux	W/m^2
q_{max}	Maximum heat flux	W/m^2
R	Planetary radius	km
r	Radius	km
R_c	Cylindrical tank radius	m
R_N	Nose radius	m
R_t	Throat radius	m
R_e	Endcap radius	m
S	Reference surface area	m^2
S_{nm}	Spherical harmonics coefficient of degree n and order m	-
t	Current time	s
T_c	Chamber temperature	K
t_c	Chamber wall thickness	m
$t_{b,a}$	Ascent burn time	s
$t_{b,l}$	Propulsive landing burn time	s
t_c	Thickness of cylindrical tank	m
t_e	Thickness of tank endcaps	m
TW	Thrust to weight ratio	-
TW_{max}	Maximum thrust to weight ratio	-
TW_{min}	Minimum thrust to weight ratio	-
U	Number of unviolated constraints	-
V	Velocity	m/s
V_c	Local circular velocity	m/s
v_e	Exhaust velocity	m/s
V_g	Flight velocity	m/s
V_p	Propellant tank volume	m^3
V_w	Chamber wall volume	m^3
V_{eq}	Equilibrium velocity	m/s
V_f	Fuel tank volume	m^3
V_f	Fuel volume	m^3
V_{ox}	Oxidiser tank volume	m^3
V_{ox}	Oxidiser volume	m^3
$V_{w,f}$	Fuel tank wall volume	m^3
$V_{w,ox}$	Oxidiser tank wall volume	m^3
W	Vehicle weight	N
x	State variables	-
y	Coupling variables	-
z	Design variables	-
Z_{aero}	Aerodynamic design variables	-
Z_{ascent}	Ascent design variables	-
$Z_{descent}$	Descent design variables	-
Z_{prop}	Main engine performance design variables	m
Z_{veh}	Vehicle design variables	-

Contents

1

Introduction

Even before the advent of spaceflight, humankind has looked towards the universe and considered the possibility of human settlements on other planets. From wild science fiction tales to legitimate interplanetary concepts, the idea of humans breaching the confines of Earth and building a permanent home elsewhere has gripped the imagination of many. Mars, the only other planet in our solar system that could possibly host such a settlement within today's technological limits, has always been the focal point of the proposals; yet this vision has yet to come to fruition. With the technological advances of the last two decades as well as the emergence of private companies in the space sector, one could say the race to Mars has actually begun. Not just for mankind to set foot on Mars, but to build a permanently crewed Martian base.

The last 20 years has seen the proposal of many different architectures for crewed missions, with one of the most recent mission scenarios being outlined in NASA's ISRU-to-the-wall campaign. The placement of stations, called nodes, in circular orbits about both Earth and Mars permits more controlled and efficient movement between the two bodies than a direct trajectory, and better facilitates the transfer of payloads, propellant, and crew. Interplanetary vehicles dock to the nodes, and movement between the nodes is thus undertaken by an interplanetary vehicle. This construction clearly calls for a shuttle vehicle to aid the transportation between the node and the planet's surface. The design of such a shuttle is therefore of high interest, and two such concepts have been developed for the vehicle on Mars; named the Hercules [38] and the Charon [22]. However, as of yet, no global optimisation scheme has been applied to the design of the vehicle and its trajectories, and it is therefore of value to explore the results an optimisation scheme could potentially have on the design.

In Chapter 2 the state-of-art is first presented, covering the current state of human Martian exploration, single-stage-to-orbit vehicle heritage, and Martian crewed vehicle research. Chapter 3 follows with the methodology of numerical optimisation, which includes multidisciplinary design optimisation, optimal control theory, and the software implementation. The design of the various disciplines within the optimisation scheme is then handled, with the vehicle design and sizing presented in Chapter 4, the aerodynamics in Chapter 5, and the trajectory modelling in Chapter 6. The software architecture, integration of the disciplines, and algorithm performance is then handled in Chapter 7. The results found by the optimisation scheme for the optimum vehicle are presented in Chapter 8, and the consequent sensitivity analysis with respect to the optimum solution and the optimisation as a whole in Chapter 9. Finally, the conclusions and recommendations are given in Chapter 10.

2

The State-of-Art

Mars has been one of the focal points of the space industry since the birth of the rocket. Although humans have yet to set foot on Mars, decades' worth of research, concepts, and plans have been made for human settlements. In this chapter, the state-of-art is handled, presenting the current plans for human Martian exploration, previous and current Martian ascent vehicle research, and crewed Single State To Orbit (SSTO) vehicles and vehicle research. The mission scenario that contextualises the need for the Martian SSTO vehicle is then discussed, as well as the necessary Martian infrastructure to accompany the vehicle. The research question and objectives are then presented last.

2.1. Vehicle Heritage

Exploring the heritage of SSTO vehicles as well as the current research of crewed Martian vehicles provides a search space for the vehicle design. It also allows for a wider understanding of the possibilities as well as the issues that arise when designing an SSTO for Mars. This section presents the history of SSTO and Martian vehicle research, but is first preluded by the current status of Martian exploration which details the need for the Martian vehicle.

2.1.1. Current Status of Human Martian Exploration

In the last decade, there has been a great push towards the first human on Mars. The presence of a permanent human settlement is of great interest to the scientific community, as it pushes the frontiers of human technology. There is also a great interest in the Martian resources, as well as more in-depth research of Mars itself, as thus far only automated machines have conducted the research. On another level, it is also the start of the expansion of the human species into the universe, and could perhaps even provide a way to prevent extinction of humankind on Earth.

The two current frontrunners in the race to Mars are NASA and SpaceX. SpaceX plans to go directly to Mars. Although the plans proposed in 2016 have been delayed significantly, the main transportation system intended for the architecture is making rapid progress. The Starship launch vehicle is a fully reusable Two Stage To Orbit (TSTO) vehicle, of which the booster stage, called the 'Super Heavy', ensures the vehicle escapes Earth's gravity well. The upper stage is the spacecraft that continues past LEO[1].

NASA, however, has determined a different approach. In August 2013, twelve space agencies that form the International Space Exploration Coordination Group (ISECG) issued the second edition of the *Global Exploration Roadmap*, documenting the international coordination efforts for future space missions and goals, including the exploration of Mars [50]. NASA utilises the architecture proposed by the ISECG and relies on coordinated efforts from other agencies such as ESA and ROSCOSMOS. In the proposal, the exploration of

---

[1] `https://www.spacex.com/vehicles/starship/`

Mars, and later the sustained human presence on Mars, is part of a greater long-term campaign. The mission scenario presented by the ISECG sends first robotic and human missions to the Moon, to advance technological readiness for crewed Mars missions, with eventually crewed Mars missions planned after 2030.

The ISECG identifies three phases for a settlement on Mars: Earth Reliant, Proving Ground, and Earth Independent. NASA plans to land astronauts on the Moon as part of the Proving Ground phase as early as 2024, and is currently working on the Artemis program and Lunar Gateway to achieve this[2].

From this conference, NASA conducted a study named the In-Situ-Resource-Utilisation-To-The-Wall study (ISRU-to-the-wall). It presents a conceptual transportation architecture designed to support future lunar and Mars campaigns aimed at establishing a permanent and self-sustaining human presence beyond Earth in the next half century, as a prelude to settlement and colonization [38]. In this, it is established that a taxi vehicle between the Martian surface from orbital node is essential to support a Martian settlement. The shuttle vehicle operations can be seen in Figure 2.1 as given by Komar et. al. [38], as it ferries cargo such as propellant and payload.

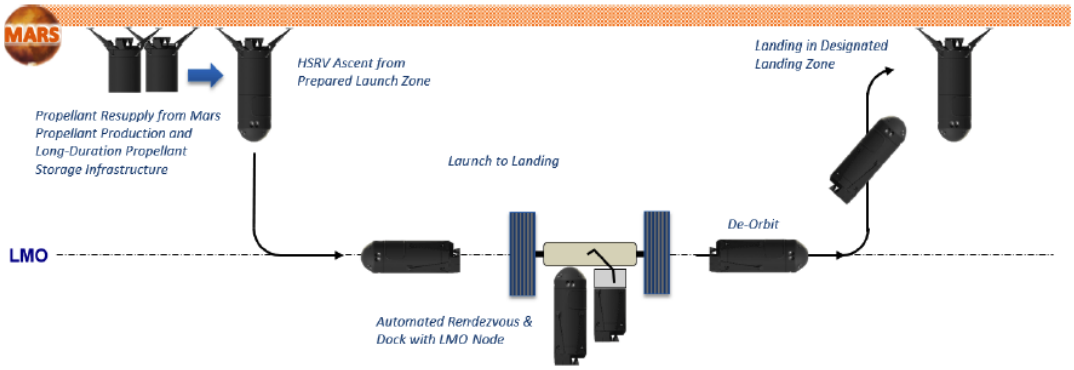

Figure 2.1: The mission operations for the Mars shuttle vehicle as given by Komar et. al. [38]

2.1.2. Single-Stage-to-Orbit Vehicle Heritage

The term SSTO refers to vehicles that expend no hardware to reach orbit. The benefit of this is that no hardware needs replacement after each launch, cutting manufacturing costs, as well as the delivery of the hardware and reassembly of the vehicle if the vehicle does not land on Earth. The vehicle is therefore much more suited for reusability, although for a vehicle to be fully reusable other factors must also be accounted for, as the vehicle must sustain multiple uses.

Non-recurring costs however, such as development costs, are much higher for SSTO vehicles than for multi-stage vehicles as engineering challenges for SSTO vehicles are substantial. The gravity well of Earth is deep enough that a very large volume of propellant is needed to reach an orbit about Earth, which is why launch vehicles jettison stages to shed mass and thereby minimise the propellant load. Technological advances to increase the propulsion efficiency, in turn decreasing propellant mass, have been the subject of much interest, however these have proven to be exceedingly expensive. These challenges have so far lead to no SSTO vehicle passing the development phase, many not even the conceptual. The gravity wells on the Moon and on Mars, however, do not pose the same challenge as on Earth, due to the bodies being much less massive. An SSTO for Mars is therefore a concept that is much easier to realise, vehicle's the transportation to Mars and other such factors notwithstanding.

Some examples of reusable SSTO vehicles designed for Earth can be found in Table 2.1. It should be noted that although the Space Shuttle and the Buran are examples of reusable vehicles, they are technically not SSTO vehicles, as they are rocket-launched. They do, however, closely resemble an SSTO in all other aspects, and have also actually flown, and can therefore serve as references. The Space Shuttle programme was, however, much more successful than the Buran. The Buran only once without crew before funds ran out (even though

---

[2] `https://www.nasa.gov/specials/artemis/#how`

Table 2.1: A number of conceptual and flown reusable vehicles

Name	Year Flown	Year Cancelled	Crewed	Launch	Propulsion
HOTOL[3]	-	1988	No	Horizontal	Airbreathing jet engine
Buran [26]	1988	1988	Yes (last and only flight uncrewed)	Rocket launch	Rocket engine
Skylon [65]	-	1993	No	Horizontal	Hybrid air-breathing and rocket engine
HORUS[4]	-	1994	Yes	Horizontal	Airbreathing
DC-X[5]	-	1994	No	Vertical	Rocket engine
X-33[6]	-	2001	No	Vertical	Aerospike
Space Shuttle[7]	1981	2011	Yes	Rocket launch	Rocket engine
XCOR Lynx [60]	-	2016	Yes	Horizontal	Rocket engine

the Buran was designed for crew), compared to 133 successful Space Shuttle flights.

2.1.3. Martian Crewed Vehicle Research

Much research has been conducted into how best to transport crew to and from the Martian surface, with varying conclusions. There have been stand-alone studies, as well as studies that have been continued and iterated over the years. Here, an overview of these plans and their progress made is presented.

From 1993 to 2009, NASA conducted a series of 5 studies called the Mars Design Reference Mission (DRM). A design reference mission is a plan that is that aims to identify the mission scenario, the technologies, the difficulties, the associated risks, and sometimes the cost of an endeavour, and is used to guide its technological development efforts. There have been a series of DRMs since 1993, each one a continuation of the previous, whilst expanding the options, scenarios and technologies available. Each iteration represents a snapshot of work in progress in support of planning for future human exploration of the Martian surface [29].

There have been other studies since the last DRM in 2009. In 2010 Hickman et. al. [28] continued to explore the architecture prescribed by the DRMs, however using the Bring Your Own Propellant approach, leading to both an SSTO and a TSTO concept. In 2017, as part of the ISRU-to-the-Wall campaign, Komar et. al. designed a reusable SSTO shuttle vehicle named Hercules [38], and that same year Cerimele et. al. designed a vehicle to land 20 metric tonnes of cargo on the martian surface using a mid lift-to-drag vehicle [12]. In 2019 Polsgrove et. al. explored design options for both a SSTO and TSTO configuration for a non-reusable Martian Ascent Vehicle (MAV) [54], and most recently, Gaffarel et. al. designed a fully reusable SSTO for a crew of 6 in 2021 [22]. An overview of these vehicle concepts is given in Table 2.2, with the Hercules vehicle and the Martian Ascent Vehicle (MAV) shown in Figure 2.2.

---

[3] `https://www.flightglobal.com/secret-files-reveal-us-interest-in-uk-hotol-spaceplane/85249.article`

[4] `https://www.hq.nasa.gov/pao/History/x-33/dcxtests.html#flight4`

[5] `https://www.nasa.gov/mission_pages/shuttle/flyout/index.html`

[6] `https://www.nasa.gov/centers/armstrong/history/experimental_aircraft/X-33.html`

[7] `http://www.astronautix.com/h/horus.html`

Table 2.2: A selection of crewed Martian concept vehicles

Author	**Year**	**Vehicle Type**	**Crew**	**Propellant**	**Target Orbit [km]**	**Reusable**
Zubrin [72]	1992	SSTO	4	LOX/LCH$_4$	Earth direct	No
NASA (DRM 5.0) [18]	2009	SSTO	6	LOX/LCH$_4$	250 x 33793	No
Hickman et. al. [28]	2010	TSTO	6	LOX/H$_2$	250 x 33793	No
Hickman et. al. [28]	2010	SSTO	6	LOX/LCH$_4$	250 x 33793	No
Komar et. al. [38]	2017	SSTO	4	LOX/LCH$_4$	500 x 500	Yes
Cerimele et. al. [12]	2017	Mid L/D Lander	4	LOX/LCH$_4$	-	No
Polsgrove et. al. [54]	2019	TSTO	4	LOX/LCH$_4$	250 x 33900	No
Gaffarel et. al. [22]	2021	SSTO	6	LOX/LCH$_4$	500 x 500	Yes

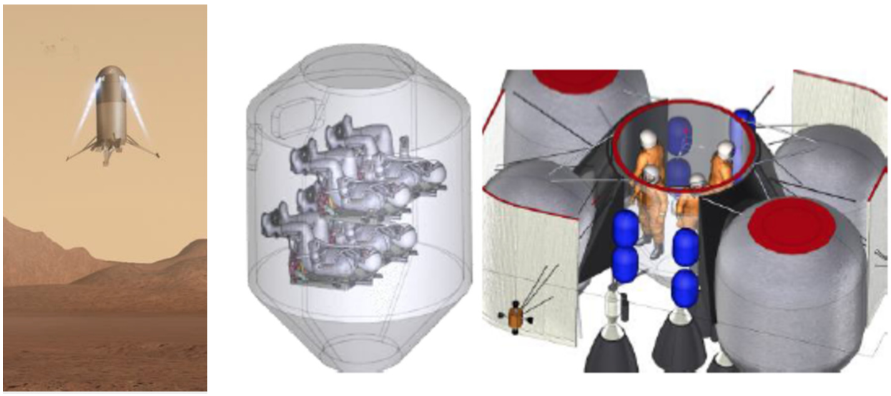

Figure 2.2: The ISRU-to-the-wall campaign's Hercules vehicle [38] (left) and the MAV configuration by Polsgrove et. al. [54] (centre, right)

As can be seen from Table 2.2, only two of the seven concept vehicles are designed to be reusable, where the other concepts are designed for one-time crewed ascent or descent only. However, as discussed in Section 2.1.1, if a human presence on Mars is to be sustained, a reusable vehicle is necessary that is capable of ferrying crew and cargo both ways. This scenario has only been explored thus far by by Komar et. al and Gaffarel et. al.. Neither of these two designs, however, have applied the usage of a global optimisation method to the design process. There is therefore a knowledge gap, as the design of the vehicle has not yet been guided by a global optimisation scheme.

2.2. Mission Overview

This section presents the mission scenario that necessitates the crewed SSTO vehicle. It begins with outline of the mission scenario, followed by the mission requirements, and lastly presents the infrastructure on Mars that is necessary for the endeavour, both on the surface and in orbit.

2.2.1. Mission Scenario

In May 2014, NASA released *Pioneering Space: NASA's Next Steps on the Path to Mars*, presenting the philosophy behind the pioneering of Mars [50]. Within this philosophy, sustainability is key. This means sustainability with respect to the transportation, habitability systems, maintenance, and the international partnerships, as all must be evolvable over decades [50]. The ability for the settlement to become self-sufficient therefore also relies heavily on the utilisation of in-situ resources. While previous mission studies focused on exploration of Mars, the sustainability philosophy ensures the investigation of In-Situ Resource Utilisation (ISRU) systems at the architectural and campaign level to enable a sustained human presence on Mars.

A team at NASA Langley Research Center considered conceptual designs for the infrastructure centered around ISRU in 2015. Their investigation, known as the ISRU-to-the-Wall study, has lead to the development of a

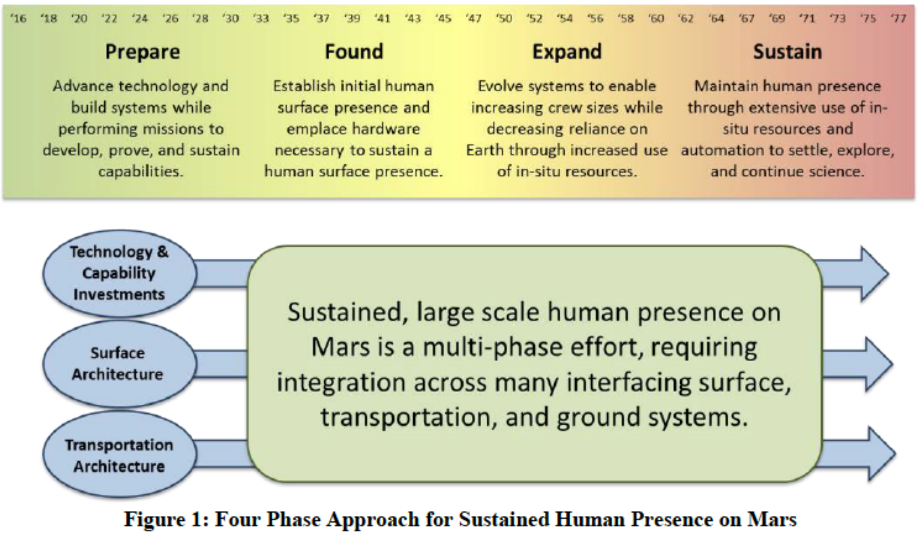

Figure 2.3: The four-phase approach for sustained human Martian presence [4]

multi-phase, multi-decade conceptual campaign following the sustainability philosophy presented by NASA [38]. This campaign follows on from the Global Exploration Roadmap [30], as discussed in Chapter 2. In this, the strategy towards pioneering Mars is broken down into four phases spanning multiple decades: Prepare, Found, Expand, Sustain. These are seen in Figure 2.3. The Prepare phase advances the necessary technologies, and also contains the human exploration of bodies to prove those technologies. The Found phase is the first human mission to Mars. The Expand phase is to increase the infrastructure laid down by the Found phase, such that increased capabilities in terms of resource exploitation, power generation, and human presence are developed. The Sustain phase is the gradual migration away from Earth dependence, and ensures that human presence can be sustained without reliance on Earth for resources.

The mission scenario presented here for the MSc research is based on the mission scenario envisioned in the NASA ISRU-to-the-wall campaign [4] [38], built upon three founding principles: reusable space transportation systems, maximum leveraging of Martian resources through ISRU, and the development of significant robotic capabilities for autonomous operations both on the Martian surface and in orbit.

The initial missions to Mars are uncrewed, focusing on delivery of necessary payloads for the surface infrastructure of a crewed Mars base, as per the Prepare phase. This will involve deploying the habitation modules, initiating the in-situ resource acquisition and processing, the propellant production, building the storage infrastructure, and setting up critical systems such as power and thermal control. Once the base is established to a degree sufficient for human settlement, the Found phase begins, followed by the Expand phase, and then the Sustain phase. To transport crew and cargo, an orbital node in a Lower Martian Orbit (LMO) of 500 km is placed during the Prepare phase, with a shuttle vehicle taxiing between the node and the Martian surface. The crewed mission concept of operations can be seen in Figure 2.4.

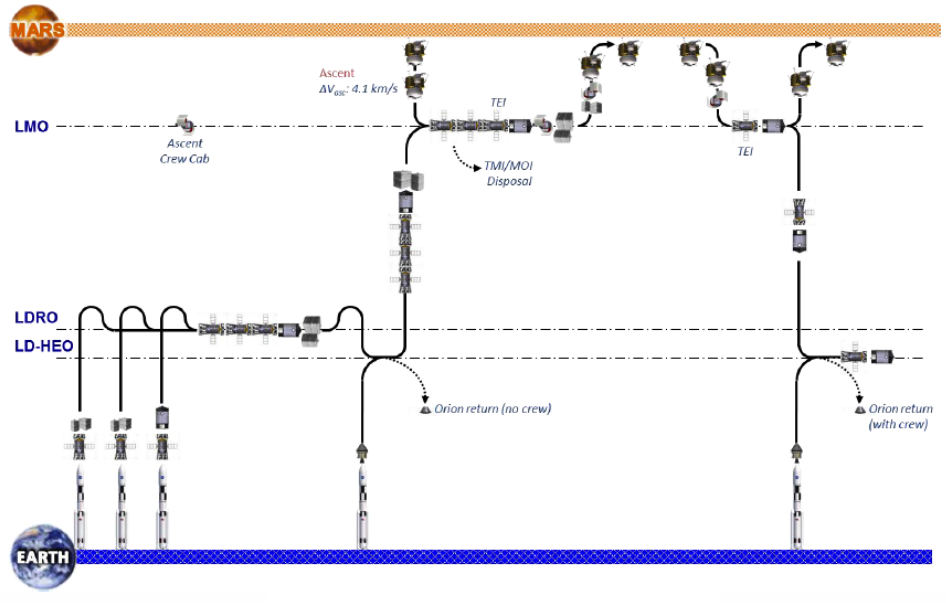

Figure 2.4: The crew mission concept of operations (LD-HEO: Lunar-Distant High Earth Orbit, LDRO: Lunar Distance Retrograde Orbit, TEI: Trans-Earth Injection, TMI: Trans-Mars Injection, MOI: Mars Orbit Insertion) [4]

As shown in Figure 2.4, the crew is first transported by Orion to a node in Lunar Distance Retrograde Orbit (LDRO), then begin their interplanetary journey to Mars. At Mars, a Mars Orbit Insertion (MOI) is performed and they dock with the Martian node in LMO. from the node the shuttle vehicle un-docks (in the figure named the Ascent Crew Cab, as crew from the Martian surface are also taken up to the Martian orbital node) and then descend to the Martian surface.

The long-term goal is that the settlement will gradually reduce its dependence on Earth, and eventually become self-sustaining, called for by the Sustain phase of the campaign. For this, the need for reusable space transportation becomes self-evident, applying especially to the shuttle vehicle between the Martian surface and the orbital node. Mars lacks the resources to manufacture a new ascent and descent stage with every delivery of crew or cargo, meaning it is critical for the vehicle to be reusable if the goal of the Sustain phase is to be achieved. The development of a reusable SSTO shuttle vehicle for crew is crucial for mission success.

2.2.2. Vehicle Requirements

As seen in Chapter 2, the research conducted in the field of crewed Martian mission have predominantly been focused on crewed one-way ascent vehicles, as opposed to a sustainable Martian shuttle vehicles. The mission scenario outlined in this section, however, calls for a reusable shuttle vehicle to transport crew and cargo. In order to fulfil its objective, it is subject to a number of requirements, which are listed below. These requirements are derived from the needs of such a vehicle on Mars and its subsequent performance, as well as remaining within the same mission scenario as the Charon and Hercules vehicles such that they may serve as references.

- MR-010: The vehicle shall transport 1200 kg payload, which includes a crew of 6, between the Mars base and an orbital node in LMO
- MR-020: The vehicle shall be reusable
- MR-030: The vehicle shall utilize propellant produced in-situ
- MR-040: The vehicle shall ensure the safety of the crew

2.2.3. Necessary Martian Infrastructure

In order to investigate the vehicle design, the infrastructure that would be present on Mars must be established. The includes the location and infrastructure of the base on the surface, and the infrastructure of the orbital nodes.

Location

The location of the base is highly important, as it impacts the climate the human settlement is subjected to, the in-situ resources available, the surroundings available for scientific research, and the latitude from which the vehicle will launch. NASA has identified 50 locations (called exploration zones) on Mars that have the potential to sustain a settlement, as seen in Figure 2.5 [25].

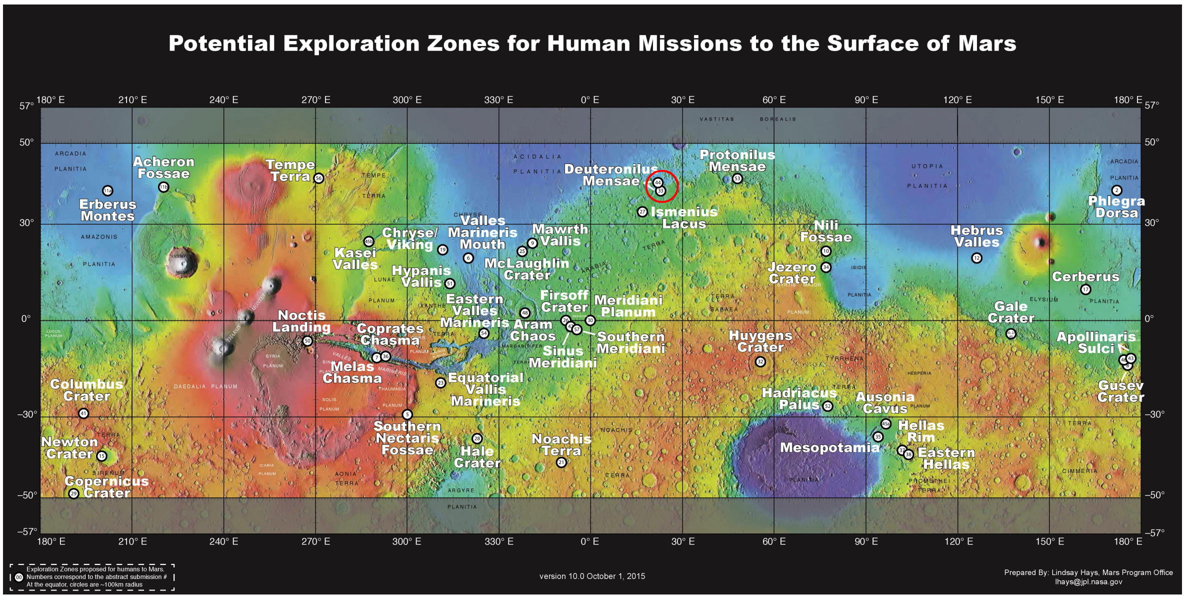

Figure 2.5: Locations of investigated exploration zones on Mars as provided by NASA [25]

In order to determine which location is best suited, a few criteria are determined: habitability for the crew, abundance of resources, ease of resource extraction, and the value of the scientific research that can be conducted at the location. Of the locations presented, Deuteronilus Mensae was deemed most suitable by the Human Landing Site Workshop, as ice resides close to the surface and is therefore easily acquired, as well as the location being less susceptible to dust storms [25]. Gaffarel et. al. also use this as their Martian base location [22]. Deuteronilus Mensae is the name given to the region that covers 344° - 325° West and 40° – 48° North, and lies at -3.7 km elevation [47]. It is circled in red in Figure 2.5. The Charon vehicle's base coordinates are taken, setting the base at 42.5° North and 25.5° East, due to the ability to therefore compare the optimum vehicle designs for the same scenario.

Martian Base Infrastructure

To sustain human presence in both the Earth-dependent and Earth-independent phases of the campaign, the Martian base must be able to provide a number of crucial things: power, habitation, propellant production, water production, and industry (for tasks such as maintenance of systems, water generation, and food production). Further, there must be a launch facility, a landing site, and mobility equipment to transport the shuttle vehicle from the landing site to the launch facility. These must be at a safe distance from the Martian base, as well as be located such that the shuttle does not pass over the base to minimise risk. The architecture of the base and the interactions between each facility can be seen in Figure 2.6, based on the architecture of the ISRU-to-the-wall campaign [38].

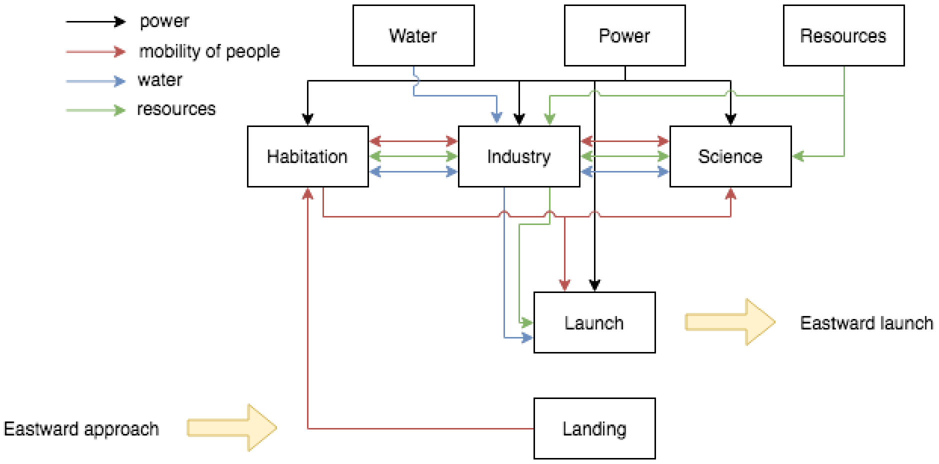

Figure 2.6: The infrastructure of the Martian base based off of the architecture in the ISRU-off-the-wall campaign [38]

Although the settlement will rely on Earth during the Found and Expand phase, the goal is to become Earth-independent. The industry plant in Figure 2.6 must therefore be capable of recycling and manufacturing parts for the shuttle vehicle, and offer maintenance capabilities which are performed autonomously. Further, the industry plant generates and stores the propellant for the vehicle, for which the water in ice form is used. Other autonomous systems include mobile offloading equipment after vehicle landing, and propellant transportation to the launch site. All these facilities are connected to a power grid.

Orbital Infrastructure

As in the ISRU-to-the-wall campaign, the orbital node is placed in a LMO orbit during the Prepare phase. The node primarily functions as the port between the interplanetary transportation vehicle and the Martian surface. The shuttle vehicle delivers cargo and crew arriving from Earth from the node in LMO to the Martian base, refuels at the base, and returns to the node with 6 other crew members and cargo (for provisions such as fuel and food). The node therefore has multiple docking ports for the vehicles, and allows for the transport of cargo and crew between the interplanetary transport vehicle and the shuttle vehicle, as well as incorporating a habitation module for the crew such that short-duration stays are possible. In order to be self-sustaining, the node must be capable of autonomous maintenance and assembly. Propellant and other equipment and goods needed for node maintenance and human habitation are delivered by the shuttle vehicle when it arrives from the Martian base.

The 500 km circular orbit is chosen for the node by Komar et. al. [38] to reduce the propellant mass requirements for the shuttle vehicle. An elliptical orbit for the node would reduce the delta-V necessary for the interplanetary transport vehicle to circularise before rendezvous with the node, however the delta-V saved would be added to the budget for the shuttle vehicle. As the interplanetary transportation systems are planned to arrive only once per year, as opposed to twice per year for the shuttle vehicle, shifting the burden to the interplanetary vehicle is more efficient.

To allow for communication between the Martian base, the node, the shuttle vehicle, and Earth, a number of communication relay satellites is required in a configuration around Mars. This will consist of three satellites in circular orbit, as per the design of the Charon vehicle's mission architecture by Gafferel et. al. [22]. Three satellites is the minimum number required to allow for 100% uptime communication and full coverage of Mars.

2.3. Research Goals

From the research conducted into the possible future concepts for a sustained human presence on Mars, it is clear that a crewed reusable Martian SSTO vehicle design is necessary. However, no global optimisation method has yet been applied, and it is therefore of value of explore the results that would be obtained through the usage of one. The research objective is presented below:

Research Objective:
To investigate the optimal design of a crewed reusable Martian single-stage-to-orbit shuttle vehicle, with respect to its gross take off weight, by using a multi-disciplinary design optimisation scheme to determine the various key aspects of its design and of its ascent and descent trajectories

This research objective can be split into individual sub-objectives. These are identified as the following:

- SO1 - To identify the various aspects of the vehicle design relating to the optimal vehicle design (the design variables)
- SO2 - To use the design variables to develop models to simulate the ascent and descent trajectories
- SO3 - To implement the design of the vehicle and the trajectories into an MDO to find the optimum design

From these goals, the primary research question can be formulated. Again, the primary research question can be broken down into sub-questions that are essential in answering the primary research question. Therefore, the primary research question is presented below:

Research Question:
What is the optimal design of a crewed reusable Martian single-stage-to-orbit shuttle vehicle and its trajectory in terms of its gross take off weight?

As an optimisation must always have an objective function, meaning a goal or direction, its Gross Takeoff Weight (GTOW) is taken. In reality, a vehicle will be optimised for cost, however in this case it has been chosen to optimise its mass. There are a variety of cost models that may be used to estimate the costs associated with a vehicle, however the Martian shuttle vehicle is a concept that will still take decades to realise. The material and perhaps manufacturing costs may be estimable, however the development costs, operational costs, possible training costs, transport costs, propellant costs, and other hidden costs cannot be estimated within any reasonable accuracy. The inaccuracies arise due to the lack of operational reference vehicles, as well as the time scale of the concept. The operational and transport costs, however, are largely tied to the mass of the vehicle, as the propellants it uses must be produced, and the vehicle must be transported to Mars. The GTOW incorporates both the dry mass and propellant mass, and therefore is an indicator of the costs.

This research objective can be broken down into individual sub-questions to clearly define how the primary research question must be answered.

- SQ1 - How does the mission scenario affect the GTOW
    - SQ1.1 - How do the target insertion orbit and subsequent rendezvous strategy affect the GTOW
    - SQ1.2 - How does the Martian base location affect the GTOW
- SQ2 - How do the imposed constraints affect the GTOW
    - SQ2.1 - What is the effect of presence of crew on the GTOW
    - SQ2.2 - How does a change in payload affect the GTOW
- SQ3 - How do different ascent thrust profiles affect the GTOW

The novelty of this research is the application of an MDO to the design of a Martian SSTO using an MDO scheme. Using an MDO scheme ensures that the optimum design is found when taking various disciplines into account simultaneously, and exploiting their interactions. This is a method can therefore be superior to sequentially engineering the design.

This research can aid allocation of the design and engineering efforts to the dominant factors that affect the vehicle and trajectory design. Knowing what the factors in the design are that have the most effect on the GTOW, and therefore usually also on cost, is a great benefit. The results will be able to serve as a preliminary concept from which other studies can refine the design of the vehicle and trajectories.

3

Numerical Optimisation Theory

The optimisation of the vehicle and trajectory designs requires the implementation of an optimisation scheme. For this, various different optimisation concepts are necessary, which are outlined in this chapter. Firstly, the basics of the global optimisation scheme that is responsible for the optimisation of the design as a whole is outlined. Optimal control law, that is responsible for the guidance of the vehicle throughout the trajectory, is then discussed, and lastly various types of optimisers, as well as the software implementation, is presented.

3.1. Multidisciplinary Design Optimisation

Finding the optimal design of a vehicle is a very complex process, and requires the use of Multidisciplinary Design Optimisation (MDO) methods. This technique allows for many different disciplines, often have conflicting objectives, to be taken into account concurrently. This section covers the basics of MDO. It begins with the formulation of an MDO, then defines and discusses the various parameters involved.

3.1.1. MDO Formulation

The MDO can be formulated as shown in 3.1, as presented by Balesdent [6].

$$\begin{aligned} \text{minimise} \quad & f(x,y,z) \\ \text{with respect to} \quad & z = \{z_{sh}, \bar{z}_k\} \\ \text{subject to} \quad & g(x,y,z) \leq 0 \\ & h(x,y,z) = 0 \\ & \forall i, \forall j \neq i, y_i = \left\{c_{ij}(x_i, y_i, z_i)\right\}_j \\ & \forall i, R_i(x_i, y_i, z_i) = 0 \end{aligned} \tag{3.1}$$

3.1.2. MDO Variables

Three different types of variables can be identified in the MDO. They are defined as the following:

- z: these are the design variables, and are the ones that are changed throughout the optimisation process to obtain the optimal design. z_{sh} denotes the shared variables, the $\bar{z}_k$ the variables that are specific to one subsystem only.
- x: these are the state variables. These can vary throughout the optimisation process, however they are not independent variables and depend on the design variables. These variables vary in order to find the equilibrium in the state equations.
- y: these are the coupling variables. As the subsystems are not independent from each other, variables are needed to express the coupling between them.

3.1.3. MDO Constraints

Constraints form the search area for the optimisation. Two types can be identified, defined as the following:

- g: these are inequality constraints. These are limitations set which parameter values are not allowed to cross
- h: these are equality constraints. These are binding constraints that force a solution to meet a certain value

3.1.4. MDO Functions

Functions are central to an MDO. The following functions are defined as follows:

- $f(x,y,z)$: this is the objective function of the optimisation. This function defines the fitness of the current solution
- $c(x,y,z)$: this is a coupling function. There can be more than one function, as they define the coupling interactions between the subsystems, and compute the coupling variables y. $c_{ji}(x_i,y_i,z_i)$ defines the coupling from subsystem i to j
- $R(x,y,z)$: this is the residual function. The residuals quantify the satisfaction of the state equations

3.1.5. MDO Methodology

Balesdent [6] investigated various different MDO methodologies, as within the MDO method can be applied in many different ways. For example, multiple optimisers can be used (multi-level methods), but also a single optimiser can be used (single-level methods). Further, it can also be defined whether the coupling constraints are checked at every individual iteration, or whether the consistency of coupling is only checked for consistency once a solution is found.

Van Kesteren investigated the use of different MDO methods [34], and deemed the Multi Discipline Feasible (MDF) method to be the most effective when applying MDO to launch vehicles. This method is monolithic, meaning it contains one system only. It is therefore is a single-level method, and is the most common method that is applied to launch vehicle design. All constraints are checked at every iteration, meaning the optimisation is guaranteed to converge on a solution in which the coupling is consistent. Consequently, however, the method takes longer to converge than others, and is more computationally expensive. The architecture of an MDF can be seen in Figure 3.1, as given by Balesdent [6]. As can be seen, the design variables are the input, each subsystem is analysed as the design progresses, and the constraints and objective function are the output of the analysis. The optimiser than uses these to determine the fitness of the design.

3.1.6. The Objective

In order to set up the MDO, the objective(s) for the objective function must be defined, as well as the constraints. The objective defines what the optimiser should minimise (or optimise), and is therefore the goal of the optimisation scheme.

In previous MDOs conducted by van Kesteren [34], Miranda [44], and Rozemeijer [58], both the GTOW and cost are taken as objectives. However, as also mentioned in Section 2.3, the mission scenario for the Martian vehicle is still decades away, as well as the vehicle being the first of its kind. This not makes estimating the manufacturing costs hard to estimate, due to the technological advances in areas such as materials and propulsion, as well as manufacturing itself, but that also other costs associated with development, transport, and operation, as well as other costs are exceedingly difficult to forecast. As a vehicle's GTOW has a strong correlation to its cost, predominantly transport and operations, the GTOW is chosen to be the single objective function for the Martian vehicle. The objective function can therefore be written as the following, where M_i is the initial mass of the vehicle before launch:

$$J = M_i \tag{3.2}$$

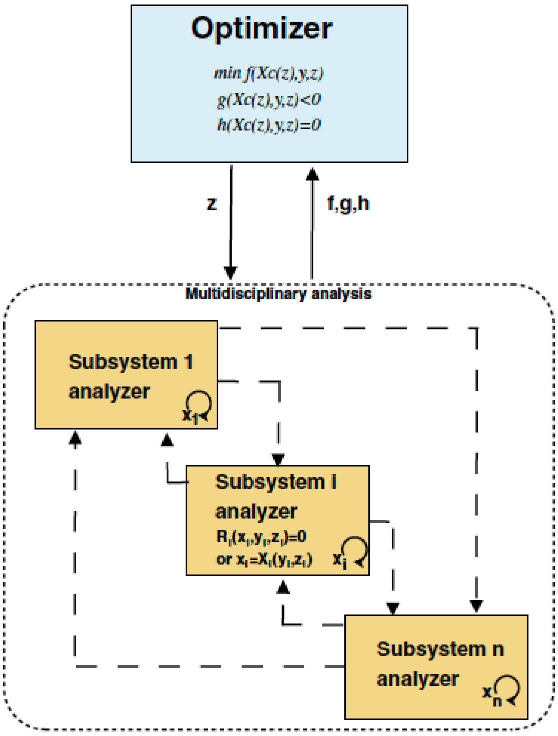

Figure 3.1: The architecture of an MDF as given by Balesdent [6]

3.2. Optimal Control Law

Optimal control covers the different types of methods by which to optimise a dynamical system. The consequence of this is that as well as satisfying constraints, the dynamics also must be satisfied, meaning that a control input is needed, hence its given name.

The optimal control problem can be formulated as presented by Boere [10]. A set of first-order differential equations that describe the dynamics of the system is written as Equation 3.3, where s is the state equation, as u is the control law that must satisfy the objective function, and t the time.

$$\dot{x} = s(x(t), u(t)) \tag{3.3}$$

Boundary conditions are then imposed upon the problem, that can be formulated as Equation 3.4, where t_f denotes the final time.

$$h_f(x(t_f), u(t_f), t_f) = 0 \tag{3.4}$$

The control functions $u(t)$ must be found such that the cost function (seen in Equation 3.5) is minimised.

$$J = \phi(x(f_f, t_f)) + \int_{t_f}^{t_0} L(x(t), u(t))dt \tag{3.5}$$

The dynamical system (3.3) is continuous, however the boundary conditions (3.4) are discrete. In order to overcome this, the Pontryagin Minimum Principle is used. The Lagrangian form is first defined by Equation 3.6, as given by Betts [8]. λ denotes the adjoint or costate variables for the continuous (differential equation) constraints, and μ the discrete constraints.

$$\hat{J} = [\phi + \mu^T H_f] + \int_{t_0}^{t_f} \lambda^T(t)[s(x(t), u(t)) - \dot{x}]dt \tag{3.6}$$

The Hamiltonian is then defined, shown in Equation 3.7, in combination with the auxiliary function, Equation 3.8. The conditions for optimality are then given in Equations 3.9 and 3.10, called the Euler-Lagrange equations [8].

$$H = \lambda^T(t)s(x(t), u(t)) \tag{3.7}$$

$$\bar{F} = f + \mu_f^T \tag{3.8}$$

$$\dot{\lambda} = -H_x^t \tag{3.9}$$

$$0 = H_u^T \tag{3.10}$$

$$\lambda_{t_f} = \bar{F}_{x_t = t_f}^T \tag{3.11}$$

The optimal control problem can be solved using the direct method. The direct method transforms the optimal control problem into a Non-Linear Programming (NLP) problem [10]. The NLP is then solved for a finite set of variables. By transforming the problem to an NLP problem, there is no need for analytical expressions or initial guesses, meaning that the convergence region is large. The NLP can then be solved using a variety of different techniques. The finite set of parameters can be described as shown in 3.12, where p number of parameters are used.

$$u(u_{p_i}, t) = \begin{cases} u_{p_{11}} + u_{p_{12}} t & \text{if } t \in [t_0, t_1] \\ u_{p_{21}} + u_{p_{22}} t & \text{if } t \in [t_1, t_2] \\ & \vdots \\ u_{p_{n1}} + u_{p_{n2}} t & \text{if } t \in [t_{n-1}, t_n] \end{cases} \tag{3.12}$$

The problem can then be reformulated as shown below.

$$\begin{aligned} \text{minimise} \quad & f(x(t_f), t_f) \\ \text{with respect to} \quad & u_{p_i}, i = 1, ..., n \\ \text{subject to} \quad & \dot{x}(t) = s(x(t)u(u_{p_i}, t)) \\ & h_f(x(t_f), u(u_p t_f), t_f) = 0 \end{aligned}$$

The direct approach can be solved using the explicit method. To reduce the number of design variables involved, parametric laws can be introduced, such as a pitch control law, as implemented by Balesdent [6], van Kesteren [34], and Miranda [44]. This law defines the required dynamical state of the vehicle at specific timestamps in the trajectory, interpolating the points between the timestamps.

3.3. Optimisers

Once the optimisation problem has been set up, the optimiser itself must be chosen. As there is only one objective in this optimisation, only single-objective optimisers are used. Previous work on MDO for launch vehicles by Miranda [44], van Kesteren [34], Rozemeijer [58], [14] Contant, and Haex [23], have shown that implementing metaheuristic optimisation schemes can be utilised with success.

Metaheuristic optimisation falls under a branch of optimisation techniques called Genetic Algorithm (GA)s. A GA, as the name suggests, is inspired by the Darwinian theory of evolution, and implements biologically inspired operators such as mutation, crossovers, and selection. The vast range of ways they can be modified to suit both the problem and the user's needs make them hugely powerful tools. Although there are many ways in which a genetic algorithm may be constructed, there are a number of fundamentals that are almost present. A schematic of a basic genetic algorithm is given in Figure 3.2.

As seen in Figure 3.2, to start the algorithm, an initial population must be generated using the design variables, of which each individual's fitness is then assigned. The fitness is a value that indicates how 'well' the individual performs. Various GA operators can then be applied, such as, but not limited to, selection, crossover,

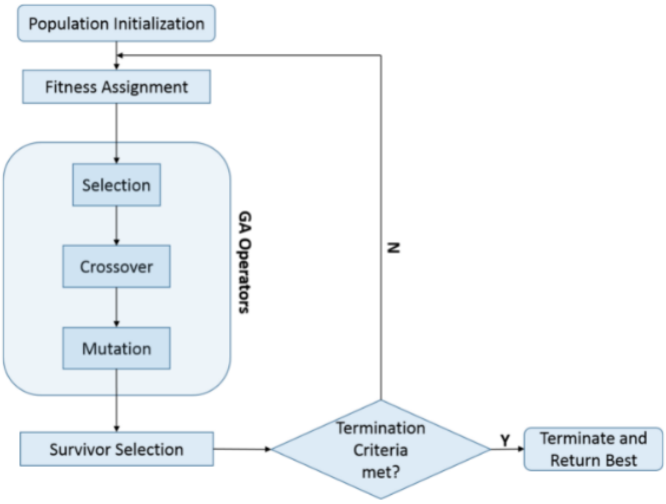

Figure 3.2: A schematic of a simple genetic algorithm as given by Deshpande and Kumar [17]

and mutation. These operators generate new individuals within the population either from the existing individuals, or new ones. How this is done is GA-specific. The population size, however, remains constant, and therefore only the number of best performing individuals of the population size then progress to the next step, where the termination criterion must be met for the algorithm to stop. If is has been met, the algorithm terminates, and the population is returned. If not, the fitness of the new population is evaluated, and the cycle continues.

GAs are highly relevant for industrial applications, because they are capable of handling problems with non-linear constraints, multiple objectives, and dynamic components [56]. Throughout MDOs completed at the TU Delft, various GAs have been investigated and implemented, including Particle Swarm Optimisation (PSO) (Miranda [44], van Kesteren [34]), Particle Swarm Optimisation Generational (PSOG) (Rozemeijer [58]), Multi-Objective Evolutionary Algorithm on Decomposition (MOEA/D) (Rozemeijer [58]), and Differential Evolution (DE) (Rozemeijer [58], van Kesteren [34], Haex [23], Miranda [44], Contant [14]). The choice of optimiser, as well as the associated settings, is discussed in parallel with the discipline integration into the MDO scheme in Section 7.4.

3.4. Software Implementation

To implement the MDO, a software tool must be chosen. Although there are various libraries available for trajectory and vehicle modelling, as well as optimisation methods, in popular software such as Python and MATLAB [58], the choice that is made in this optimisation is Tudat.

Tudat (TU Delft Astrodynamics Toolbox) is a powerful set of C++ libraries that support astrodynamics and space research[1]. It is publicly available on Github[2], and is used across the faculty to simulate and optimise vehicles, satellites, trajectories, and other phenomena. The environment offers various integrators and propagators, acceleration models, environmental models, and aerodynamic guidance models. For optimisation purposes, ESA's Parallel Global Multiobjective Optimizer (PaGMO) library is implemented, which is an optimisation library that supports metaheuristic optimisers, to name but a few capabilities[1]. Due to this, the focus of the optimisation is the architecture and the implementation of all the various necessary inputs, as opposed to developing the individual aspects needed for the optimisation from scratch. Rozemeijer [58], Miranda [44], van Kesteren [34], and Haex [23] all implement the MDO of their vehicles successfully using Tudat.

---

[1] `https://tudat.tudelft.nl/`

[2] `https://github.com/Tudat`

[3] `https://esa.github.io/pagmo2/`

4

Vehicle Design and Sizing

The design of the vehicle is a combination of various different disciplines that must individually be addressed, however when combined they determine the vehicle design. This chapter covers the disciplines that determine the characteristics of the vehicle itself, and handles their respective validation. The main engine performance is first discussed, followed by the geometry and mass disciplines.

4.1. Main Engine Performance

The main engine propulsion system is responsible for providing the thrust that propels the vehicle to the desired orbit, as well as providing the necessary deceleration before landing. In order to size the propulsion system, the fundamentals of rocket propulsion must be understood, as well as choices concerning propellant and engine type must be made. This section presents the chosen engine configuration, propellant choice, the governing principles, and the validation of the propulsion discipline.

4.1.1. Engine Configuration

There are three main types of rocket engines for launch vehicles: solid motors, liquid bi-propellant engines, and a hybrid engines. A bi-propellant engine consists of a fuel and an oxidiser that are combusted, and a solid motor is a hard grain that is ignited. A hybrid motor usually consists of a solid fuel and liquid oxidiser that is vaporised and passed over the solid grain (although the opposite is sometimes also implemented).

The engine configuration choice must fulfil two main requirements (that are stated in Section 2.2.2): the vehicle must be reusable (MR-020), and the vehicle must utilise propellant that is produced in-situ (MR-030). The fuels and oxidisers generally used in solid and hybrid engines cannot be produced on Mars, meaning that they are impossible to manufacture in-situ. A solid motor can also not be turned off and then restarted, meaning it is not reusable. As the solid motor and the hybrid engine cannot comply with the requirements, the only option is to use a liquid bi-propellant engine. A liquid bi-propellant is therefore the configuration choice.

A liquid bi-propellant can further be broken down into pressure-fed systems and pump-fed systems. In a pressure-fed system, the propellant is pushed into the combustion chamber due to the pressure of either the tank or the pressurant gas. A pump-fed system, on the other hand, utilises turbopumps to transfer the propellant from the tank to the combustion chamber, which are driven by different means depending on the cycle configuration. These include an electric motor, exhaust gases, and a pre-burner. Although pump-fed systems are more complex than pressure-fed systems, they can offer mass benefits, as no external pressure tanks are needed [31]. Pressure-fed systems also are characterised by lower thrust than pump-fed systems, and limited throttle capabilities [21]. These two characteristics are large drawbacks and consequently the engines are chosen to be pump-fed. The propulsive landing the vehicle must execute requires the engines to be deep-throttled, and for the vehicle to launch without expending stages it must have a high thrust to weight ratio. The decision to use a pump-fed system is also made by Gaffarel et. al. for the Charon vehicle [22], and Komar et. al. for Hercules vehicle [38]. This is further restated by Hickmann et. al. [28] when investigating the optimum design for the MAV.

Typically pump-fed engines still require a pressurant such that a positive suction head for the pump is maintained [27]. In order to overcome this, the Hercules vehicle uses the gas from the main propellant tanks as a pressurant, thereby also eliminating the need for helium, an element that is not found in sufficient quantities on Mars. This method is similar in form and function to the Integrated Vehicle Fluids (IVF) system in development at United Launch Alliance [38]. The Charon vehicle further also does not use pressurant for their engines [22], and SpaceX's methalox Raptor engine incorporates an autogenous pressurisation system to eliminates the need for a pressurisation system. The Raptor's fuel tank pressurisation can be achieved through the use of gas from the fuel line after leaving the regenerative cooling circuit, while the oxidiser tank pressurant can be obtained from the turbopump discharge[1]. With this knowledge, it is assumed that such a system will also be possible for the Martian shuttle vehicle engines, and a pressurisation system is thus not integrated in the bi-propellant engines.

4.1.2. Propellant Type

The propellant type is crucial for the propulsion system, as it determines many aspects of the engine performance, as well as engine design. As stated by vehicle requirement MR-020 and MR-030, however, the propellants used must be produced from the available Martian resources, as well as be applicable for an engine that restarts.

The chosen oxidiser and fuel combination for the vehicle is chosen to be liquid methane (LCH_4) as the fuel and liquid oxygen (LOX) as the oxidiser. This combination, as opposed to LOX and hydrazine or LOX and liquid hydrogen (LH2), is chosen for a number of reasons. Hydrazine is an incredibly toxic fuel, and handling it poses a huge risk. Due to this, hydrazine is not considered appropriate considering the safety of the colony on Mars. LH2 is, on the other hand, non-toxic, and can easily by synthesised through electrolysis using the water found in the Martian ice caps. The standard Oxygen-to-Fuel mixture ratio (O/F) ratio of 8, however, means that a very high volume of liquid hydrogen is needed, putting pressure on the rate of water extraction when acknowledging that the human colony also requires water. The low density of liquid hydrogen when compared to liquid oxygen (70 $\mathrm{kg/m^3}$ to 1150 $\mathrm{kg/m^3}$), coupled with the high O/F ratio, also means that a very high volume of liquid hydrogen is needed, affecting the required tank volume.

LCH_4 can be synthesised through the Sabatier reaction, shown in Equation 4.1. Water must still be electrolysed for the liquid oxygen oxidiser, however the volume of production is much lower due to the lower O/F ratio of 3.5 [42]. CO_2 is in abundance on Mars, as the atmosphere is mostly composed of CO_2.

$$\mathrm{CO_2 + 4H_2 \rightarrow CH_4 + 2H_2O} \tag{4.1}$$

Due to the high O/F ratio and the low density of liquid hydrogen, the methalox combination (LOX/LCH_4) is chosen as the most appropriate propellant combination. As seen in Chapter 2, almost all Martian vehicles also use the methalox combination, with the two exceptions being the SSTO and TSTO vehicles designed by Hickman et. al. that use the LOX/LH2 combination [28]. The Starship vehicle being developed by SpaceX for interplanetary journies including Mars will also be propelled using methalox engines, namely the Raptor engines [63].

4.1.3. Ideal Rocket Theory

In chemical propulsion, thrust is generated by converting the chemical energy in the propellant to kinetic energy by combusting the propellants in the combustion chamber, which are then expelled out of the nozzle at high velocities opposite to the direction of flight. The thrust force can be described by Equation 4.2, where F denotes the thrust, $\dot{m}$ the mass flow rate, v_e the exhaust velocity, p_e the exhaust pressure, p_a the ambient

---

[1] `https://spaceflight101.com/spx/spacex-raptor/`

pressure, and A_e the nozzle exhaust area. This equation, as well as all other equations in this subsection, are taken from Zandbergen [70]. The thrust can also be written as Equation 4.3, where it is dependent on the thrust coefficient C_f and the characteristic velocity c^*, both being parameters by which engine performances are typically characterised.

$$F = \dot{m} v_e + (p_e - p_a) A_e \tag{4.2}$$

$$F = \dot{m} C_F c^* \tag{4.3}$$

The engine specific impulse, I_{sp}, is another characteristic of engine performance, and can be determined by the thrust coefficient and the characteristic velocity. This is seen in Equation 4.4, where g_0 denotes the Earth's gravitational acceleration at sea level. The specific impulse can also be used to calculate the thrust, as shown in Equation 4.5.

$$I_{sp} = \frac{C_F c^*}{g_0} \tag{4.4}$$

$$F = \dot{m} I_{sp} g_0 \tag{4.5}$$

These engine performance parameters, the thrust coefficient and the characteristic velocity, can be calculated using Ideal Rocket Theory. Ideal Rocket Theory is the name given to the the fundamental concepts for propulsion design that have a number of assumptions associated with them. These are that the fluid is a perfect, calorically ideal gas of constant homogeneous chemical composition; the flow is steady, isentropic, mono-dimensional, with purely axial velocity; no friction or other external forces act on the gas flowing in the nozzle.

In order to determine the propulsion system performance, the characteristic velocity and the thrust coefficient must be determined such that the thrust and specific impulse can be obtained. First the Vandenkerckhove parameter is defined, given by Equation 4.6, where γ denotes the ratio of specific heats. The characteristic velocity can then be obtained as seen in Equation 4.7, where R_A denotes the universal gas constant, M_W the molecular mass, and T_c the chamber temperature. The throat area can then be determined using Equation 4.9, where p_c denotes the chamber pressure.

$$\Gamma = \sqrt{\gamma} \left(\frac{2}{\gamma + 1} \right)^{\frac{\gamma+1}{2(\gamma-1)}} \tag{4.6}$$

$$c^* = \frac{1}{\Gamma} \sqrt{\frac{R_A}{M_W} T_c} \tag{4.7}$$

To determine the thrust coefficient, first the expansion ratio is needed. The expansion ratio ε is the ratio between the throat area A_t and the exhaust area A_e of the nozzle. This is given in Equation 4.8, where p_c denotes the combustion chamber pressure. The throat area can first be found from the characteristic velocity, as seen in Equation 4.9. The thrust coefficient relationship is then given in Equation 4.10.

$$\varepsilon = \frac{A_e}{A_t} = \frac{\Gamma}{\sqrt{\frac{2\gamma}{\gamma - 1} (\frac{p_e}{p_c})^{(\frac{2}{\gamma})} \left(1 - (\frac{p_e}{p_c})^{(\frac{\gamma}{\gamma-1})} \right)}} \tag{4.8}$$

$$A_t = \frac{c^* \dot{m}}{p_c} \tag{4.9}$$

$$C_F = \Gamma \sqrt{\frac{2\gamma}{\gamma - 1} \left(1 - \left(\frac{p_e}{p_c} \right)^{(\frac{\gamma-1}{\gamma})} \right)} + \left(\frac{p_e}{p_c} - \frac{p_a}{p_c} \right) \varepsilon \tag{4.10}$$

4.1.4. Main Engine Performance Design Variables

The design of the propulsion system can be approached in various manners. The design variables, however, must represent the inputs that the greatest effect on the design, or be the variables that characterise an engine. These are identified below.

$$Z_{prop} = \left[p_c, O/F, D_e, \dot{m}\right]$$

The chamber pressure (p_c) of an engine has a direct effect on the engine thrust, as well as its structural mass. It also affects the manner in which the pump system must be designed, which can be one of the most challenging aspects of designing a pump-fed engine [21] [23]. The mixture ratio (O/F) is necessary, as it determines the thermochemical characteristics of the combustion process. The exit diameter (D_e) is chosen as it determines the expansion ratio of the engine, and greatly determines the geometry of the engine as well as having an effect on the overall geometry of the vehicle. Lastly, the mass flow ($\dot{m}$) of the engine is determined to be a design variable as it also has a great effect on the size of the engine, as it sizes the throat, as well as greatly influencing the thrust. In Section 7.2 the search space of the design variables is given.

4.1.5. Propellant Thermochemistry

As seen from the Ideal Rocket Theory presented in Section 4.1.3, in order to determine the engine performance, the specific heat ratio γ, mean molar mass M_W, and chamber temperature T_c for the engine are needed. These properties, however, are dependent on the chemical reactions within the combustion chamber and nozzle, which in turn are dependent on the design variables chamber pressure and mixture ratio.

In order to determine these properties as a function of the input design variables, the online NASA programme Chemical Equilibrium with Applications (CEA) is used. CEA is a publicly available programme that calculates chemical equilibrium product concentrations from any set of reactants, and determines thermodynamic and transport properties for the product mixture[2]. It therefore calculates the specific heat ratio, mean molar mass, and chamber temperature directly from the chamber pressure, mixture ratio, and known propellants. To implement this within the MDO, a database of the three thermochemical properties is constructed, dependent on the chamber pressure and mixture ratio. The database therefore acts as a two-dimensional look-up table, between which the points are interpolated such that the thermochemical properties can be retrieved for any combination of chamber pressure and mixture ratio (between their respective bounds). This method has been successfully implemented by Haex [23], Rozemeijer [58], and van Kesteren [34].

For the construction of the database, the bounds for the chamber pressure and mixture ratio must be set, given in Table 4.1. The upper bound of 33 MPa is the current record for chamber pressure in a rocket engine, held by SpaceX's Raptor engine (which is also a pump-fed methalox engine) [49], and the lower bound is set to 0.5 MPa to allow for a wide range of chamber pressures. The chamber pressure has a direct link to the thrust of the engine, and as the number of engines will be varied in the optimisation (as will be further discussed in Section 4.2), the engines' thrust must also accommodate a wide range. The mixture ratio, however, does not vary as widely, as it only determines the stoichiometric relations of the propellants. Its range is set between 3 and 4, as all mixture ratios found in literature for methalox engines are in that range.

Table 4.1: The bounds of the design variables associated with the propulsion system

Variable	**Minimum**	**Maximum**
p_c [MPa]	0.5	33
O/F [-]	3	4

---

[2] `https://www.grc.nasa.gov/www/CEAWeb/`

4.1.6. Main Engine Performance Validation

In order to validate the model, its calculated engine performance must be compared to that of literature. This determines whether the model is sufficiently accurate, as well as allowing the model inaccuracies to be quantified. Ideal Rocket Theory deviates from reality, therefore quality factors must be calculated by comparing the modelled performance to real engine performance, which can then applied to the modelled thrust and specific impulse. The quality factors are the thrust quality factor, given in Equation 4.11, and the propellant consumption quality factor, given in Equation 4.12. ξ_T denotes the thrust quality factor, ξ_P the propellant consumption quality factor, F_r the real thrust, F_m the modelled thrust, $I_{sp,r}$ the real specific impulse, and $I_{sp,m}$ the modelled specific impulse.

$$\xi_T = \frac{F_r}{F_m} \tag{4.11}$$

$$\xi_P = \frac{I_{sp,r}}{I_{sp,m}} \tag{4.12}$$

Various pump-fed methalox engines are found in literature. Their design variables are used as input for the model, and the thrust and specific impulse calculated by the model are compared to the real values found in literature. These can be found in Table 4.2. It should be noted that the thrust and specific impulse values given are for vacuum conditions.

Table 4.2: The validation data for the engine performance. Values appended with * are calculated using engine data taken from the literature. The thrust and specific impulse values are for vacuum conditions

Engine	Input	Value	Performance	Real	Modelled	Quality Factor	Value
MIRA [33] [41]	p_c [MPa]	6	F [N]	98000	106988	ξ_T	0.916
	O/F [-]	3.4	I_{sp} [s]	365	417	ξ_P	0.875
	$D_e [m]$	2.97*					
	$\dot{m} [kg/s]$	26.2*					
RD-185 [37]	p_c [MPa]	14.7	F [N]	179000	191907	ξ_T	0.933
	O/F [-]	3.4	I_{sp} [s]	378	405	ξ_P	0.933
	D_e [m]	1.5					
	$\dot{m}$ [kg/s]	48.3*					
ACE-42R [33] [19] [20]	p_c [MPa]	4.7	F [N]	420000	446928	ξ_T	0.940
	O/F [-]	3.12	I_{sp} [s]	343	363	ξ_P	0.944
	D_e [m]	1.5					
	$\dot{m}$ [kg/s]	124.9					
Raptor[3] [33] [41]	p_c [MPa]	30	F [N]	3285000	3325070	ξ_T	0.988
	O/F [-]	3.8	I_{sp} [s]	359	361	ξ_P	0.994
	D_e [m]	4					
	$\dot{m}$ [kg/s]	940.0*					

The four engines that are used to validate the model are chosen as they provide a wide range of thrust; the propulsion model must be valid for a wide range of thrust due to the unknown number of engines (discussed later in Section 4.2). The MIRA engine produces the lowest thrust, at 98 kN, followed by the RD-185 which is almost double that at 179 kN. The ACE-42R engine produces 420 kN of thrust, and the Raptor has by far the highest thrust, at 3290 kN.

The expected range for the quality factor is 0.92-1.00, and the propellant consumption quality factor ranges from 0.85-0.99 [31] [64]. As can be seen from Table 4.2, not all of the the quality factors fall within this range. The MIRA engine's thrust quality factor is 0.4% smaller than what the margins allow, however this could be due to the exhaust diameter and the mass flow having been derived from the data available. This results in a lowered accuracy of the input values, as they are derived using Ideal Rocket Theory and not from experimental data, consequently impacting the modelled thrust and specific impulse values. The Raptor engine's

---

[3] `https://www.nasaspaceflight.com/2016/10/its-propulsion-evolution-raptor-engine/`

propellant consumption efficiency, on the other hand, is greater than what the margins allow. This could be due to the fact that the Raptor engine is still under development, and that consequently some inconsistencies arise the data that is available. Nevertheless, 0.4% is a very small deviation from the expected margins, and therefore the values for both the Raptor and the MIRA are deemed acceptable. From the validation data, it can be said that the propulsion system discipline is validated.

The quality factors determined from the validation are given in Table 4.3, obtained by taking the mean of each respective factor over the four engines. the manner in which they are applied is given in equations 4.13 and 4.14, where F_a and $I_{sp,a}$ denote the adjusted thrust and specific impulse, respectively.

Table 4.3: The quality factors determined from the propulsion system validation

Factor	**Value**
ξ_T [-]	0.944
ξ_P [-]	0.937

$$F_a = \xi_T F_m \tag{4.13}$$

$$I_{sp,a} = \xi_P I_{sp,m} \tag{4.14}$$

4.2. Vehicle Mass and Geometry

Due to the strong relationship between the geometry and mass of the vehicle, they are presented in parallel in this section. The vehicle geometry is defined by the need to house the crew, the tanks, the engines, and all the other necessary subsystems, as well as the requirement to retain its structural integrity throughout its mission duration. It is further also highly influential to the performance of the vehicle, as it determines its aerodynamic performance, as well as the vehicle mass.

The vehicle layout is based on Charon's layout, determined by Gaffarel et. al. [22], as seen in Figure 4.1. The crew capsule is located atop the vehicle, followed by the propellant tanks shown in black, and the engines at the rear end of the vehicle, with the landing legs shown in the deployed position. The aerodynamic shell of the vehicle is shown in white, with the thermal protection system in black (left side). The aerodynamic surfaces are also shown- wings (top), and two body flaps (bottom).

Figure 4.1: The vehicle layout as designed by Gaffarel et. al. [22]

The geometry of the vehicle can be split into three main components that are held together by two strucutres (when the landing legs are retracted). Namely, the crew capsule, the tanks, and the engines, with the forward and aft skirts connecting the crew capsule to the tanks, and the tanks to the thrust structure (that house the engines), respectively. The total length of the vehicle is therefore calculated as the compound length of these five components. This is seen in Equation 4.15. The calculation of each component's length will be discussed in its respective section.

$$L_{tot} = L_{capsule} + L_{skirt,f} + L_{tank,f} + L_{tank,ox} + L_{skirt,a} + L_{engines} \tag{4.15}$$

The mass estimation of the vehicle is done by breaking the vehicle down further into more subcomponents, estimating those masses, then summing them. This is shown in Figure 4.2. Certain subcomponent masses that do not heavily depend on the the overall vehicle or trajectory design will be taken from the Charon SSTO vehicle, such as the life support system. The calculation of each component's mass will be discussed in its respective section.

4.2.1. Geometry and Mass Design Variables

The design of the vehicle, and consequently its mass and geometry, can be approached in many ways. The design variables, however, must represent the inputs that have the most probable chance of having the greatest effect on the design, or be the variables that characterise the vehicle's performance. These are identified below.

$$Z_{veh} = \left[n_{eng}, M_{p,a}, M_{p,l}, D_v\right]$$

The engine number, n_{eng}, greatly determines the vehicle's performance. The vehicle must be able to reach the target orbit, as well as be able to land, which is in large part determined by the available thrust. The number of engines determines the necessary engine performance and therefore also determines whether this is achievable. The ascent and landing propellant masses, $M_{p,a}$ and $M_{p,l}$, are necessary to determine the total required propellant mass for the launch and return. The vehicle diameter D_v is of course necessary to determine the vehicle dimensions. The bounds for each component is given in Section 7.2.

4.2.2. Material Selection

The properties of the chosen vehicle material in great part define the performance of the structure, and therefore consequently also co-determine certain geometries and masses. The structural integrity of the vehicle must also be guaranteed. The materials for the the main load-carrying structures must therefore be determined, namely the tanks. Other materials do not have to be selected as the total component mass is predetermined.

Due to the requirement that the vehicle must be reusable and therefore maintainable on Mars (MR-020), is it necessary that the resources from which the materials are produced are found in-situ, as well as that they must be manufacturable in-situ. Although the Mars settlement will be able to manufacture certain materials, the production of high-level alloys and composites requires high energy and sophisticated infrastructure [22]. The structure of the vehicle will be therefore be made from the aluminium alloy QQ-A-250/4. Only the tanks will be made from a carbon epoxy composite, IM7-977. These will, however, be manufactured on Earth and shielded from corrosion by the aluminium. The materials chosen are also the materials chosen by Gaffarel et. al. for the Charon vehicle [22]. The materials and their properties can be found in Table 4.4.

Material Type	**Material Name**	**Density [kg/m^3]**	**Tensile Strength [MPa]**
Aluminium alloy	QQ-A-250/4	2740	312
Carbon epoxy composite	IM7-977	1770	5300

Table 4.4: The materials and their respective properties chosen for the vehicle [71]

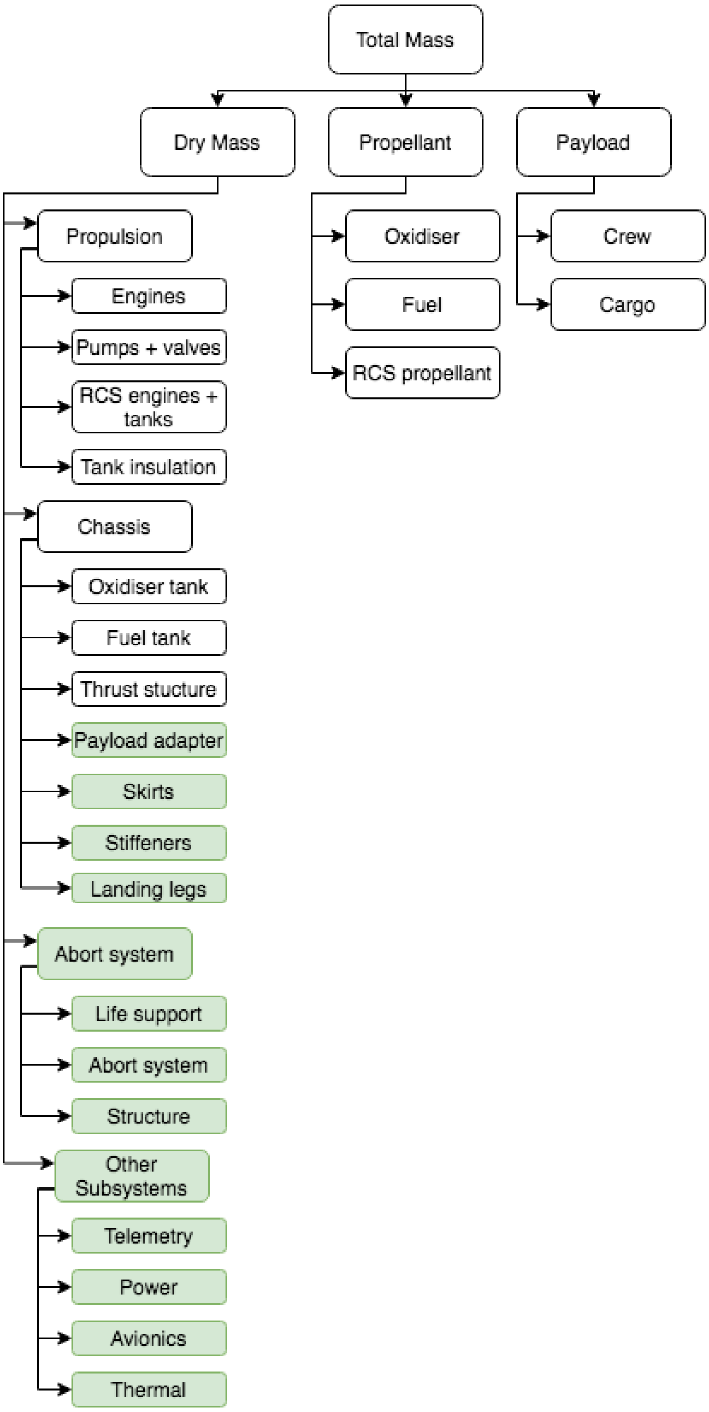

Figure 4.2: The mass breakdown of the vehicle, where the masses in green denote the masses taken from the Charon vehicle by Gafferel et. al. [22]

4.2.3. Propellant Sizing

Although the ascent and landing propellant masses are set as design variables, there will always be a certain fraction of propellant that is unusable due to boil-off as the propellant is cryogenic. The total ascent and landing propellant mass is therefore given by Equation 4.16, where M_p denotes the total propellant mass, $M_{p,a}$ the ascent propellant mass, $M_{p,l}$ the landing propellant mass, and k_{boil} the boil off fraction, set to 0.03 [52]. The propellant sizing for the RCS engines will be discussed in Subsection 4.2.4.

$$M_P = (M_{p,a} + M_{p,l})(1 + k_{\text{boil}}) \tag{4.16}$$

Once the main engine propellant mass is known, the O/F ratio can be used to determine how much fuel and oxidiser is needed. This can be done using Equations 4.17 and 4.18, where M_p denotes the propellant mass, M_o the oxidiser mass, and M_f the fuel mass.

$$M_o = M_p \frac{O/F}{1 + O/F} \tag{4.17}$$

$$M_f = M_p \frac{1}{1 + O/F} \tag{4.18}$$

However, as will be elaborated upon in Section 6.7, transfer, docking, rendez-vous, and entry burn manoeuvres are still required for the vehicle to dock and start the descent phase. The delta-Vs for these manoeuvres are known (see Section 6.7), however the required propellant mass is unknown. The propellant mass, and consequently the vehicle total mass, is iterated until the sufficient accuracy is obtained. This can be seen from Figure 4.3.

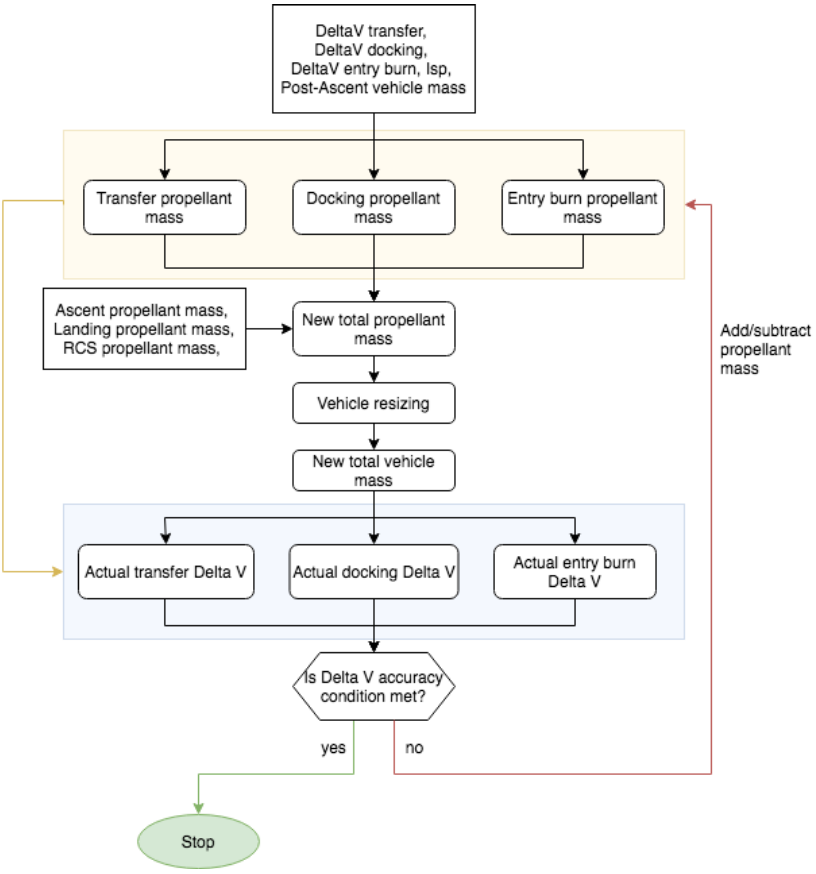

Figure 4.3: A schematic of the iterative process of finding the propellant mass

As is shown in Figure 4.3 the propellant masses necessary for the burns are calculated using the Tsiolkovsky equation (Equation 4.19) using the vehicle mass that does not include the transfer, docking, or entry burn propellant masses. M_i denotes the initial vehicle mass, before the burn, ΔV the delta V, I_{sp} the specific impulse, g_0 Earth's standard gravity, and M_P the propellant mass. The propellant tanks and thus also the vehicle is resized to accommodate the propellant mass (the methodology of this is discussed further in this section). The delta-Vs achieved using the current propellant mass and total vehicle mass are then obtained, again using the Tsiolkovsky equation, however rearranged for delta-V. If the actual delta-Vs are within 1 m/s of the necessary delta-Vs, then the propellant mass has been found. If not, propellant mass is added or subtracted, as necessary.

$$M_P = M_i \left(e^{\dfrac{\Delta V}{I_{sp} g_0}} - 1 \right) \tag{4.19}$$

4.2.4. Propulsion System Sizing

As can be seen from the mass breakdown in Figure 4.2, the propulsion system can be broken down in various sub-components. The calculation of the masses and dimensions of each are presented here.

Main Engines

As determined in Section 4.1, the main engines will be liquid bi-propellant engines. In order to determine the mass of the engines, a parametric estimation law for pump-fed bipropellant engines is used. This relationship is given in Equation 4.20, as derived by Akin [3].

$$M_{eng} = (7.81 \times 10^{-4})F + (3.37 \times 10^{-5})F\sqrt{\varepsilon} + 59 \tag{4.20}$$

The length of the engines is determined by the combined length of the nozzle the combustion chamber. The length of the nozzle L_n can be found using Equation 4.21, where θ_{eq} is the equivalence half-angle (standard is 15° as given by Zandbergen [70]), and R_t is the throat radius.

$$L_n = 0.8\left(\sqrt{\varepsilon} - 1\right) \frac{R_t}{\tan\theta_{eq}} \tag{4.21}$$

The length of the combustion chamber can be obtained by first calculating the chamber volume V_c using the characteristic length L^* associated with the propellant combination and the throat area A_t, seen in Equation 4.22 taken from Zandbergen [70]. The characteristic length of an engine is determined by the time required for complete burning of fuel [35]. Characteristic lengths usually vary between 0.3 and 3 m [64], however for methalox engines, the ranges are generally reduced to 0.8 - 1.4 m [69], with Bae et. al. [5] and Kim et. al. [36] using 1.05 m and 1.35 m as their characteristic lengths, respectively. The characteristic length is taken as the mean value of the two, 1.2 m. This value can be retrieved in Table 4.8, alongside other assumed values for the propulsion system, in the validation of the mass and geometry, Section 4.2.8.

$$L^* = \frac{V_c}{A_t} \tag{4.22}$$

To determine the combustion chamber area, A_c, Equation 4.23 used, where ε_c denotes the contraction ratio of the engine. The contraction ratio is the ratio of the subsonic combustion chamber area to throat area, and is usually found in the 2-4 range [55]. The size of the engine, however, influences the contraction ratio, with values over 3 being preferred for smaller engines, and values around 2.5 not being uncommon for larger engines [70]. As the engine size is still unknown, the contraction ratio is set to the middle of the range, namely 3. This can be retrieved from Table 4.8.

$$\varepsilon_c = \frac{A_c}{A_t} \tag{4.23}$$

The length of the combustion chamber can then be obtained by Equation 4.24, and the total engine length by Equation 4.25. The addition of the chamber and nozzle lengths to find the total length is multiplied by a factor of 1.5 to accommodate the presence of piping and valves.

$$L_c = \frac{V_c}{A_c} \tag{4.24}$$

$$L_{eng} = 1.5(L_c + L_n) \tag{4.25}$$

RCS Engines

The main purpose of the RCS engines is to control the attitude of the vehicle during the rendez-vous and docking phases, during the re-entry phase, and to provide the torque for the in-flight turn-over before the propulsive landing. The RCS thrust and RCS propellant mass must be sufficient for this. Propellant may be conserved during the re-entry phase by utilising control surfaces to control the vehicle's attitude, however the atmosphere of Mars is thin and in this early a phase of conceptualisation it cannot be certain that the surfaces provide sufficient torque. It is therefore assumed that the RCS provides all the necessary torque. However, as the trajectory simulation of the vehicle does not include any active moment control, no active RCS control is included either. However, as the RCS engines and propellant still contribute to the vehicle's GTOW, they are taken into account in the design of the vehicle.

As the objective of the optimisation is the vehicle's GTOW, the goal to reduce the mass is what determines the RCS choices. To determine the engine and propellant masses, the RCS choices made for the Charon and Hercules vehicles are consulted. The total mass of the RCS systems (including propellant) for both vehicles totals 1% of the total GTOW. Therefore this is the RCS total mass that is added to the MDO vehicle once the total wet mass is known. The level of engine thrust and placement of the engines is not necessary to determine in this study. However, in line with the optimiser GTOW objective and the vehicle requirement MR-030 to use propellant produced in-situ, bi-propellant engines are chosen. The RCS propellants can subsequently be stored in the main propellant tanks. This eliminates the need for separate pressurant and monopropellant tanks. The engines are further assumed to make up 7% of the total RCS mass, in line with Hercules and Charon.

4.2.5. Chassis Sizing

This section covers the mass and dimensions of the vehicle chassis, which is the supporting structure of the vehicle. As shown in the mass breakdown chart in Figure 4.2, it can be broken down into various subcomponents, which are discussed here.

Thrust Structure

The thrust produced by the engines must be directed along a load path toward the propellant tanks, which are the main load bearing structures within the vehicle. A thrust structure creates this load path, housing the engines within it, and connects to the aft skirt and tanks. This can be seen in Figure 4.4, where the 9 Charon engines are attached to the thrust structure.

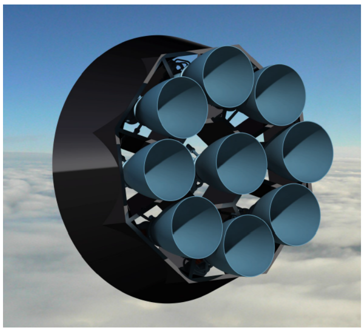

Figure 4.4: The configuration of the engines and the thrust structure designed by Gaffarel et. al. [22]

In order to estimate the mass of the thrust structure, Equation 4.26 is used, as given by Akin [3]. M_{ts} denotes the thrust structure mass, and F_T the total thrust produced by all the engines.

$$M_{ts} = 2.55 \times 10^{-4} F_T \tag{4.26}$$

Propellant Tanks

To optimise the mass of the vehicle, the tanks are designed as load-bearing structures. This is a common practice in industry, as it eliminates the need for separate load-carrying structures around the tanks. However, this means that the tanks also must be able to carry the launch and entry loads that the vehicle is subjected to.

The volume of the propellant can be calculated from the fuel and oxidiser masses, as outlined in Section 4.2.3. This is done using Equation 4.27 where V_p denotes propellant tank volume, M_p mass, ρ_p propellant density, and k_{ull} the ullage fraction set to 0.1.

$$V_p = (1 + k_{\text{ull}}) \frac{M_p}{\rho_p} \tag{4.27}$$

Although spherical propellant tanks are the most efficient shape in terms of mass, the propellant mass for single-stage-to-orbit vehicles is very large, and therefore it greatly determines the size of the vehicle. In terms of volume, elliptical tanks are much more efficient when combined with a common bulkhead tank. Disadvantage of a shared bulkhead is are issues regarding insulation, however as the propellants are be held at similar temperatures, this does not impose serious problems. The layout of example tanks that share a bulkhead is given in Figure 4.5 (the other elements are not representative of the vehicle geometry).

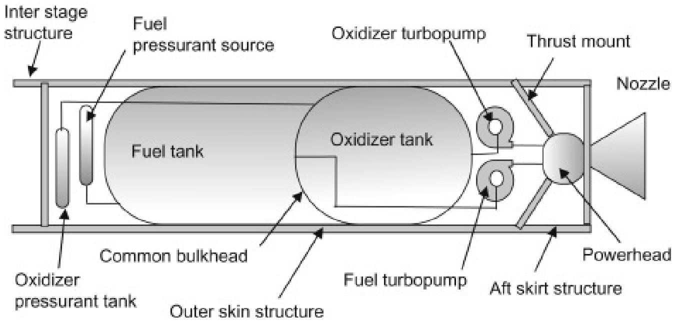

Figure 4.5: Schematic of a fuel and oxidiser tank sharing a bulkhead, also called an elliptical tank [61]

An R_c/R_e ratio (tank eccentricity e) of 0.707 is recommended by Sforza [61] to be the most mass-efficient geometry for the tank, where R_c denotes the cylindrical tank radius, and R_e the endcap radius. The minimum thicknesses for the cylindrical section and the endcaps (t_c and t_e) can then be obtained using Equations 4.28 and 4.29 respectively, where p_t denotes the tank pressure, σ_y the yield stress of the material, and k_d the load factor. The tank pressure for liquid pump-fed engines usually lies between 2 and 3.4 bar [11], and is therefore taken as 2.7 bar. The load factor k_d is taken as 2, as prescribed by Zandbergen [70]. If the tank thickness is calculated to be smaller than the minimum thank thickness, however, then the minimum tank thickness is used. The minimum tank thickness is set to 3 mm, and can be found in Table 4.8.

$$t_c = \frac{p_t R_c}{(\sigma_y / k_d)} \tag{4.28}$$

$$t_e = \frac{1}{2} \frac{p_t R_e}{(\sigma_y / k_d)} \tag{4.29}$$

The tank radius can then also be used to find the oxidiser tank length (L_{ox}) using Equation 4.30, and the fuel tank length using Equation 4.31 (L_f). V_f and V_{ox} denote the fuel and oxidiser volumes, respectively.

$$V_{ox} = 2\left[\frac{2}{3}\pi R_c^2 (eR_e)\right] + \pi R_c^2 L_{ox} \tag{4.30}$$

$$V_f = \pi R_c^2 L_f \tag{4.31}$$

The volume of the tank walls for the oxidiser tank is found using Equation 4.32 as provided by Sforza [61], and for the fuel tank using Equation 4.33, where e denotes the eccentricity e, and $V_{w,ox}$ and $V_{w,f}$ denote the tank wall volumes for the oxidiser and the fuel, respectively. From the volume, the tank mass can be calculated using the density of the tank material. Note that the common bulkhead volume is included in the oxidiser tank volume.

$$V_{w,ox} = 2\pi\left(R_c l_c t_c + R_c^2 t_e + \frac{1}{4}\frac{R_c^2 t_e}{e}\ln\left[\frac{1+e}{1-e}\right]\right) \tag{4.32}$$

$$V_{w,f} = 2\pi R_c l_c t_c + \pi\left(R_c^2 t_e + \frac{1}{4}\frac{R_c^2 t_e}{e}\ln\left[\frac{1+e}{1-e}\right]\right) \tag{4.33}$$

The masses of the oxidiser and fuel tanks is then obtained by multiplying the tank wall volume by the tank material density (as given in Section 4.2.2). This is seen in Equation 4.34, where M_t denotes the tank mass, V_w the tank wall volume, and ρ_t the tank material density.

$$M_t = V_w \rho_t \tag{4.34}$$

The total propellant tank mass can then be obtained by summing the oxidiser tank mass, and the fuel tank mass, which is then multiplied by the k_m factor to account for mounting provisions, propellant management devices, and in/outlet provisions [70]. For composite tanks, this factor is set to 1.85. This equation can be seen in 4.35.

$$M_{pt} = (M_{t,ox} + M_f) k_m \tag{4.35}$$

The mass of the tank insulation can then be found using Equation 4.36, as given by Akin [3], where M_{ins} denotes the insulation mass, and A_{tank} the surface are of the tank mass. This tank surface area can be found using Equation 4.37.

$$M_{ins} = 1.123 A_{tank} \tag{4.36}$$

$$A_{tank} = 2\pi\left(R_c l_c + R_c^2 + \frac{1}{4}\frac{R_c^2}{e}\ln\left[\frac{1+e}{1-e}\right]\right) \tag{4.37}$$

The valves can be estimated by the relationship in Equation 4.38, as given by Schlingloff [59].

$$M_{val} = 0.0268 {\frac{F_T p_c}{10^8}}^{0.71} \tag{4.38}$$

Tank Stiffeners

Buckling failure is always the critical failure mode for tanks [61], and this mode is investigated by Gafferel et. al. for the Charon vehicle [22]. Instead of increasing the thickness of the tanks enough to increase the critical buckling load to a sufficient value, Gaffarel et. al. add 40 stiffeners to the outside of the tanks to support the structure. This does not increase the mass of the vehicle by a significant amount (approximately 45 kg only), however the critical buckling load is increased for Charon from 9.9 MPa to 185 MPa, which a significant increase. The maximum stress experienced by the Charon tanks is calculated to be 20 MPa. Although this value was obtained for specifically the Charon tank, it can be assumed that the buckling load experienced by the shuttle vehicle for all reasonable geometries will never exceed 185 MPa, therefore the 40 stiffeners will also be used for the vehicle. Although the length of the tanks are subject to change with respect to the length of Charon's tanks, the mass of the stiffeners is comparatively very low and therefore they are taken as a constant of 45 kg.

Skirts and Payload Adapter

Skirts are structures that allow for more space between the tanks and the attached structures, and act as load paths. They can be placed above and below the tanks, allowing other subsystems to be housed in the space between. The aft skirt is the load bearing structure connecting the thrust structure to the tanks, and the forward skirt the structure connecting the tanks to the crew capsule. These structures are taken from the Charon vehicle. Their combined length is 1.355 m, derived from the Charon dimensions by Gaffarel et. al. [22].

The payload adapter is the structure that connects the crew capsule to the vehicle, as well as housing the abort release system that allows the capsule to separate from the rest of the vehicle in case of an emergency. The mass of the Charon vehicle's adapter is also taken, namely 700 kg, as this is highly unlikely to change. The masses of the skirts and the payload adapter can be found in Table 4.5.

Table 4.5: The masses of the vehicle skirts, as taken from Gaffarel et. al. [22]

Structure	**Mass [kg]**
Forward skirt	778.20
Aft skirt	625.50
Payload adapter	700 kg

Landing Legs and Actuation System

The landing legs are the structure on which the vehicle is supported when it stands on the surface of Mars. They must, of course, be able to hold the fully-fuelled and weight of the vehicle, as well as not fail during the landing. Although there are bounds that limit the landing angle and velocity, as is discussed in Section 6.5.2, the dynamic loading on the legs are much higher than the static loads.

Both the Charon and Hercules vehicles use four landing legs as support. The Charon vehicle's landing legs are designed for a landing velocity of 6.1 m/s [22], and Hercules' a velocity of 2.5 m/s [39]. As the maximum touchdown velocity of the shuttle vehicle is 2.5 m/s (see Section 6.5.2), both of these structures are able to handle the maximum touchdown velocity. However, the final GTOW of the shuttle vehicle is yet unknown, and the landing legs of the Hercules and Charon vehicles are designed for their respective GTOWs. The Charon vehicle's legs are designed for a higher GTOW than those of the Hercules, as well as for a higher landing velocity, and are therefore a safer choice. The total mass of the Charon landing legs and the actuation system is 3600 kg.

4.2.6. Abort System Sizing

As the safety of the crew must be guaranteed, given by MR-040, an abort strategy and system must be included in the design of the vehicle. As seen in Figure 4.2, the mass and dimensions of the crew capsule are taken from Gaffarel et. al. [22]. This section first covers the abort strategy that the capsule must endure, then follows with the mass and dimensions determined for of the capsule.

Abort Strategy

In the event of an emergency, there must be a contingency plan to get the crew to safety. This therefore calls for an abort system. Both SSTO vehicles Hercules (Komar et. al. [38]) and Charon by (Gaffarel et. al. [22]) equip the crew capsule with engines and parachutes such that in the case of an abort, the crew capsule separates from the main vehicle, which is then jettisoned. The crew capsule is therefore able to reach either the surface through the Abort To Surface (ATS) strategy, or an orbit through the Abort To Orbit (ATO) strategy from which the crew can be recovered.

The Charon abort modes are: ATS during ascent, ATO during ascent, ATO before or after docking, ATO before reentry, and ATS after reentry. The mission profile phases are shown in Figure 4.6, with the associated abort mode explained below the figure.

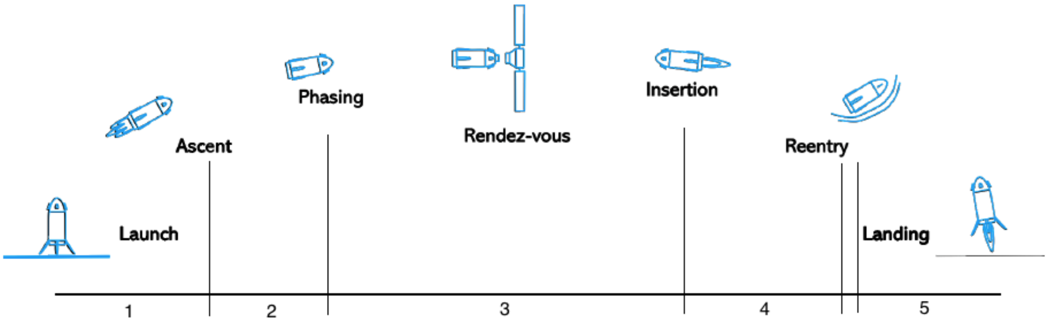

Figure 4.6: The abort modes associates with each phase of flight, as described by Gaffarel et. al. [22]. Graphics also adapted from Gaffarel et. al.

1. This phase of flight starts as soon as the crew is seated in the vehicle on the launch pad, ending when the vehicle reaches the limiting abort velocity of Mach 8 (as required for Apollo abort modes, as given by Gaffarel et. al. [22]). Between these velocities ATS is used, and the capsule is propelled away from the vehicle to an altitude at which it deploys the parachutes, and then performs the propulsive landing including airbag deployment. The abort at Mach 8 is the most demanding, as the crew must be propelled away from the vehicle travelling at this velocity. In this scenario the crew will be subject to 8 g_{earth} acceleration.
2. Once Mach 8 has been reached, ATS is no longer possible, as the velocities are too high. The capsule must therefore ATO, which it does by propelling itself to an orbit of 170 km altitude, where it can remain for 4 Martian days to await rescue.
3. Once the phasing orbit has been reached, the abort mode remains ATO, where the capsule detaches from the vehicle.
4. To initiate the reentry phase, the vehicle performs a burn such that the vehicle enters the reentry corridor (discussed in Chapter 6). ATO can be triggered between this moment and an altitude of 246 km, increasing its orbital altitude such that it can remain in the increased orbit to await rescue.
5. Below 246 km altitude there is a phase where no abort is possible due to the extreme velocity and heat loading experienced. Once the heat loading has decreased below 2 kW/m^2, ATS is possible, where the capsule is detached and uses the parachutes to decelerate.

Abort Propulsion System and Deceleration

The Charon abort thrust is provided by 3 clusters of 2 bi-propellant engines, placed at 120° from each other. For fast ignition, the propellant combination is chosen to be hydrogen peroxide/hydrazine. This combination is hypergolic, meaning it is self-igniting, allowing for a pressure-fed combustion cycle. This means there is no need for turbo-machinery, making the operation of the abort system faster. They provide 1065 kN in total, and are sized for a maximum 3-second abort burn.

The deceleration is initially provided by parachutes, then a propulsive landing is needed to decelerate enough to land on the Martian soil, which is softened by airbags. First a cluster of 5 drogue chutes are deployed to decelerate the capsule to a low enough velocity for the main parachutes to deploy. They drogue chutes are consequently jettisoned once the capsule has been decelerated enough, deploying the 3 main parachutes. For redundancy, one extra drogue chute and main parachute is included in the capsule. The propulsive landing is provided by the engines, but the landing itself is dampened by airbags as the capsule does not have landing legs.

Capsule Layout and Mass Breakdown

The crew capsule is comprised of various subcomponents such as the abort system, life support, and the structure. These ensure the safety of the crew as well as the integrity of the capsule structure itself. The components, and their masses, are listed in Table 4.6, as given by Gaffarel et. al. [22].

Table 4.6: The mass breakdown of the crew capsule and the abort system

System	**Component**	**Mass [kg]**
Life Support		456.35
	O_2	73.20
	O_2 tank	3.09
	O_2 distribution	3.00
	Food	111.50
	Water	20.30
	Urine tanks	0.40
	Toilet	80.00
	Water condenser	30.00
	Thermal heating	50.00
	Insulation	13.86
	Light	15.00
	Filter	6.00
	Pressurisation	50.00
Abort System		4259.08
	Engines	425.00
	H_2O_2	206.80
	H_2O_2 tank	1499.60
	N_2H_4	159.00
	N_2H_4 tank	836.38
	He	37.70
	He tank	276.60
	Drogue chute	120.00
	Main chute	120.00
	Chute deployment	60.00
	Airbags	500.00
	Sensors	10.00
	Computer	3.00
Structure		4025.34
	Pressurised capsule	2925.34
	Capsule main shell	500.00
	Capsule nose shell	80.00

	Docking mechanism	325.00
	Insulation	5.00
	Seats	190.00
Total Mass		8740.77

The layout of the capsule is further also taken from Gaffarel et. al., and can be seen in Figure 4.7. The crew are seated in spacesuits in the crew capsule atop the vehicle. The crew seats are shown in grey, positioned such that the crew is facing the hatch. The hatch is the opening through which the crew enters the orbital node, and can be seen at the top of the capsule, surrounded by the parachutes in red. One of the abort engine clusters is shown in dark green, mostly concealed by their aerodynamic shroud, and linked to the propellant tanks in blue. The various life support components are shown in purple. The diameter of the capsule is determined by the vehicle diameter (a design variable). The height of the capsule, however, remains the name to accommodate the crew and the subsystems, and is given as 4.78 m by Gaffarel et. al. [22].

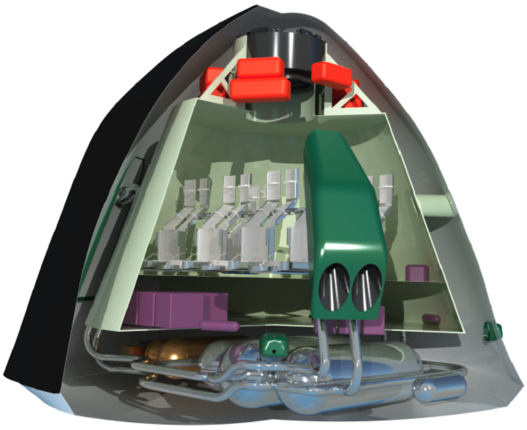

Figure 4.7: The crew capsule layout as designed by Gaffarel et. al. [22]

4.2.7. Other Subsystem Sizing

The vehicle requires other subsystems, such as avionics, telemetry, power, and thermal subsystems. These are taken from the Charon vehicle by Gaffarel et. al. [22], and can be found in Table 4.7.

Table 4.7: The masses of various subsystems for the vehicle, as given by Gaffarel et. al. [22]

Subsystem	**Mass [kg]**
Avionics	220.00
Telemetry	30.96
Power	1046.58
Thermal	2399.04

4.2.8. Vehicle Mass and Geometry Validation

In order to determine whether the calculated mass and geometry of the vehicle is accurate, it must be compared to values found in literature. However, as no vehicle that resembles the shuttle vehicle has been yet been built or flown, the shuttle vehicle is first broken down into its subcomponents, which are individually validated. Then, the vehicle as a whole will be compared to the concept vehicles, Charon and Hercules. Table 4.8 shows all the determined and assumed values that are used to size the vehicle's subcomponents, unless otherwise stated.

Table 4.8: The assumed and determined values used in the mass and geometry sizing of the vehicle

Name	**Value**
ρ_f [kg m^{-3}]	1140
ρ_{ox} [kg m^{-3}]	438
ρ_t [kg m^{-3}]	1770
σ_y [Pa]	5300
θ_{eq} [deg]	15
ε_c [-]	3
e [-]	0.707
k_d [-]	2
k_m [-]	1.85
k_{ull} [-]	0.1
k_{boil} [-]	0.03
L^* [m]	1.2
t_{min} [m]	0.003

Main Engines

The first subcomponent of the vehicle to be validated is the main engines. To validate the engine mass, the input values are found in literature and used in the software. This is shown in Table 4.9. It should be noted that the engine selection used to validate the engine mass calculation differs slightly to the engine selection used for validate their performance, due to the data available.

Table 4.9: The validation data for the engine mass of methalox engines. Values appended with * are calculated using engine data taken from the literature

Engine	**Input**	**Value**	**Real Mass [kg]**	**Calculated Mass [kg]**	**Difference [%]**
RD-169 [37]	p_c [MPa]	14.7	215	219	1.9
	O/F [-]	3.4			
	D_e [m]	0.5			
	$\dot{m}$ [kg/s]	55.1*			
MIRA [33] [41]	p_c [MPa]	6	250	237	-5.2
	O/F [-]	3.4			
	$D_e[m]$	2.97*			
	$\dot{m}[kg/s]$	26.2*			
RD-167 [37]	p_c [MPa]	16.7	570	590	3.5%
	O/F [-]	3.4			
	D_e [m]	2.4			
	$\dot{m}$ [kg/s]	94.9*			
RD-190 [37]	p_c [MPa]	14.7	1470	1275	-13.5%
	O/F [-]	3.4			
	D_e [m]	1.5			
	$\dot{m}$ [kg/s]	48.3*			

As can be seen, the difference in mass is reasonable for engines under 600 kg, with the MIRA having the largest difference of 5.2%. However, for the RD-167 the difference is much larger, at 13.5%. A single engine mass of 1470 kg, however, is very large and highly unlikely to be used for the vehicle, and therefore can a divergence of 13.5% is still acceptable.

The dimensions of the engine must also be validated, namely the length. Table 4.10 presents the validation of the engine length. Again, it should be noted that some different engines are used to validate the software's calculation of the engine lengths than the engine performance and mass, due to the engine length data available.

Table 4.10: The validation data for the engine mass of methalox engines. Values appended with * are calculated using engine data taken from the literature

Engine	Input	Value	Real Length [m]	Modelled Length [m]	Difference [%]
RD-169 [37]	p_c [MPa]	14.7	1.7	1.5	-11.7
	O/F [-]	3.4			
	D_e [m]	0.5			
	$\dot{m}$ [kg/s]	55.1*			
RD-182 [37]	p_c [MPa]	17.2	2.8	3.5	25.0%
	O/F [-]	3.4			
	D_e [m]	1.5			
	$\dot{m}$ [kg/s]	291.0*			
RD-192 [37]	p_c [MPa]	25.7	4.05	4.55	12.3%
	O/F [-]	3.5			
	D_e [m]	2.0			
	$\dot{m}$ [kg/s]	660.0*			

As can be seen, the calculated engine lengths deviate up to 25% from the real engine lengths. This is large, however the calculated engine length is dependent on many assumed yet highly influential variables, such as the characteristic length, the contraction ratio, and equivalence half-angle. Although the knowledge of the length of the engines is necessary to determine the geometry of the vehicle, it has a relatively small role in influencing its optimal design. Though the engine lengths influence the total vehicle length, it is comparatively a small especially considering a 25% uncertainty of that relatively small length. The deviation of 25% is therefore still deemed acceptable, due to the relatively small influence, as well as the deviations being derived from unknown variables.

Propellant Tanks

To validate the dimensions and the masses of the propellant tanks, three common bulkhead tanks used in launcher stages are used. This can be seen in Table 4.11, alongside the parameters that have been altered such as mixture ratio, propellant density, and tank material density.

Table 4.11: The validation of the common bulkhead tank. Values appended with * are derived using the stage data taken from the literature.

Stage	Input	Value	Sizing	Real	Modelled	Difference [%]
Ares I[3]	Propellant	LOX/LH2	M_t [kg]	9312*	8945	0.43
	ρ_f [kg m^{-3}]	71.0	L_t [m]	20.9*	20.99	-3.94
	ρ_t [kg m^{-3}]	2810				
	D_v [m]	5.5				
	M_p [kg]	138000				
	O/F [-]	5.117				
	t_{min} [m]	0.005				
S-II [13]	Propellant	LOX/LH2	M_t [kg]	15539	16088	3.53
	ρ_f [kg m^{-3}]	71.0	L_t [m]	19.58	22.50	14.89
	ρ_t [kg m^{-3}]	2840				
	D_v [m]	10.06				
	M_p [kg]	442343				
	O/F [-]	5.5				
	t_{min} [m]	0.0047				
S-IV-B [13]	Propellant	LOX/LH2	M_t[kg]	4749	4887	2.90
	ρ_f [kg m^{-3}]	71.0	L_t [m]	13.69	14.47	5.70
	ρ_t [kg m^{-3}]	2840				
	D_v [m]	6.604				
	M_p [kg]	107072				
	O/F [-]	4.419				
	t_{min} [m]	0.0037				

As can be seen, there is a little variance between the modelled mass of the common bulkhead tank, and the mass of the ones found in literature. The mass, however, is highly dependent on the material used. All three stages use an aluminium alloy, however only the material properties of the S-IC stage (same launcher as the S-II and S-IV-B) are known. Therefore it is assumed that the S-II and S-IV-B stages are made of the same material, and these properties are taken. However, as the material density greatly affects the mass, this introduces inaccuracy, which could be the reason for the 3.53% and 2.90% errors in tank mass. It is evident that the difference in mass for the Ares I tank is merely 0.43%, for which the material density is known.

The length of the tanks are dependent on the eccentricity of the tanks, which is set to 0.707. As none of the tanks' eccentricities are known, this introduces inaccuracies, and consequently, errors. Tank eccentricities can be both higher and lower than 0.707, and as can be seen from the tank length deviations, the modelled lengths show both an estimation that can be too high and too low. Due to this, the tank properties are considered validated.

Total Vehicle

Finally, the total modelled wet mass and the total length of the vehicle (legs retracted) are compared to those of the Charon and Hercules vehicles. The comparisons are shown in Table 4.12 (the payload mass has also been added to the input, as although this is not a design variable, it is a variable that is susceptible to change). As can be seen, for the wet masses, are 0.16% and 2.85%, for Charon and Hercules, respectively. The discrepancy between the real and modelled wet masses is greater for the Hercules vehicle than the Charon vehicle, as many components used in to size the vehicle are taken straight from Charon, and not sized for Hercules. However, it is a small difference of 2.82% and the wet mass can be considered validated. The total length of the vehicles are both under 5%. This is within an acceptable range, and can also be considered validated.

---

[3] `https://www.nasa.gov/pdf/231430main_UpperStage_FS_final.pdf`

Table 4.12: The validation of the total vehicle mass and length.

Vehicle	**Input**	**Value**	**Sizing**	**Real**	**Modelled**	**Difference [%]**
Charon [22]	$M_{P,a}$ [kg]	133685	M_t [kg]	168107	168377	0.16
	$M_{P,l}$ [kg]	2487	L_t [m]	17.40	18.25	4.89
	D_v [m]	6.14				
	$\dot{m}$ [kg s^{-1}]	82.9				
	p_c [MPa]	20.0				
	D_e [m]	1.06				
	O/F [-]	3.12				
	n_{eng} [-]	9				
	M_{PL} [-]	1200				
Hercules [38]	$M_{P,a}$ [kg]	121714	M_t [kg]	162819	167467	2.85
	$M_{P,l}$ [kg]	10501	L_t [m]	19.20	18.24	-5.00
	D_v [m]	6.0				
	$\dot{m}$ [kg s^{-1}]	68.9				
	p_c [MPa]	13.8				
	D_e [m]	1.076				
	O/F [-]	3.4				
	n_{eng} [-]	5				
	M_{PL} [-]	5750				

5

Aerodynamics

The aerodynamics of the shuttle vehicle are central to its performance. The drag forces on the vehicle are dominant during its ascent, whilst upon reentry both the lift and drag forces dictate the trajectory taken by the vehicle. In this chapter, the principles of aerodynamic performance are outlined, followed by the choice of the aerodynamic modelling software, and its validation. The aerodynamic design variables are then presented, and lastly, the calculation methods and implementation of the software within Tudat are discussed.

5.1. Principles

The geometry of the vehicle determines the aerodynamic loading on the vehicle, namely lift and drag. Without these values, the motion of the vehicle cannot be determined (see Chapter 6). To determine these values, Equations 5.1 and 5.2 are used, where L denotes lift, D drag, C_L and C_D their respective lift and drag coefficients, ρ the air density, V the velocity of the vehicle, and S the reference surface area. As can be seen, lift and drag are dependent on their respective dimensionless coefficients. These are parameters that are dependent on factors such as the geometry of the vehicle, the in-flight Mach number, the vehicle's angle of attack, and the atmospheric properties. These coefficients are most commonly determined using software.

$$L = \frac{1}{2} C_L \rho V^2 S \tag{5.1}$$

$$D = \frac{1}{2} C_D \rho V^2 S \tag{5.2}$$

5.2. Software Methodology

There are multiple ways in which the aerodynamic coefficients can be obtained. Haex [23] opts to utilise validated data collected by Weiland [67] from various reentry vehicles. This method, however, cannot be implemented as the data collected is for Earth reentry vehicles (thereby involving a different atmospheric profile).

In order to determine the aerodynamic coefficients software must therefore be used. Missile DATCOM is an external programme that was developed to provide an aerodynamic design tool which has the predictive accuracy suitable for preliminary design, and the capability for the user to easily substitute methods to fit specific applications [9]. Although the latest versions of Missile DATCOM are subjected to International Traffic in Arms Regulations (ITAR) and therefore not available to non-U.S. persons, an older version (1999, revision 3) of the software is distributed as a supplement to the book *Design Methodologies for Space Transportation Systems* [24]. The 1997 version has further found widespread use throughout the TU Delft [58] [34].

Missile DATCOM determines the normal and axial coefficients of a user-defined vehicle at various user-defined angles of attack and Mach numbers. The flight conditions for these calculations are determined by a user-defined altitude (on Earth) or Reynold's number. Integrating the Missile DATCOM software directly into the Tudat code is very inefficient, and therefore constructing a database of aerodynamic coefficients for various vehicle geometries as a function of Mach number and angle of attack is taken. Using a MATLAB script validated by Contant [14], the normal and axial coefficients produced by Missile DATCOM are used to obtain the vehicle's lift and drag coefficients. These are then written into separate C_L and C_D files, sorted as a function of angle of attack and Mach number, and the optimisation tool consequently uses the aerodynamic files pertaining to the Missile DATCOM geometry that most resembles the optimiser vehicle geometry. The geometries that are used as input are discussed further in Subsection 5.4.

Missile DATCOM is able to determine the aerodynamic coefficients for a maximum of 20 angles of attack and 20 Mach numbers per run. The angles of attack and Mach numbers chosen are given in Table 5.1. As can be seen, the intervals between the angles of attack are decreased between angles 40° and 60°. This is due to the $C_{L,max}$ most likely being located between these values, and so more datapoints are required to characterise this region. An angle of attack higher than 70° is unnecessary, therefore this is taken as the upper limit. Due to the fast changes in aerodynamic properties throughout the transsonic regime, more datapoints are also taken between Mach 0.9 and 1.1. As can also be seen from the validation data (discussed further in Subsection 5.3), there is very little change in the aerodynamic properties for Mach numbers greater than 7. Therefore only three data points are taken above Mach 7.

Table 5.1: The angles of attack and Mach numbers for which the coefficients are determined

α [deg]	-10	-5	0	5	10	15	20	25	30	35
	40	43	47	50	53	55	57	60	65	70
M [-]	0.0	0.3	0.6	0.9	0.95	1.0	1.05	1.1	1.4	1.7
	2.0	2.5	3.0	3.5	4.0	5.0	7.0	10.0	15.0	20.0

It must be noted, however, that Missile DATCOM does have its shortcomings as described in the manual [9], as well as noted by van Kesteren [34] and Rozemeijer [58]. Missile DATCOM overestimates the wave drag in the subsonic and transsonic regimes, and upon inspection by Rozemeijer [58], it is found that the forebody drag is what causes the increase. This is a flaw that has been corrected in the later versions of the software, however these fall under ITAR and therefore cannot be used. Due to the fact that there is very limited aerodynamic data available for Martian vehicles, as well as limited available software that is applicable (software for high Mach numbers and angles of attack), it is opted to still use Missile DATCOM, however with the knowledge of this limitation. The aerodynamic coefficients for the sub- and transsonic regimes are, however, only used throughout a short period in the ascent phase.

5.3. Software Validation

Missile DATCOM is software that is validated for flight in the Earth's atmosphere, but can be used to obtain aerodynamic coefficients in a Martian atmosphere. Benito and Johnson use Missile DATCOM to estimate their vehicle performance in a Martian atmosphere, thereby confirming that the software can be used for Martian atmospheric conditions [7]. In order to simulate the Martian atmosphere, the airflow density must be decreased, as the Martian atmosphere is much less dense than that of Earth's. This is done by setting the Missile DATCOM (Earth) altitude to a higher value. At hypersonic speeds, the composition of the atmosphere can also play a role, however on Mars the specific heat ratio is 1.3755, very close to that of Earth, which has a specific heat ratio of 1.4. It therefore follows that the coefficients are nearly independent of CO_2 concentration, and are essentially the same as those obtained using air [53]. However, although Missile DATCOM is validated, it has only been done so for Earth's atmosphere and therefore still requires validation to be used for a Martian atmosphere.

The validation of the aerodynamic model on Mars is difficult, as there is both no in-fight data for similar vehicle geometries and very limited data obtained through other methods for a large range of Mach numbers and angles of attack. To validate the software, the aerodynamic data available from two crewed reusable Martian concept vehicles is used- the experimental data from a sub-scale wind tunnel test of the Hercules vehicle by Adler et. al. [2], and the CFD data (Cart3d Euler CFD) of the CobraMRV vehicle by Cerimele et. al. [12]. Although flight data for Martian landers is available, the Missile DATCOM software must be validated for vehicles of similar geometries to the Martian shuttle vehicle. The geometry of the vehicles is used as input for Missile DATCOM, and the results compared to the given data. The CFD results for the CobraMRV can be seen in Figure 5.1, and the results obtained through Missile DATCOM are presented in Figure 5.2. In order to simulate the Martian atmosphere, an Earth altitude of 50 km is chosen, which correlates to a Martian altitude of 30 km.

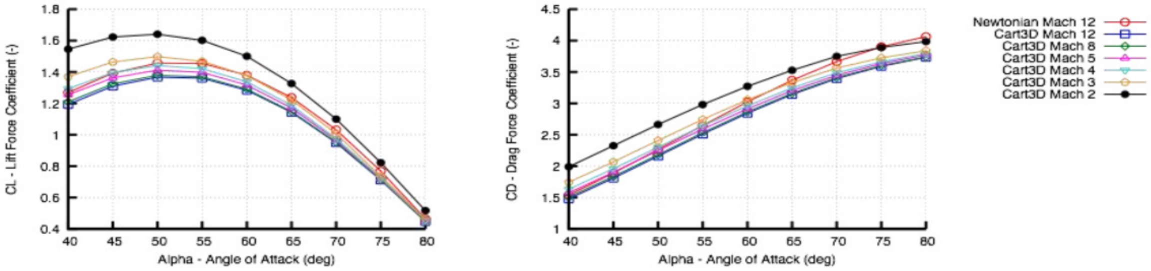

Figure 5.1: The aerodynamic coefficient data for the cobraMRV vehicle [12]

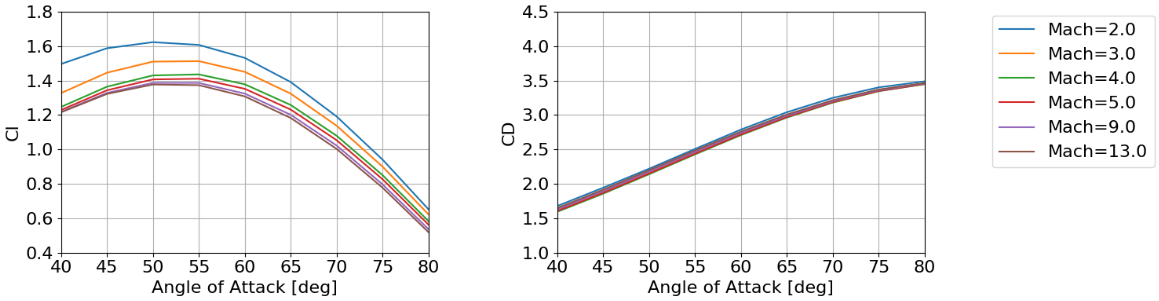

Figure 5.2: The aerodynamic coefficient data for the cobraMRV vehicle using Missile DATCOM

As can be seen, the lift and drag coefficients as a function of α at different Mach numbers is very similar for both sets of data. The $C_{L,max}$ for all Mach numbers peak between 50° and 55°, and decrease with increasing Mach number from approximately 1.6 for Mach 2 to just under 1.4 for Mach numbers greater than 5. The greatest discrepancy between the two data sets is for the C_D at Mach 2. However, this Mach number for angles of attack (αs) above 40° is unlikely to occur throughout either of the ascent and descent phases. During the descent, the propulsive turn will most likely happen at a Mach number above 2 (the Hercules vehicle turns at a Mach of 2.5 [39], and the Cobra at 2.7 [12]), after which the aerodynamic coefficients will no longer be significant during the propulsive landing. Therefore, the 20% difference in C_D value at an α of 40° at Mach 2 is of less importance. Similarly, during the ascent, an α of greater than 40° is very unlikely. The aerodynamic coefficients can therefore be considered validated for this range of α.

However, as the trajectory will also involve αs between 0° and 40°, another data set must be used to validate a lower α range. This is done using the experimental data obtained in a sub-scale wind tunnel test for the Hercules vehicle by Adler et. al. [2]. The windtunnel used is suitable for Reynold's numbers up to 1×10^6. This is therefore used as the Reynold's number value in the Missile DATCOM simulation, as opposed to a specific altitude. The comparison of the data can be seen in Figure 5.3, where the Mach number is adjusted to correspond to the dynamic pressures (Q) in the windtunnel (for example, a Q of 15 psf is equal to a Mach number of approximately 11).

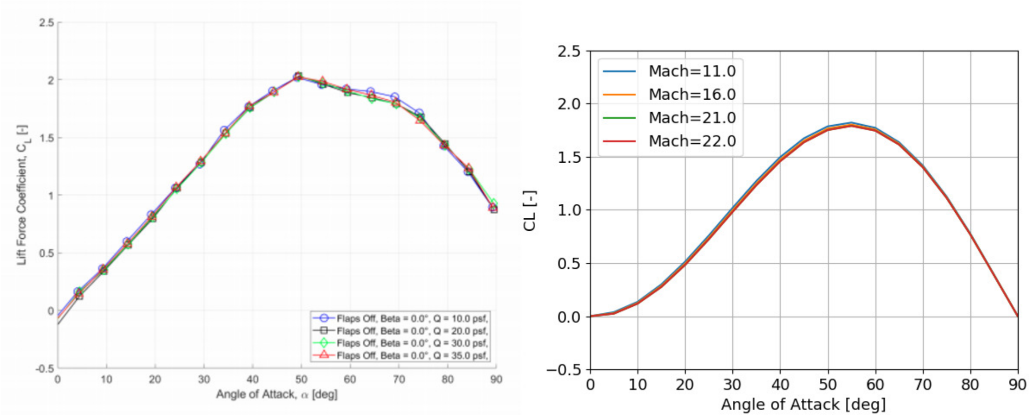

Figure 5.3: The C_L data obtained by Adler et. al. [2] (left), and the C_L data obtained by Missile DATCOM (right)

As can be seen, the data is very similar up until an α of approximately 50°, which is when the wind tunnel data reaches a $C_{L,max}$ of 2. The Missile DATCOM data reaches a lower $C_{L,max}$ of 1.7 at a greater α, 55°. However, the discrepancy between the two data sets is minimal, and Missile DATCOM can therefore be considered validated up until 55°. After the $C_{L,max}$ is reached, the Missile DATCOM C_L returns to 0 as the α reaches 90°, yet the windtunnel data returns to a C_L of 0.8. This, of course, is a very large difference, and one that is also not reflected in the CobraMRV data. The C_L for the CobraMRV also tends back towards 0 as α reaches 80°. Logically, it would seem that at an α of 0, no lift would be produced by a cylindrical axisymmetric body, however in order to validate this notion, another data set is needed, and at the point of writing, none has not been found for the necessary flight and atmospheric conditions.

Although the difference between the Hercules data and Missile DATCOM data is significant above 55°, the importance of the values at these αs must be evaluated. Both the Hercules [39] and the CobraMRV [12] vehicles have a trim α of 55°, above which the vehicle does not fly (propulsive turn excluded). The Missile DATCOM bounds for α is 70, and although there is a significant difference between the Hercules data and the Missile DATCOM data, almost all the data up until 55° is very similar. With no other applicable data available and a very similar set of coefficients, the Missile DATCOM lift coefficient calculation can be considered validated.

Noticeably, there is no drag coefficient data available for the Hercules wind tunnel test, meaning that the drag coefficients for αs between 0° and 40° are left unvalidated. This is also the case for the subsonic and transsonic flight regimes, for which there is also no data available. This is very unfortunate, as Missile DATCOM is known to overestimate the drag in these regimes, and the possibility to evaluate the deviation also for Martian atmospheric conditions would have been very valuable. However, data to validate vehicles with a similar geometry on Mars is extremely scarce. Therefore, based off of the data from the CobraMRV, the Missile DATCOM drag coefficient calculation can also be considered validated.

5.4. Aerodynamics Design Variables

The aerodynamic coefficients of the vehicle are determined by many factors, namely the vehicle's geometry, the air density, the mach number, and the angle of attack, as seen in Equation 5.3. The variables that are determined by the trajectory are, of course, the air density, the mach number, and the angle of attack. The vehicle geometry is therefore the independent variable that determines the coefficients.

$$C_L = C_L(\alpha, M, \text{geometry}); \qquad C_D = C_D(\alpha, M, \rho, \text{geometry}) \tag{5.3}$$

The vehicle geometry within Missile DATCOM is determined by its diameter, its length, the eccentricity of the nose and the body, its protrusions (such as fins and/or inlets), and its nose shape. Missile DATCOM also requires the vehicle to be axisymmetric.

The diameter of the vehicle, as well as the length, are necessary to determine the basic proportions of the vehicle, and are part of the vehicle sizing design variables (see Section 4.2.1). To complete a basic vehicle, its nose contour must also be defined. Missile DATCOM offers the availability of 5 pre-defined pointed noses, namely the conical, tangent ogive, L-V Haack, power law, and von Karman. However, when assessing all the Martian vehicles, a common trait is that all the noses are blunted, as this ensures that the shock wave produced whilst flying above Mach 1 is detached from the vehicle body, thereby reducing heat and creating more drag than conical nose[46]. Reducing drag during the ascent is less of an issue as the Martian atmosphere is much thinner. In Missile DATCOM, however, there is only one blunted nose possible. A vehicle body contour with such a blunted nose is depicted in Figure 5.4. As there is only one contour for a blunted nose, it cannot be considered a design variable, but is taken as part of the standard geometry.

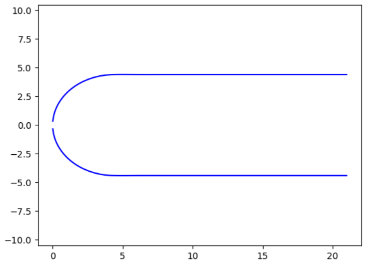

Figure 5.4: The body contour of a rocket with a spherical nose

Fins and other lifting surfaces and protrusions are also available as geometrical inputs. However, although the placement and size of fins and lifting surfaces will affect the aerodynamics of the vehicle, their use is primarily to ensure the stability and control of the vehicle in-flight. As the simulation of the vehicle's trajectory does not concern the inclusion of aerodynamic moments about the vehicle, the control moments of the vehicle are outside of the scope of the research question. Their inclusion in the MDO would mean their optimisation is unnecessary, and will most likely result in inaccurate conclusions. The geometry design variables for the vehicle are therefore only the diameter and the length of the vehicle, as seen below.

$$Z_{aero} = [D_v, L_v]$$

In order to build the aerodynamic database from which Tudat selects the most appropriate geometry, the bounds and intervals of the independent variables for which the coefficients will be evaluated, must be defined. The maximum geometry is determined by the size of the SLS payload bay. The SLS will have various launch configurations, depending on payload mass and whether crew will be transported in the Orion capsule, but Block 2 Long is the configuration that is capable of launching the largest payload. The Block 2 Long further has two possible diameters, 8.4 m and 10 m [1]. The various (as of now conceptual) payload fairings, as well as CobraMRV vehicle inside the Block 2 long 10 m SLS payload bay, can be seen in Figure 5.5. The two right-most fairings in the diagram on the left show the difference between the 8.4 m and 10 m diameter fairing.

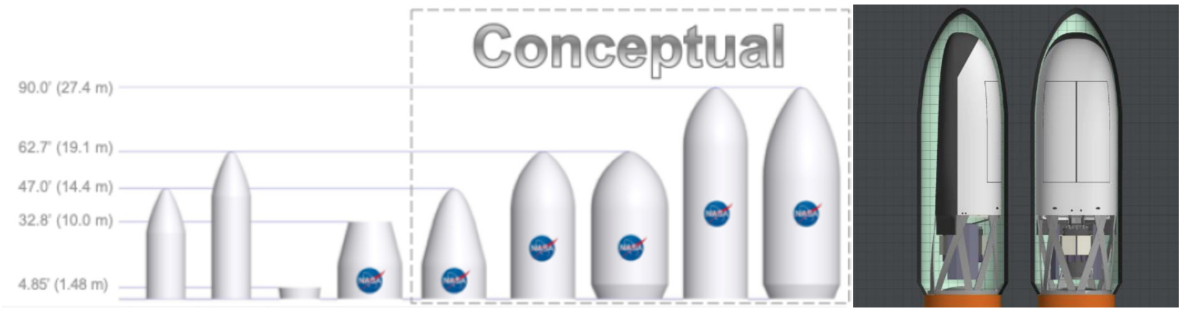

Figure 5.5: The various SLS payload fairings [1] (left), and the CobraMRV inside the SLS Block 2 fairing [12] (right)

The internal diameter of the 8.4 m and 10 m Block 2 Long payload fairings are 7.5 m and 9.1 m, respectively. Both have a height of 27.4 m [1], and as can be seen, the 10 m diameter fairing tapers to a nose much earlier (at 19.1 m) than the 8.4 m diameter fairing (at 23.5 m). The full length of the fairing is therefore not available, as the spherical nose in Missile DATCOM (Figure 5.4) is wider than that of the SLS fairing nose at the top. Therefore the maximum length of the vehicle body (excluding the nose) is set to the height as which the fairing starts to taper, so 19.1 m for the 10 m diameter fairing, and 23.5 m for the 8.4 m fairing. The length of the nose is equal to the radius of the vehicle, as per Missile DATCOM. A geometry constraint is therefore that the vehicle must be able to fit within either of the payload fairings.

The minimum bounds are found by consulting the approximate sizes of other similar concept vehicles- Hercules, Charon, and the CobraMRV. Charon has a total length of 17.4 m and a diameter of 6.14 m [22], Hercules a length of 19.2 m and a diameter of 6.0 m [38], and the CobraMRV has a length of 19.8 m and a maximum width of 8.8 m. The minimum length of the vehicle is therefore set to 14 m, and the minimum diameter set to 5 m. The minimum diameter of the vehicle is not reduced further, as a crew size of 6 is still required to fit inside the abort capsule. A reduction of the diameter more than one meter would have implications on the safety and comfort of the crew. This is supported by the fact that Hercules transports a crew of 4, yet still has a diameter of 6.0 m. The minimum value of the vehicle length is taken as 13 m. The bounds and intervals of the vehicle length and diameter can be found in Table 5.2.

Table 5.2: The bounds and intervals of the aerodynamic independent variables

Variable	**Minimum [m]**	**Maximum [m]**	**Interval [m]**
D_v	5.0	9.0	0.5
L_v	13.0	26.0	1.0

It should be noted that SpaceX's Starship is most likely not an option to transport the Martian shuttle vehicle to Mars. The Starship payload bay tapers at a much earlier location, and has a maximum height of 17.24 m (although a 22 m configuration will also be available), shown in Figure 5.6. Therefore neither the Charon, the Hercules, nor the CobraMRV fit inside the Starship. These three vehicles are, of course, designed with specifically the SLS payload fairing in mind.

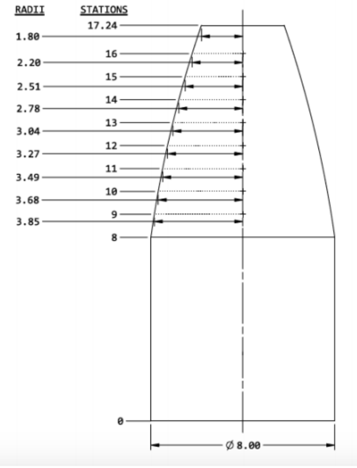

Figure 5.6: SpaceX's Starship payload bay[1]

---

[3] `https://www.spacex.com/media/starship_users_guide_v1.pdf`

6

Trajectory Modelling, Considerations, and Guidance

The trajectory discipline is responsible for determining the trajectory that transports the cargo and crew to and from the orbital node. To obtain the trajectory, not only must the vehicle's motion be addressed, but also the various constraints that the vehicle must adhere to, and the guidance that is implemented for this end. This chapter covers the modelling of the ascent and the descent phases, the constraints placed upon them, the guidance laws implemented, their, numerical modelling, and their validation.

6.1. Environment Models

In order to be able to determine the forces acting upon the vehicle to reliably simulate its trajectory, the environment at Mars must be modelled to a sufficient degree of accuracy. This section covers the various models needed to simulate the Martian environment.

6.1.1. Mars Overview

Mars is the fourth planet from the Sun, and the second smallest planet in our solar system, lying the farthest away from the Sun out of all the terrestrial planets. Named after the Roman god of war due to its reddish color, it is also called the 'Red Planet'. It is also the planet that is thought to be the most hospitable to life, with the exception of Earth. Table 6.1 presents an overview of Martian parameters taken from the NASA Mars Fact Sheet[1].

Table 6.1: An overview of Martian properties taken from the NASA Mars Fact Sheet

Parameter	**Value**
Mass	0.64171×10^{24} kg
Volume	16.318×10^{10} m^3
Equatorial radius	3396.2 km
Polar radius	3376.2 km
Semi-major axis	227.92×10^{6} km
Sidereal orbital period	686.980 days
Sidereal rotational period	24.6229 hours
Inclination of equator	25.19°
Mean temperature	-63°C

---

[1] `https://nssdc.gsfc.nasa.gov/planetary/factsheet/marsfact.html`

6.1.2. Martian Gravity

As the motion of an object in orbit is governed most dominantly by the force of gravity, the differences caused through the change of a gravitational model can be considerable, and the Mars' gravity must therefore be modelled to a sufficient degree of accuracy. One method of modelling gravity is Newton's law of gravitation, as given in Equation 6.1, where $\hat{\boldsymbol{g}}$ denotes the gravitational acceleration vector, G the gravitational constant, M the mass of Mars, R the distance from Mars' centre of mass, $\hat{\boldsymbol{r}}$ a unit vector directed from the centre of Mars to the location, R_M the radius of Mars, and r the distance from the Martian surface to the location. Mars is a smaller celestial body than Earth, and is much less massive, resulting in a surface level acceleration of approximately 30% of that at Earth.

$$\hat{\mathbf{g}} = -\frac{GM}{R^3}\hat{\boldsymbol{r}} = \begin{pmatrix} 0 \\ 0 \\ -\frac{GM}{(R_M+r)^2} \end{pmatrix} \tag{6.1}$$

There are alternatives to Newton's law to model a planet's gravity, of which one of the most common is the usage of spherical harmonics. Spherical harmonics are functions defined on the surface of a sphere, and can therefore be able to describe the gravitational potential of a body to a much higher degree. Spherical harmonics can be also implemented to varying degrees of complexity as seen in Figure 6.1, and therefore add versatility to a model. They are defined by Equation 6.2, where G denotes the gravitational constant, M the mass of Mars, r the distance from the centre of Mars, R_M the radius of Mars, λ and ϕ the latitude and longitude, P the associated Legendre functions of degree n and order m, and C and S coefficients.

$$U = \frac{GM}{r} + \frac{GM}{r}\sum_{n=2}^{\infty}\sum_{m=0}^{n}\left(\frac{R_M}{r}\right)^n \left[C_{nm}\cos(m\lambda) + S_{nm}\sin(m\lambda)\right] P_{nm}(\sin\phi) \tag{6.2}$$

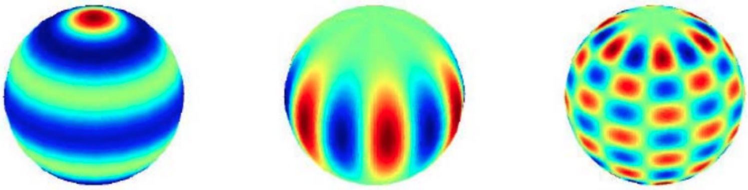

Figure 6.1: Illustration of three kinds of harmonics. From left to right: zonal, sectorial, and tesseral harmonics[1]

Of course, the higher the complexity of the spherical harmonics implemented, the more computational effort is needed, thereby increasing the time of each run in the optimisation process. A tradeoff between simulation run time and accuracy is evident. Tudat allows for the implementation of the central gravity model as well as the usage of spherical harmonics. During the ascent phase of the mission, the central gravity model is be used. The magnitude of the thrust acting upon the vehicle is several orders of magnitude greater than the fluctuations in gravitational acceleration, as well as the short duration of the ascent leaving little time for the gravitational fluctuations to take effect.

The descent phase, however, does require a higher order to be modelled, as gravity is one of the dominant forces upon the vehicle's return. Consequently the fluctuations in gravitational acceleration have a much more noticeable effect, and warrant a more accurate gravity model. To determine what order and degree is needed to achieve a sufficient accuracy, however, multiple runs of a descent trajectory are simulated using different orders and degrees, and the landing location is compared to a benchmark. The benchmark used is a spherical harmonics model using order and degree 20, and the differences are presented in Table 6.2.

---

[2] `http://seom.esa.int/cryotraining2016/files/CTC16/Day4/3_Forsberg_grace_sep2016%202.pdf`

Table 6.2: The difference in final state of the vehicle using various Martian gravity models

Model	Difference [m]
Central gravity	1117
SH (1,0)	1106
SH (1,1)	562
SH (2,0)	278
SH (2,2)	76

As is expected, the higher the degree and order that is used in the spherical harmonics models, the smaller the difference, with the central gravity model performing the worst. To ensure an accuracy of less than 100 m, a degree and order of 2 is implemented for the spherical harmonics model.

6.1.3. Martian Atmosphere

During its ascent and descent, the vehicle will experience all the different layers of the Martian atmosphere, affecting the local pressure, density, and temperature. The vehicle design and trajectory are dependent on these variables, meaning the atmospheric model must be one of sufficient accuracy.

One commonly used method is the exponential atmosphere model[3]. This model uses a scale height to determine the pressure, density, and temperatures at each altitude. This model is shown in Equation 6.3. The density of the atmosphere can subsequently be found using the equation of state.

$$\begin{aligned} h \leq 7000 \text{ km} \qquad & T = -31 - 0.000998h \\ & p = 0.699e^{-0.00009h} \\ h > 7000 \text{ km} \qquad & T = -23.4 - 0.00222h \\ & p = 0.699e^{-0.00009h} \end{aligned} \tag{6.3}$$

Commercially available models for the Martian atmosphere based off of simulations and lander and spacecraft data can also be used. One of these is the Mars Climate Database (MCD), distributed by ESA. The MCD is a database of meteorological fields derived from General Circulation Model numerical simulations of the Martian atmosphere and validated using available observational data [43]. This model is therefore able to simulate the fluctuations in atmospheric properties in the Martian atmosphere to a higher degree.

Tudat is able to implement both an exponential atmosphere model, and the most recent MCD model. Due to the large influence of the atmosphere on the trajectory of the vehicle, the exponential atmosphere model is not chosen, as a higher level of accuracy is needed. However, the Tudat model is only available for altitudes above 50 km altitude, and is therefore incomplete for the Martian vehicle trajectory simulations. An atmospheric model is therefore developed for the simulations from the commercially available MCD data.

The model developed from the MCD data is a 2D model, meaning that it is independent of latitude and longitude, but is a function of altitude. The atmospheric properties between latitudes of 5 and 40 degrees and longitudes of -30 and 5 degrees are taken at 10-degree intervals and averaged to produce one atmospheric profile. The data stored as a function of altitude contains information regarding the local density, pressure, temperature, gas constant, molar mass, and specific heat ratio. How these properties are calculated, and the subsequent atmospheric model developed, is given in Appendix A. The atmospheric profiles found for the Martian temperature, pressure, and density can be seen in Figures 6.2 and 6.3, respectively, when compared to the exponential atmosphere model.

---

[3] `https://www.grc.nasa.gov/www/k-12/airplane/atmosmrm.html#:~:text=The%20Martian%20atmosphere%20is%20an,to%20the%20edge%20of%20space.&text=The%20heated%20gas%20is%20then,decreases%20as%20we%20increase%20altitude.`

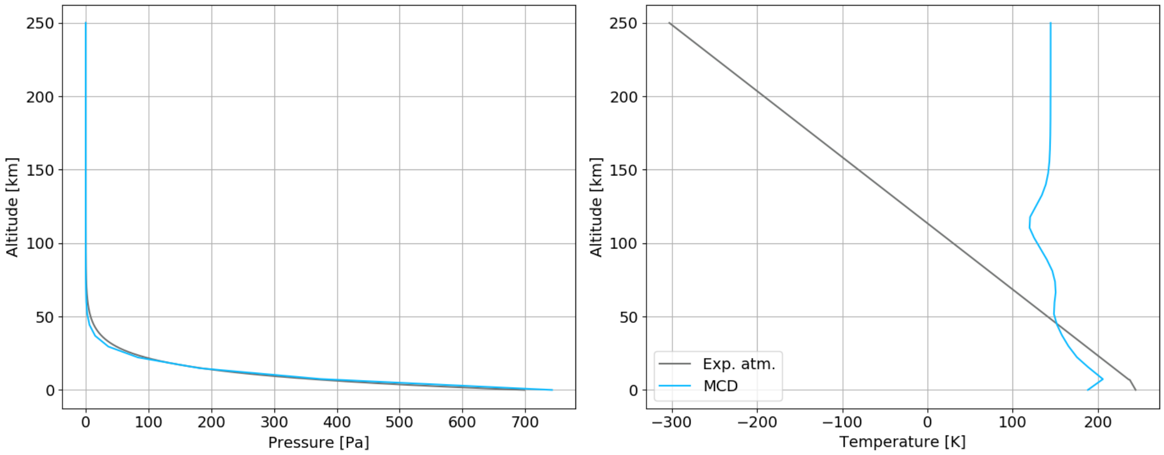

Figure 6.2: The a vertical profile of the Martian atmospheric pressure and temperature as modelled by the MCD data and the exponential atmosphere model.

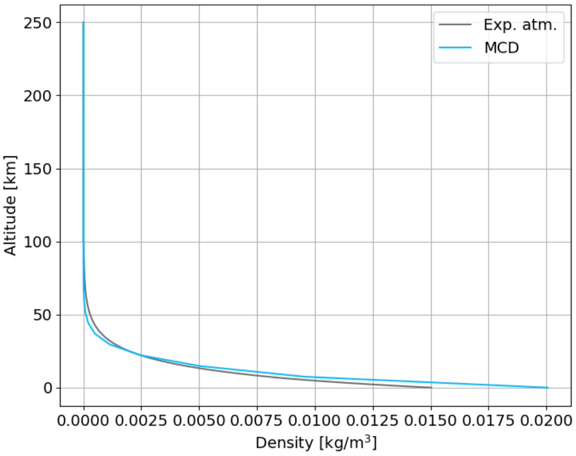

Figure 6.3: The a vertical profile of the Martian atmospheric density as modelled by the MCD data and the exponential atmosphere model.

6.2. Flight Mechanics

This section covers the motion of the shuttle vehicle throughout its ascent to and its descent from the node. In order to express this, the relevant reference frames and associated state variables are presented and discussed, followed by the basics of motion of a vehicle through a planetary atmosphere.

6.2.1. Reference Frames

In order to describe the motion of a body, its state must be represented with respect to a reference point. For this, reference frames are used. A reference frame consists of a coordinate system to which motion can be related, and many different frames exist in order to best describe particular motions and orientations. This section presents the various reference frames used to describe the motion of the vehicle.

Mars-Centered

Two reference frames can be applied to Mars: an inertial and a rotating reference frame. An inertial frame refers to a coordinate system that has no net force acting upon it, and therefore is in a state of constant rectilinear motion, constituting of a right-handed orthogonal axis system. This reference frame is applied to Mars, as seen in Figure 6.4. In reality Mars's spin axis is not completely stable and 'wobbles', however this motion is considered to have so little effect that the reference frame can be considered inertial (for applications such as the MSc research). A rotating reference frame is very similar to an inertial reference frame, however, as the x-axis is fixed to the surface of the planet, it rotates about the z-axis as the planet rotates. This is shown in Figure 6.5, given by Mulder et. al. [48].

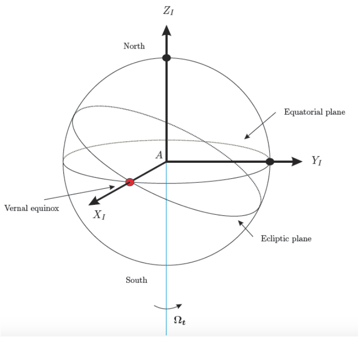

Figure 6.4: The Mars-centered inertial reference frame from Mulder et. al. [48]

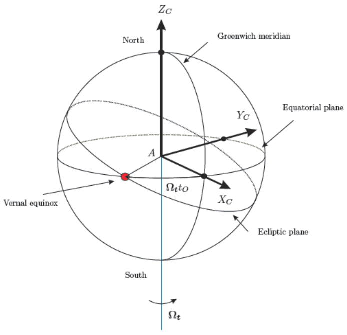

Figure 6.5: The Mars-centered rotating reference frame from Mulder et. al. [48]

Body-Fixed

A body-fixed reference frame has the origin of the reference at the associated body's centre of mass. This is shown in Figure 6.6. The x-axis lies in the plane of symmetry of the vehicle, the z-axis orthogonally downward, and the y-axis completes the right-hand rule. The thrust force T acts through the centre of motion of the vehicle, and is expressed in both Cartesian coordinates (T_x, T_y, T_z) and spherical coordinates (T, ε_T, ψ_T) in the figure (see Section 6.2.1 for more information on state variables).

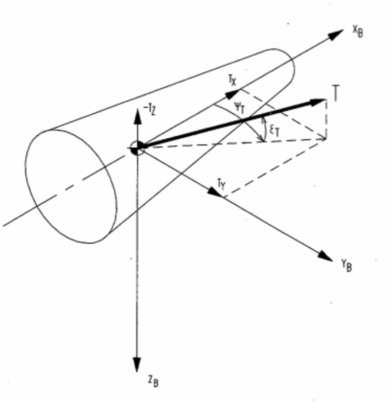

Figure 6.6: The body-fixed reference frame as displayed in relation the the thrust force [45]

Aerodynamic

The aerodynamic reference frame is utilised to express the lift and drag forces on the body, as well as to express the attitude of the body with respect to the airflow. It's origin is at the body's centre of mass, therefore coinciding with that of the body-fixed reference frame. This is shown in Figure 6.7, where the left image is a representation of the vehicle's attitude angles (angle of attack α, angle of slideslip β, bank angle μ) and angular rates (roll p, pitch q, and yaw r), and the right image is a representation of the lift (L) and drag (D) forces on the vehicle. On the right, the vehicle velocity with respect to the atmosphere V_A is also shown, as well as the angles of attack and sideslip (α_A, β_A).

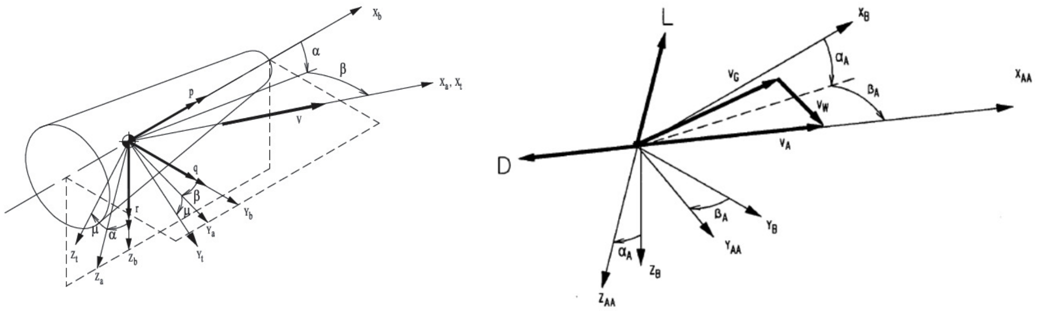

Figure 6.7: The aerodynamic reference frame as displayed in relation to the attitude of the vehicle (left) taken from Mulder et. al. [48], and the lift and drag forces (right) taken from Mooij [45]

Frame Transformation

Transformation between reference frames is necessary to be able to describe the motion of the vehicle in the appropriate manner. To do this, translation and rotation between frames must be performed, as given by Equation 6.4. The translation from frame A to B is denoted by S, and the rotation by $\mathbb{T}_{BA}$. $\mathbb{T}_{BA}$ is a transformation matrix, which describes the successive Euler transformations needed, as depicted in Figure 6.8.

$$F_B = S_{BA} + \mathbb{T}_{BA} F_A \tag{6.4}$$

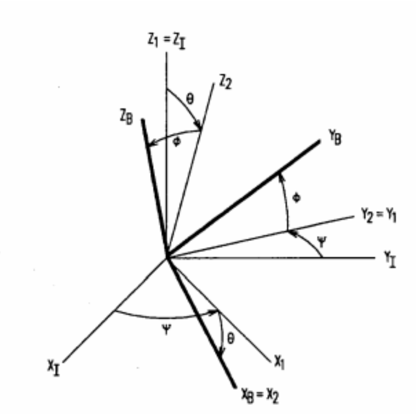

Figure 6.8: The successive Euler transformations needed to to rotate from the inertial Mars-centered (index I) to the body-fixed reference frame (index B) as given by Mooij [45]

6.2.2. State Variables

State variables specify the state of a system, such that its future behaviour can be determined if no other forces are to act upon the system. This therefore requires knowledge of a variable's mass, as well as its motion with respect to the chosen reference frame. Just as with reference frames, different state variables are chosen to describe an object's motion in different situations, in order to most intuitively describe the motion. The state variable mass, however, it always a state variable. This section presents the different state variables chosen to describe the vehicle's motion.

Cartesian

Cartesian coordinates are with respect to an orthogonal reference system, as seen in Figure 6.9, and can therefore be applied to the inertial and rotating reference frames. The position and velocity of the body care given as following:

$$\begin{aligned}\text{Position}: x, y, z\\ \text{Velocity}: \dot{x}, \dot{y}, \dot{z}\end{aligned} \tag{6.5}$$

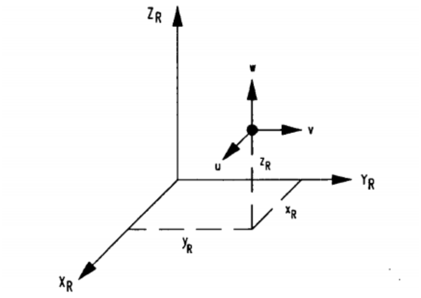

Figure 6.9: A Cartesian coordinate system [45]

Spherical

Spherical coordinates also also ways to describe position and velocity, as seen in Figure 6.10. The longitude is measured positively East, and the latitude is measured along the meridian from the Equator and positive in the North direction. The distance is measured between the centres of mass of the central body and the vehicle. The groundspeed is the relative velocity, measured with respect to the rotating reference frame. The flight-path angle is measured with respect to the local horizon. The heading defines the direction of the projection of the groundspeed in the local horizontal plane with respect to the local North.

Position: Distance r, Longitude τ ($0° \leq \tau \leq 360°$), Latitude δ ($0° \leq \delta \leq 90°$)
Velocity: Groundspeed V, Flight-path angle γ ($-90° \leq \gamma \leq 90°$), Heading χ ($-180° \leq \delta \leq 180°$)

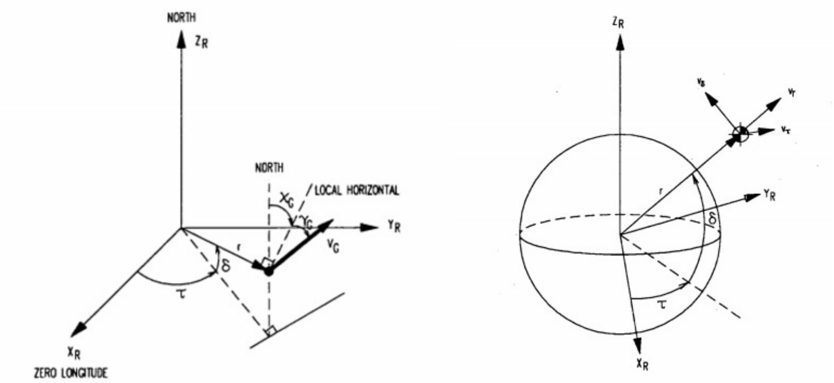

Figure 6.10: The six spherical flight parameters (left) and a vehicle of which the position is described using spherical coordinates, and the velocity using Cartesian coordinates (right) as given by Mooij [45]

Orbital

The instantaneous motion of a body in an orbit is always defined by the six classic orbital elements, as seen below. The semi-major axis defines the size of the orbit, and the eccentricity the shape. The inclination indicates the tilt with respect to the central body, and the argument of pericentre and right ascension of the ascending node both describe the orientation of the orbit with respect to the central body. The position of the orbiting object is described by the true anomaly in degrees, with respect to the pericentre. The orbital elements are shown in Figure 6.11.

a: Semi-major axis
e: Eccentricity ($0 \leq e \leq 1$)
i: Inclination ($0° \leq i \leq 180°$)
ω: Argument of pericenter ($0° \leq i \leq 360°$)
Ω: Right ascension of the ascending node ($0° \leq i \leq 360°$)
θ: True anomaly ($0° \leq i \leq 360°$)

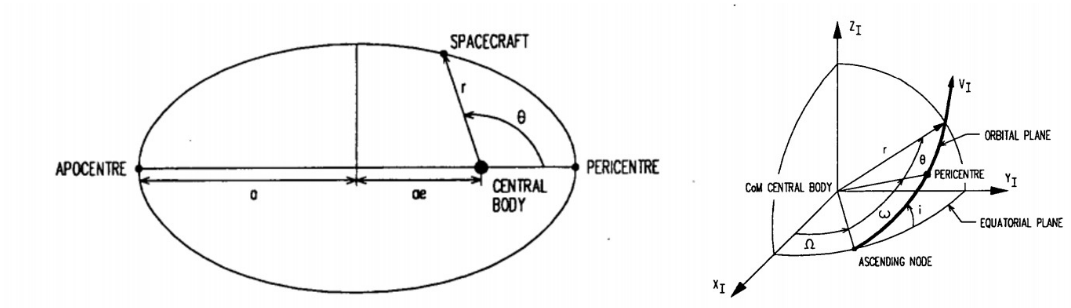

Figure 6.11: Definition of the orbital elements a, e, θ (left) and ω, Ω, and i (right) as given by Mooij [45]

6.2.3. Equations of Motion

The equations of motion for the vehicle are expressed in the Mars-centered inertial reference frame, using spherical coordinates. The rate of change of the position state variables are given in Equations 6.6-6.8, and the rate of change of the velocity state variables are given in Equations 6.9-6.11. The rate of change of mass is given in Equation 6.12. In these equations, T represents thrust, L lift, D drag, θ the pitch angle, μ the bank angle, $g(r)$ the gravitational acceleration as a function of the radial distance, ω_M the angular velocity of Mars, m_v the vehicle mass, and q the rate of change of mass, as given by Mooij [45]. The equations assume a rigid body, no wind, no angle of sideslip, and no out-of-symmetry-plane thrust. As can be seen, it is possible for denominators to go to 0 if r, m_v, or V are equal to exactly 0, or if γ or δ are equal to exactly 90°; these instances are highly unlikely to occur during the propagation.

$$\dot{r} = V \sin\gamma \tag{6.6}$$

$$\dot{\delta} = \frac{V \cos\gamma \cos\chi}{r} \tag{6.7}$$

$$\dot{\tau} = \frac{V \cos\gamma \sin\chi}{r \cos\delta} \tag{6.8}$$

$$\dot{V} = \frac{T\cos(\theta-\gamma) - D}{m_v} - g(r)\sin\gamma + \omega_M^2 r \cos\delta(\sin\gamma\cos\delta - \cos\gamma\sin\delta\cos\chi) \tag{6.9}$$

$$\dot{\gamma} = \frac{\left[L + T\sin(\theta-\gamma)\right]\cos\mu}{m_v V} + \left(\frac{V}{r} - \frac{g(r)}{V}\right)\cos\gamma + 2\omega_M \sin\chi\cos\delta + \frac{\omega_M^2 r\cos\delta(\cos\gamma\cos\delta + \sin\gamma\sin\delta\cos\chi)}{V} \tag{6.10}$$

$$\dot{\chi} = \frac{\left[L + T\sin(\theta-\gamma)\right]\sin\mu}{m_v V\cos\gamma} + \frac{V\cos\gamma\sin\chi\tan\delta}{r} + 2\omega_M(\sin\delta - \cos\chi\cos\delta\tan\gamma) + \frac{\omega_M^2 r\sin\delta\cos\delta\sin\chi}{V\cos\gamma} \tag{6.11}$$

$$\dot{m}_v = -q \tag{6.12}$$

6.3. Numerical Modelling

In order to obtain the path the vehicle takes, its state must be integrated and propagated. There are many different integrators and propagators available, and each have their associated benefits and drawbacks. The main trade-off that must be made to determine the most appropriate combination is between calculation time and accuracy. Various options for both are presented and discussed in this section.

6.3.1. Propagation Methods

An integrator and propagator work in tandem to obtain the vehicle's state at each point in time. The integrator determines how to integrate the dynamic equations to obtain the next 'step', the propagator determines how the step is placed. This is done by using various state variables associated with a propagator to calculate the next state, which can then be transformed back to the desired state variables. Various propagators are available in the Tudat environment. These are listed below (USM stands for Unified State Model, and MRP for Modified Rodriquez Parameters)[4].

Table 6.3: The various propagators available in the Tudat environment

Propagator	**State Variables**	**Method**
Cowell	Cartesian	Models the Newtonian forces
Encke	Cartesian	Calculates deviations from a Kepler orbit
Keplerian	Keplerian	Models the Gauss planetary equations
Modified Equinoctial Elements	Modified Keplerian	Models the Gauss planetary equations, but in order to avoid singularities, the Keplerian elements are modified
USM Quaternions	USM	Uses three parameters from a velocity hodograph in combination with quaternions
USM MRP	USM	Uses three parameters from a velocity hodograph in combination with MRP
USM Exponential Map	USM	Uses three parameters from a velocity hodograph in combination with exponential map

Although the vehicle will be launched into, and descend from, an orbit, the ascent and descent trajectories do not resemble orbits. Almost all the supported propagators use methods of propagation of which the path will mostly resemble an orbit. These propagators are therefore not able to sufficiently or accurately describe an ascent or descent trajectory. The Cowell propagator is therefore the best choice.

6.3.2. Integration Methods

Integration of ordinary differential equations is not possible analytically, therefore numerical integration schemes are a necessity. A basic integration scheme can be defined by Equation 6.13 as given by Noomen [51]. h denotes the step size, and Φ is given in Equation 6.14, which is integrator-dependent.

$$y_{n+1} = y_n + h\Phi \tag{6.13}$$

$$\Phi = \dot{y_n} = f(t_n, y_n) \tag{6.14}$$

An important difference between integrators is whether they implement variable step size. A variable step-size integrator is able to autonomously determine the size of the steps that should be taken. A planetary flyby is a scenario in which this can play a greatly beneficial role when compared to a fixed step-size integrator. During the coast toward the planet, the dynamics of the spacecraft do not vary much with time, therefore using a very small step size introduces unnecessarily large computational time; however once close to the planet, the dynamics will change rapidly, and the step size must be small to be able to accurately determine the trajectory. Therefore having a variable step-size (if set appropriately) can increase the accuracy as well as decrease the computational time taken for the integration.

Tudat offers various integrators, both fixed and variable step, shown in Table 6.4. Euler and Runge-Kutta 4 integrators are fixed step, with the rest being variable. The numbers associated with the Runge-Kutta-Fehlberg (RKF) integrators denote its' order and order of truncation. For example, the RKF4(5) integrator is a fourth-order integrator, that has a truncation of order 5. The RKF6(7) is therefore more accurate than the RKF4(5) as

---

[4] `https://tudat.tudelft.nl/tutorials/applicationWalkthroughs/propagatorTypesComparison.html`

it has a higher order, however due to the fact that more computations are necessary for the RKF6(7) for each step, it is more computationally expensive.

Table 6.4: The integrators provided by the Tudat environment

Integrator	**Step**	**Stage**	**Step size**
Euler	Single	Single	Fixed
RK4	Single	Multi	Fixed
RKF4(5)	Single	Multi	Variable
RKF5(6)	Single	Multi	Variable
RKF7(8)	Single	Multi	Variable
RKF8(7)DP	Single	Multi	Variable
Adams-Bashforth-Moulton	Multi	Multi	Fixed
Bulirsch-Stoer	Extrapolation	Multi	Variable

The choice of integrator comes down to a trade off between accuracy and speed. To identify the optimal integrator for the vehicle, the integrators are tested and compared for these properties, as the optimum integrator must adhere to a minimum accuracy whilst being as computationally inexpensive as possible. In order to determine the (relative) accuracy of an integrator, an ascent launched from the equator on the Martian mean surface (altitude 0) is simulated using a high order integrator with strict tolerance settings to act as a benchmark. The other integrators, using various tolerance settings, are consequently compared to the benchmark simulation. The RKF8(7)DP integrator is chosen as it has the highest order. The minimum step size, relative tolerance, and absolute tolerance of the benchmark are all set to 1e-14 in order to stay above the machine epsilon of 1e-15.

The initial conditions and design variables used in the benchmark simulation are found below in Tables 6.5 and 6.6, respectively.

Table 6.5: The initial conditions used to simulate the integrator comparison ascent

Variable	**Value**
r_0 [m]	3389530
δ_0 [deg]	0.0
τ_0 [deg]	0.0
V_0 [m/s]	0.01
γ_0 [deg]	86.0
χ_0 [deg]	90.0

Table 6.6: The design variables used to simulate the integrator comparison ascent

Design Variable	**Value**
	Vehicle
p_c [Pa]	150e5
O/F [-]	3.12
D_e [m]	1.06
$\dot{m}$ [kg/s]	82.0
n_{eng} [-]	6
$M_{p,a}$ [kg]	80000
$M_{p,l}$ [kg]	2487
D_v [m]	8.0
M_{PL} [kg]	1200
	Trajectory
Thrust law [-]	1
TW_{min} [-]	1.5
TW_{max} [-]	4
Pitch angles [deg]	γ_0, 69.04, 50.65, 25.84, 6.38, 0

Figure 6.12 presents the change in semi-major axis, with respect to the benchmark, of the simulations using the variable step size integrators with different tolerance settings (found in the figure legend). Only the variable step-size integrators are tested, as the fixed step size integrators do not perform nearly as well, as verified by Rozemeijer [58]. The integrators use the same minimum step size as the benchmark, but set the maximum set size to 10, to test the accuracy of the integrator whilst using the step size variability. As can be seen, the RKF4(5) integrator performs exceedingly well compared to the other integrators. In order to achieve an accuracy that is within 100 m, the RKF4(5) integrator is chosen using a tolerance setting of 1e-7 to ensure the least number of function evaluations.

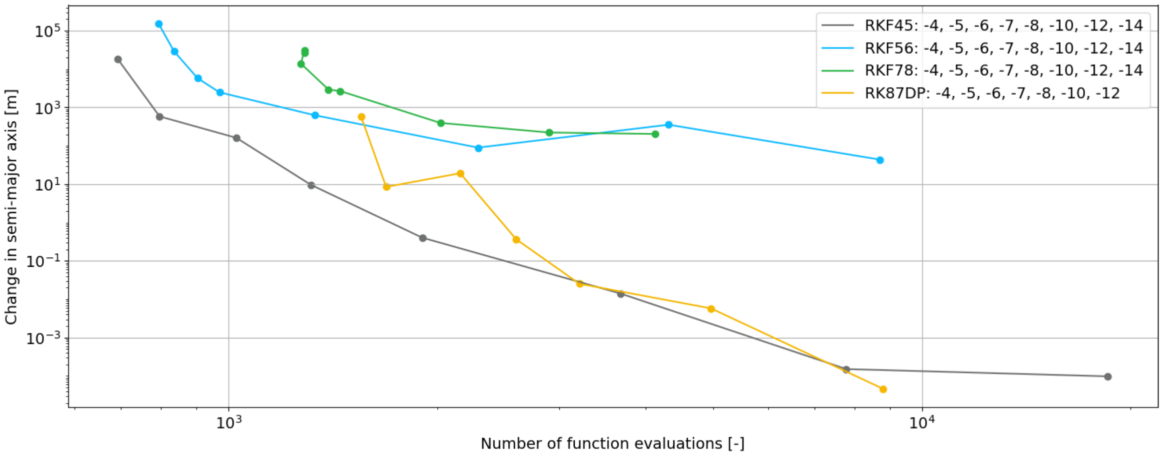

Figure 6.12: A comparison of the variable step-size integrators, using various tolerance settings

6.4. Ascent Considerations, Constraints, and Guidance

In this section, the considerations associated with ascent and the necessary guidance are presented.

6.4.1. Ascent Considerations

When considering ascent, there are two basic methods: the Direct Ascent (DA) and the Hohmann Transfer Ascent (HTA). These are depicted in Figure 6.13. The DA trajectory is selected such that its summit point coincides with desired orbit. In the HTA, the vehicle first is propelled to a low-altitude circular parking orbit, just outside the densest part of the central body's atmosphere (for Earth this would be approximately 200 km [66]). The vehicle then coasts for a period, and is then injected into a Hohmann transfer orbit to reach the final desired orbit.

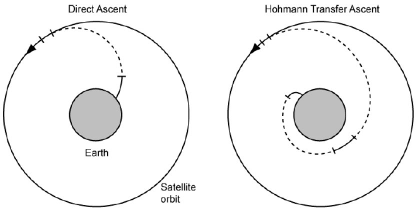

Figure 6.13: The two basic ascent methods as given by Wakker [66]

There are benefits and drawbacks associated with each method. Overall, the HTA requires less propellant as there is less gravity loss due to the less steep ascent. However, the flight time is much longer, and a global ground network is required for communication. As the infrastructure at Mars does not allow for global ground network, the HTA method is not possible, and the DA is used.

6.4.2. Ascent Constraints

Constraints must be placed upon the vehicle and its trajectory to ensure the vehicle and crew's safety and performance. This section covers the constraints placed upon the vehicle during the ascent phase.

Maximum acceleration g_{mars} during nominal operations

The maximum acceleration experienced by the vehicle during nominal operations is determined by the maximum loading the crew is able to experience. Although humans can sustain up to 8 g_{earth} of a short period of time [40], the maximum load for the vehicle should be set to a value such that the crew is able to endure it over at least a couple minutes whilst not sacrificing their health and comfort. The fact that the crew has spent considerable time on Mars, where the gravitational acceleration is considerably less than on Earth, must also be taken into consideration. The maximum g-load value that a crew can withstand on Mars is therefore considered the same as the maximum g-load that a crew can withstand on Earth. The crew in the Space Shuttle experienced a maximum load of 3 g_{earth} upon reentry[5], whereas the Apollo crew experienced up to 7 g_{earth}[6]. In accordance with Charon [22], the maximum load is set to 4 g_{mars}, and is written as the following:

$$\dot{v}_{max} = 4 \text{ g}_{mars} \tag{6.15}$$

Maximum mechanical load

The maximum mechanical load (g-load) is set to the same value as the maximum acceleration the crew is subject to under nominal operations. This is 4 g_{mars}.

$$n_{max} = 4 \text{ g}_{mars} \tag{6.16}$$

Maximum stagnation heat flux

The maximum stagnation heat flux is a very important constraint as it ensures the structural integrity of the vehicle is not compromised, and the vehicle does not burn upon ascent or reentering. The maximum heat flux is set to 250 kW/m^2, as this is what has been estimated for the Space Shuttle vehicle by Curry [15]. This constraint can therefore be written as the following:

$$q_{max} = 250 \text{ kW/m}^2 \tag{6.17}$$

6.4.3. Ascent Guidance

The optimisation of a rocket ascent trajectory is a complex problem, as it is characterised by highly non-linear dynamics. In order to optimise the trajectory in terms of mass, the propellant consumption must be minimised. This is done using both aerodynamic guidance, and thrust magnitude modulation. These methods are presented in this subsection, as well as the calculation of the ascent burn time, as both guidance laws rely on this being determined before the start of the simulation.

Ascent Aerodynamic Guidance

The optimisation of the ascent trajectory is performed by optimising the pitch angle using a parametric pitch law. This utilises the direct parametric method discussed in Section 3.2. The usage of a parametric pitch law is a common first-stage method for trajectory optimisation. Desai et. al. [16] implement ascent trajectory optimisation for the MAV in this manner, and the Hercules vehicle also partially implements this law [39]. At the TU Delft, the parametric pitch law was first applied by van Kesteren [34], and has further been used

---

[5] `https://www.space.com/42109-soyuz-launch-failure-astronaut-crew-good-health.html`

[6] `https://history.nasa.gov/SP-368/s2ch5.htm`

by Miranda [44], Rozemeijer [58], and Haex [23], thus working successfully for a variety of different launch vehicles and target orbits.

The parametric pitch law defines the pitch angles at user-defined control nodes over the trajectory, and are considered part of the trajectory design variables. Throughout the optimisation process, the optimal pitch angles are found at the defined control nodes, between which the pitch is linearly interpolated. The number of control nodes used is defined by the user, spaced equally along the ascent trajectory. An example can be seen in Figure 6.14, where the flight path angle is optimised using five nodes by modulating the angle of attack. As can be seen, the nodes are spaced equally over the ascent time, and the vehicle's flight path angle closely follows the desired flight path angle imposed by the pitch law.

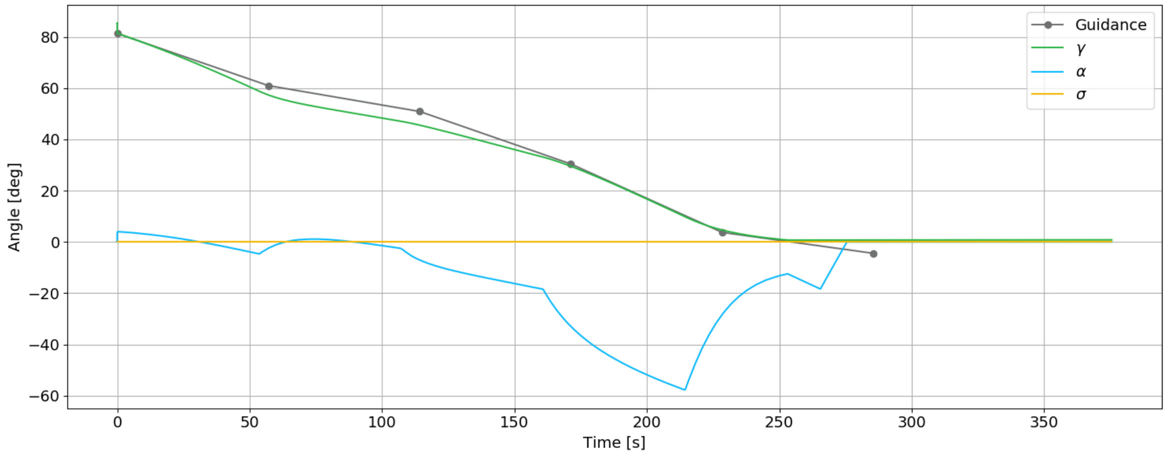

Figure 6.14: An example of the vehicle's body orientation angles during an ascent trajectory, compared to the Tudat guidance. γ denotes the flight path angle, α the angle of attack, and σ the bank angle

A control law is needed to ensure that the desired pitch angle dictated by the guidance is attained by the vehicle. The control law is shown in Equation 6.18, where α denotes the angle of attack, K the gain factor, γ the flight path angle, and γ_d the desired flight path angle as determined by the pitch law.

A discrepancy between γ_d and γ will lead to much larger effects on the vehicle's trajectory at higher velocities. Although the implementation of a high gain factor can reduce this error, it can also lead to overshoot and large immediate changes in angle of attack at lower velocities. The gain factor is therefore increased proportionally to the vehicle's velocity. This can be seen in Equation 6.19, where the gain is increased linearly from 1 to 7 with as a function of velocity, until the velocity reaches a value of 1 km/s. For velocities greater than 1 km/s the gain remains at 7.

$$\alpha = K(\gamma - \gamma_d) \tag{6.18}$$

$$\begin{aligned} V \leq 1000 \text{ m/s:} \qquad & K = 0.006V + 1 \\ V > 1000 \text{ m/s:} \qquad & K = 7 \end{aligned} \tag{6.19}$$

The pitch law nodes are placed along the ascent trajectory, spaced equally over the total burn time. For this, the total ascent burn time must be known a priori. How this is calculated, is presented later in this subsection.

Ascent Thrust Guidance

Not only is aerodynamic guidance implemented to optimise the vehicle's GTOW, thrust magnitude guidance is also implemented. There are various ways in which the thrust can be modulated, however three thrust laws are selected and implemented for the MDO that determine the thrust as a function of the Thrust-to-Weight (TW) ratio. As discussed in Section 6.4.2, there are limitations to the maximum acceleration the vehicle may experience, expressed in terms of g-load. The three thrust laws that are established are therefore also limited by their minimum and maximum TW ratio (TW_{min}, TW_{max}). TW_{min} and TW_{max} are therefore also design variables. The three thrust laws are chosen as all three are very different to one another, and they can be highly tailored depending on their TW_{min} and TW_{max} values. All three laws as are progressive, meaning that the TW_{min} will always be the starting TW ratio of the ascent, and it culminates at the TW_{max}. Regressive thrust laws, where the opposite is implemented, are also possible, however this would result in very high engine masses due to the exceedingly high thrust needed, dictated by the high TW ratio at the start of the ascent. The engines would then not be used to their full capacity during the rest of the ascent as the TW ratio would decrease, resulting in an inefficient design. The three thrust laws are described below, where the order number refers to the order of the equation representing the TW ratio. The thrust laws are further presented graphically in Figure 6.15.

Thrust law order 0:
The TW ratio is set to the maximum TW ratio. This is expressed in 6.20, where TW denotes the current TWt ratio, M denotes the current vehicle mass, and g the current gravitational acceleration. This law is chosen due to its simplicity.

$$TW = \frac{T_{tot}}{Mg} \tag{6.20}$$

Thrust law order 1:
The TW ratio is expressed by a linear relationship between TW_{min} and TW_{max}, as a function of time. This is seen in 6.21, where $t_{b,a}$ denotes the total ascent burn time and t the current time (assuming the initial time is equal to 0). This law is chosen as this is also the law implemented by Gafferel et. al. [22].

$$TW = \left[\frac{TW_{max} - TW_{min}}{t_{b,a}}\right] t + TW_{min} \tag{6.21}$$

Thrust law order 2:
The TW ratio is expressed by a quadratic relationship between TW_{max} and TW_{min}, as a function of time. This is seen in 6.22, where t denotes the current time. The quadratic coefficients a, b, and c are determined by a least squares fitting in the optimisation tool. The equation is always scaled to resemble the TW curve shown in Figure 6.15. This law is chosen as it attains a higher TW ratio earlier in the ascent than thrust law 1, and therefore is a 'medium' between thrust laws 0 and 1. [22].

$$TW = at^2 + bt + c \tag{6.22}$$

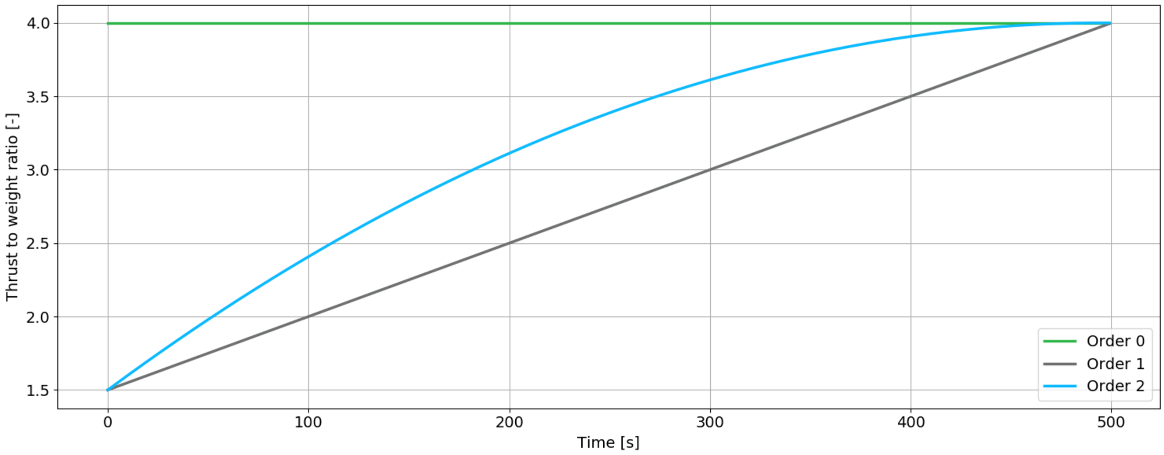

Figure 6.15: The three thrust magnitude laws where TW_{max}, TW_{min}, and $t_{b,a}$ are taken as 4, 1.5, and 500 s, respectively

Thrust law orders 1 and 2 rely on the knowledge of the total ascent burn time to determine the current TW ratio. How this is calculated, is presented below.

Determination of the Ascent Time

Both the aerodynamic guidance and the two of the three thrust magnitude laws (laws 1 and 2) require the total ascent time to be known in order for them to be implemented. Haex [23], Rozemeijer [58], Contant [14], and van Kesteren [34] set the ascent burn time as a design variable (the propellant mass is then calculated as the product of the ascent burn time and total propellant mass flow). This ensures that all the propellant is used, leading to optimum fuel consumption, as well providing the knowledge of the exact burn out moment. In their research, the vehicles operate at maximum thrust capacity and so the engine mass flow is constant over time. However, as modulating the thrust in accordance with a thrust law also modulates the engine mass flow, this method cannot be used for the Martian shuttle vehicle.

One option to solve this issue is to set the ascent burn time as a design variable alongside the ascent propellant mass. This would mean that the ascent burn time determines the ascent thrust time, where an overestimation of the burn time would lead to an engine burnout earlier than the design burn time, and an underestimation of the burn time would lead to excess weight (too much propellant). The bounds for the propellant mass, however, are large and so the bounds for the burn times would also have to be large, leading to large discrepancies between the actual and design burn times. The optimisation process would be compromised due to this large inefficiency, as well as the need to optimise another design variable. The mass of the propellant needed for the transfer, docking, and entry burns are also determined by the assumption that all the ascent propellant mass is consumed upon the ascent, thereby also producing errors in the GTOW.

Instead, the ascent burn time is estimated before the actual trajectory simulation takes place by calculating the TW ratio at every instance, and therefore the mass flow, until all the propellant is used. The ascent burn time is therefore obtained after the vehicle sizing but before the simulation of the ascent. The total engine thrust, mass flow, specific impulse, total vehicle mass, and total ascent propellant are known from the propulsion system and vehicle sizing.

If thrust law 0 is chosen for the thrust guidance, the TW ratio at every instance is known as it is set to the maximum TW ratio. The mass flow can be calculated from the TW ratio using the vehicle's mass and engine properties (Equation 6.20 and Equation 4.5), and so the ascent burn time is obtained. If thrust laws 1 of 2 are used, the process is iterative, as the TW ratio is dependent on a known total ascent burn time. An initial guess for the ascent burn time is used to then calculate the TW ratio at every instance, however if the total ascent burn time obtained does not equal the initial burn time guess, the guess is increased or decreased accordingly, until they are within 1 second of each other.

When using this method, some other issues arise that must be addressed. As the thrust magnitude is dependent on the TW ratio, it is also dependent on the gravitational acceleration acting upon the vehicle. In the method outlined above, the Martian surface gravity (3.711 m/s^2 [7]) is used to determine the TW ratio, however in the ascent simulation itself, the gravitational acceleration is dependent on the altitude, which is of course unknown. This can lead to differences between the calculated TW ratio before the simulation and the actual TW ratio during the simulation. The calculated ascent time is therefore always an underestimation of the actual ascent time, as the TW ratio is always underestimated due to the usage of the surface gravity.

To demonstrate this effect, an ascent trajectory for both the Hercules and Charon vehicles is simulated using a (non-optimised) pitch angle profile. The pitch angles are then both increased and decreased between -30% and 30%, as seen in Figure 6.16 on the left, such that the maximum altitudes attained by the vehicles are also increased and decreased. The effect of the changes in altitudes reached on the difference between estimated burn time (using the surface gravitational acceleration) and the actual simulated burn time (dependent on altitude) is clear to see in the rightmost figure in Figure 6.16. As the maximum altitude increases, so does the discrepancy between the calculated and simulated burn times due to the decrease in gravitational acceleration, and therefore TW ratio.

---

[7] `https://nssdc.gsfc.nasa.gov/planetary/factsheet/marsfact.html`

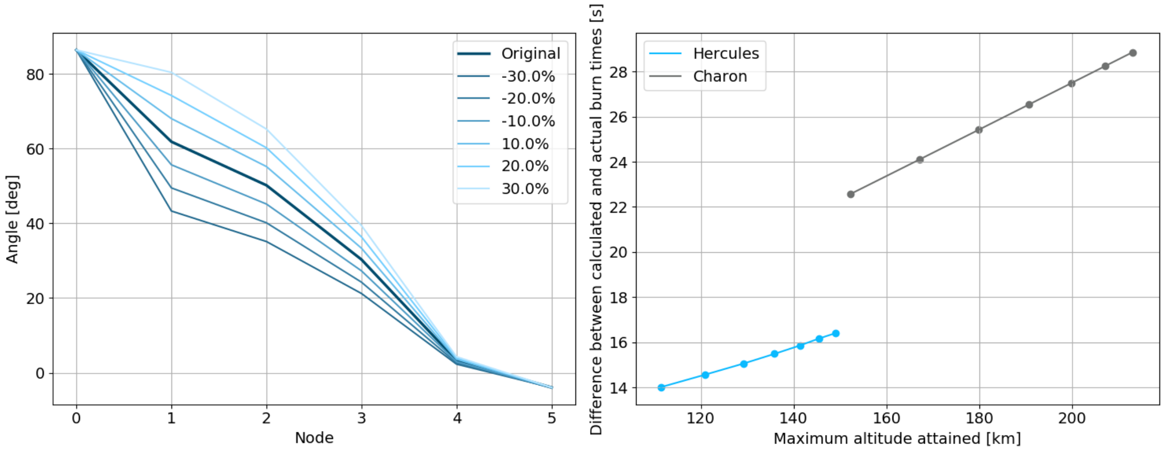

Figure 6.16: The variations in pitch profile (right) and the maximum altitude attained per pitch angle variation (left)

Although this effect is unwanted, sufficient optimisation of the ascent profile can still be attained. If the optimiser is still able to sufficiently optimise the trajectory whilst an error between calculated and actual burn times is present, then this method of burn time calculation can still be considered acceptable. This will be determined in the validation of the ascent profile, in Section 6.6.

6.4.4. Ascent Design Variables

The ascent design variables comprise of the variables needed for the aerodynamic guidance and thrust magnitude guidance. These are given below, where θ_{1-6} denote pitch angles 1-5, TL the thrust law order, and TW_{min} and TW_{max} the minimum and maximum TW ratios, respectively. It should be noted that the initial flight path angle is set to the value of θ_1, therefore θ_1 refers to the launch pitch angle.

Six pitch control nodes are implemented, in order to ensure sufficient variability within the trajectory and allowing for a sufficient optimisation, whilst reducing the number of design variables. TL is necessary to determine the thrust over the ascent, and subsequently TW_{min} and TW_{max} are necessary to express the thrust profiles. The search space for these variables is given in Section 7.2.

$$Z_{ascent} = [\theta_{1-6}, TL, TW_{min}, TW_{max}]$$

6.5. Descent Considerations, Constraints, and Guidance

In this section, the considerations and constraints associated with Entry, Descent, and Landing (EDL) are presented, followed by the implemented guidance to ensure the constraints are satisfied.

6.5.1. Descent Considerations

When considering descent through an atmosphere, there are three basic types of entry: ballistic entry, gliding entry, and skipping entry, as seen in Figure 6.17. As the vehicle must be able to return to the Martian base with sufficient accuracy, the vehicle must be a lifting body that uses actuators and/or control surfaces to steer its trajectory accordingly. The vehicle will therefore complete a gliding entry.

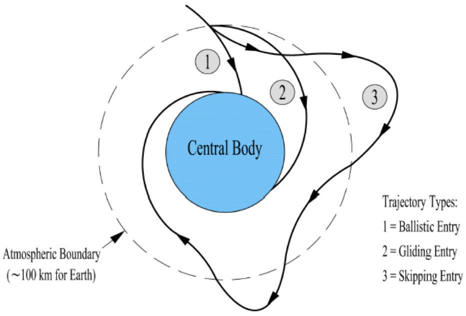

Figure 6.17: The three basic types of entry as given by Mooij [46]

For gliding entry vehicles, there are three main constraints that compose the ’entry corridor’, which is the enclosure of all entry and descent trajectories that fulfil the constraints and guarantee a safe flight until landing. It is determined by the three following constraints as given by Mooij [46]:

- Equilibrium-glide condition (’soft constraint’, under which no skipping occurs)
- Maximum stagnation heat flux
- Maximum mechanical load

These constraints can be expressed as a function of velocity and air density, and are thereby a function of altitude. This is seen in Equations 6.23 - 6.25, defining the equilibrium glide condition, the stagnation heat flux, and the mechanical load constraints, respectively. ρ denotes the density, W the weight of the vehicle, S the reference surface area, C_L the lift coefficient, C_D the drag coefficient, q_{max} the maximum allowable heat flux, R_N is the nose radius of the vehicle, m is the empirical constant, n is a constant equal to 0.5 for laminar and 0.2 for turbulent flows, V_{eq} the equilibrium velocity, V_c the local circular velocity, V_g the flight velocity, g_0 the Mars’ surface gravitational acceleration , and $n_{g,max}$ the maximum allowable g-load. These equations are used to solve for each limiting velocity, to produce the entry corridor altitude-velocity (h-V) graph, as seen in Figure 6.18. In order to ensure the safety of the vehicle and the crew, the vehicle must fly within the bounds of the entry corridor.

$$\rho_{eq} = \frac{2W/S}{C_L}\left(\frac{1}{V_{eq}^2} - \frac{1}{V_c^2}\right) \tag{6.23}$$

$$\rho_{q,c} = \rho_0\left[R_N^n \frac{q_{max}}{c^*}\left(\frac{V_c}{V_{q,c}}\right)^m\right]^{\frac{1}{1-n}} \tag{6.24}$$

$$\rho_g = 2n_{g,max}\frac{m g_0}{V_g^2 S\sqrt{C_D^2 + C_L^2}} \tag{6.25}$$

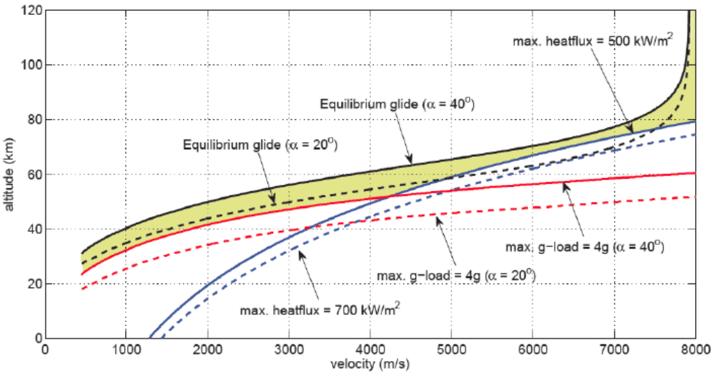

Figure 6.18: The entry corridor for an example vehicle as given by Mooij [46]

6.5.2. Descent Constraints

Constraints are placed on the vehicle and its trajectory such that the vehicle is not damaged, the crew remain safe, and the vehicle lands in the desired location. In order for the EDL design to be valid, the constraints cannot be violated. The constraints associated are presented in this section.

Maximum acceleration g_{mars} during nominal operations

As seen in 6.5.1, the vehicle must adhere to a maximum deceleration constraint. As discussed for the ascent in 6.4.2, this is limited by the maximum value the crew can handle. This is therefore set to the same value as for the ascent, namely 4 g_{mars}.

$$\dot{v}_{max} = 4 \text{ g}_{mars} \tag{6.26}$$

Maximum stagnation heat flux

As discussed in Subsection 6.4.2, the maximum stagnation heat flux is a constraint that is necessary to ensure the structural integrity of the vehicle. This constraint remains the same as prescribed in Subsection 6.4.2. It is restated below.

$$q_{max} = 250 \text{ kW/m}^2 \tag{6.27}$$

Maximum mechanical load

The maximum mechanical load (g-load) is set to the same value as the maximum acceleration the crew is subject to under nominal operations. This is 4 g_{mars}.

$$n_{max} = 4 \text{ g}_{mars} \tag{6.28}$$

Maximum touchdown velocity

As the vehicle will execute a propulsive landing, it must land with a low enough velocity as to not compromise the structural integrity of the vehicle or the crew's safety. Both the Charon and the Hercules vehicle land vertically, landing at 6.1 m/s [22] and 2.5 m/s [39], respectively. To remain conservative, the maximum landing velocity of 2.5 m/s is also taken, shown below.

$$V(t_f)_{max} = 2.5 \text{ m/s} \tag{6.29}$$

Maximum touchdown pitch angle

As the vehicle lands, its attitude must be such that it does not topple over. This is, of course, determined by the location of the centre of mass, however as this changes per vehicle and a global maximum is needed, an estimation of the maximum pitch angle is needed. For this, the Apollo lunar module is taken as a reference, which has a maximum pitch angle of 5° [57]. The proportions of the Apollo lunar module, however, are very different to the expected proportions of the Martian shuttle vehicle. The Apollo lunar module dimensions are a height of 6.99 m with the legs extended, and a width of 9.45 m [32]. Assuming a maximum pitch angle of 5°, this results in a 0.61 m maximum tilt offset at the top of the lander, which is 6.5% of the lander's width. This is shown in Figure 6.19, where x denotes the tilt offset. However, when the 5° touchdown pitch angle applied to the Charon vehicle (height of 17.82 m and width of 6 m [22]), the offset is 1.56 m. When reducing the maximum pitch angle to 2°, Charon's offset becomes 0.62 m, and assuming the vehicle's maximum width is 10 m (the 9 m maximum diameter with 1 m added for the landing legs), the relative offset becomes the

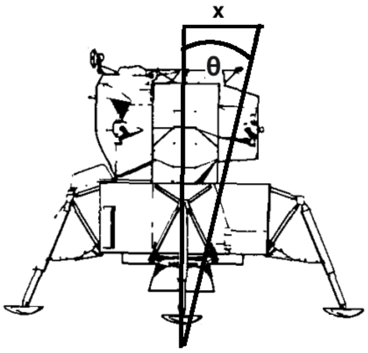

Figure 6.19: The maximum touchdown pitch angle (θ) and tilt offset (x) as adapted from Rogers [57]

approximately same as that of the Lunar Module's. The maximum touchdown pitch angle is therefore set to 2°, shown below.

$$\theta(t_f)_{max} = 2^\circ \tag{6.30}$$

Throttle limitations

An engine can be throttled to decrease the thrust produced by an engine and allowing for more control over a vehicle's velocity. An engine cannot be throttled over the entire thrust range, however, as reducing propellant flow introduces many issues, such as combustion instability [31]. The throttle range must therefore be constrained. As engine systems for retro-propulsion usually require a throttle level of 10%-20% [38] (the engine thrust is reduced to 10%-20% of its maximum capacity), the shuttle vehicle engines are also assumed to be deep-throttled. The minimum throttle is therefore taken to be 20%. This range is validated by both the Charon and Hercules vehicles, as their throttle ranges are 10% [22] and 20% [39], respectively. The vehicle throttle range can be expressed as follows where k_T denotes the throttle range:

$$0.20 \leq k_T \leq 1.0 \tag{6.31}$$

6.5.3. Descent Guidance

The guidance of the vehicle throughout the reentry has various phases: the gliding entry, the 180° turn to intiate the retroburn, and the propulsive landing itself. The guidance implemented for each phase is presented here.

Gliding Entry

During the gliding entry both the angle of attack and the bank angles are modulated. These are discussed below.

Angle of Attack

The longest part of the descent in terms of time of flight is the gliding phase of the entry. As seen in Section 6.5.1, to protect the vehicle from the heat loads, an angle of attack is necessary. The angle of attack is therefore set to a value that is held throughout the descent until the vehicle turn-over. As this angle of attack directly affects the vehicle's lift and drag, and therefore its motion through the atmosphere, this value is made to be a design variable. A guidance law specific to the angle of attack could also be implemented, however this is deemed unnecessary at this stage of the design. The angle of attack, as discussed in Section 6.5.1, co-determines whether the vehicle's trajectory remains within the entry corridor, and can be attained with a single angle of attack, as demonstrated by Charon [22]. Angle of attack modulation is usually implemented for range control [46], as it changes the lift and drag properties, and therefore allows for multiple EDL trajectories dependent on the angle of attack. As this research aims to find one single optimum EDL trajectory, however, this is unnecessary.

Bearing Angle

In order to return to the Martian base, the correct heading angle must be found. This can be done by using the vehicle's latitude and longitude to calculate the vehicle's bearing angle using the haversine function. This method is also applied successfully by Haex [23]. The equations to do this are given in Equation 6.32, 6.33, and 6.34, with 6.34 being the haversine function itself. δ denotes latitude, and τ longitude, with the subscript MB denoting that of the Martian base. The bearing angle guidance is implemented when the vehicle altitude is below 50 km, which is when the density of the atmosphere increases to a notable density. The guidance law is presented in 6.35, where χ denotes the heading angle, χ_{tar} the target bearing angle, and σ the bank angle.

$$Y = \cos\delta_{\text{MB}} \sin(\tau_{\text{MB}} - \tau) \tag{6.32}$$

$$X = \cos\delta \sin\delta_{\text{MB}} - \sin\delta \cos\delta_{\text{MB}} \cos(\tau_{\text{MB}} - \tau) \tag{6.33}$$

$$\chi_{\text{tar}} = \text{atan2}(Y, X) \tag{6.34}$$

$$\begin{array}{llllr}
h > 50 \text{ km}: & \sigma = 0 & & & \\
h \leq 50 \text{ km}: & \chi < \chi_{tar} & \text{and} & |\Delta\chi| > 9^\circ & \sigma = -60^\circ \\
 & \chi < \chi_{\text{tar}} & \text{and} & |\Delta\chi| \leq 9^\circ & \sigma = -60\left(\dfrac{\chi - \chi_{\text{tar}}}{9}\right)^\circ \\
 & \chi > \chi_{\text{tar}} & \text{and} & |\Delta\chi| > 9^\circ & \sigma = 60^\circ \\
 & \chi > \chi_{\text{tar}} & \text{and} & |\Delta\chi| \leq 90^\circ & \sigma = 60\left(\dfrac{\chi - \chi_{\text{tar}}}{9}\right)^\circ \\
 & \chi = \chi_{\text{tar}} & & & \sigma = 0^\circ
\end{array} \tag{6.35}$$

A guidance law to mitigate a skipping entry is not implemented, as bank angle law already intrinsically reduces the upwards lift direction whilst banking. As skipping is cause by a net upwards force, as well as the low atmospheric density of the Martian atmosphere, there is a low chance of skipping entry. This assumption is assessed in the trajectory validation, in Section 6.6.

Turn-Over

The vehicle must perform a propulsive landing, meaning that it must turn about its centre of mass to attain an angle of attack of 180°, before executing a retroburn to decelerate itself to a sufficiently low touchdown velocity. This must be performed as late as possible, in order to perform the rotation at the lowest velocities, thereby ensuring the vehicle experiences the least aerodynamic torque [22]. The turn and retroburn that follows must be completed without violating the constraints set upon it by the maximum crew acceleration, and the landing must be performed such that the landing legs can withstand the dynamic forces.

The flip is performed two-dimensionally, and guided by increasing the angle of attack of the vehicle until the angle of attack has reached 180° and the vehicle is flying with the engines in the direction of flight. The rotation rate is modelled as a constant rate, which is also implemented by Haex [23]. The rotation rate $\dot{\alpha}$ is set to 60 deg/s, where the angle of attack is increased from its gliding entry value until 180° is reached. This is seen in Equation 6.36, where t denotes the current time, t_{turn} the time at which the turn-over occurs, and $\dot{\alpha}$ the rotation rate.

$$\alpha = \dot{\alpha}(t - t_{\text{turn}}) \tag{6.36}$$

A rotation rate of 60 degrees per second, when assuming a vehicle length of 16 m, results in a g-force of 2.36 g_{mars}, allowing the forces to stay below the 4 g_{mars} constraint. The g-force on Earth is calculated using

Equation 6.37, where rpm denotes the rotations per minute, and R denotes the rotor radius in cm. This can then be converted to g-force on Mars.

$$g_{earth} = 1.118 \times 10^5 R(\text{rpm})^2 \tag{6.37}$$

Propulsive Landing

Once an angle of attack of 180° is attained, the retroburn is initiated. As a maximum load constraint is placed upon the vehicle (see Subsection 6.5.2), the engine(s) must be throttled such that this constraint is not violated. This can be see in Equation 6.38, where $a_{T,max}$ denotes the maximum acceleration due to the thrust force, n_{max} the maximum allowable g-load (with respect to Martian gravity), a_g the acceleration due to gravitational forces, and a_{aero} that due to aerodynamic forces. From the maximum calculated thrust acceleration, the necessary TW ratio can be obtained.

$$a_{T,max} = n_{max} a_g - \left\| (\vec{a}_{aero} + \vec{a}_g) \right\| \tag{6.38}$$

The deceleration of the vehicle thus initiates the landing, and as the angles of the attack, bank angle, and angle of sideslip are held at constant values (180°, 0°, and 0°, respectively), the landing is a gravity turn. A gravity turn is near optimal in terms of fuel losses as it eliminates the rotational rates about the vehicle's velocity vector by using gravity to steer the turn.

The gravity turn is a zero-lift turn, therefore the angle of attack of the vehicle must be 0° to induce zero lift (or in this case, 180°), and the thrust vector is always aligned with the velocity vector. Different gravity turns of the same delta-V require less fuel for increasing thrust levels. Theoretically, gravity turns are therefore most efficient if infinite thrust is used at the instant before touchdown [42]. Vehicles have finite propulsion capabilities, and so there is a minimum altitude and maximum velocity a vehicle can attain to land safely. The effect of the thrust and retroburn conditions on the landing is shown in Figure 6.20, where propulsive descent 2 is the most propellant efficient, but requires more thrust than landing 1. The retroburn altitude is therefore set as a design variable in the optimisation.

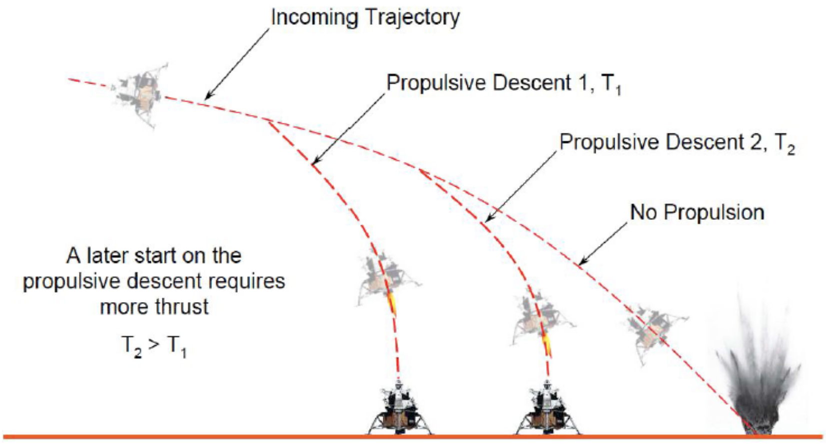

Figure 6.20: The geometry of various gravity turns as given by Mooij [46]

During the retroburn, once a velocity of 2 m/s has been achieved, the thrust is reduced and maintained so that the vehicle descends at a constant rate of 2 m/s. This ensures that the maximum touchdown velocity constraint of 2.5 m/s is not violated. However, due to the imposed throttle constraint there is a minimum thrust level that can be delivered by the engines. If the necessary thrust is less than what is possible by the engines, one of the engines is shut off and the landing is continued with the remaining engines. If no engines remain, all engines are consequently shut off as they cannot comply with the throttle limitations.

6.5.4. Descent Design Variables

The descent design variables comprise of the variables needed for the guidance, and the initial conditions. These are given below, where δ_0 denotes the initial latitude, τ_0 the initial longitude, γ_0 the initial flight path angle, α the angle of attack held during the gliding entry phase, and h_{rb} the retroburn altitude. The search space for these variables is given in Section 7.2.

$$Z_{descent} = [\delta_0, \tau_0, \gamma_0, \alpha, h_{\mathrm{rb}}]$$

6.6. Trajectory Validation

In order to determine whether the ascent and descent disciplines are sufficiently capable of numerically modelling a trajectory on Mars, as well as whether the optimiser is able to optimise the trajectory using the guidance laws implemented, both ascent and EDL phases must be validated. This is presented in this section.

6.6.1. Ascent Phase Validation

To validate the ascent phase, the Tudat model is used to replicate both the Charon and the Hercules ascent trajectories. As the Charon vehicle properties and ascent properties are all known, the trajectories obtained by Gaffarel et. al. [22] can easily be compared to the Tudat model by using the known Charon variables directly as model input. The initial conditions and the design variables used can be found in Tables 6.7 and 6.8, respectively. It should be noted that the Charon ascent methodology is that burnout occurs before the target orbit is attained, and that the vehicle coasts. The pitch angles are therefore taken not until the target orbit attained but until burnout, as the parametric pitch law is only implemented during the ascent burn. The Charon pitch angles are extracted from the available code on Github[8].

Table 6.7: The initial conditions used to simulate the Charon ascent, where the negative altitude is due to Deuteronilus Mensae lying under the Martian geoid

Variable	**Value**
h_0 [km]	-3700
δ_0 [deg]	42.5
τ_0 [deg]	25.5
V_0 [m/s]	0.01
χ_0 [deg]	90.0

---

[8] `https://github.com/gaffarelj/DSE-Mars-SRV`

Table 6.8: The design variables used to simulate the Charon ascent trajectory

Design Variable	**Value**
Vehicle	
p_c [Pa]	200e5
O/F [-]	3.12
D_e [m]	1.06
$\dot{m}$ [kg/s]	82.9
n_{eng} [-]	9
$M_{p,a}$ [kg]	133685
$M_{p,l}$ [kg]	2487
D_v [m]	6.14
M_{PL} [kg]	1200
Trajectory	
Thrust law [-]	1
TW_{min} [-]	1.5
TW_{max} [-]	4
θ_1 [deg]	88.5
θ_2 [deg]	73.60
θ_3 [deg]	56.60
θ_4 [deg]	45.43
θ_5 [deg]	37.89
θ_6 [deg]	32.66

Figures 6.21 and 6.22 present the comparison between the Tudat ascent simulation and the Charon vehicle simulation by comparing the ascent profiles in terms of lateral distance and airspeed, and comparing the vehicle masses and TW ratios over the course of the ascent.

As can be seen, the TW ratios and the masses of the vehicle throughout the ascent are almost identical. The reason that the Tudat simulation's TW ratio does not reach exactly 4, is due to the discrepancy between the estimated and real thrust times.

The ascent profiles of both vehicles are further very similar, with the most noticeable difference between the two trajectories being the location of the vehicle burnout, after which the trajectories diverge. The vehicle model in Tudat burns out at an earlier location than the Charon vehicle. This could be due to different atmospheric models used (Charon uses the exponential atmosphere) as well as differences in aerodynamic properties of the vehicle. It could also be due to discrepancies in the placement of the pitch angle nodes. Due to the ascent thrust time estimation in the Tudat simulation, the exact time as which the pitch angles are defined by the guidance law could slight differ to Charon's. Due to the differences in vehicle state at burn out, the state of the vehicle at the target orbit (607 km) also differs as the differences in burn out state are propagated. The comparison of the orbits does show, however, that the model is capable of replicating an ascent trajectory on Mars to a satisfactory degree.

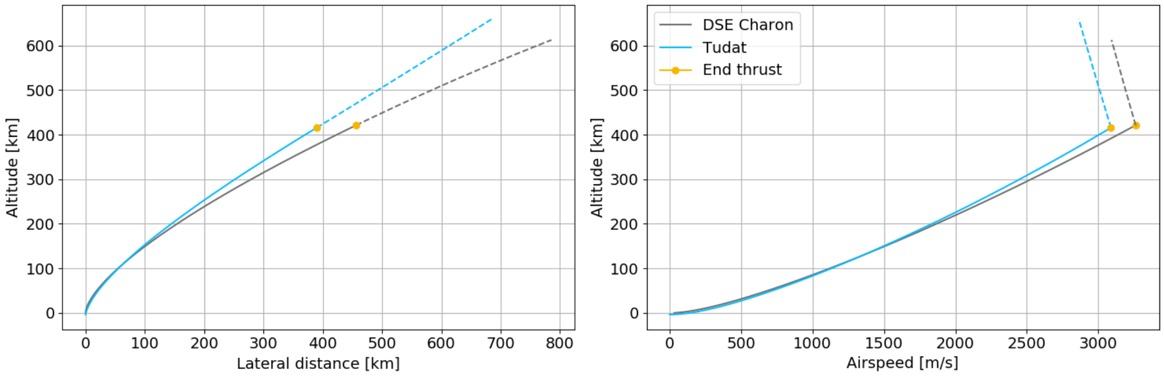

Figure 6.21: The altitude and airspeed profiles of the Tudat simulation compared to that of the Charon vehicle as given by Gaffarel et. al. [22]

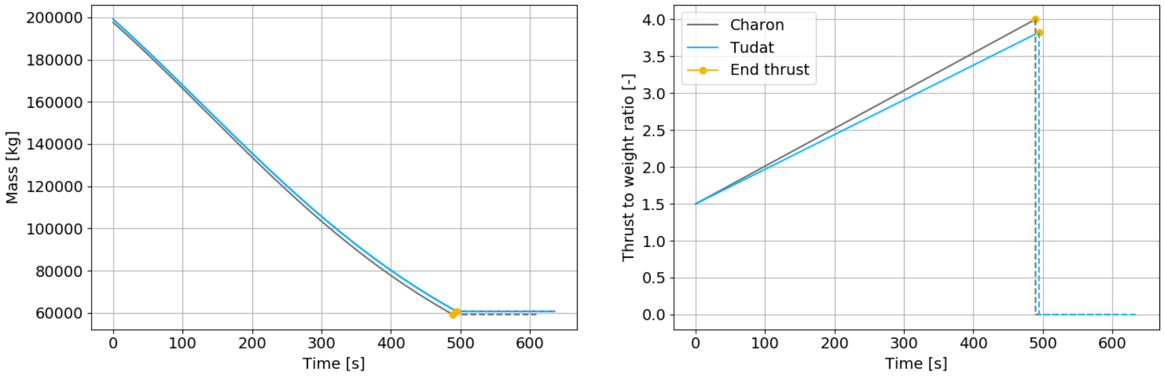

Figure 6.22: The vehicle mass and TW ratios over the course of the ascent trajectory for the Tudat ascent simulation and the Charon vehicle, as given by Gaffarel et. al. [22]

To test the model's ability to sufficiently optimise an ascent trajectory through the usage of the pitch and thrust guidance laws, the Hercules vehicle is used. As the pitch angles are unknown, the optimiser must be used to obtain the trajectory. The algorithm, architecture, and implementation of the optimiser is covered in Chapter 7.

The initial conditions taken for the Hercules are given in Table 6.9. They are almost identical to those used for the Charon vehicle, however although Hercules also launches from Deuteronilus Mensae, the exact coordinates chosen by Komar et. al. differ slightly from those Charon by Gaffarel et. al.. The design variables used for Hercules are given in Table 6.10, and the optimum solution found for three different seeds are given in Table 6.11. The target orbit for the Hercules vehicle has a pericentre altitude of 108 km, an eccentricity of 0.0178, and an inclination of 43.9°.

Table 6.9: The initial conditions used to simulate the Hercules ascent

Variable	**Value**
h_0 [km]	-3700
δ_0 [deg]	43.9
τ_0 [deg]	23.6
V_0 [m/s]	0.01
χ_0 [deg]	90.0

Table 6.10: The design variables used to simulate the Hercules ascent trajectory

Design Variable	**Value**
Vehicle	
p_c [Pa]	138e5
O/F [-]	3.4
D_e [m]	1.076
$\dot{m}$ [kg/s]	68.9
n_{eng} [-]	5
$M_{p,a}$ [kg]	96800
$M_{p,l}$ [kg]	10501
D_v [m]	6.0
M_{PL} [kg]	5750
Trajectory	
Thrust law [-]	1
TW_{min} [-]	2.112
TW_{max} [-]	7.864

Table 6.11: The final state of the optimum Hercules trajectory found using various seeds. Target orbit is a pericentre altitude of 108 km, *e* of 0.0178 and inclination of 43.9°

Seed	**Final Orbital State**	**Value**	**Difference with Target [%]**	**Fitness**
500	Pericentre altitude [km]	108.067	0.0620	1.48661196e+08
	e [-]	0.01781	0.07584	
	i [deg]	44.4921	1.3487	
1500	Pericentre altitude [km]	108.248	0.22962	2.19775630e+08
	e [-]	0.01780	-0.0034	
	i [deg]	44.7625	1.9646	
2500	Pericentre altitude [km]	108.174	0.1611	2.22203957e+08
	e [-]	0.01769	-0.6134	
	i [deg]	44.5356	1.4478	

As can be seen from the results in Table 6.11, the algorithm performs very well and is able to determine the design variables such that the target orbit is reached. With the exception of the inclinations, all the differences between the target and resultant orbital parameters are under 1%. Seed 500, which has the lowest fitness score, is plotted in Figures 6.23 - 6.26, to compare the ascent profiles. AGL stands for Above Ground Level.

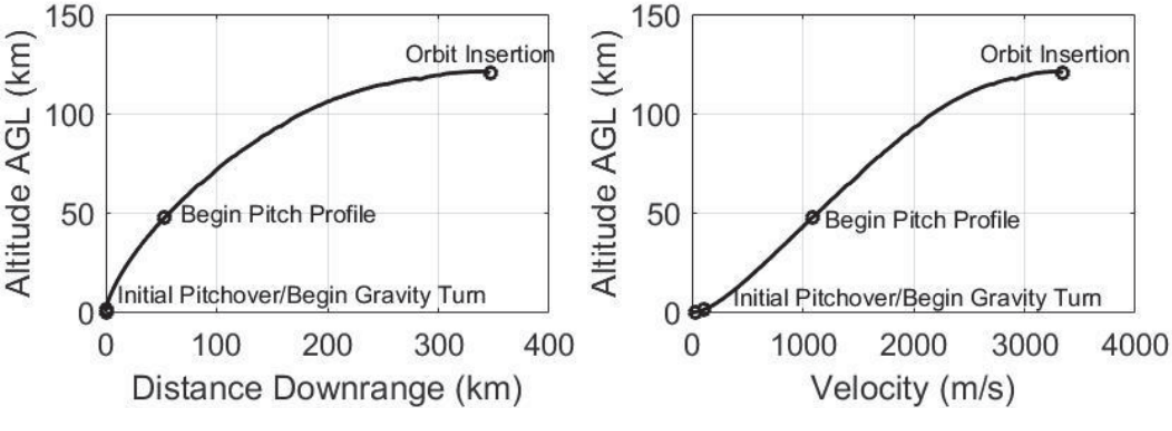

Figure 6.23: The Hercules ascent profile (left) and the velocity profile (right) as given by Komar et. al. [39]

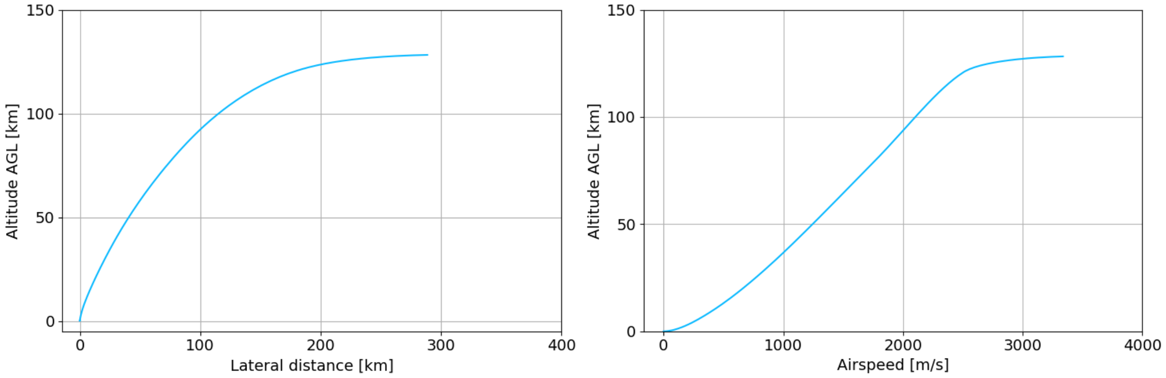

Figure 6.24: The optimum Tudat simulation ascent profile (left) and the velocity profile (right) for the Hercules vehicle

As can be seen from figures, 6.23 and 6.24, the two ascent profiles are very similar, with the most noticeable differences found in the downrange profile (left figures in 6.23 and 6.24). However the injection point occurs at the same altitude and very similar airspeeds are achieved over the course of the ascent. The downrange distance for the Hercules, however, is approximately 350 km, whereas the downrange distance for the Tudat vehicle is less than 300 km, which is the two characteristics where the two profiles differ. This can be attributed to the burn time, as seen in Figures 6.25 and 6.26.

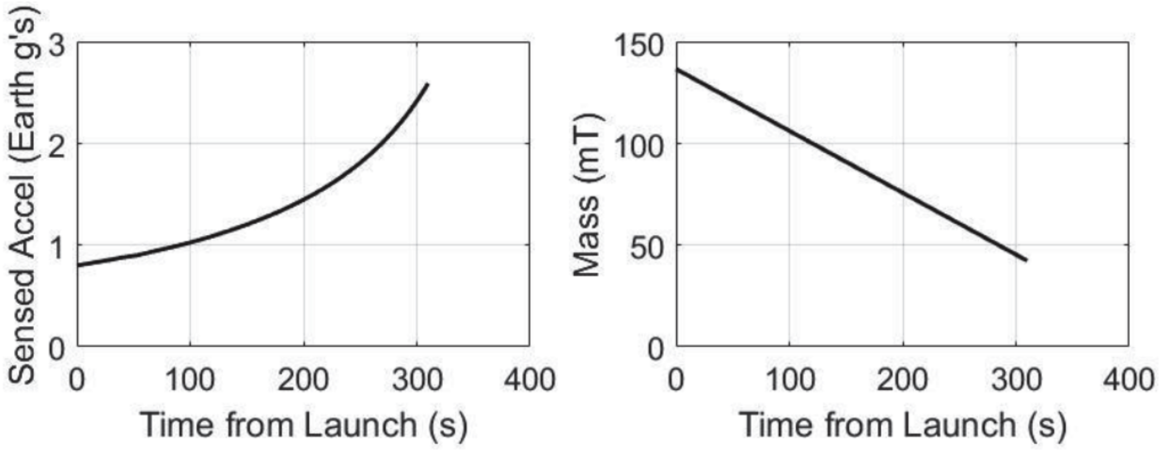

Figure 6.25: The Hercules thrust profile profile (left) and the mass profile (right) as given by Komar et. al. [39]

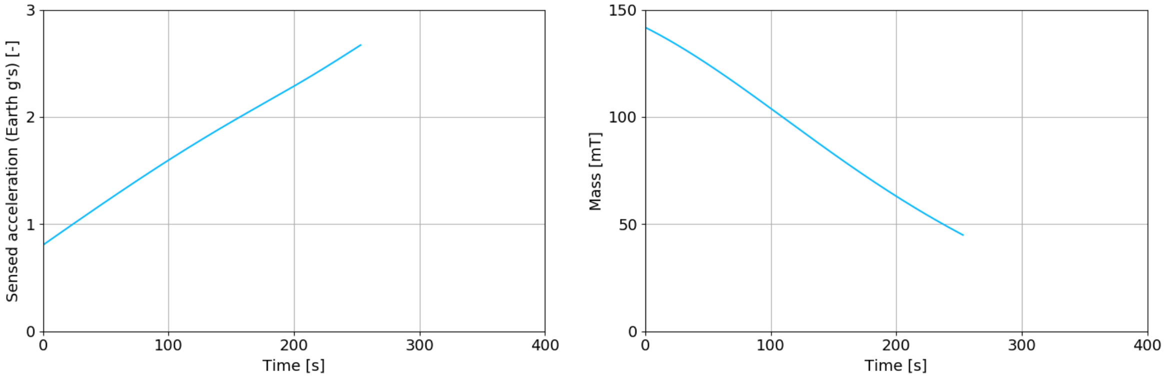

Figure 6.26: The optimum Tudat simulation ascent thrust profile (left) and the mass profile (right) for the Hercules vehicle

The burn time for Hercules found by Komar et. al. is approximately 310 seconds [39], as the Tudat simulation reaches a burn time of only 253 seconds and 289 km downrange. However this can be attributed to the implemented thrust law.

As can be seen in Figure 6.26, the thrust law used by Hercules cannot be replicated by any of the three thrust laws implemented in the model. Instead, thrust law 1 is used as it resembles Hercules' exponential thrust law the closest of the three. However, this difference increases the Tudat model's mean mass flow with respect to that of Hercules, resulting in a shorter burn time for the simulation, with burn times of 310 seconds and 253 seconds for the Hercules and Tudat vehicle, respectively. However, the small difference between the target and achieved orbital parameters seen in Table 6.11 validate the ascent optimisation model. Furthermore, the presence of a difference between calculated and real burn times due to the implementation of a thrust law evidently allows for a sufficient optimisation of the ascent to be performed. The usage of six nodes is also deemed sufficient to be able to optimise the trajectory. The ascent discipline can therefore be considered validated.

6.6.2. EDL Phase Validation

To validate the EDL phase, the Tudat model is used to replicate both the Charon and the Hercules descent trajectories. Although certain parameters are known for both vehicles (retroburn altitude, initial flight path angle, angle of attack), other guidance choices such as the implemented propulsive landing and landing velocities, remain unknown. It is therefore chosen to run an optimisation of the EDL phase for both vehicles, as opposed to directly using the known variables as input. The Charon vehicle trajectory is replicated first. The initial conditions and design variables used to model the Charon vehicle taken from Gaffarel et. al. [22], can be found in Tables 6.12 and 6.13 respectively. The optimisation is conducted using three seeds, for which the results can be found in Table 6.14.

Table 6.12: The initial conditions used to simulate the Charon descent trajectory

Variable	**Value**
h_0 [km]	80
V_0 [m/s]	3500
χ_0 [deg]	45.04

Table 6.13: The design variables used to simulate the Charon ascent trajectory

Design Variable	**Value**
p_c [Pa]	200e5
O/F [-]	3.12
D_e [m]	1.06
$\dot{m}$ [kg/s]	82.9
n_{eng} [-]	9
$M_{p,a}$ [kg]	133685
$M_{p,l}$ [kg]	2487
D_v [m]	6.14
M_{PL} [kg]	1200

Table 6.14: The final state of the optimum Charon trajectory found using various seeds. The Martian base is located is 42.5° latitude and 25.5° longitude.

Seed	**Final State**	**Value**	**Difference with Target [%]**	**Fitness**
1500	δ [deg]	42.5956	0.9560	1.69186e+09
	τ [deg]	25.0872	-4.1279	
	r w.r.t. Martian surface [m]	0	-	
	V [m/s]	-2.4723	-	
	θ [deg]	-0.6580	-	
	$M_{p,l}$ consumed [%]	99.6393	-	
2500	δ [deg]	42.1931	-3.0682	2.07823e+09
	τ [deg]	25.1825	-3.1748	
	r w.r.t. Martian surface [m]	0	-	
	V [m/s]	-2.4501	-	
	θ [deg]	-1.4093	-	
	$M_{p,l}$ consumed [%]	99.9998	-	
3000	δ [deg]	42.1732	-3.2672	1.24795e+09
	τ [deg]	25.4515	-0.4849	
	r w.r.t. Martian surface [m]	0	-	
	V [m/s]	-2.2261	-	
	θ [deg]	-0.8308	-	
	$M_{p,l}$ consumed [%]	99.8851	-	

As can be seen from Table 6.14, the optimiser is indeed able to successfully determine the design variables and simulate the Martian EDL phase, and adhering to the trajectory constraints. The discrepancy between the target coordinates and the actual coordinates, however, go up to almost 5%, which are values that are much higher than differences found when optimising the Hercules ascent. However, this is due to the necessity of adhering to the landing constraints. All three seeds use more than 99% of their propellant to land, meaning that the retroburn altitude falls between very slim margins. The optimiser also needed 200 generations to find three valid solutions, whereas the ascent only needed 100, mirroring the slim margins for the landing conditions. The Charon vehicle, however, was designed to land with a velocity of 6.1 m/s, therefore the fact that almost all the landing propellant is used to adhere to the 2.5 m/s maximum velocity constraint, is logical, and also shows that the optimiser is able to obtain a trajectory that allows for the a lower landing velocity than what the vehicle was designed for. The optimum EDL trajectory found by seed 3000 is shown in Figure 6.27.

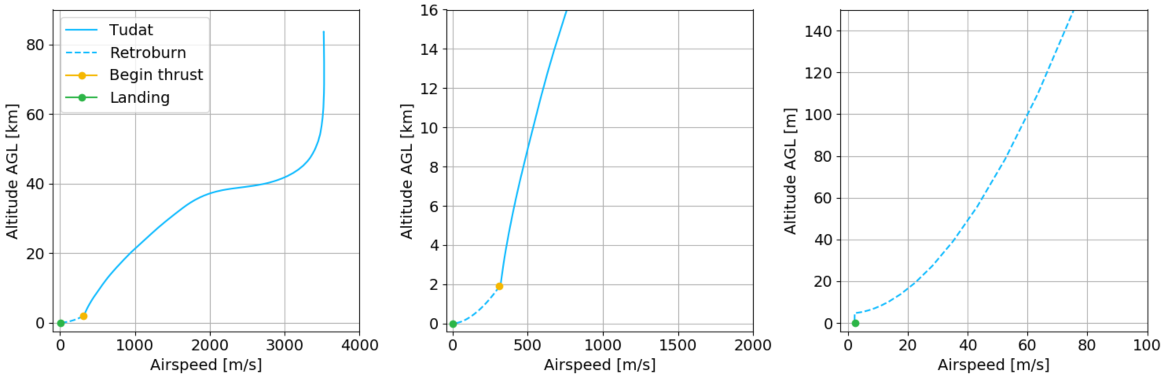

Figure 6.27: The Charon airspeed-altitude profiles as obtained by the Tudat simulation

As seen in Figure 6.27 the entry corridor is maintained, with the vehicle levelling at an altitude of approximately 40 km due to the increased atmospheric density and angle of attack. The retroburn is initiated at an altitude of 2 km above the ground, and the controlled landing (constant downward velocity of 2 m/s) is only initiated at an altitude of 10 m. This shows extremely efficient propellant usage.

Figures 6.28 and 6.29 further show the altitude and velocity profiles as a function of time, as well as the flight

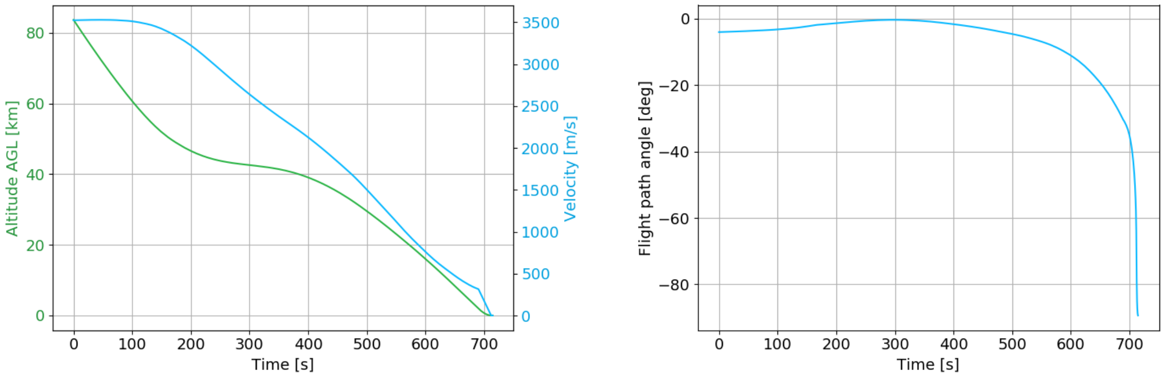

Figure 6.28: The altitude and velocity profiles for Charon as obtained by the Tudat simulation

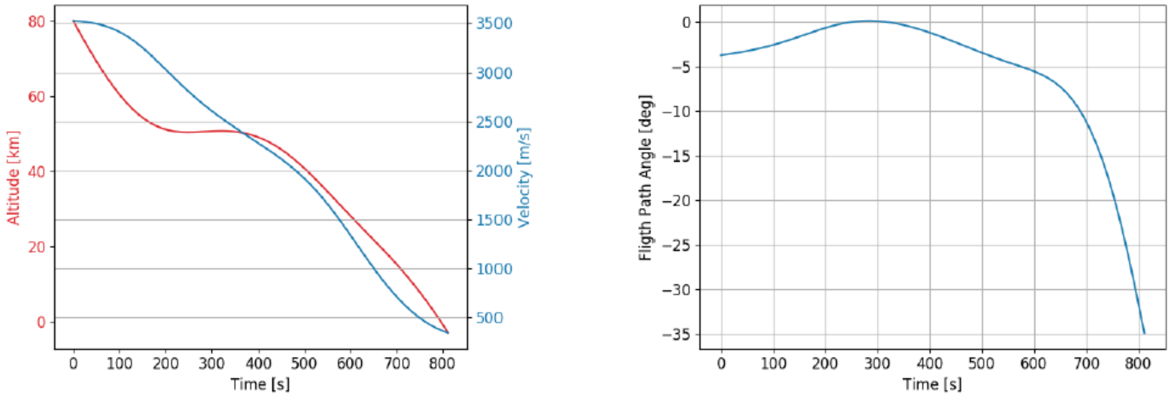

Figure 6.29: The altitude and velocity profiles for Charon as obtained by Gafferel et. al.[22]

path angles for the Tudat simulation, and as obtained by Gafferel et. al. [22], respectively.

As can be seen from Figures 6.28 and 6.29, the Tudat simulation shows an increase in vehicle lift at a lower altitude than that of the Charon vehicle, as it levels off at approximately 40 km altitude, and Charon at an altitude of 50 km. This could be due to differences in atmospheric and aerodynamic vehicle properties, as well as differences in maintained angles of attack. The Charon vehicle descent time is also longer, taking 800 seconds compared to the 700 seconds of the Tudat simulation. However, the optimiser is still able to replicate the Charon vehicle's descent trajectory sufficiently.

The EDL phase of the Hercules vehicle is next optimised. The initial conditions used and design variables used to model the Hercules vehicle taken from Komar et. al. [39] can be found in Tables 6.15 and 6.16, respectively, and the results for the three seeds can be found in Table 6.17.

Table 6.15: The initial conditions used to simulate the Hercules descent trajectory, taken from [39]

Variable	**Value**
h_0 [km]	132
V_0 [m/s]	3300
χ_0 [deg]	43.9

Table 6.16: The design variables used to simulate the Hercules descent trajectory

Design Variable	**Value**
Main Engine	
p_c [Pa]	138e5
O/F [-]	3.4
D_e [m]	1.076
$\dot{m}$ [kg/s]	68.9
Vehicle	
n_{eng} [-]	5
$M_{p,a}$ [kg]	96800
$M_{p,l}$ [kg]	10501
D_v [m]	6.0
M_{PL} [kg]	5750

Table 6.17: The final state of the optimum Hercules trajectory found using various seeds. Target martian base location is 43.9° latitude and 23.6° longitude.

Seed	**Final State**	**Value**	**Difference with Target [%]**	**Fitness**
1500	δ [deg]	43.9293	0.2936	6.63556e+08
	τ [deg]	23.7705	1.7054	
	r w.r.t. Martian surface [m]	0	-	
	V [m/s]	-2.4876	-	
	θ [deg]	-0.3025	-	
	$M_{p,l}$ consumed [%]	43.2627	-	
2500	δ [deg]	43.9421	0.4210	1.5322e+08
	τ [deg]	23.6046	0.0469	
	r w.r.t. Martian surface [m]	0	-	
	V [m/s]	-2.1490	-	
	θ [deg]	-0.2996	-	
	$M_{p,l}$ consumed [%]	42.2150	-	
3000	δ [deg]	57.5449	-1.4583	6.04518e+08
	τ [deg]	23.6363	0.3636	
	r w.r.t. Martian surface [m]	0	-	
	V [m/s]	-1.6898	-	
	θ [deg]	-0.2989	-	
	$M_{p,l}$ consumed [%]	82.8467	-	

As can be seen from the results in Table 6.17, the algorithm is able to to successfully optimise the design variables to attain an EDL trajectory that satisfies all the constraints. The optimiser converges on the correct landing latitude and longitude, whilst adhering to the landing constraints imposed. The accuracy with which the landing location is achieved is noticeably higher for the Hercules vehicle compared to the Charon vehicle, with the differences between the attained and target coordinates remaining under 2%. What is also noticeable is that landing propellant consumption is much less than that of the Charon vehicle, lying between 40% and 85%. This indicates that the margin between which the design variables, especially the retroburn altitude, must lie is larger. This is supported by the fact that the Hercules vehicle only needed 100 generations, as opposed to Charon's 200, to obtain three valid solutions. The optimum trajectory found using seed 1500, which has the lowest fitness score, is plotted in Figure 6.31. The Hercules EDL trajectory is shown in Figure 6.30.

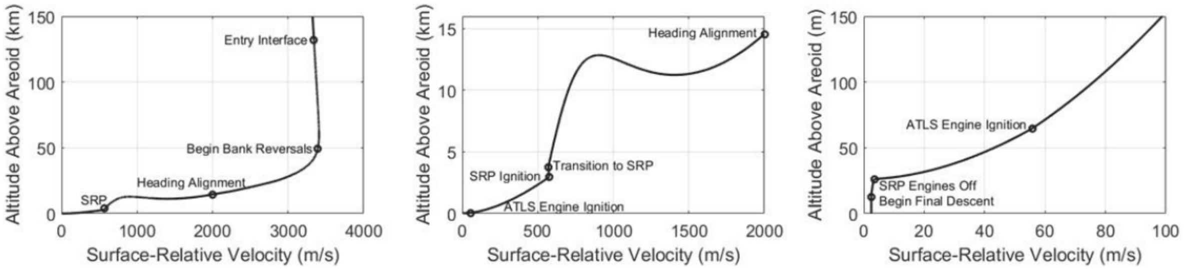

Figure 6.30: The Hercules airspeed-altitude profiles as presented by Komar et. al. [39]

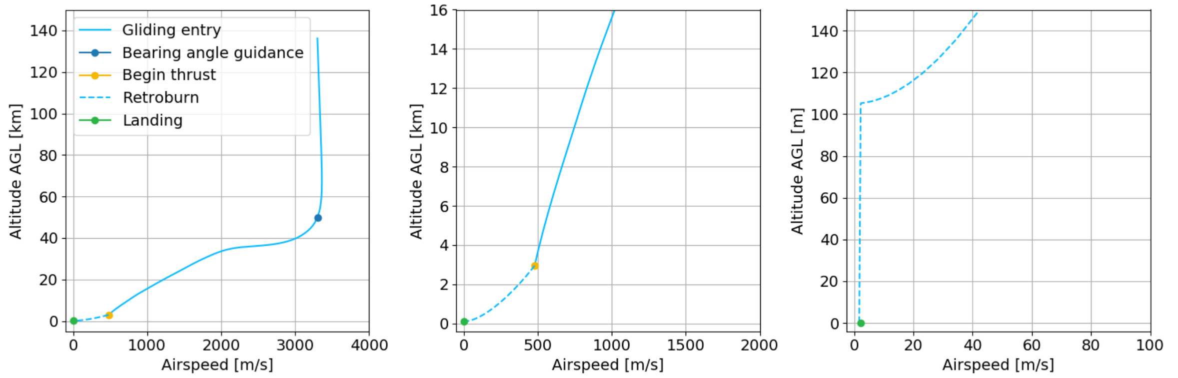

Figure 6.31: The Hercules airspeed-altitude profiles as obtained by the Tudat simulation

From Figures 6.30 and 6.31 some differences between the two trajectories can be noted. The vehicle in the Tudat simulation remains at a higher altitude for a longer period of time, as well as initiating the final landing phase (where the velocity is held at 2 m/s) at a higher altitude than the Hercules vehicle. These differences can be attributed to a number of factors. The gliding entry phase of the descent is determined by aerodynamic and gravitational forces, therefore the environmental models used, as well as the calculated aerodynamic properties of the vehicle and the angle of attack at which the vehicle is held, greatly impact the trajectory. These factors are unknown for the Hercules vehicle and therefore cannot be compared, however these factors have an undoubted influence on the ascent profile.

Further, the propulsive landings differ. The Hercules vehicle initiates its final descent at an altitude of approximately only 30 m, and the Tudat vehicle initiates this at an altitude of approximately 100 m. The Hercules vehicle first initiates the retroburn using the main engines, however where the Tudat vehicle only uses the main engines to land, the Hercules vehicle switches to its landing engines once a velocity of 2.5 m/s is reached. These differences therefore lead to landing profiles that differ, and not due to the possible shortcomings of the trajectory model. The landing propellant consumption of the Tudat vehicle being only 40% to 85% may also perhaps be attributed to these differences, or perhaps that the optimiser obtains a more optimum solution. With both the Charon and Hercules vehicles' EDL trajectories sufficiently replicated, the descent trajectory discipline can be considered validated.

6.7. Target Orbit, and Rendezvous Strategy, and Vehicle De-orbit

A crucial part of the mission scenario is the target orbit into which the vehicle must be injected, the orbital node altitude itself, the rendezvous strategy, and the deorbiting prior to the vehicle's reentry. These orbits define the terminal and initial conditions for the vehicle for the ascent and EDL phases, respectively. In this section the target orbit, the rendezvous and docking strategy, and the entry conditions are determined.

As discussed in Section 2.2.2, the Martian base location in this research is set to the same coordinates as those determined by Gaffarel et. al.. As the location of the Martian base has a latitude of 42.5°, the orbit of the orbital node must also have an inclination of 42.5° or higher. The inclination change, however, must be small to minimise propellant needed for inclination changes or propellant for a dogleg manoeuvre as these are very propellant-intensive.

As determined in Chapter 2, the orbital node lies at 500 km altitude, and its orbit is circular. In order for the launch window to the orbital node to be available every day, the node's orbit is chosen to have a repeating ground track that passes over the Martian base once per day. Due to the same mission scenario taken in this research as that of Charon, the same target orbit and rendezvous strategy is taken as given by Gaffarel et. al. for the Charon vehicle [22]. The orbital parameters are given in Table 6.18. The argument of periapsis and right ascension of the ascending node are not included as they are continuously changing as the orbit precesses.

Table 6.18: The orbital parameters for the node orbit and the phasing orbit

Parameter	**Node Orbit**	**Insertion Orbit**
h	500 km	607.74 km
e	0	0
i	44.96°	44.96°

To calculate how many revolutions are made by the node, the methodology outlined by Wertz is used [68]. It takes into account the precession of the argument of periapsis, the right ascension of the ascending node, and the mean anomaly due to the oblateness (J2) of Mars, and is an iterative process and is outlined in Appendix B. At an altitude of 500 km and with a repeat of once per day, and orbit for the node is found such that the node completes 11.7 revolutions per day.

In order to rendezvous with a station in orbit, space vehicles always first ascend to a phasing orbit, from which the rendezvous and docking phases can begin. This is to mitigate the high risk associated with a direct ascent to the node. A phasing orbit allows for a longer amount of time to correct any injection errors or intermediate errors that may occur, as well as to prepare for the rendezvous procedure. In Figure 6.32 a Hohmann rendezvous manoeuvre is depicted between two coplanar circular orbits, as adapted from Wakker [66].

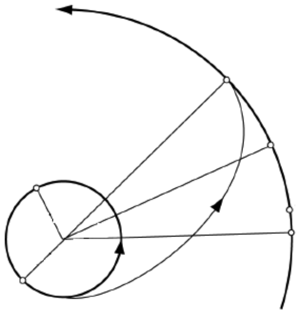

Figure 6.32: The geometry of a transfer flight between two coplanar circular orbits, taken from Wakker [66]

In order for the scope of the graduation thesis to remain manageable, the MDO of the vehicle will not include the rendezvous and docking procedures. These manoevres do, however, require propellant and therefore the delta-V of these procedures must be known. In line with all previous choices, the delta-V determined by Gaffarel et. al. is assumed [22]. Using the MDO total vehicle mass, the necessary propellant mass for each delta-V injection can be calculated (see Subsection 4.2.3).

The Charon vehicle ascends to a circular phasing orbit that lies at an altitude of 607.740 km and an inclination of 44.96°. From this altitude, a Hohmann transfer is performed to reduce the altitude such that it is within 1000 m of the node. From there the docking procedure ensues, which is in three phases. The delta-V necessary for these phases are given in Table 6.19. As no docking delta-V is indicated, the Hercules docking delta-V is taken, to remain conservative. After the undocking from the node, the Charon vehicle uses a delta-V of 261 m/s to de-orbit, and initiate the EDL phase.

Table 6.19: The delta-V required for the vehicle to be transferred from the insertion orbit to docking with the orbital node

Manoeuvre	**Initial Orbit**	**Orbit After Burn**	**Delta-V [m/s]**
Hohmann transfer	607.74 km	500 km	45.84
Rendezvous and docking	500 km	Docked to node	80.4
De-orbit burn	500 km	Reentry conditions	261
Total			**387.24**

7

Software Architecture and Algorithm Performance

In the previous chapters the development and the validation of the propulsion system, mass and geometry, aerodynamics, and ascent and EDL disciplines are discussed. The disciplines can now be integrated and linked within the MDO scheme. To successfully merge them, the construction of the MDO itself must first be determined, followed by the choice of the optimiser and its settings. This step is crucial to obtain a solution that can be considered optimal, as well as obtaining it in an efficient manner. This chapter first covers the architecture of the MDO, followed by the design variable search space, the discussion and selection of the chosen optimiser and associated settings, and lastly the fitness functions.

7.1. MDO Architecture

As discussed in Section 3.4, the MDO tool is developed using the Tudat[1] libraries. These are powerful libraries that incorporate a wide variety of functionalities and abilities for the usage of trajectory modelling. These functionalities include (but are not limited to) a range of mathematical tools for applications such as reference frame transformations, readily available atmosphere and gravity models for various planets, the definition of a custom vehicle for propagation, choices of integrators and propagators, and custom aerodynamic and thrust guidance law capabilities. The Tudat environment also allows for the usage of the ESA-developed PaGMO[2] optimisation library. Both the Tudat and PaGMO libraries are developed in C++ and are publicly available on Github[3][4], and allow for these capabilities to be combined into one unified simulation environment. This environment has been shown to be successful for many other MDO applications by Haex [23], van Kesteren [34], Miranda [44], Rozemeijer [58], and Contant [14].

In Figure 7.1 the full MDO architecture is presented. It is categorised into the vehicle disciplines in light blue, the trajectory disciplines in green, and the optimiser in purple, which are connected as the results obtained from one section are fed into the next. As can be seen, there are also various colour-coded inputs. The inputs in blue signify the models and components implemented in the propagation of the vehicle's trajectory that are pre-determined by the user, such an environment models. The inputs in red signify factors that affect the algorithm performance, such as settings and constraints. The inputs in orange signify the inputs that are determined through the usage of databases developed prior to the MDO development, from which data is retrieved as necessary, such as the CEA database. An explanation detailing the MDO architecture follows after Figure 7.1.

---

[1] `https://tudat.tudelft.nl/`

[2] `https://esa.github.io/pagmo2/`

[3] `https://github.com/Tudat`

[4] `https://github.com/esa/pagmo2`

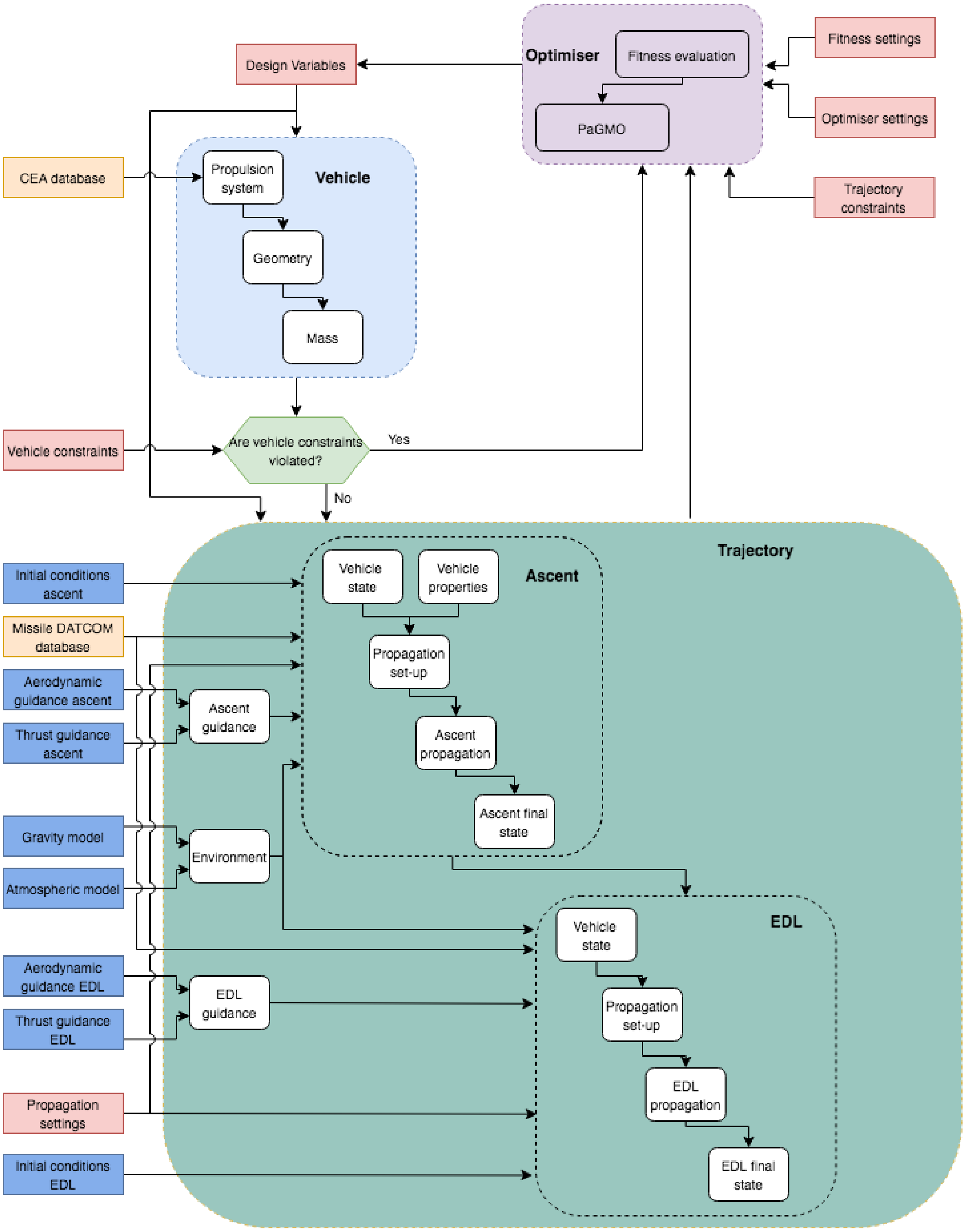

Figure 7.1: The MDO architecture

The optimisation begins at the optimiser in purple, where the selected optimiser algorithm selects the design variables from the search space for the population that are fed into the vehicle disciplines in blue. The vehicle design variables are used to obtain the performance of the vehicle propulsion system, the geometry of the vehicle, and the GTOW and other mass properties of the vehicle. The vehicle is then reviewed to determine whether the vehicle violates any of the imposed vehicle constraints, such as whether the engines fit within the cross-sectional area, or whether the initial TW ratio of the vehicle is greater than 1. If any are violated, the vehicle is immediately given a penalty and bypasses the trajectory simulation, thereby saving computational time. If the vehicle passes, it then progresses to the evaluation of its trajectory, in dark green. The trajectory design variables, as well as the vehicle properties, are then used to simulate its ascent and its EDL trajectory. The integrator and propagator settings in red determine how the vehicle is propagated, and the environmental models and aerodynamic and thrust guidance laws determine the forces on the vehicle. The properties of the vehicle, as well as its final mass, are then used as inputs for the EDL phase of the trajectory simulation, alongside the inputs previously mentioned. After the simulation of the EDL phase, the final states of the vehicle are then fed back into the optimiser, in purple, where the fitness of the vehicle and its trajectory is evaluated using the trajectory constraints and fitness settings, in red. The optimiser, using the optimiser settings, in red, utilises the fitness to calculate the next set of design variables into the MDO scheme. This loop in continued until a user-define termination setting is reached.

7.2. Search Space

The search space the optimiser operates within is determined by the bounds associated with each design variable. Throughout Chapters 4 to 6, the design variables used for each discipline are identified, from which the properties of the vehicle and the trajectory can be obtained and evaluated. Table 7.1 re-states these design variables alongside the bounds that have been determined for each respective variable. The reasoning for each boundary can be found in their respective chapters.

Table 7.1: The design variables identified for the MDO

Vehicle	**Lower bound**	**Higher bound**
p_c [MPa]	5.0	33.0
O/F [-]	3.0	4.0
D_e [m]	0.7	1.3
$\dot{m}$ [kg/s]	20	200
n_{eng} [-]	3	14
$M_{p,a}$ [kg]	90000	160000
$M_{p,l}$ [kg]	700	9000
D_v [m]	5.0	9.0
Ascent	**Lower bound**	**Higher bound**
θ_1 [deg]	85.0	90.0
θ_2 [deg]	50.0	80.0
θ_3 [deg]	30.0	70.0
θ_4 [deg]	10.0	60.0
θ_5 [deg]	0.0	30.0
θ_6 [deg]	-10.0	10.0
TL [-]	0	2
TW_{min} [-]	1.1	3.0
TW_{max} [-]	2.0	4.0
EDL	**Lower bound**	**Higher bound**
δ_0 [deg]	5.0	40.0
τ_0 [deg]	-30.0	5.0
γ_0 [deg]	-10.0	-0.01
α_0 [deg]	35	65
h_{rb} [m]	1000	5000

7.3. Fitness Evaluation

In order for the optimiser to force the solution into an optimum with respect to the desired objective function, fitness functions are used. Based on a set of criteria, an individual's fitness is evaluated, which is used to determine the relative performance of the individual. The fitness function is therefore critical in developing an algorithm that both converges, and does so without ambiguity. For example, there must be significant changes in fitness depending on the individual's solution, such that a swift optimisation can take place. If all fitness values are approximately the same, the solver will likely not converge as quickly.

As discussed in Chapter 3, the objective function is to minimise the fitness value, therefore the individual with the lowest fitness value is identified as the optimum. To achieve this, a penalty system is implemented, where the violation of a constraint or the deviation of a parameter from its desired value imposes a penalty on the fitness. The value of this penalty is dependent on the severity of the violation. As seen in Figure 7.1, the vehicle must first pass the vehicle constraints if its trajectory is to be simulated. If not, a penalty is imposed, which is given the value of 1×10^{15}, which is higher than any other penalty. This guarantees that these solutions perform the least favourable.

The violation of a 'hard' trajectory constraint imposes a trajectory penalty of 1×10^{11}. These constraints are, as described in more detail in Subsections 6.4.2 and 6.5.2, a maximum angle of attack during ascent, a maximum mechanical load, a maximum stagnation heat flux, a maximum touchdown velocity, a maximum touchdown pitch angle, and a maximum throttle capability. Another constraint is added in the simulation to remove any ambiguity of the landing location, and that is the final altitude. The final altitude of the vehicle must be within 1 m of the Martian base's altitude. The constraints can be seen in 7.1, where α denotes the angle of attack, q the stagnation heat flux, n the load factor, V_{final} the final velocity, h_{MB} the Mars base altitude, h_{final} the final vehicle altitude, θ_{final} the final pitch angle, P_T the trajectory penalty value, and P the penalty. As described in Subsection 6.5.2, the maximum throttle capability is already directly implemented in the landing, and it is therefore not necessary for it to be added to the fitness function. Any violation of these constraints results in a penalty of 10^{11}, which are added if multiple are violated.

$$\left.\begin{aligned} \alpha &> 60^\circ \\ q &> 250 \ \text{ kW/m}^2 \\ n &> 4 \\ V_{\text{final}} &> 2.5 \ \text{ m/s} \\ \theta_{\text{final}} &> 2^\circ \\ h_{\text{final}} - h_{\text{MB}} &> 1 \ \text{ m} \end{aligned}\right\} P = P_T \tag{7.1}$$

However, there are targets that the vehicle must achieve, namely the target orbit, determined by the final pericentre altitude, the final eccentricity, the final inclination, and the landing location expressed by the final latitude and longitude (the final altitude has already been taken into account in the hard constraint fitness). The combination of fitness penalties as a function of these final parameters is combined with a bound system. If the final parameter deviates from its target by more than the bounded value, a penalty is added. However, to force the solution to converge more accurately towards the optimum and not just within the bound, gradient fitness functions are set. These functions, for pericentre altitude (r_p), eccentricity (e), inclination (i), latitude (δ), and longitude (τ) are found in Equations 7.2, 7.3, and 7.4, respectively, where P denotes the penalty, P_T the trajectory fitness penalty of 1×10^{11}, the subscript tar the target parameter, and final the simulated final parameter. These value were taken as it as shown that these values worked the best whilst calibrating the optimiser. Similar values have been used by Haex [23] and Rozemeijer [58].

$$\begin{array}{lll} \left|r_{\text{p,final}} - r_{\text{p,tar}}\right| > 50000 \text{ m}: & P = 5P_T & \\ \left|r_{\text{p,final}} - r_{\text{p,tar}}\right| \leq 50000 \text{ m} & P = 1 \times 10^8 \left|\dfrac{r_{\text{p,final}} - r_{\text{p,tar}}}{r_{\text{p,tar}}}\right| & r_{\text{p,final}} - r_{\text{p,tar}} > 0 \\ & P = 5 \times 10^8 \left|\dfrac{r_{\text{p,final}} - r_{\text{p,tar}}}{r_{\text{p,tar}}}\right| & r_{\text{p,final}} - r_{\text{p,tar}} < 0 \end{array} \tag{7.2}$$

$$\begin{array}{ll} |e_{\text{final}} - e_{\text{tar}}| > 0.05: & P = 5P_T \\ |e_{\text{final}} - e_{\text{tar}}| \leq 0.05 & P = 1 \times 10^8 \left|\dfrac{e_{\text{final}} - e_{\text{tar}}}{0.05}\right| \end{array} \tag{7.3}$$

$$\begin{aligned} |i_{\text{final}} - i_{\text{tar}}| > 3^\circ: &\qquad P = 5P_T \\ |i_{\text{final}} - i_{\text{tar}}| \leq 3^\circ &\qquad P = 1 \times 10^8\, |100(i_{\text{tar}} - i_{\text{final}})| \end{aligned} \tag{7.4}$$

$$\begin{aligned} |\delta_{\text{final}} - \delta_{\text{tar}}| > 3^\circ: &\qquad P = P_T \\ |\delta_{\text{final}} - \delta_{\text{tar}}| \leq 3^\circ &\qquad P = 1 \times 10^8 \left|100\left(\frac{\delta_{\text{tar}} - \delta_{final}}{3}\right)\right| \end{aligned} \tag{7.5}$$

$$\begin{aligned} |\tau_{\text{final}} - \tau_{\text{tar}}| > 3^\circ: &\qquad P = P_T \\ |\tau_{\text{final}} - \tau_{\text{tar}}| \leq 3^\circ &\qquad P = 1 \times 10^8 \left|\left(100\frac{\tau_{\text{tar}} - \tau_{\text{final}}}{3}\right)\right| \end{aligned} \tag{7.6}$$

In order to reward a solution for adhering to a constraint, the number of constraints that are not violated is multiplied by a negative fitness factor, as seen in Equation 7.7 for the ascent, and Equation 7.8, where U denotes the number of unviolated constraints, F_{tar} the target orbit factor, F_{loc} the landing location factor, and F_{safe} the landing safety factor. These three factors are set to 1, unless their respective requirements are met.

$$P = -1 \times 10^6 U F_{\text{tar}} \tag{7.7}$$

$$P = -1 \times 10^5 U F_{\text{loc}} F_{\text{safe}} \tag{7.8}$$

The requirements for the target orbit factor are that the pericentre is within 10 km of the target, the eccentricity within 0.005, and the inclination within 1.0 degree. The requirements for the landing location factor are that the landing latitude and longitude are within 0.1 radians (5.72958 degrees) of the target, which corresponds to a distance of 340 m. Lastly, the landing safety factor requires the landing altitude, velocity, and pitch angle constraints to be met. If the requirements for these factors are met, the corresponding factor increases from 1 to 2. This rewards the solution for adhering the constraints.

Lastly, in order to ensure that the objective function of minimising the GTOW is maintained, a fitness function is added that is dependent on the GTOW. This is shown in Equation 7.9. The total fitness of a solution is the summation of all the amassed penalties. This negative fitness is only awarded if all the constraints are met.

$$P = -1 \times 10^{15} \frac{1}{GTOW} \tag{7.9}$$

7.4. Optimiser Choice and Performance

Obtaining a solution that can be considered optimal and in an efficient manner is dependent not only on the fitness functions, but also on the performance of the optimiser. This means that the optimiser choice, as well as the various settings associated with the optimiser, determine the convergence behaviour of the optimisation. This section first discusses the choice of optimisation algorithm, followed by the chosen settings.

7.4.1. Optimiser Choice

As discussed in Section 3.3, the optimiser choices for the MDO fall under the branch of evolutionary algorithms, which have been shown to be highly successful optimisers for MDO applications as they are able to handle highly dynamic problems that involve non-linear constraints. There are various available evolutionary algorithms provided by the PaGMO library, of which the more successful ones have been investigated by previous bodies of work. The investigations conducted by van Kesteren [34], Contant [14], and Rozemeijer [58] show that the both the PSO and the PSOG optimisers are always outperformed by the DE1220 algorithm. However, the DE1220 algorithm was shown to be outperformed by the MOEA/D algorithm by Rozemeijer [58]. It should be noted that although the MOEA/D algorithm is multi-objective, its settings can also be changed such that it becomes a single-objective optimiser.

To determine which optimiser is most suitable for the optimisation of the Martian vehicle, their performances are observed over the evolution of 500 generations, using a population size of 100. The performance is expressed by tracking the mean fitness and lowest fitness per 5 generations for 3 different seeds. Although an optimal result is not yet found at 500 generations, this a high enough number of generations to be able to evaluate the algorithm performance , and to identify the optimal choice. A population size of 100 is taken, as it is the median of the population sizes investigated in the following sections. The results for each seed are presented in Figure 7.2.

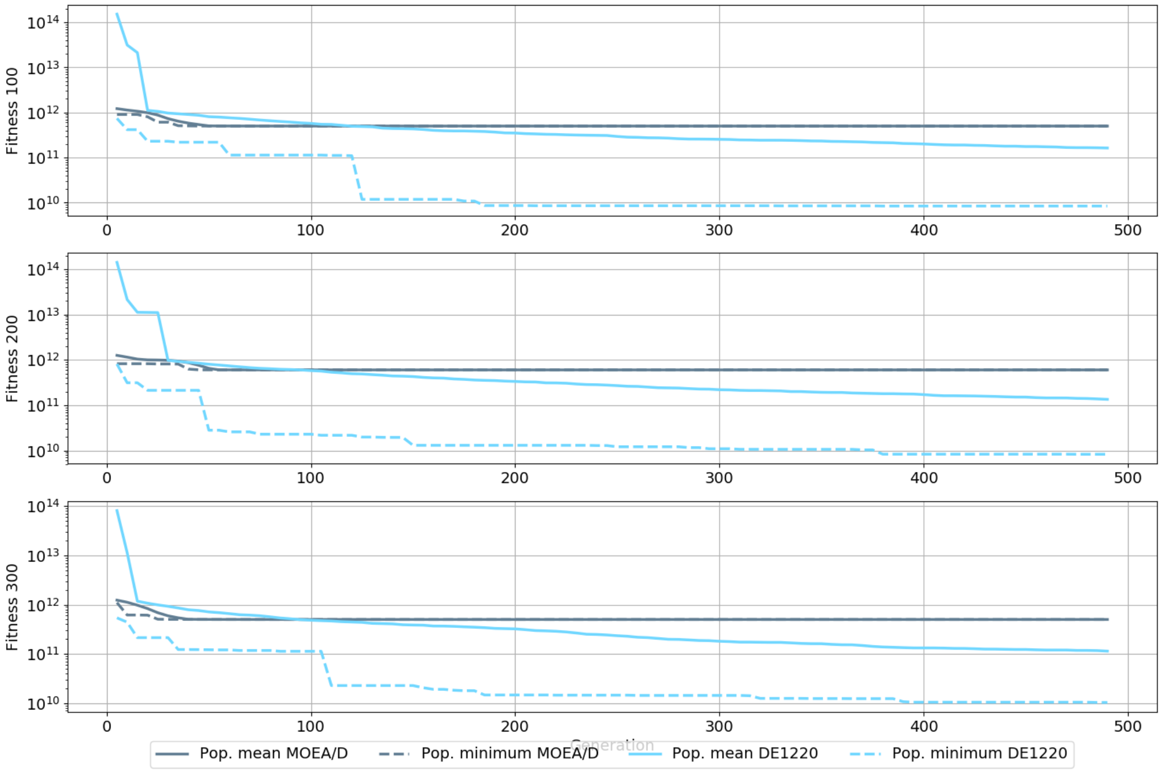

Figure 7.2: The mean fitness and minimum fitness of each population for optimisers DE1220 and MOEA/D.

As can be seen from Figure 7.2, the population mean for the DE1220 optimiser is much greater than the population mean the MOEA/D optimiser at the beginning of the optimisation for all three seeds. However, the difference between the two algorithms is swifty reduced , and within 150 generations the DE1220 mean is less than that of the MOEA/D. The stagnation of the MOEA/D mean and minimum show that in all cases, the algorithm gets stuck in a local minimum. Further, the best performing individual of the DE1220 for all three seeds finds solutions that have a lower fitness than that of the MOEA/D algorithm. The DE1220 algorithm outperforms the MOEA/D in every case, and is therefore is chosen as the MDO optimiser.

7.4.2. Optimiser Settings

Not only does the optimiser itself need to be determined, there are other parameters that must be set in order for the the optimiser to operate at its highest performance. The optimum population size is an important parameter to identify for the optimiser, as it also determines the performance of the MDO. A population size that is too small prevents the optimiser from being able to explore the search space thoroughly, leading to potentially getting stuck in local minima. A large population size, however, hinders the convergence of the optimisation, leading to unnecessary computational time and effort as well as a potentially sub-optimum solution compared smaller population sizes.

The termination setting of the MDO is another parameter that must be determined. There are many ways in which this can be implemented. It can be dependent on the fitness values found in each generation, such as dependency on the minimum fitness found, the population mean fitness, or the gradient of the fitness values. For example, if the mean fitness found over a certain number of generations does not decrease by a user-determined value, the MDO can be programmed to stop. Another termination condition is also the number of total generations run, which is the condition that is chosen by Haex [23], Rozemeijer [58], van Kesteren [34], and Miranda [44], and will also be used in this research. As the determination of the optimiser population size and the maximum generation count are dependent on the convergence of the fitness values, these two parameters are analysed in parallel.

To test the convergence behaviour of the algorithm, the optimisation is run using seeds 100, 200, and 300 for 3000 generations. An evolution of 3000 generations is chosen as 500 (which was the value used to determine the optimiser choice) is too low a generation count to determine the true convergence behaviour. The MDO schemes by Haex [23] and Rozemeijer [58] both had a similar number of design variables, and they used a maximum generation count of 2000 and 3000, respectively. The population sizes chosen are 60, 80, 100, and 120. This range is chosen as the population size should be 2-3 times the number of design variables as prescribed by the PaGMO DE1220 manual (therefore a minimum of 46), and the population size range encapsulates the population sizes chosen by Haex [23], Rozemeijer [58], van Kesteren [34], and Miranda [44] (80, 100, 100, and 70, respectively). Figure 7.3 presents the evolution of the mean and minimum fitnesses for each population size for each seed. Once a fitness is negative, it is known that the vehicle has adhered to all the constraints, and that it is being optimised for GTOW.

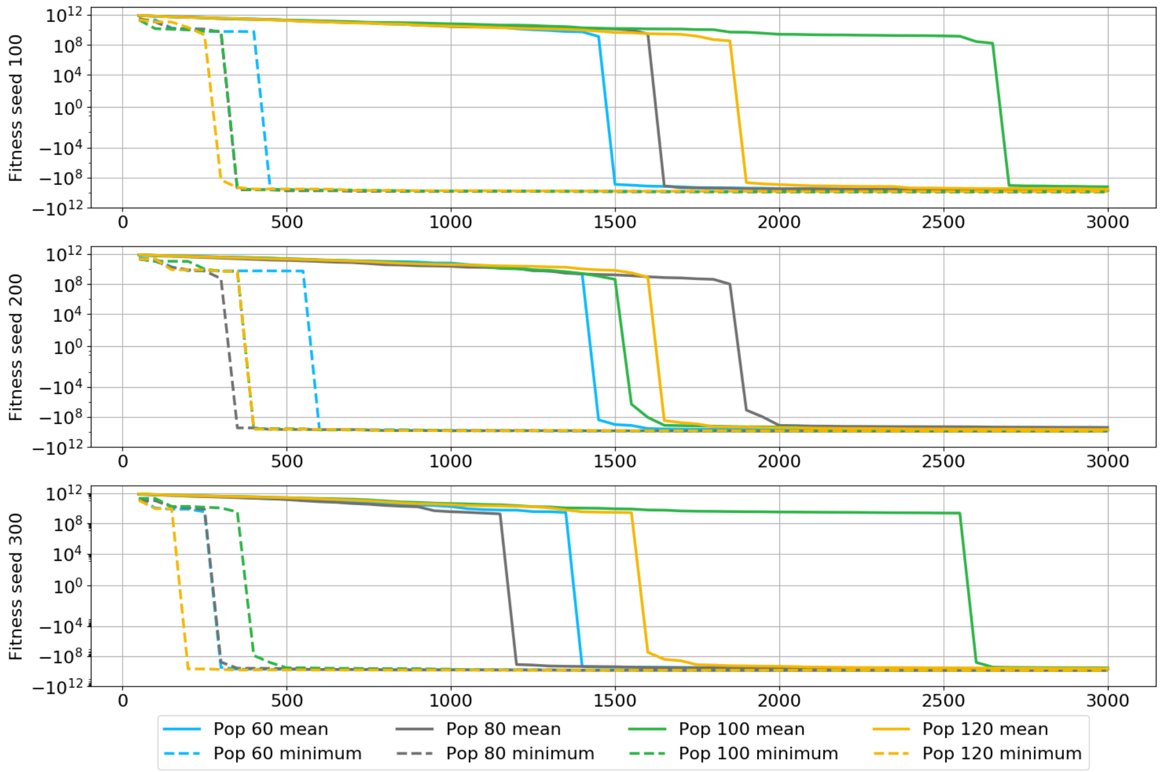

Figure 7.3: A comparison of mean and minimum fitnesses for three seeds for population sizes 60, 80, 100, and 120.

As can be seen from Figure 7.3, the behaviour of the fitnesses for all populations is very dependent on the seed, and that there is no clear-cut rule to which the populations' behaviour adhere to. For example, the means of seeds 100 and 300 for population size 100 take more than 2500 generations to go negative. On the other hand, for seed 200, it only takes 1500 generations. The order in which the population sizes first obtain a solution with negative fitness also differs, however population 120 is the fastest for two out of the three seeds, most likely due to it having the greatest search space. In order to more closely inspect the populations' convergence behaviour, Figure 7.4 is presented, showing the evolution of the minimum fitness from generation 1000 onward.

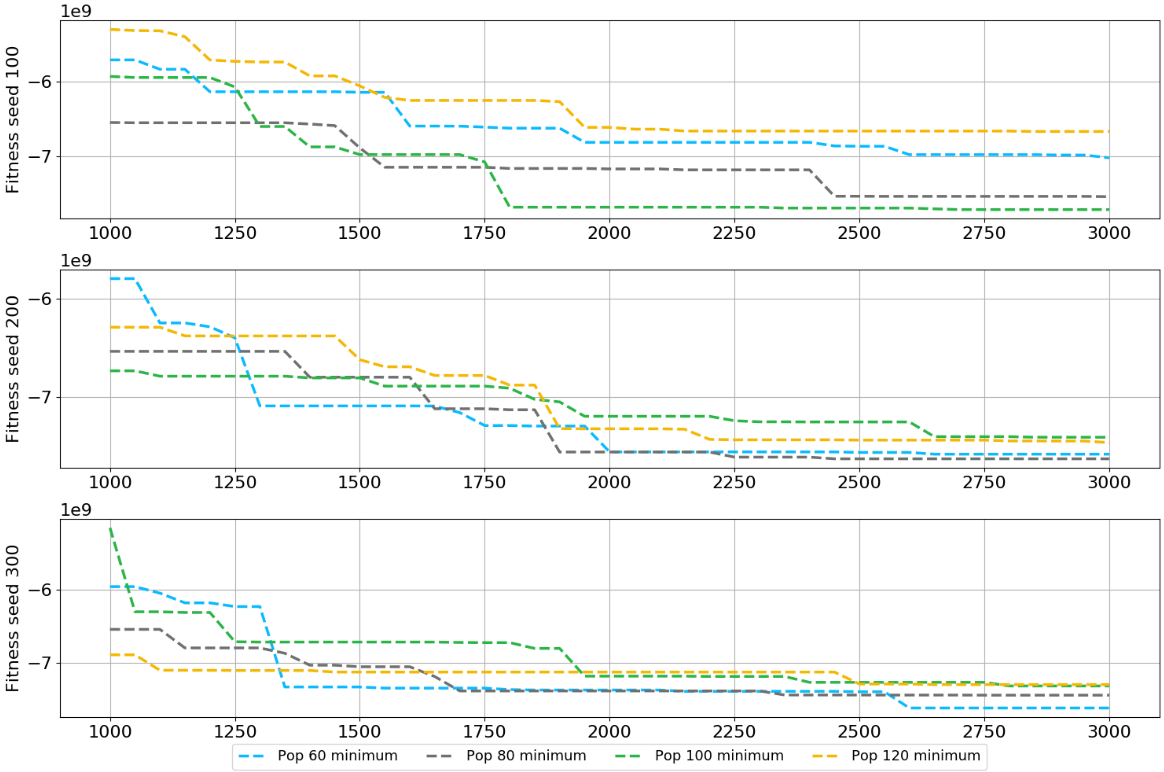

Figure 7.4: A comparison the minimum fitnesses for three seeds for population sizes 60, 80, 100, and 120.

Again, as seen in Figure 7.4, there is no overall trend by which there is a guarantee that a certain population size outperforms all others. It is certain, however, that population size 120 performs the least favourable, as it does not converge well, and ultimately always obtains the least optimal solution. Likewise, although population size 100 for seed 100 obtains a seed optimum, population size 100 for seeds 200 and 300 also does not converge well. This leaves the decision to be made between population sizes 60 and 80 as these always performs well. Both seeds 60 and 80 obtain a seed optimum (seed 300 and seed 200, respectively), however seed 80 comes in second in seeds 100 and 300, whereas seed 60 does comparatively worse in seed 100. Therefore seed 80 is chosen as the population size.

It is also not very clear as to what value the termination generation count shoud be set, as the fitnesses can still been seen to be decreasing close to the end of the simulation. Therefore the termination condition remains 3000 generations. Of course the question remains whether perhaps there is an optimum solution to be found past 3000 generations. This is the intrinsic dilemma associated with optimisation schemes, that there always is a potentially better solution if more computational power is allotted. The general trend of all three seeds is, however, that the optimum found is not greatly improved upon past generation 2000. The convergence behaviour is clearly more dependent upon the seed than on the generation count, and due to this the termination is set at 3000.

Other optimiser settings such as the cross-over and differential mutation parameters are determined by the DE1220 algorithm itself, and therefore do not have to be set by the user.

8

Result Generation and Analysis

As the various optimiser disciplines are now developed and validated, and the optimiser and relevant settings are identified, the search for the optimum vehicle and trajectory design begins. This chapter presents the result generation and analysis of the various optimum vehicles found. A baseline case is first discussed, followed by explorations of different scenarios and their effects on the optimum solution of the vehicle and its trajectory.

8.1. Baseline Case

The mission scenario for the baseline case has been discussed and identified in Chapter 2 and 6, where the vehicle requirements, Martian base location, target orbit, and rendezvous strategy are taken to be the same as that of the Charon vehicle [22]. The baseline case serves as a reference to which the other scenarios can be compared, to understand the effects of certain choices and constraints on the optimum solution. The baseline case will also be compared directly to the Charon vehicle design, as both vehicles are designed for the same mission scenario. The baseline scenario is given below.

Baseline Scenario:

- **Payload:** A payload mass of 1200 kg is taken on the ascent and the descent
- **Mars Base:** The Mars base is located at 42.5° North and 25.5° East, which is the location from which the vehicle launches and where the vehicle lands
- **Target Orbit:** The target orbit into which the vehicle is injected is a circular phasing orbit at an altitude of 607.74 km at an inclination of 44.96°
- **Rendezvous:** The rendezvous and docking procedure necessitates a delta-V of 45.84 m/s for the Hohmann transfer and 80.4 m/s for the docking phase
- **Entry:** The vehicle initiates the atmospheric reentry with an entry burn of 261 m/s, and the EDL phase begins at an altitude of 80 km with a velocity of 3500 m/s and a heading of 45.04°
- **Thrust Law:** The vehicle utilises thrust law 1

Although each run of the MDO will produce an optimum design, as seen in Section 7.4, the MDO is dependent on the seed, leading to a different solution found per seed. To understand the convergence behaviour of the optimum solution, 10 seeds are used to find 10 optimum vehicles and their associated trajectories. These optima, their design variables, and their trajectory are then compared. To verify that the MDO is indeed optimising for the objective function, the GTOW of each solution is first plotted against its respective fitness, shown in Figure 8.1.

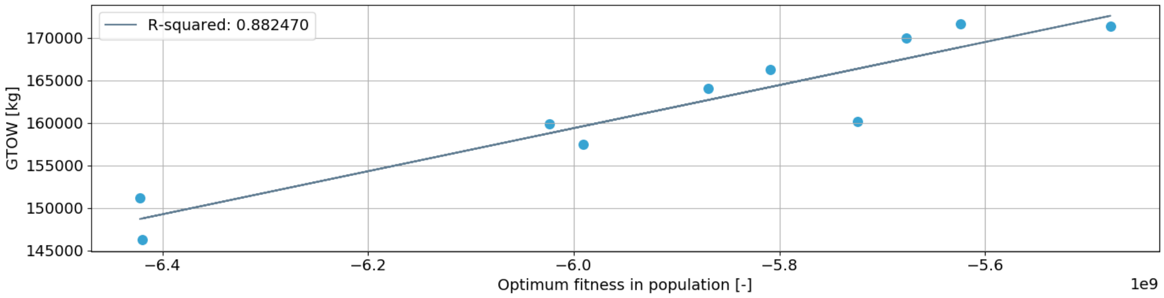

Figure 8.1: The GTOW and fitness of each optimum individual for each seed

As can be seen from Figure 8.1, there is a strong relationship between the fitness of an optimum solution found and its associated GTOW, with a robust linear regression shown, and an R^2 value of 0.882. This shows that the algorithm optimises effectively for the GTOW as desired.

Figure 8.2 shows the breakdown of each of the 10 optimum vehicles' GTOW, alongside that of the Charon vehicle, shown on the leftmost side, in the boldened colour. The GTOW values of the MDO optima lie around the value of the Charon vehicle, with some lying above, however many also lying below. This shows that the optimiser is able to find solutions that reduce the vehicle's GTOW compared to Charon's, with seed 300 showing that significant mass reductions are possible, as it obtains a GTOW than is more than 20,000 kg less than that of Charon. These mass reductions stem predominantly from the reduction of the ascent propellant, identifying the ascent as well as propellant efficiency as the bottleneck of the design. The dry masses of all the vehicles lie approximately around 25000 kg, only increasing or decreasing marginally with increasing and decreasing GTOW masses, respectively, due to different necessary tank sizes. The propellant required for the transfer, docking, and entry burns (falling under the category 'other') do not change by any significant amount across the seeds, with also little variation occurring in the landing propellant. The optimum vehicle's design variables, engine properties, and mass breakdown are given at the end of this section in Table 8.1, and the results of all the seeds are given in Appendix C.1.

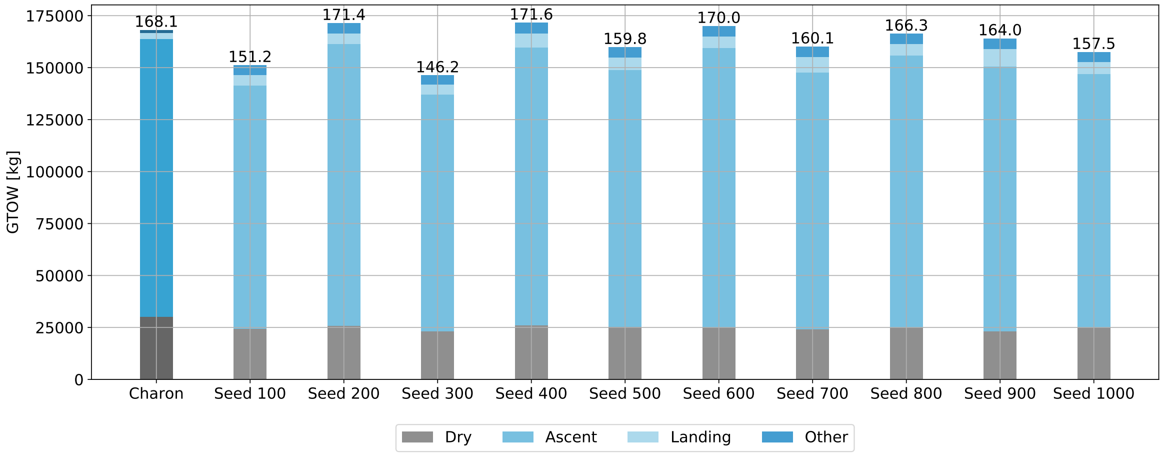

Figure 8.2: The breakdown of each optimum vehicle's mass, compared to that of Charon as given by Gaffarel et. al. [22]. The values above each seed's breakdown indicates the GTOW in tonnes

To understand the convergence of the solutions with respect to the design variables, as well as to compare the design variables found by the MDO to those of Charon, box and whisker plots are used to present the design variables for the solutions. Figures 8.3 - 8.5 show the design variables for all 10 optima, with the variables that are used for the Charon vehicle shown in red, as determined by Gaffarel et. al. [22]. Note that the engine and total thrust values are also shown as a comparison, however they are not design variables.

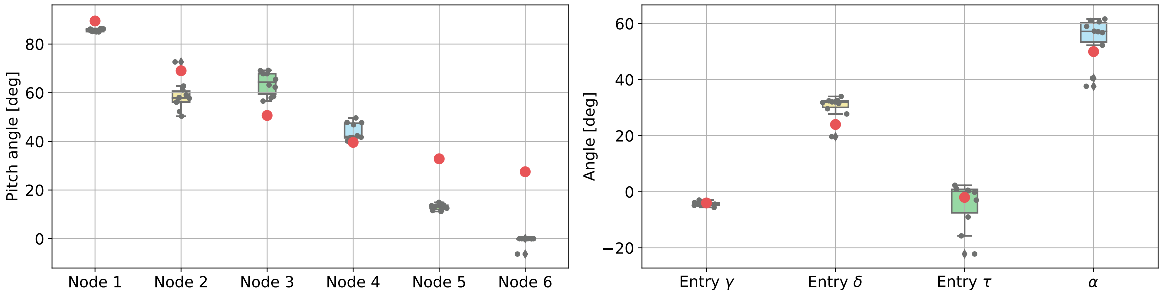

Figure 8.3: The pitch angles for each node (left) and the entry condition angles (right), with Charon's variables shown in red

From the left plot of Figure 8.3 it is clear that the MDO implements a different ascent profile compared to that of Charon. The MDO vehicle is injected directly into the target orbit, whereas the Charon implements a gravity turn followed by an attitude change. Although a gravity turn is the most efficient manner to ascend to an orbit on an airless planet, the presence of an atmosphere can compromise its efficiency. This could therefore be the reason for some of the MDO solutions requiring less propellant mass. With respect to variable convergence, nodes 1, 5, and 6 have the tightest margins due to the launch and eccentricity bounds, whereas nodes 2, 3, and 4 show more leniency in their margins. This is likely due to differences in thrust levels, ascent burn times, and aerodynamic effects, as well as there being no orbital bounds in this region that the trajectory must adhere to, leading to less strict constraints.

The entry angles shown on the right in Figure 8.3 show very little flexibility for the entry flight path angle (γ), however the entry latitude (δ), entry longitude (τ), and angle of attack (α) margins are much more lenient. The entry γ is highly influential on the vehicle's trajectory and greatly dictates the vehicle's motion and therefore whether it abides by the conditions of the entry corridor. Although the α value is also determined by entry corridor conditions, due to its influence on stagnation heat flux and aerodynamic properties, the allowable range that the α value may fall between shows that many α values satisfy these conditions, and that the α is not a variable that drives the design. However, as it co-determines the aerodynamic forces on the vehicle and therefore also the lateral distance covered by the vehicle during the descent, it impacts the entry coordinates. This can be seen by the large margins in the entry δ and τ. The Charon entry angles are all very similar to the MDO optimum vehicles' values, with the most constraining parameter, the entry γ, falling exactly in the MDO optimum vehicles' margin.

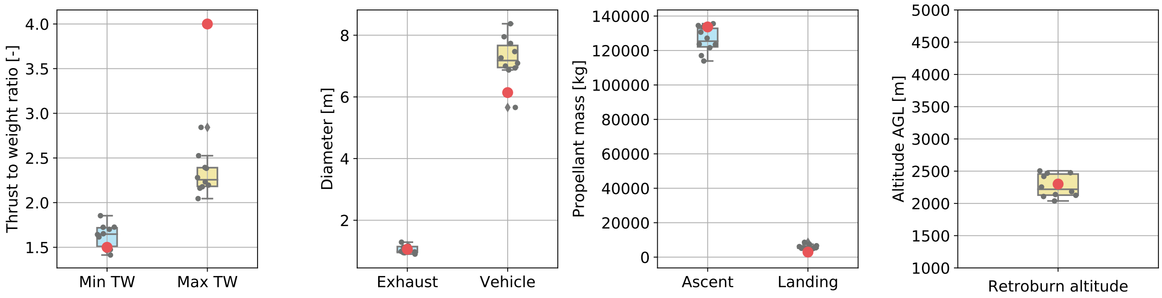

Figure 8.4: (Left to right) The minimum and maximum TW ratios, the exhaust and vehicle diameters, the ascent and landing propellant masses, and the retroburn altitude. Charon's variables are shown in red

Figure 8.4 shows the optimum TW ratios, exhaust and vehicle diameters, ascent and landing propellant masses, and the retroburn altitude. What is interesting to see is that the minimum TW of Charon falls within the range of the MDO solutions, yet the optimum MDO vehicles' maximum TW ratios are almost all lower than 2.5, a significant difference with Charon's maximum TW ratio of 4. This shows that a high maximum TW ratio is unnecessary, perhaps leading to higher propellant masses due to the higher necessary thrust and therefore mass flow. The efficiency of the Charon vehicle's and the MDO vehicles' propellant consumption can directly be seen in the third figure from the left, where the optimum ascent and landing propellants are given. As can be seen, the Charon vehicles' ascent propellant mass lies at the higher end of the MDO vehicles'

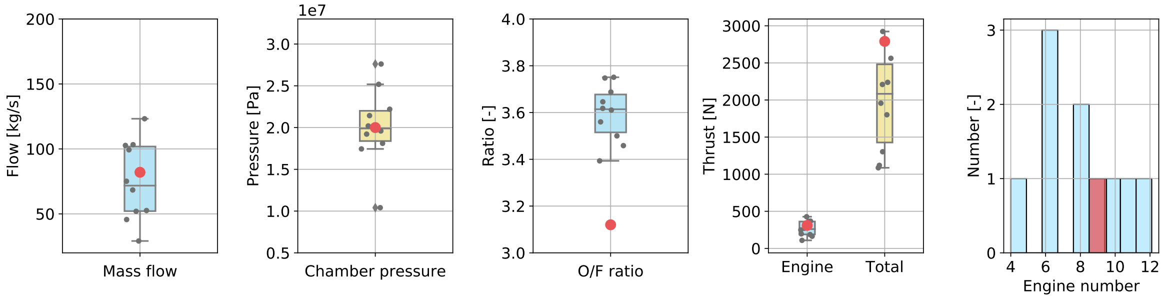

Figure 8.5: (Left to right) The engine mass flow, the engine chamber pressure, the mixture ratio, the engine thrust and total thrust values, and the engine number. Note that the engine and total thrust values are not design variables. Charon's variables are shown in red

range, showing that more efficient solutions are possible. The Charon landing propellant mass, on the other hand, is on the lower end of the MDO vehicles' range. This is most likely due to the fact that the Charon vehicle lands with 6 m/s as opposed to the maximum velocity of 2.5 m/s implemented in the MDO simulation. It could also be due to the fact that the ascent propellant is the bottleneck of the optimiser, meaning that the landing propellant has less impact on the overall GTOW. The optimiser therefore prioritises vehicles' ascent propellant consumption, leading to less optimisation of the landing propellant mass.

The second figure from the left in Figure 8.4 shows that the Charon exhaust diameter falls within the margins, but interestingly it also shows that almost all of the the MDO vehicles' diameters are much larger than that of the Charon vehicle. This could show that although Mars has an atmosphere, evidently the drag forces during the ascent are not so large that the optimiser favours a more aerodynamic vehicle shape, such as one with a reduced vehicle diameter. The most rightmost figure in the Figure 8.4 further shows that all retroburn altitudes fall within 2000 m and 2500 m, with the Charon vehicle's retroburn altitude falling within that margin.

Figure 8.5 shows the design variables associated with the engine performance, as well as the engine thrust and total thrust produced by the engines for all the vehicles. As can be seen from the rightmost figure, there is no strong convergence of the vehicle design with respect to engine number. Although 6 engines is the preferred engine number, this is a slim margin, within only 3 out of the 10 vehicles using 6 engines, and other engine numbers ranging from 4 to 12 engines.

This range is mirrored by the very large range of total thrust values, shown in the fourth figure from the left. However, the Charon vehicle's total thrust is greater than almost all the MDO vehicle's total thrust values, which is due to its higher maximum TW ratio used (as shown in Figure 8.4). The large range of total thrust, when combined with the small range of engine thrust, is due to the large range in engine number used. Although the total thrust for the Charon vehicle is larger than those obtained by the MDO solutions, the engine thrust falls within the MDO range. The Charon vehicle's values for mass flow and chamber pressure also fall within the MDO vehicle's ranges, however the mixture ratio is much smaller than that of the MDO vehicles. The mixture ratio determines the thermochemical properties of the propellant combination and therefore has an influence on the thrust and specific impulse of the engines, as well as therefore also the engine mass and total mass. Clearly a mixture ratio of between 3.4 and 3.8 yields more favourable engine performance when compared to Charon's.

To evaluate the effect of the vehicle and trajectory design variables on the ascent and EDL phases, the trajectories are plotted. The ascent phases can be seen in Figures 8.6 - 8.8, where the colour of the trajectory indicates its GTOW rank, namely the lighter the colour, the greater its GTOW. The vehicle with the lowest GTOW, the optimum, is therefore shown in the darkest colour, and is also shown in bold.

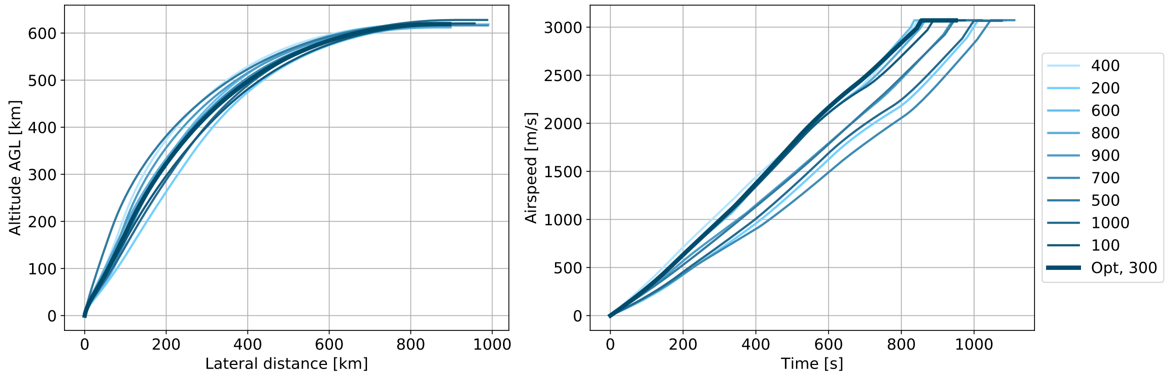

Figure 8.6: The ascent profiles and airspeed as a function of time for the baseline results

As can be seen from Figure 8.6 on the left, the ascent profiles of the solutions are very varied between flight times of 0 and 400 seconds, however from that moment they converge to a more common profile due to the target orbit constraints imposed. The optimum trajectory, however, is found exactly within the range. From the right-most figure, it can be seen that the the optimum trajectory has one of the shortest ascent burn times, thereby being reducing its delta-V losses due to gravity.

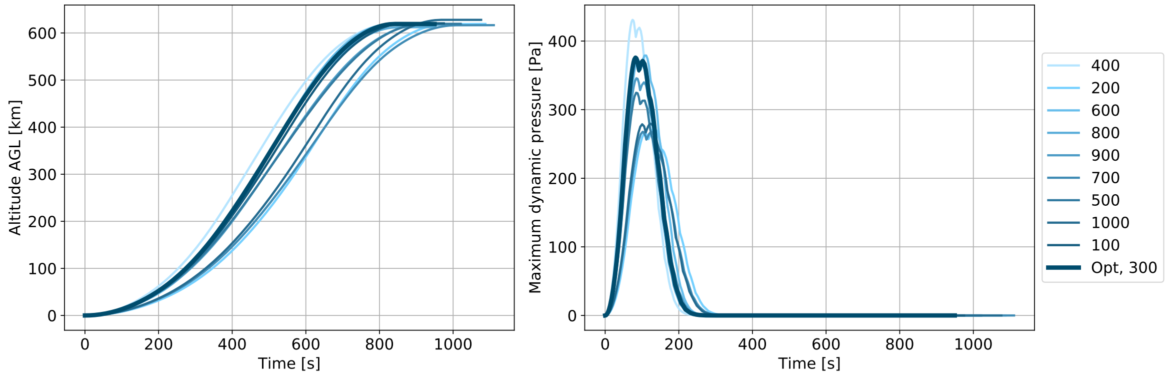

Figure 8.7: The altitude and the dynamic pressure as a function of time for the baseline results

This can also be seen from Figure 8.7, where the optimum trajectory is one of the quickest to gain altitude. There is, of course, a trade-off between gravitational and aerodynamic forces. Higher velocities result in higher aerodynamic loads and therefore drag, whereas reducing the time to reach the target altitude results in lower gravitational losses. This trade-off can be seen in the figure on the right in Figure 8.7, where the optimum vehicle's high velocity results in high dynamic pressures. However, evidently the gains from reducing the gravitational losses are greater than the losses incurred by higher drag forces.

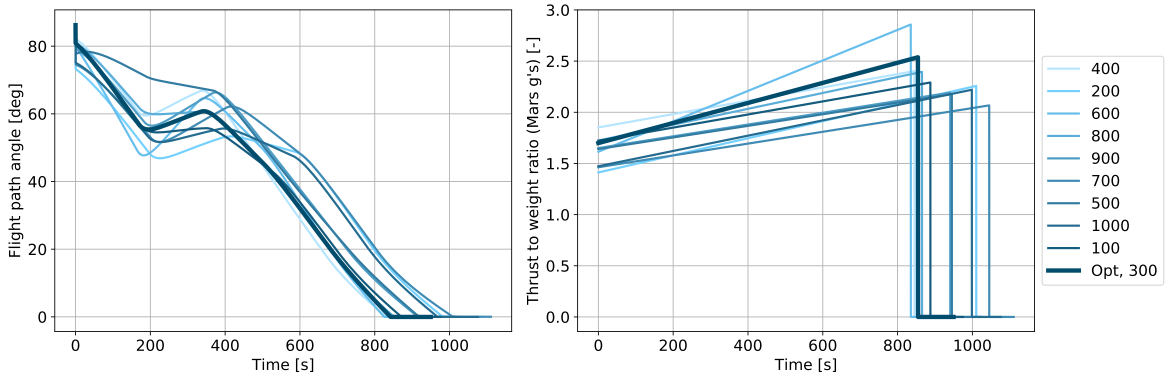

Figure 8.8: The flight path angle and TW ratio as a function of time for the MDO baseline results

From the flight path angles in Figure 8.8 it can be seen that the variations in ascent profiles at the start of the ascent (left, Figure 8.6) are due the varying flight path angles. They do, however, all follow the same trend. The optimum vehicle's faster ascent can also be attributed to the its comparatively higher minimum and maximum TW ratio, as seen in the rightmost figure in Figure 8.8. The behaviour of the solutions' EDL trajectories is also assessed. The trajectories are shown in Figures 8.9 - 8.11.

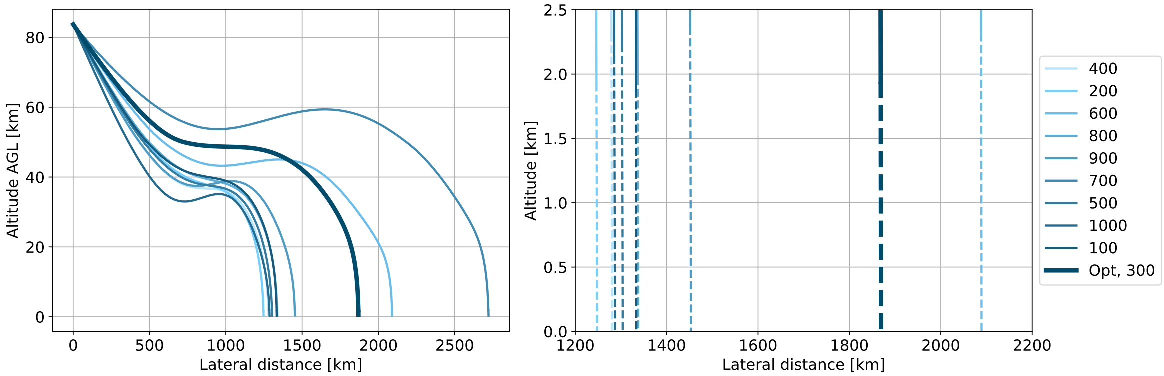

Figure 8.9: The EDL profiles for the MDO baseline results. The dashed line style indicates the propulsive landing

As can be seen in Figure 8.9, the differences in entry parameters have a large effect on the EDL profile. Firstly, the entry γ has a very large effect on the profile at start of the EDL phase. Although all the values lie within a very small range, these conditions are propagated over a great distance and therefore cause very large differences. The density of the atmosphere increases to a notable value at an altitude of approximately 50 km which can be seen to affect the trajectories as they plateau once lift force is generated. The shape of the vehicle, mach number, and angle of attack also all determine the in-flight aerodynamic properties of the vehicle, which induce large differences in trajectory, as seen directly from the EDL profiles.

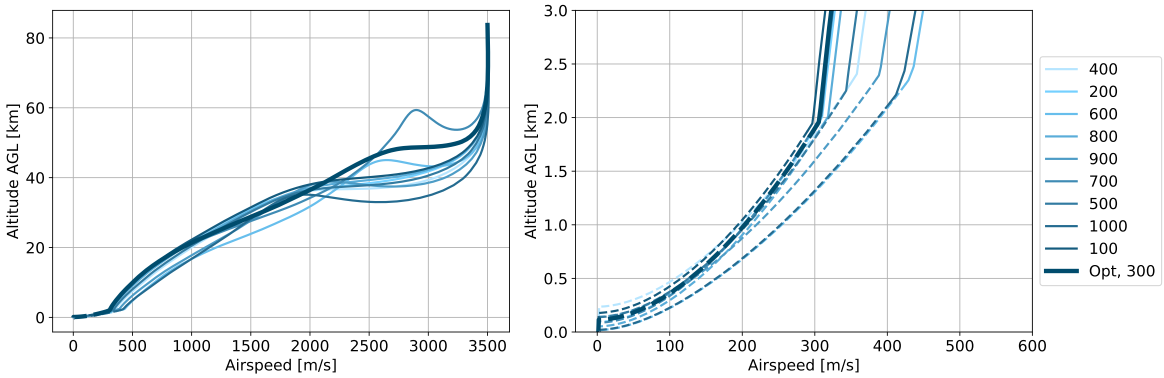

Figure 8.10: The entry corridor for the MDO baseline results. The dashed line style indicates the propulsive landing

Figure 8.10 shows the entry corridor of the EDL phases. Although the EDL profiles differ greatly (Figure 8.9), it can be seen from the entry airspeed-altitude graphs in Figure 8.10 that they all must adhere to the constraints imposed by the entry corridor. The effect of the EDL phase on the landing propellant consumption can be directly observed from the rightmost figure in Figure 8.10. The optimum trajectory has one of the lowest velocities out of the 10 solutions before the start of the retroburn (the retroburn is denoted by the dashed line style). This leads to a lower landing propellant mass needed, and therefore a lower GTOW. The trajectories all reach the 2 m/s constant landing phase within 200 m of the ground, and therefore do not need to use much propellant for the controlled landing, leading to an efficient propellant use.

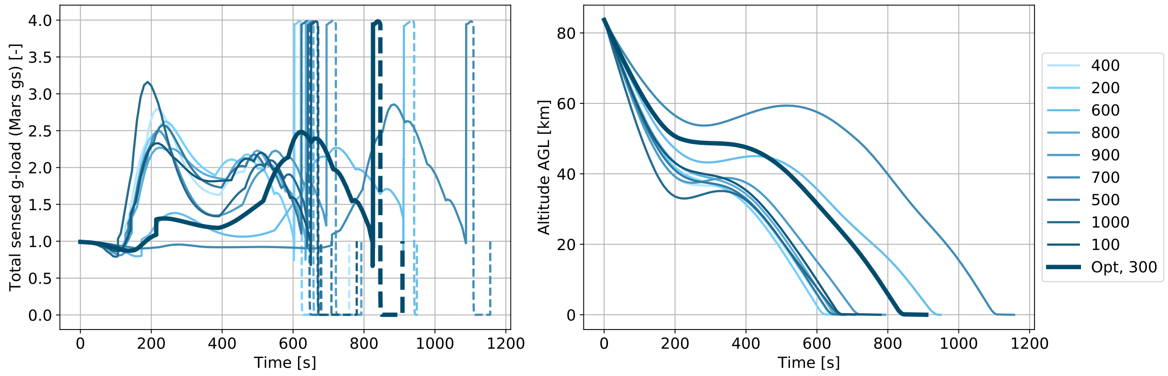

Figure 8.11: The sensed acceleration (left) and the altitude (right) as a function of time for the MDO baseline results

The reason for the optimum solution's low velocity before the initiation of the retroburn can be seen from Figure 8.11. The optimum trajectory has one of the longest EDL flight times, leading to a longer period of time to reduce the velocity through drag, before the retroburn. As can be seen from the leftmost figure, all trajectories adhere to the maximum load constraint of 4 g_{mars}. The design variables, engine properties, and mass breakdown for the optimum solution (seed 300) can be found in Table 8.1. All results for the 10 seeds can be found in Appendix C.1.

Table 8.1: The optimum vehicle for the baseline case and the values used by Gafferel for the Charon vehicle [22]

Design Variable	**Value MDO**	**Value Charon**
Optimum Trajectory Design Variables		
Node 1 [deg]	86.205	89.50
Node 2 [deg]	58.012	73.60
Node 3 [deg]	63.165	56.60
Node 4 [deg]	42.330	45.43
Node 5 [deg]	13.578	37.89
Node 6 [deg]	0.075	32.76
Min TW [-]	1.701	1.5
Max TW [-]	2.525	4
Entry γ [deg]	-3.620	-4
Entry δ [deg]	27.755	24
Entry τ [deg]	-9.011	-2
Entry α [deg]	57.292	50
Retroburn altitude [m]	2125	2300
Optimum Vehicle Design Variables		
Mass flow [kg/s]	51.974	82.9
Chamber pressure [Pa]	18110229	20000000
O/F ratio [-]	3.618	3.12
Engine number [-]	6	9
Ascent propellant [kg]	113905	138344
Landing propellant [kg]	4754	27101
Exhaust diameter [m]	0.902	1.06
Vehicle diameter [m]	7.469	6.14
Engine Properties		
Specific Impulse (vac) [s]	387.770	371
Engine thrust (vac) [kN]	186.575	310
Total thrust (vac) [kN]	1119.453	2790
Mass Breakdown		
Dry mass [kg]	21941	30221
Propellant mass [kg]	123084	137886
Payload mass [kg]	1200	1200
GTOW [kg]	**146226**	**168107**

8.2. Target Orbit Change

As observed in Section 8.1, the ascent propellant consumption is the bottleneck of the design, as the ascent propellant mass is the largest contributor of the GTOW. Therefore optimising the ascent is of great importance. The target orbit determines the delta-V needed to reach the orbital node, together with the rendezvous strategy. In this section, two other mission scenarios are explored: the scenario as outlined by Komar et. al. for the Hercules vehicle [39], and a direct ascent to the orbital node's altitude. Although a direct ascent to the rendezvous target's altitude is never implemented in practice due to the high risks involved, it is still an interesting hypothetical case. Below is a summary of the two mission scenario cases, where all other parameters remain the same as in the baseline case (see Section 8.1 for details).

Hercules:

- **Mars Base:** The Martian base is located at 43.9° North and 23.6° East
- **Target Orbit:** The target orbit into which the vehicle is injected is a phasing orbit at an altitude of 108 km, with an eccentricity of 0.0178, and an inclination of 43.9°
- **Rendezvous:** The rendezvous and docking procedures necessitate a total transfer delta-V of 92.5 m/s and 80.4 m/s docking delta-V
- **Entry:** The vehicle initiates the atmospheric reentry with an entry burn of 200 m/s, and the EDL phase begins at an altitude of 132 km, with a velocity of 3200 m/s, and a heading of 46.1°

Direct Ascent:

- **Target Orbit:** The target orbit into which the vehicle is injected is directly into a the same circular orbit as the node, at 500 km at an inclination of 44.96°
- **Rendezvous:** Although no transfer delta-V is needed, 80.4 m/s is still reserved for docking
- **Entry:** The same entry conditions are taken as the baseline: the reentry is started with an entry burn of 261 m/s, and the atmospheric entry begins at an altitude of 80 km, with a velocity of 3500 m/s and a heading of 44.96°

The baseline vehicle case, as stated in Section 8.1, is simulated using 10 different seeds. The Hercules scenario is also simulated using 10 seeds, as it is interesting to compare the results and their convergence directly to the Hercules designed by Komar et. al. [38], and therefore a thorough exploration is needed. The direct ascent, however, has no direct comparison, and therefore only 3 seeds are used for its solutions. Figure 8.12 shows the GTOW breakdown of all three scenarios.

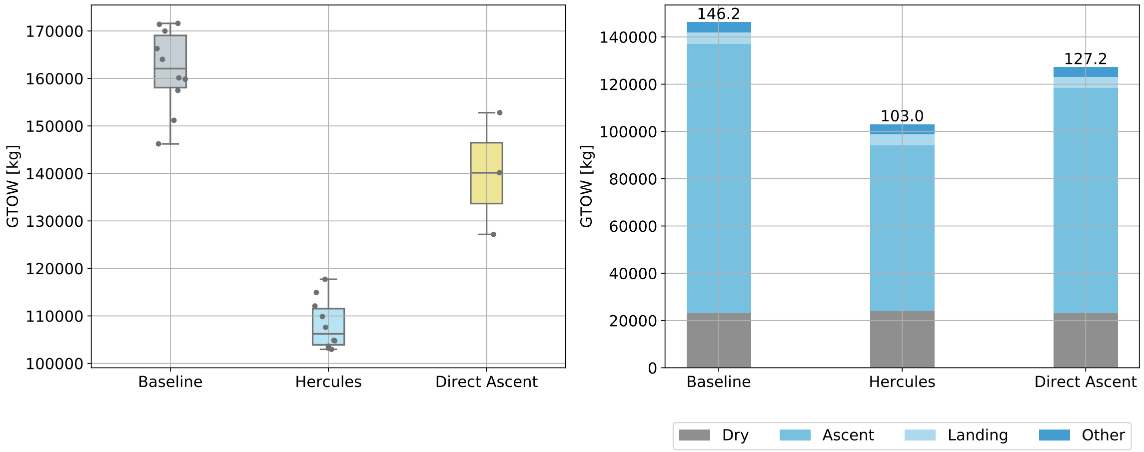

Figure 8.12: The GTOW of all the vehicles for each target orbit scenario (left) and the GTOW breakdown of each optimum vehicle's mass (right). The values above each seed's breakdown in the rightmost figure indicates the GTOW in tonnes

As is immediately clear from Figure 8.12, the final pericentre altitude is the driving factor for the vehicle's GTOW, as both the Hercules and the direct ascent scenarios lead to GTOWs that are considerably less than that of the baseline scenario. The Hercules vehicle is the most propellant-efficient, as its best-performing individual has a GTOW that is more than 40,000 kg less than that of the baseline scenario, being just 103.0 tonnes. It is evident that the reduction in mass is due to the delta-V necessary to achieve the target orbit, as the dry, landing, and other propellant masses do not vary significantly between the scenarios.

Furthermore, whereas the best performing individual for the baseline case is an outlier, the Hercules optima all lie within a much smaller range, showing more favourable convergence properties. Although less can be said about the convergence properties of the direct ascent scenario due to the presence of only 3 seeds, its values lie almost exactly between those of the Hercules and the baseline scenarios, indicating that its lower target altitude reduces the necessary ascent propellant mass.

The trajectories of the best three performing individuals from the baseline and Hercules scenarios, and all three seeds of the direct ascent scenario, are taken and plotted to compare. Figures 8.13 and 8.14 show the ascent phase for all three cases, where the solid line represents the associated scenario's optimum case, and the dashed lines represents the other two solutions for that case.

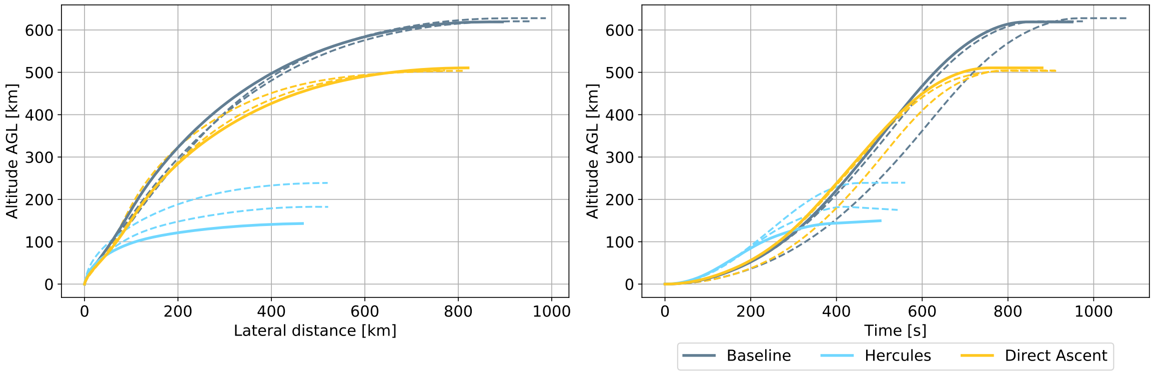

Figure 8.13: The MDO ascent profiles for the three best performing individuals in the baseline, Hercules, and direct ascent scenarios

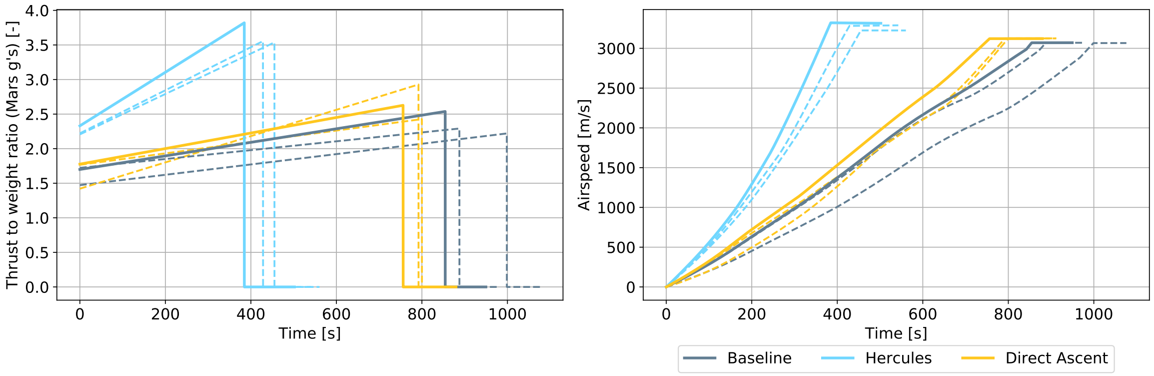

Figure 8.14: The MDO TW ratios (left) and altitude as a function of time (right) for the three best performing individuals in the baseline, Hercules, and direct ascent scenarios

As can be seen from the leftmost figure in Figure 8.13, the injection points for both the baseline and the direct ascent scenarios are at the pericentre altitude due to the eccentricity being 0. However, this is not the case for the Hercules vehicle, as the target eccentricity is 0.0178, and neither the argument of pericentre nor right ascension of the ascending node are fixed (these parameters are also not provided for the Hercules vehicle given by Komar et. al. [39]). Therefore, the orbital injection altitude is not fixed. It is clear, however, that the optimum trajectory out of the three lies at the lowest altitude, leading to lower propellant masses.

From the rightmost figure in 8.13, it can be seen that for each mission scenario, the optimum solution is the solution that reaches the target altitude the fastest, thereby reducing gravity losses. This observation is supported by the rightmost figure in Figure 8.14, where all the optima are the cases that increase their velocity the fastest. Almost all three optima also have the highest minimum and maximum TW ratios for their respective cases, as seen in the leftmost figure in Figure 8.14. It is interesting to see that where the Hercules scenario calls for much higher minimum and maximum TW ratios, due to its higher orbital injection velocity and shorter time of flight, high TW ratios are unnecessary for the direct ascent and baseline scenarios.

Figures 8.15 and 8.16 show the EDL phases for the three best performing individuals for all three scenarios. Again, the solid line represents the associated scenario's optimum case, and the dashed lines represents the other two solutions for that case.

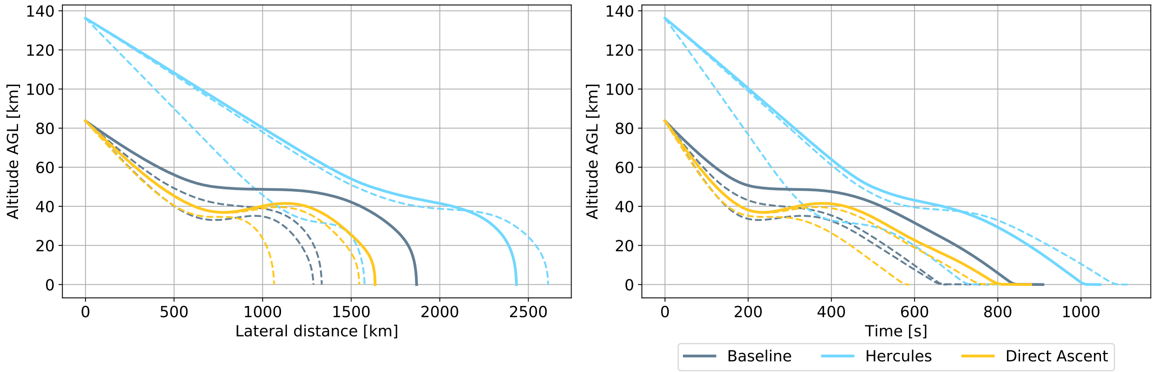

Figure 8.15: The MDO EDL profiles for the three best performing individuals in the baseline, Hercules, and direct ascent scenarios

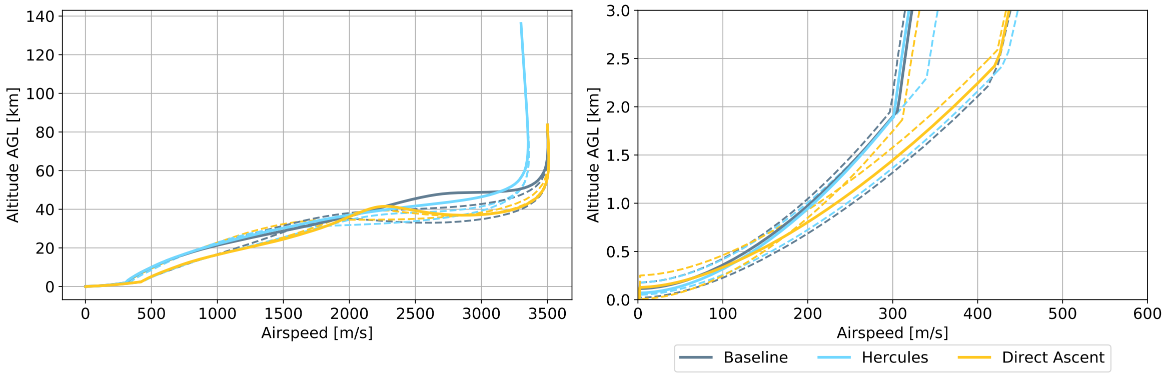

Figure 8.16: The MDO entry corridor for the three best performing individuals in the baseline, Hercules, and direct ascent scenarios

As can be seen in Figure 8.15, due to the differences in fixed initial conditions such as entry altitude and entry velocity, there are many differences in EDL profiles in terms of lateral distance and total descent time. However, almost every optimum solution for each scenario has the longest time of flight for their respective scenarios. As was observed for the baseline case, this reduces the velocity by dissipating the energy through drag, and so less propellant is necessary for the propulsive landing.

In Figure 8.16 the entry corridors can be seen, and though the EDL profiles in Figure 8.15 are clearly very different, all trajectories again must adhere to the entry corridor conditions. The rightmost figure in Figure 8.16 again shows that all solutions are optimised to reduce the controlled landing time, at which the velocity is kept at 2 m/s, and thereby reduce the necessary landing propellant.

Table 8.2 presents the design variables, engine properties, and mass breakdown for the optimum solution for all three target orbit cases. The results of all seeds for the Hercules and direct ascent cases can be found in Appendix C.2. As seen previously in Figure 8.13, the Hercules scenario results have a much steeper ascent, with a pitch node 2 angle of 70° compared to the other two angles of 58° and 52°. The higher TW ratios for the Hercules vehicles also result in a much higher total thrust for the Hercules vehicle, at 2136 kN compared to 1119 kN and 977 kN for the baseline and direct ascent cases, respectively. This is generated by the much higher engine mass flow, that is almost triple that of the baseline and direct ascent: 154 kg/s compared to 52 kg/s and 53 kg/s. This indicates that the difference in mission scenario has a direct influence in the design of the engines, as well as the propellant mass. From the results, it is therefore clear that the target orbit and subsequent rendezvous strategy has a very high influence on the GTOW of the vehicle, and that a lower target orbit is preferable.

Table 8.2: The optimum vehicle for the baseline, Hercules, and direct ascent cases

Design Variable	**Baseline**	**Hercules**	**Direct Ascent**
Optimum Trajectory Design Variables			
Node 1 [deg]	86.205	85.147	86.737
Node 2 [deg]	58.012	70.383	52.063
Node 3 [deg]	63.165	36.494	61.821
Node 4 [deg]	42.330	11.992	36.146
Node 5 [deg]	13.578	4.500	9.339
Node 6 [deg]	-8.522	-2.859	-8.390
Min TW [-]	1.701	2.333	1.778
Max TW [-]	2.525	3.872	2.643
Entry γ [deg]	-3.620	-3.023	-4.956
Entry δ [deg]	27.755	24.309	33.065
Entry τ [deg]	-9.011	-20.835	-7.626
Entry α [deg]	57.292	58.766	44.213
Retroburn altitude [m]	2125	2042	2580
Optimum Vehicle Design Variables			
Mass flow [kg/s]	51.974	153.821	53.006
Chamber pressure [Pa]	18110229	13179391	31613599
O/F ratio [-]	3.618	3.614	3.172
Engine number [-]	6	4	5
Ascent propellant [kg]	113905	70229	95364
Landing propellant [kg]	4754	4745	4517
Exhaust diameter [m]	0.902	1.257	1.238
Vehicle diameter [m]	7.469	8.105	5.141
Engine Properties			
Specific Impulse (vac) [s]	387.770	374.982	398.471
Engine thrust (vac) [kN]	186.575	533.972	195.529
Total thrust (vac) [kN]	1119.453	2135.889	977.645
Mass Breakdown			
Dry mass [kg]	21941	22734	21955
Propellant mass [kg]	123084	79027	104003
Payload mass [kg]	1200	1200	1200
GTOW [kg]	**146226**	**102960**	**127158**

As with the baseline scenario, is it interesting to compare the optimum design variables found using the MDO scheme for the Hercules scenario directly to the Hercules vehicle by Komar et. al.[38]. The Hercules vehicle, however, transports 5750 kg of crew and cargo (crew mode) to the orbital node, compared to the 1200 kg in the MDO scenario. Therefore the vehicle GTOWs cannot directly be compared to evaluate the performance of MDO scheme in achieving a lower GTOW mass than the Hercules, however it is valuable to compare the two designs nonetheless. The comparison of the optimum Hercules vehicle found using the MDO to the Hercules by Komar et. al. [38] can be found in Table 8.3. It should be noted that the Hercules vehicle also transfers 4198 kg of propellant to the orbital node once docked.

Table 8.3: The comparison of the Hercules vehicle by Komar et. al. [38] and the vehicle found using the MDO

Mass [kg]	**MDO Vehicle**	**Hercules**
Dry	22734	18898
Ascent propellant	70229	114806
Landing propellant	4745	6462
Other propellant	4052	7163
Margins	0	5542
Payload	1200	5750
GTOW	**102960**	**162819**

As can be seen from Table 8.3, the MDO vehicle has a GTOW that is substantially less than that of the Hercules vehicle, with mass reductions of 60,000 kg, which is more than half the GTOW of the MDO vehicle. These differences all lie in the differences in propellant masses, as the dry mass of the Hercules vehicle is actually less than that of the MDO vehicle. The main difference is found in the comparison of the ascent propellant masses, however the other propellant masses are also less for the MDO vehicle, due to its smaller GTOW. The Hercules vehicle reaches the target phasing orbit with a higher mass than the MDO vehicle, therefore the propellant mass expended for the transfer, docking, and entry manoeuvres is also larger for the Hercules. The effects of a higher GTOW therefore are compounded to influence all the propellant masses throughout the mission, inducing a snowball effect.

The snowball effect is also induced by the payload mass of the Hercules vehicle, as it is also almost five times greater than that of the MDO vehicle. This undoubtedly introduces a much higher necessary propellant consumption throughout all phases of the mission. The payload mass not only affects the ascent, but also the landing as the payload contributes to a greater percentage of the landing mass than during the ascent. Although the contributions of the extra payload mass and the performance of the optimiser to the GTOW cannot directly be quantified, it is interesting to further compare the designs of the two vehicles.

Figures 8.17 and 8.18 show the design variables found for the 10 optima using the MDO scheme, with the Hercules values determined by Komar et. al. [38] shown in red. Note that the pitch angles and entry initial condition angles cannot be compared, as they are not provided by Komar et. al..

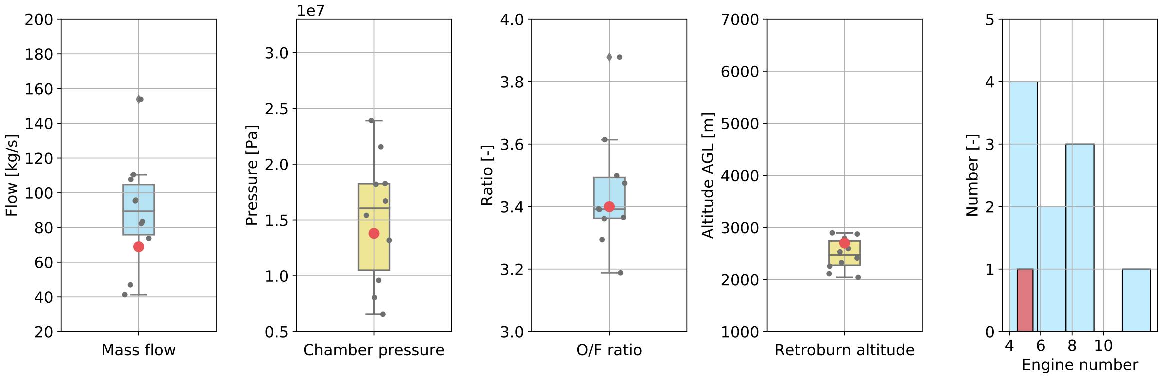

Figure 8.17: (Left to right) The minimum and maximum TW ratios, the exhaust and vehicle diameters, and the ascent and landing propellant masses for the MDO simulation for the Hercules scenario, with Hercules' variables shown in red.

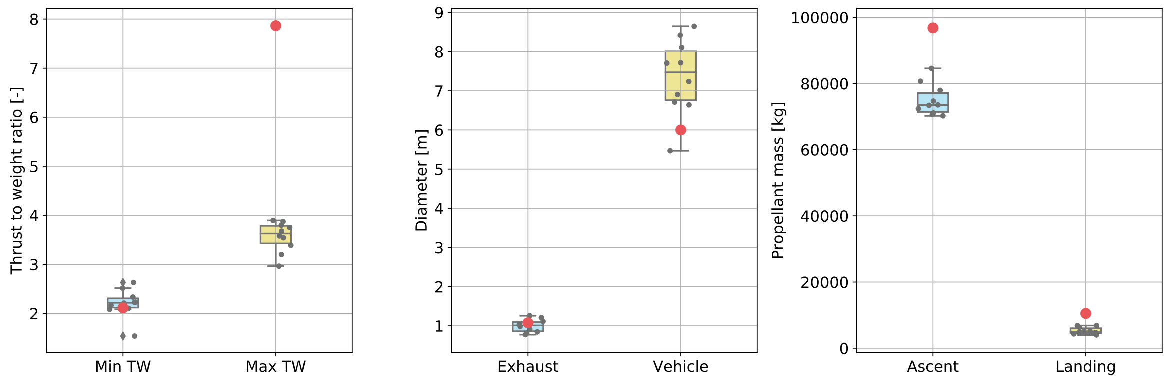

Figure 8.18: (Left to right) The engine mass flow, the engine chamber pressure, the mixture ratio, the retroburn altitude, and the engine number for the MDO simulation for the Hercules scenario, with Hercules' variables shown in red

As can be seen from Figure 8.17, the variables used for the characterisation of the engines are very similar, with very similar values for the mass flow, chamber pressure, and mixture ratio. This is mirrored in the number of engines used by the Hercules, as similar engine properties result in similar engine thrust levels. The retroburn altitude is also very similar, however the Hercules retroburn is higher, mostly likely due to the differences in landing strategy (discussed later in the next paragraph) as well as a higher landing mass.

From Figure 8.18 it is again evident that significant reductions are obtained in both the ascent and landing propellant masses. The differences in landing propellant can be attributed to the higher payload mass for the Hercules vehicle, but differences in landing strategy could also influence the propellant mass. The Hercules vehicle by Komar et. al. switches to different engines used for landing [38] after the initiation of the retroburn, whilst the MDO simulation does not. From the vehicle diameters in the middle figure is it evident that drag losses do not play a dominant role in the design of the vehicle geometry, as the vehicle diameters found by the MDO are mostly wider than the Hercules vehicle. Overall, the MDO shows very promising results for the optimisation of the vehicle with respect to the Hercules mission scenario, however should the two design be directly compared, all other factors such as payload should be held equal.

8.3. Martian Base Location Change

Not only does the target orbit affect the delta-V, but so does the location of the Martian base. A launch latitude that is closer to the equator exploits the higher rotational velocity of the location, therefore requiring less delta-V to reach the desired orbit. The EDL trajectory will also differ due to the different target orbit. In this section, two other Martian Base locations are explored, summarised below. All other parameters remain the same as in the baseline case (see Section 8.1 for details). It should be noted that the trajectory optimisation bounds for the initial latitude and longitude for both cases are also adjusted accordingly.

Latitude at 21.25°:

- **Mars Base:** The Mars base is located at the half the latitude of the baseline, at 21.25° North. The longitude and altitude remain the same, set to 25.5° East and -3700 m, respectively.
- **Target Orbit:** Due to the fact that there is no guidance law implemented in the simulation to be able to perform a dog-leg manoeuvre, the inclination of the target orbit is also set to 21.25°. The target orbit into which the vehicle is injected into is the same circular phasing orbit as the baseline case, at 607.74 km.
- **Rendezvous:** The rendezvous and docking procedure is the same as the baseline, necessitating a delta-V of 45.84 m/s for the Hohmann transfer and 80.4 m/s for the docking phase
- **Entry:** Almost the same entry conditions are taken as the baseline: the reentry is started with an entry burn of 261 m/s, and the atmospheric entry begins at an altitude of 80 km with a velocity of 3500 m/s, however a heading of 68.75° is used

Latitude at 5°:

- **Mars Base:** The Mars base is located on the equator, at 5° North, but the longitude remains the same at 25.5° East, as well as the altitude of -3700 km.
- **Target Orbit:** Due to the fact that there is no guidance law implemented in the simulation to be able to perform a dog-leg manoeuvre, the inclination of the target orbit is also an equatorial orbit at 5°. The target orbit into which the vehicle is injected into is the same circular phasing orbit as the baseline case, at 607.74 km.
- **Rendezvous:** The rendezvous and docking procedure is the same as the baseline, necessitating a delta-V of 45.84 m/s for the Hohmann transfer and 80.4 m/s for the docking phase
- **Entry:** Almost the same entry conditions are taken as the baseline: the reentry is started with an entry burn of 261 m/s, and the atmospheric entry begins at an altitude of 80 km with a velocity of 3500 m/s, however a heading of 85° is used

Three seeds are used to obtain three optimum solutions for the two new Martian base locations. Figure 8.19 shows the GTOW breakdown for the baseline case and both difference Martian base locations.

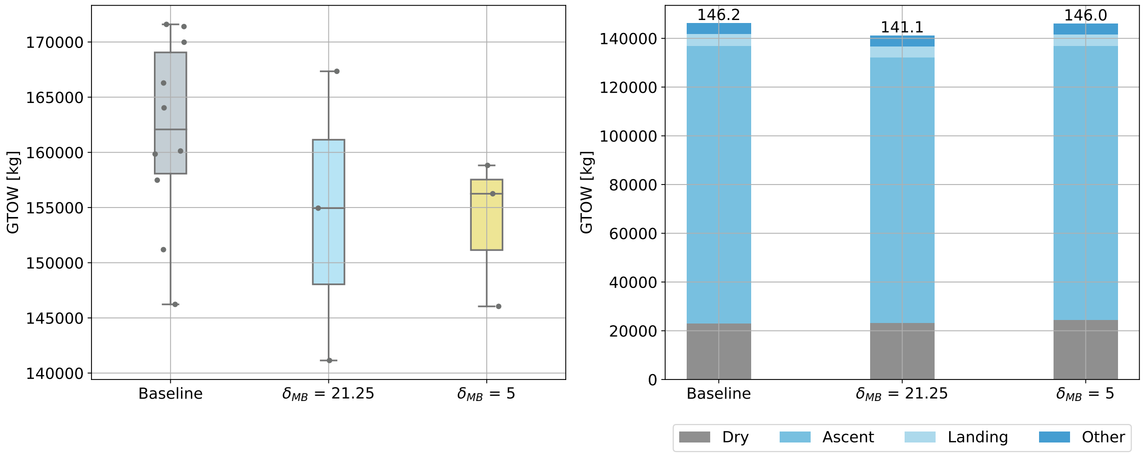

Figure 8.19: The GTOW of all the vehicles found for the for the baseline and the two difference mars base location (left) and the GTOW breakdown of each optimum vehicle's GTOW (right). The values above each case's breakdown in the rightmost figure indicates the GTOW in tonnes.

As can be seen from Figure 8.19, both the average GTOWs and the optimum GTOWs found for the two other latitude locations are less than the baseline, reflecting the expectation that a lower latitude will benefit the reduction of the GTOW. The trend of the GTOW in the box and whisker plots is also that the GTOW decreases with decreasing latitude. However, the optimum GTOW of the 5° latitude case is greater than that of the 21.25° case, at 146.0 tonnes and 141.1 tonnes, respectively. This is contrary to expectations, as the 5° latitude case should benefit more from its location compared to the 21.25° latitude case. The discrepancy between the expected and obtained values, however, may be attributable to the combined effect of a number of factors.

Firstly, the three solutions found per new latitude location, compared to the 10 solutions found for the baseline case, may not portray the behaviour of the latitude locations' GTOW accurately. The latitude location of 21.25° is shown to have a very large range in possible GTOW values, much like the baseline scenario. Should more seeds be run, perhaps it may show the optimum case to be an outlier, much like the optimum GTOW for the baseline case also is an outlier. Conversely, it could also show that the greatest GTOW of the three is an outlier. The portrayal of the behaviour may therefore be influenced by the number of seeds run. Furthermore, the difference in rotational velocity at the launch location between the baseline case and the 21.25° case is three times greater than between the 21.25° case and the 5° case, the differences in velocity equating to 47 m/s and 15 m/s, respectively. The reduction in GTOW of the 21.25° case compared to the baseline case should therefore be greater than the reduction of the GTOW of the 5° case compared to the 21.25° case.

Of course, the GTOW has not been reduced for the 5° case compared to the 21.25° case, however the combination of the low number of seeds, combined with the differences in relative rotational velocity, may lead to very similar outcomes for the 21.25° and 5° cases. This is reflected in the results, as although the optimum GTOW of the 21.25° case is 5 tonnes less than that of the 5° case, their averages are much closer in value. Perhaps if more seeds are run, the behaviour may be more accurately observed.

To understand the influence of the latitude on the trajectories, figures 8.20 and 8.21 show the ascent profiles, TW ratios, and airspeed profiles for all three cases.

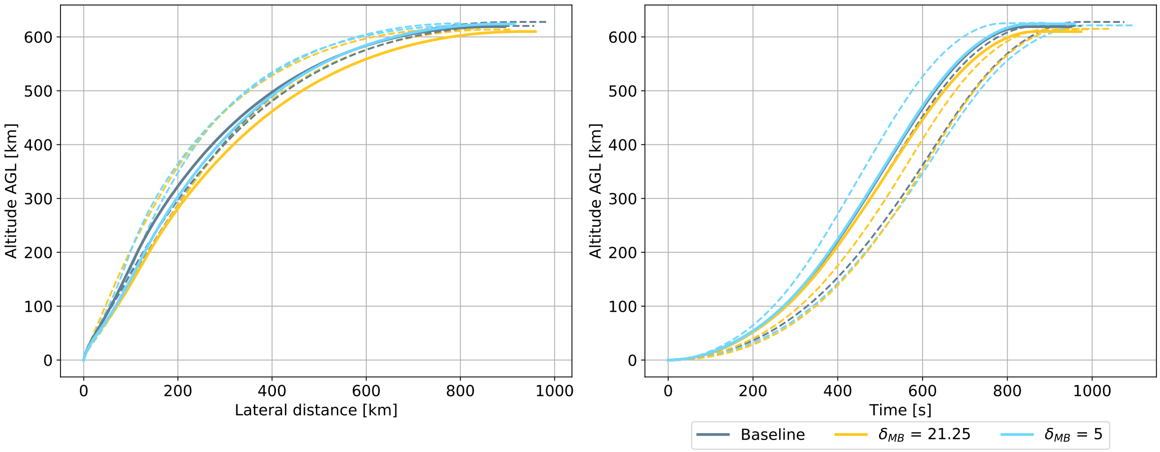

Figure 8.20: The MDO ascent profiles for the three best performing individuals in the baseline scenarios and all three seeds of both different Martian base locations

As can be seen from Figure 8.20 on the left, all ascent profiles for the optimum cases are very similar, however for all cases, the 21.25° latitude and 5° latitude cases have steeper ascent profiles as well as faster ascents than the baseline case. This indicates that the addition of the planet's rotational velocity can affect the ascent such that both its profile and ascent time are decreased, thereby reducing the ascent propellant mass. However, this trend is not replicated by all seeds, indicating that although the solutions may benefit from the added rotational velocity, the final GTOW solutions are more sensitive to other design variables and factors.

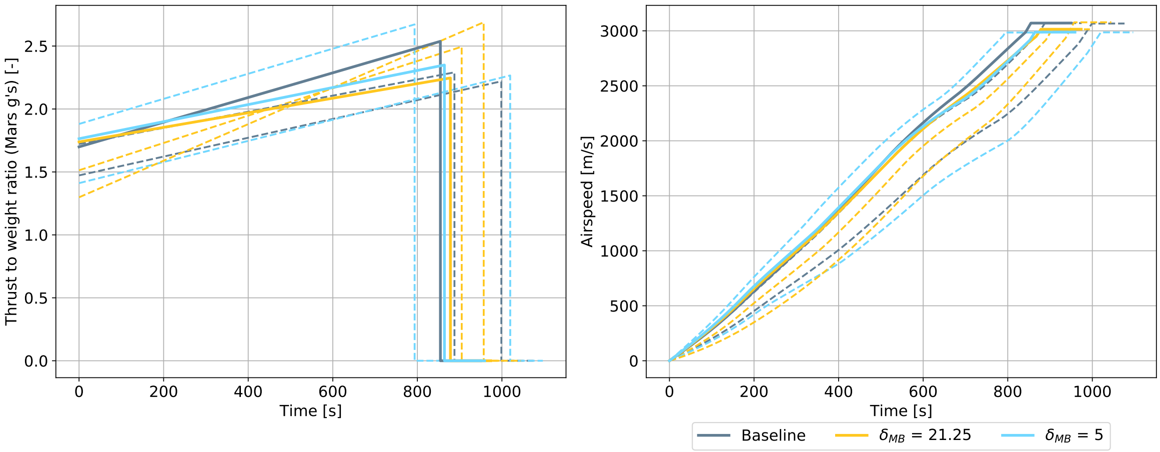

Figure 8.21: The MDO TW ratios (left) and altitude as a function of time (right) for the three best performing individuals in the baseline scenario and all three seeds of both different Martian base locations

This can also be seen in Figure 8.21 in the rightmost figure, where the 5° case has both the steepest and the least steep airspeed profiles. In both figures, there is no clear pattern that indicates the influence of the change of latitude. Therefore although the latitude location may benefit the vehicle, many other influential factors, if not optimised effectively, could potentially erase the advantage of the additional rotational velocity. Figures 8.22 and 8.23 show the EDL profiles and entry corridors for the baseline scenario and the Martian base locations.

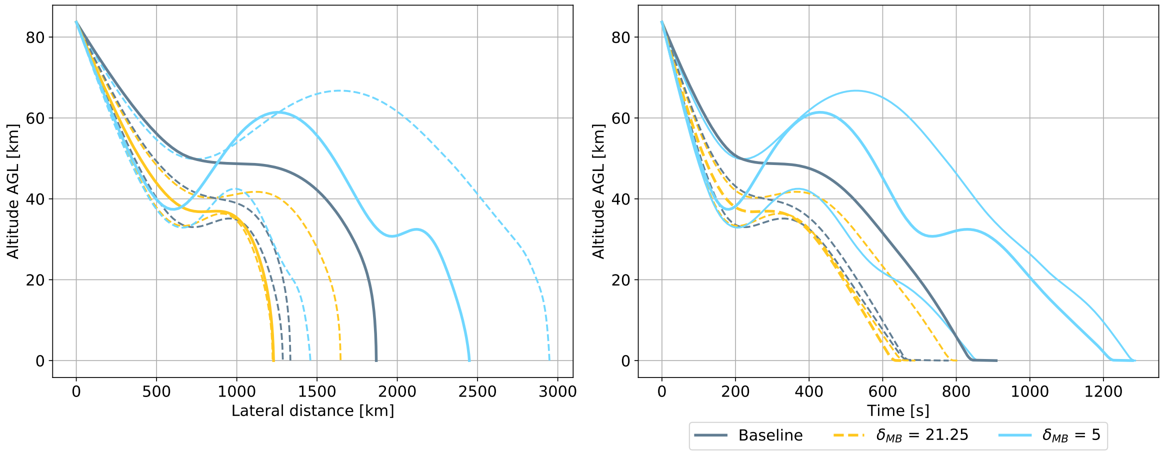

Figure 8.22: The MDO EDL profiles for the three best performing individuals in the baseline scenario and all three seeds of the Martian base locations

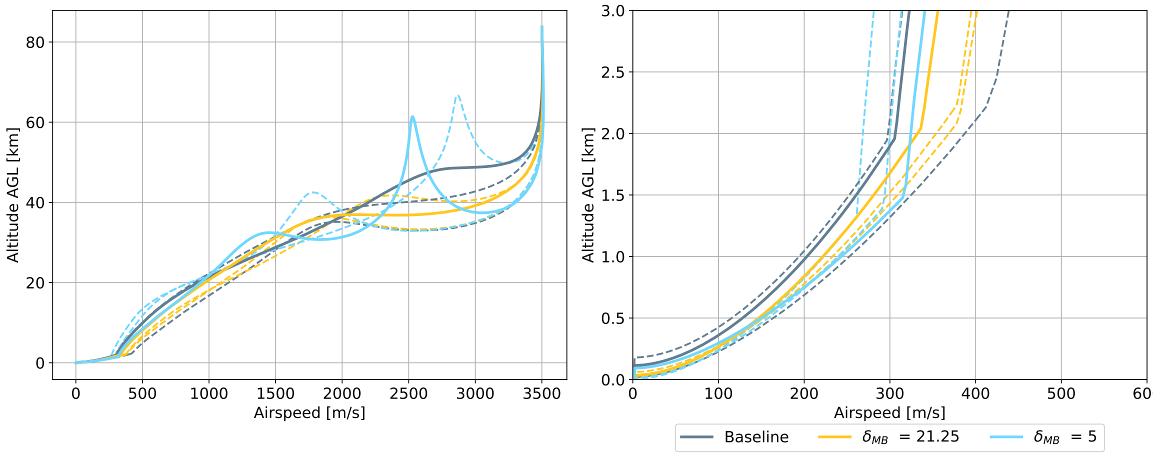

Figure 8.23: The MDO entry corridors for the three best performing individuals in the baseline scenario and all three seeds of the Martian base locations

What is immediately clear from Figures 8.22 and 8.23 is that the 5° Martian base location's solutions experience skipping entry. As no guidance law is implemented to ensure that the flight path angle remains constant during entry, if no banking is implemented, all of the generated lift is in the vehicle's negative z-axis direction (upward). This causes the forces in the upward direction to be greater than in the downward direction, and thus the vehicle skips, which can be seen from the oscillating altitudes in both Figures 8.22 and 8.23. The solutions for the baseline and for latitude 21.25° do not experience skipping.

Figure 8.24 best demonstrates the reasoning for the skipping phenomenon. As can be seen, the vehicle that lands at the Martian base located at 5° latitude implements only momentary bank angle guidance. At the equator, there is less Coriolis force acting upon the vehicle, such that less bank angle manoeuvres are necessary to stay on the correct bearing angle. The solutions pertaining to the other two locations, however, implement the maximum bank angle to counteract the Coriolis forces that 'push' the vehicles toward the equator.

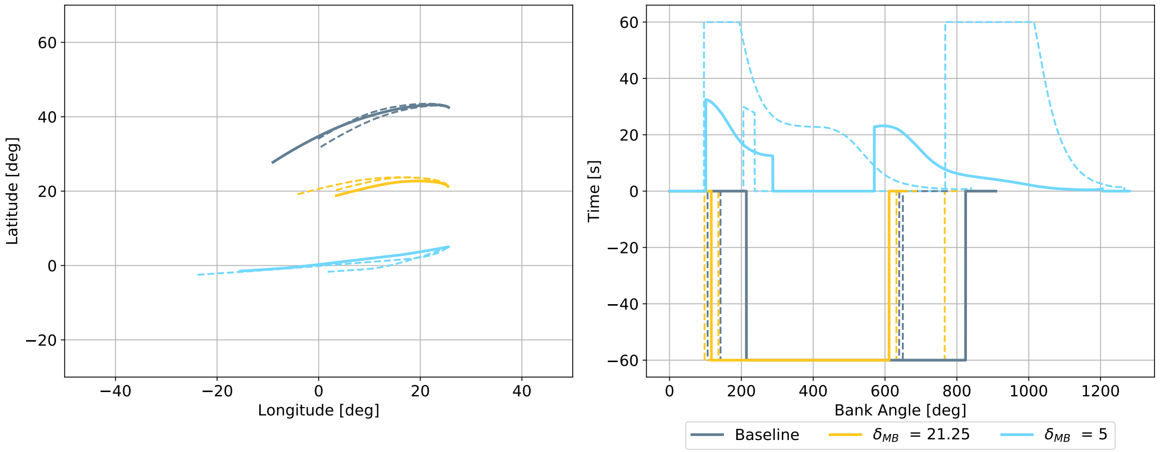

Figure 8.24: The vehicles' bank angles and their flight path over the course of the EDL phase

Table 8.4 presents the design variables, engine properties, and mass breakdown for the optimum solutions of all three Martian base locations. The results of all seeds for both changes in Martian base latitudes can be found in Appendix C.3. Overall, the reduction of latitude location is shown to affect reduce the GTOW.

Table 8.4: The optimum vehicle for all three Martian base location cases

Design Variables	**Baseline**	**Latitude 21.25°**	**Latitude 5°**
Optimum Trajectory Design Variables			
Node 1 [deg]	86.205	85.001	85.000
Node 2 [deg]	58.012	51.927	52.754
Node 3 [deg]	63.165	58.872	61.726
Node 4 [deg]	42.330	39.332	41.929
Node 5 [deg]	13.578	12.173	12.046
Node 6 [deg]	-8.522	-8.437	-7.677
Min TW [-]	1.701	1.735	1.759
Max TW [-]	2.525	2.236	2.336
Entry γ [deg]	-3.620	-5.360	-5.991
Entry δ [deg]	27.755	18.796	-1.504
Entry τ [deg]	-9.011	3.473	-15.415
Entry α	57.292	56.324	37.419
Retroburn altitude [m]	2125	2247	1617
Optimum Vehicle Design Variables			
Mass flow [kg/s]	51.974	43.174	64.684
Chamber pressure [Pa]	18110229	11604035	23016839
O/F ratio [-]	3.618	3.505	3.793
Engine number [-]	6	8	8
Ascent propellant [kg]	113905	108929	112650
Landing propellant [kg]	4754	4581	4546
Exhaust diameter [m]	0.902	0.836	0.830
Vehicle diameter [m]	7.469	6.858	7.052
Engine Properties			
Specific impulse (vac) [s]	387.770	385.092	389.759
Engine thrust (vac) [kN]	186.575	153.914	233.392
Total thrust (vac) [kN]	1119.453	1231.312	1867.139
Mass Breakdown			
Dry mass [kg]	21941	22044	23331
Propellant mass [kg]	123084	117899	22131
Payload mass [kg]	1200	1200	1200
GTOW [kg]	**146226**	**141143**	**146044**

8.4. Payload Change

To determine how the mass of the payload affects the optimal solutions, the optimal vehicle and associated trajectories are determined for two different payload cases. These are -50% and +50%, leading to payload masses of 600 kg and 1800 kg, respectively. All other parameters remain the same as the baseline case, see Section 8.1 for the details. Three seeds are used to obtain three optimum vehicles and respective trajectories for both payload cases. Figure 8.25 shows the GTOW breakdown of all three scenarios.

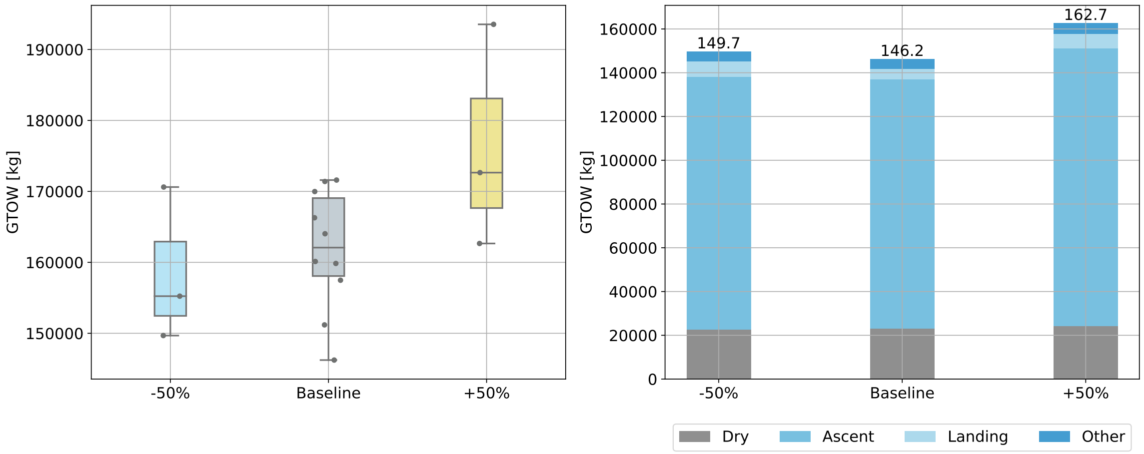

Figure 8.25: The GTOW of all the vehicles for each payload case (left) and the GTOW breakdown of each optimum vehicle's mass (right). The values above each seed's breakdown in the rightmost figure indicates the GTOW in tonnes

As is immediately clear, the payload mass has a direct effect on the vehicles's GTOW, as the -50% payload case results in a lower average GTOW, and the +50% case results in a higher average GTOW. The optimum baseline case's GTOW is lower than that of the optimal -50% case, at 146.2 tonnes and 149.7 tonnes, respectively, however this can be attributed to the number of simulations performed. Although the optimum baseline case's GTOW is lower, it can be seen from the leftmost figure in Figure 8.25 that it is an outlier, and that the mean GTOW of the baseline case lies higher than that of the -50% case. With a higher number of simulations there is a higher chance that a more optimum solution is found.

The trajectories of the best three performing individuals from the baseline case and all three seeds of payload cases are plotted to compare. Figures 8.13 and 8.14 show the ascent phase for all three cases, where the solid line represents the associated scenario's optimum case, and the dashed lines represents the other two solutions for that case.

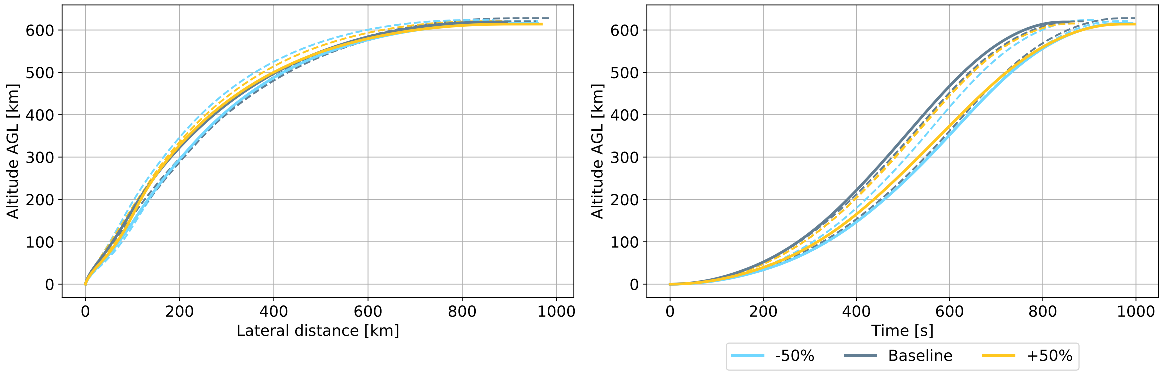

Figure 8.26: The MDO ascent profiles for the three best performing individuals in the baseline scenarios and all three seeds of the payload cases

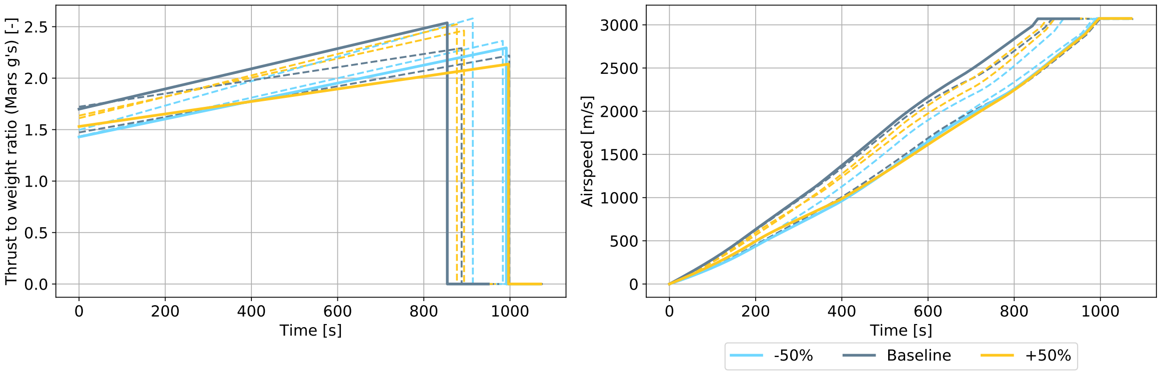

Figure 8.27: The MDO TW ratios (left) and altitude as a function of time (right) for the three best performing individuals in the baseline scenario and all three seeds of the payload cases

From the leftmost figure in Figure 8.26 it is clear that all profiles are very similar, which is to be expected as the initial conditions and target orbit are held equal, and convergence toward a common trajectory is expected. In the rightmost figure, it can be seen that the baseline case is the fastest to reach the target altitude of 607 km. This was shown to have a positive effect on the GTOW reduction in Section 8.1, and is therefore consistent with it being the optimal solution of all the cases.

The same can be seen from the TW ratios seen in Figure 8.27. All minimum and maximum TW ratios remaining similar to the baseline case. The baseline case's high minimum and maximum TW ratios leads to the baseline case also been the fastest to reach the orbital injection speed, as seen in the rightmost figure in Figure 8.27. However, there are no differences between the behaviour of individual payload cases as a whole, and so the differences in ascent trajectories are attributed to the seed usage as opposed to the payload masses themselves. Figures 8.28 and 8.29 show the EDL trajectories for the best performing 3 baseline scenarios, and all 3 seeds for the payload cases.

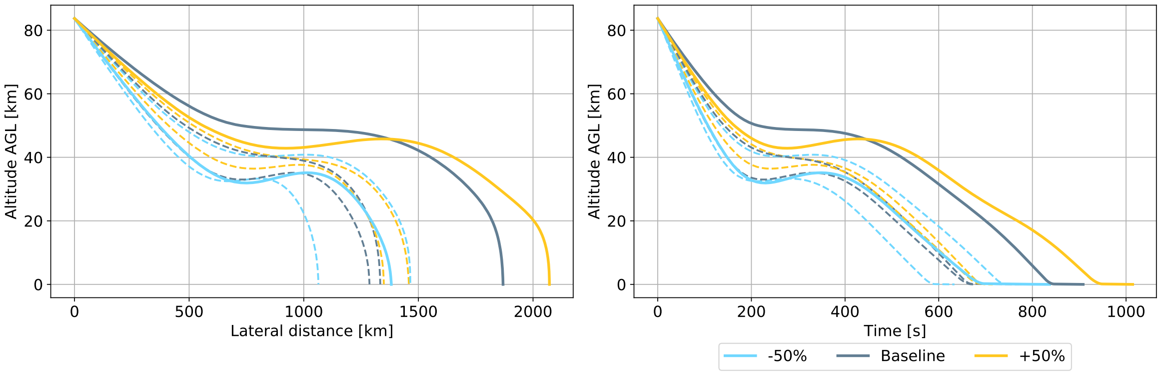

Figure 8.28: The MDO EDL profiles for the three best performing individuals in the baseline scenarios and all three seeds of the payload cases

What is interesting to see from Figure 8.28 is that the -50% has a much shorter time of flight compared to the baseline and the +50% case, due to its much faster descent. The optimum solution for the +50% payload case has the longest time of flight. As the payload mass remains the same for the EDL as during the ascent, it contributes to a greater percentage of the vehicle mass during the EDL phase than during the ascent phase. The -50% case therefore requires less thrust to decelerate the vehicle before landing due to its lower mass. Likewise, the +50% case has the longest time of flight to reduce its velocity the most before the retroburn, such that less landing propellant is needed to decelerate.

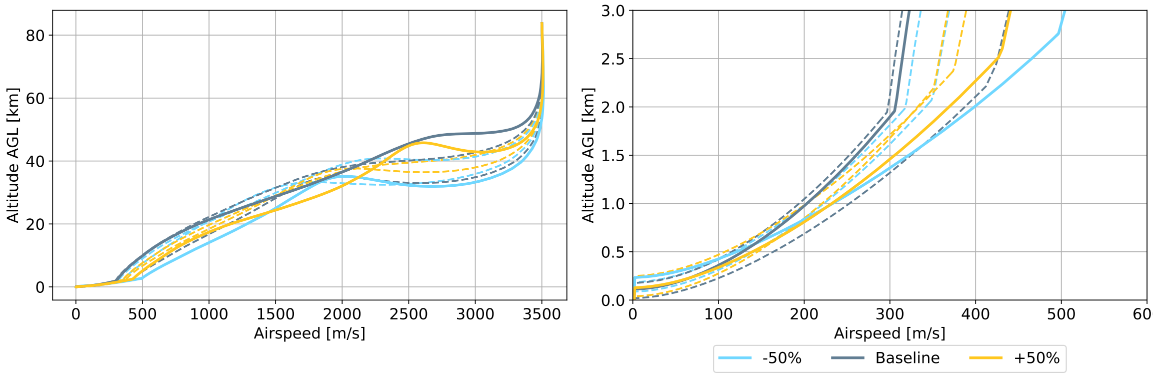

Figure 8.29: The MDO entry corridors for the three best performing individuals in the baseline scenario and all three seeds of the payload cases

In Figure 8.29 these differences can be seen, as the optimum -50% case descends the fastest, and initiates the retroburn with the highest velocity. However, the high velocity is not as detrimental to the landing propellant consumption due to its lower vehicle mass.

Table 8.5 presents the design variables, engine properties, and mass breakdown for the optimum solutions of all three payload cases. The results of all seeds for both payload cases can be found in Appendix C.4. As can be seen in Table 8.5, the pitch angles are all very similar, resulting in the very similar ascent profiles seen in Figure 8.26. However, the -50% payload case is designed for a lower total thrust compared, and the +50% is designed for a higher total thrust than the baseline. The baseline vehicle is designed for 1119 kN, the -50% payload only for 847 kN, and the +50% for 1156 kN, indicating that the payload directly influences the engine design as well as the GTOW as a whole.

Table 8.5: The optimum vehicle for all three payload cases

Design Variables	**Baseline**	**PL -50%**	**PL +50%**
Optimum Trajectory Design Variables			
Node 1 [deg]	86.205	85.008	85.309
Node 2 [deg]	58.012	54.150	53.671
Node 3 [deg]	63.165	61.622	68.056
Node 4 [deg]	42.330	47.855	43.871
Node 5 [deg]	13.578	14.625	13.341
Node 6 [deg]	-8.522	-6.899	-6.403
Min TW [-]	1.701	1.431	1.532
Max TW [-]	2.525	2.270	2.117
Entry γ [deg]	-3.620	-5.515	-4.028
Entry δ [deg]	27.755	33.697	30.406
Entry τ [deg]	-9.011	-2.193	-15.875
Entry α [deg]	57.292	35.682	42.796
Retroburn altitude [m]	2125	2749	2632
Optimum Vehicle Design Variables			
Mass flow [kg/s]	51.974	25.206	35.711
Chamber pressure [Pa]	18110229	16326220	7220105
O/F ratio [-]	3.618	3.607	3.643
Engine number [-]	6	9	9
Ascent propellant [kg]	113905	115707	12709
Landing propellant [kg]	4754	6948	6581
Exhaust diameter [m]	0.902	1.071	1.244
Vehicle diameter [m]	7.469	6.457	5.978
Engine Properties			
Specific impulse (vac) [s]	387.770	403.098	388.565
Engine thrust (vac) [kN]	186.575	94.061	128.455

Total thrust (vac) [kN]	1119.453	846.553	1156.099
Mass Breakdown			
Dry mass [kg]	21941	21328	22902
Propellant mass [kg]	123084	127153	138557
Payload mass [kg]	1200	1200	1200
GTOW [kg]	**146226**	**149681**	**162659**

8.5. Crewed vs Uncrewed Case

The fact that the vehicle is crewed leads to tighter constraints when considering the maximum load that the vehicle is allowed to experience. Here, the 4 g_{mars} constraint is lifted, to determine the effects that this constraint has on the optimal vehicle and its trajectory. The constraint is lifted to 10 g_{mars}, which is well within the limits that are typically set for launch vehicles. A maximum load limit of 10 g_{earth} is set by van Kesteren [34], Haex [23], and Rozemeijer [58], which equates to 26 g_{mars}. Three seeds are used to obtain three optimum vehicles and respectively trajectories for a maximum load of 10 g_{mars}. Figure 8.30 presents the GTOW breakdown for both maximum g-load thrust cases.

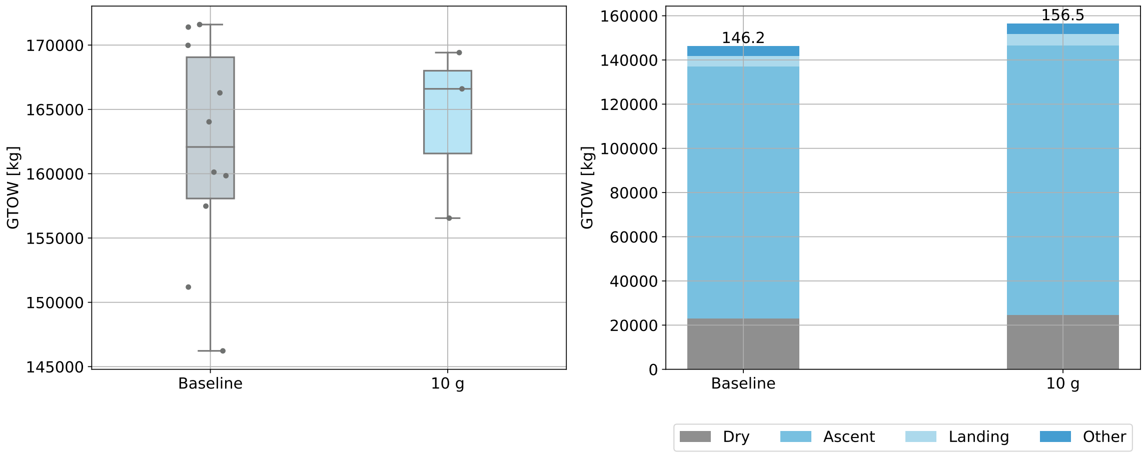

Figure 8.30: The GTOW of all the vehicles for the baseline and the 10 g max load case (left) and the GTOW breakdown of each optimum vehicle's GTOW (right). The values about each case's breakdown in the rightmost figure indicates the GTOW in tonnes.

As can be seen from the leftmost figure in Figure 8.30, the 10 g load case does not offer any reductions in GTOW, with all GTOW values remaining within the same range for the 10 g case as those of the baseline case. From the rightmost figure it is evident that the ascent propellant for the 10 g load case is greater than that of the baseline case. Furthermore, the landing propellant of the 10 g load case is greater than that of the baseline case. This can more clearly be seen in Figure 8.31.

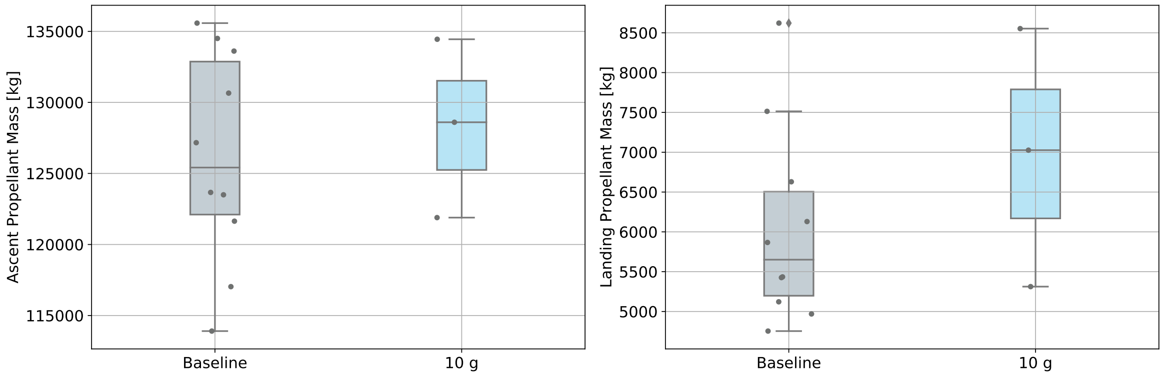

Figure 8.31: The ascent propellant (left) and the landing propallant (right) of all the vehicles for the baseline and the 10 g max load case

As can be seen in Figure 8.31, the range of the ascent propellant mass for the 10 g load case is very similar to the that for the baseline case, with the baseline case yielding a few solutions with significant reductions compared to the 10 g load case. That the ascent propellant masses remain unchanged when lifting the 4 g limit is expected, as the baseline cases (Section 8.1) show that a maximum TW ratio greater than 3 is not necessary. Therefore allowing a maximum TW ratio greater than 4 does not offer any reductions in ascent propellant. The landing propellant masses, however, are on average greater for the 10 g load cases than those for the baseline cases. This is contrary to the expected results, as a higher allowable thrust for the retroburn leads to a more efficient propellant usage. To understand this contrast, the EDL phase is plotted in Figures 8.32 and 8.33.

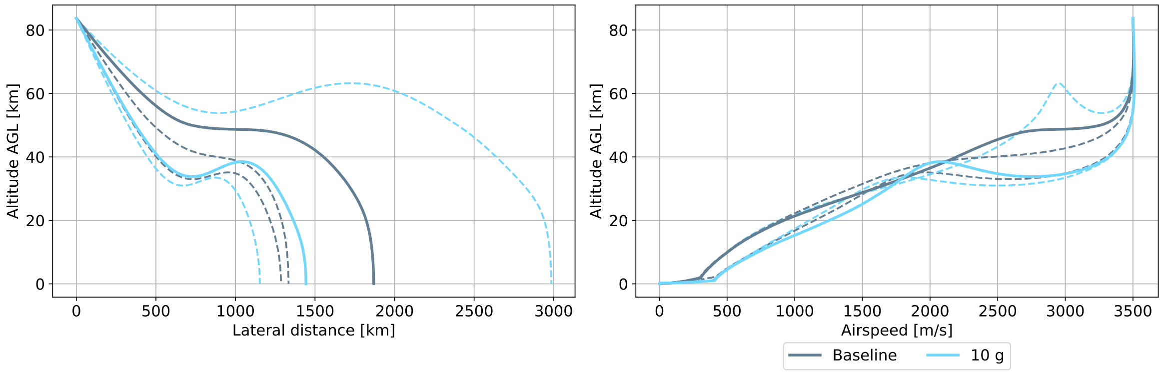

Figure 8.32: The EDL profile (left) and the entry corridor (right) for the baseline and 10 g load cases

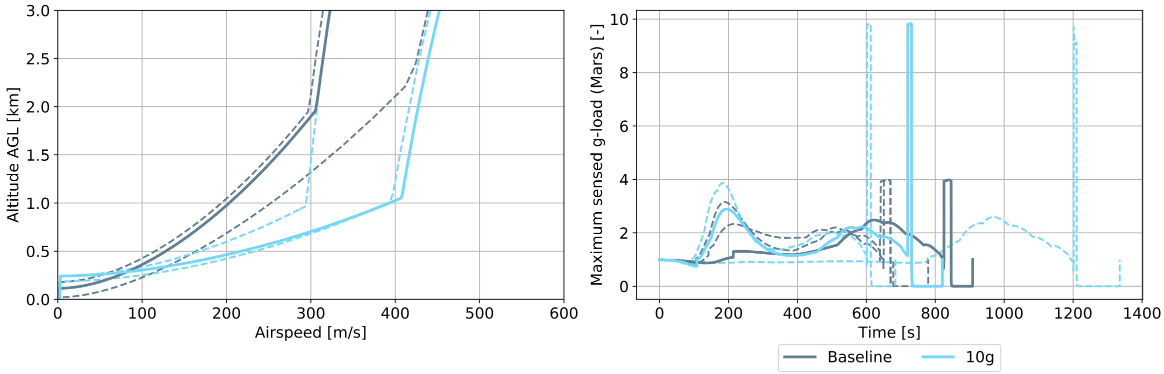

Figure 8.33: The landing phase (left) and the total sensed acceleration (right) of the baseline and the 10 g load cases

As can be seen from the both figures in Figure 8.32, the optimum 10 g load case descends faster than the optimum of the baseline case. This leads to a higher velocity when the retroburn is initiated, as can be seen from the rightmost figure in Figure 8.32. In Figure 8.33 on the left, the retroburn is plotted in more detail. The propulsive landings, due to the higher thrust, are a lot shorter in duration, as can be seen in the rightmost figure in Figure 8.33, and due to the higher allowable TW ratio, the vehicles for the 10 g load case are able to initiate their retroburns at higher velocities as well as lower altitudes whilst still landing within the determined constraints. These differences are significant, with the velocities before retroburn being up to 100 m/s higher than the baselines', and the altitudes up to 1 km lower.

This is the reason that the landing propellant mass is higher for the 10 g load case than the baseline cases. Higher available thrust during a retroburn is more efficient in terms of propellant consumption only if the same trajectory is maintained. However, due to the lower altitude and higher velocity at the start of the retroburns for the 10 g load cases, the increase in TW ratio does not result in a decrease in propellant. As discussed throughout this chapter, the bottleneck when reducing the GTOW of the vehicle is the reduction of the ascent propellant consumption, which is the component of the GTOW. The ascent is therefore the focus of the optimiser, as optimising the landing phase leads to comparatively smaller reductions in GTOW. This, in combination with the vehicles for the 10 g load cases being able to land within the identified constraints with more ease than the baseline, leads to less efficient EDL phases for the 10 g load cases when compared to the baseline cases. The increase in landing propellant for the 10 g load cases are a result, therefore, of the optimiser itself, and not due to a higher maximum load being inherently less efficient.

As the baseline cases showed that a higher TW ratio than 3 is unnecessary, large deviations in ascent trajectory for the 10 g cases from the baseline cases are not expected. Figures 8.34 and 8.35 show the ascent profiles, TW ratios and dynamic pressures for the baseline and 10 g load cases.

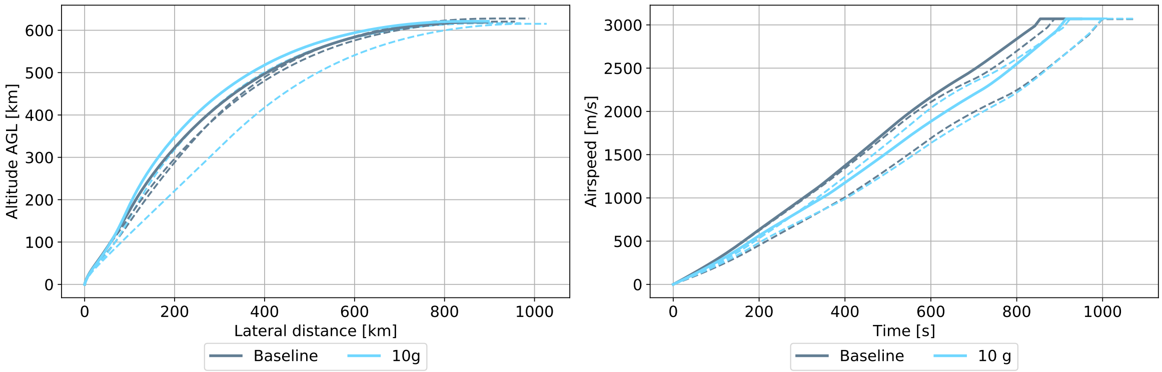

Figure 8.34: The EDL profile (left) and the entry corridor (right) for the baseline and 10 g load cases

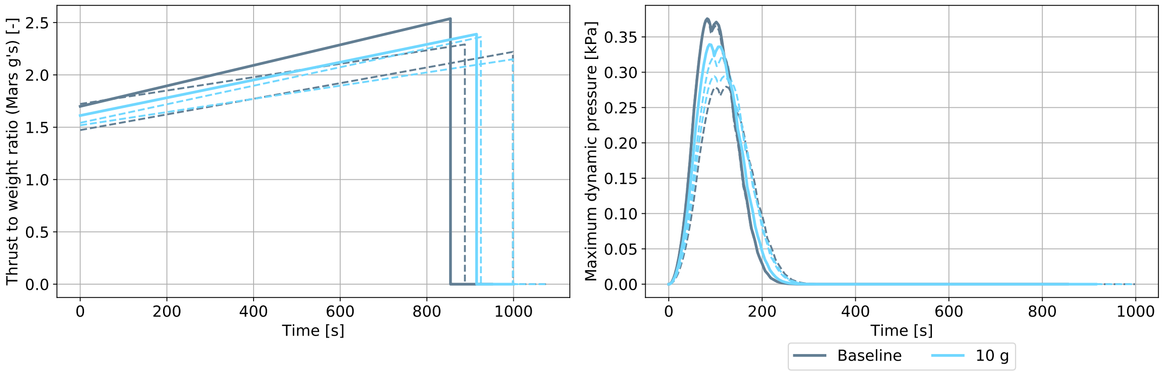

Figure 8.35: The landing phase (left) and the total sensed acceleration (right) of the baseline and the 10 g load cases

As expected, all the profiles are very similar, as seen in Figure 8.34. Again, for both cases the trajectory that ascends to the target altitude is the most optimum, as the gravity losses are reduced. In Figure 8.35 the leftmost figure shows that all minimum and maximum TW ratios lie at approximately the same values for both the baseline and 10 g load cases. The solutions with the highest minimum and maximum TW ratios are the optimum solutions, to be able to minimise the gravity losses and therefore reduce the ascent propellant masses. The maximum dynamic pressure for the optimum solutions is therefore also the highest for their respective cases, as seen in the rightmost figure in Figure 8.35.

Lastly, the design variables, engine properties, and mass breakdown for the optimum solutions of the baseline case and the 10 g load case are given in Table 8.6. The results of all seeds for the 10 g load case can be found in Appendix C.5. As can be seen, the retroburn altitude for the 10 g case, 1086 m, is half that of of the baseline case, 2125 m. This was, of course, seen in Figure 8.33. What is also interesting is that the 10 g case is designed for a total thrust almost double that of the baseline case, namely 1967 kN compared to 1119 kN. This higher thrust is produced by a greater engine number and mass flow. This higher thrust is not necessary for the ascent, however they may be sized for the propulsive landing.

Table 8.6: The optimum solutions for both load cases

Design Variable	**Baseline**	**10 g**
Optimum Trajectory Design Variables		
Node 1 [deg]	86.205	85.718
Node 2 [deg]	58.012	57.421
Node 3 [deg]	63.165	68.343
Node 4 [deg]	42.330	44.472
Node 5 [deg]	13.578	13.496
Node 6 [deg]	-8.522	-7.072
Min TW [-]	1.701	1.613
Max TW [-]	2.525	2.371
Entry γ [deg]	-3.620	-5.488
Entry δ [deg]	27.755	34.055
Entry τ [deg]	-9.011	-3.873
Entry α	57.292	39.458
Retroburn altitude [m]	2125	1086
Optimum Vehicle Design Variables		
Mass flow [kg/s]	51.974	60.313
Chamber pressure [Pa]	18110229	14813268
O/F ratio [-]	3.618	3.850
Engine number [-]	6	9
Ascent propellant [kg]	113905	121892
Landing propellant [kg]	4754	5312
Exhaust diameter [m]	0.902	1.063
Vehicle diameter [m]	7.469	6.185
Engine Properties		
Specific impulse (vac) [s]	387.770	391.403
Engine thrust (vac) [kN]	186.575	218.538
Total thrust (vac) [kN]	1119.453	1966.850
Mass Breakdown		
Dry mass [kg]	21941	21328
Propellant mass [kg]	123084	131919
Payload mass [kg]	1200	1200
GTOW [kg]	**146226**	**156546**

8.6. Thrust Law Change

As the ascent propellant consumption is the dominant factor of the GTOW, the effect of changes in thrust law on the optimum solution is explored. The thrust laws are thrust law 0 (constant TW ratio) and thrust law 2 (quadratic TW ratio profile). More information regarding these laws can be found in Section 6.4.3. All other parameters remain the same as the baseline case, see Section 8.1 for details. Three seeds are used to obtain three optimum vehicles and respectively trajectories for both thrust law cases. Figure 8.36 presents the GTOW breakdown for all three thrust law cases.

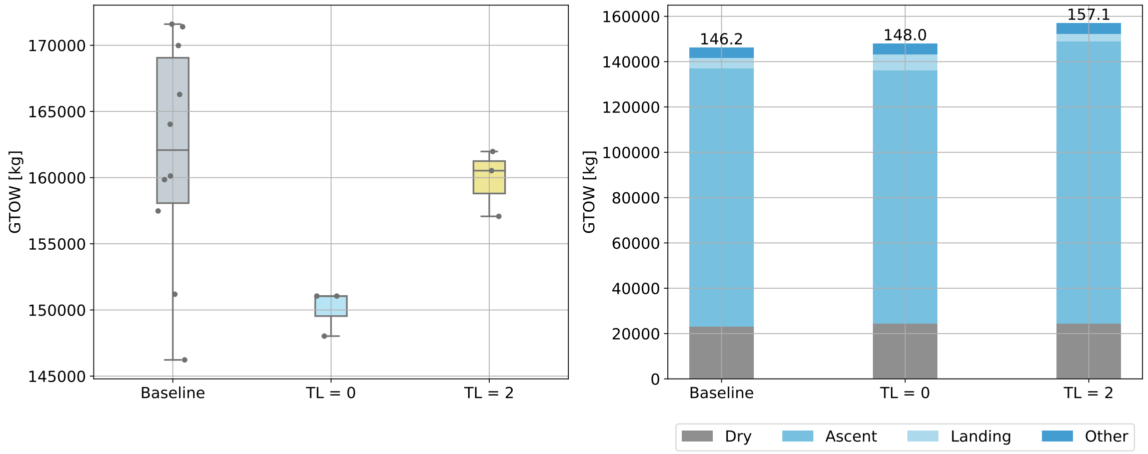

Figure 8.36: The GTOW of al the vehicles for each thrust law case (left) and the GTOW breakdown of each optimum vehicle's mass (right). The values above each seed's breakdown in the rightmost figure indicates the GTOW in tonnes

As can be seen from the leftmost figure in Figure 8.36, thrust law 0 performs very well, with all GTOW values converging to a value under 152 tonnes. Although the optimum vehicle in the baseline scenario has a lower GTOW value, this seed is an outlier, as most values lie between approximately 157 and 167 tonnes. The thrust law 2 cases also converge values within 5000 kg of each other, however they are around the same range as the mean baseline cases. In the rightmost figure it can be seen that, again, the reduction in GTOW stems from a reduction in ascent propellant mass. Although the baseline case has a lower GTOW than that of the thrust law 0, the ascent propellant mass of the thrust law 0 case is lower than that of the baseline case. The ascent propellant masses, engine thrust, and total thrust values are compared in Figure 8.37.

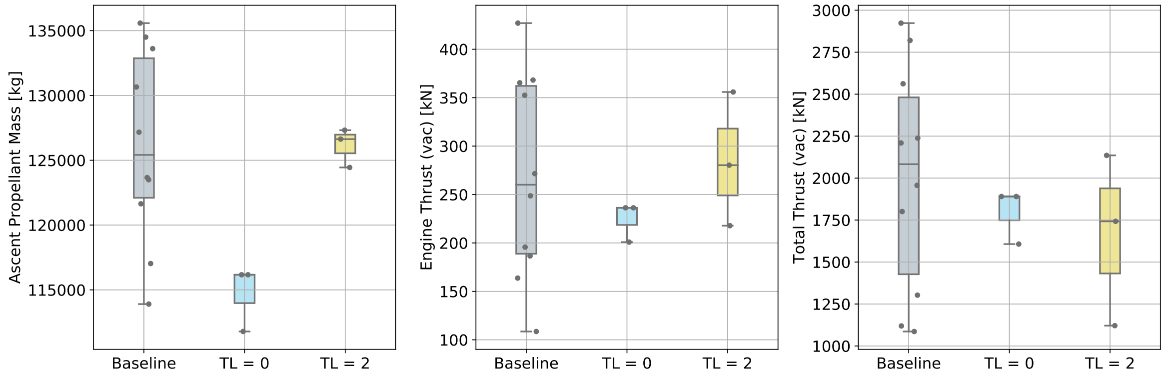

Figure 8.37: The ascent and landing propellant masses for all three thrust law cases

As can be seen in Figure 8.37 in the leftmost figure, the average ascent propellant masses of the thrust law 0 case lie much lower than those of both the baseline and the thrust law 2 cases. This reduction, however, does not seem to stem from a difference in engine capabilities, as the average of the engine thrust (as seen in the middle figure) and the total thrust (rightmost figure) of all three cases are similar. What is interesting to see, however, is that though the baseline and thrust law 2 cases both have a large range in engine and total thrust values, the thrust law 0 case converges to a much smaller region of values. This convergence is also seen when comparing the engine design variables, as given in Figure 8.38.

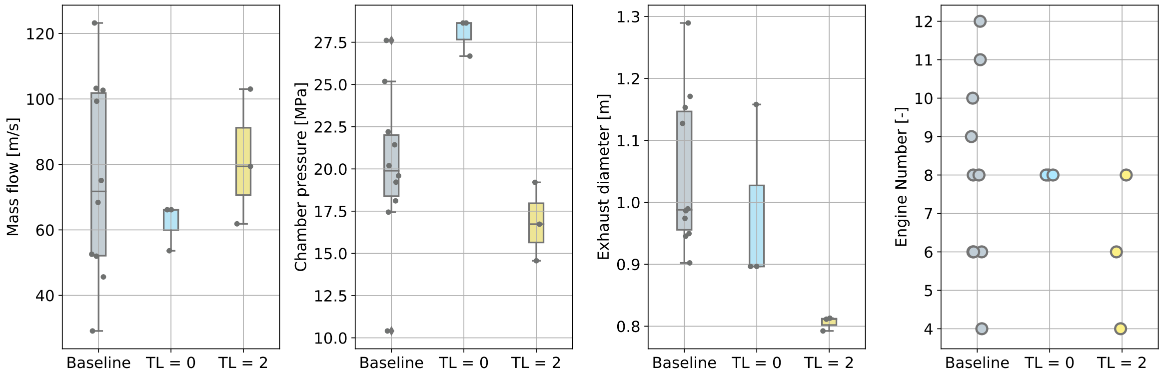

Figure 8.38: (Left to right) The engine mass flow, chamber pressure, exhaust diameter, and engine number for all three thrust law cases

As can be seen from the figures in Figure 8.38, the thrust law 0 case values converge to much smaller ranges than those of the baseline cases, with the exception of exhaust diameter. These smaller ranges therefore lead to engine thrust performances that are very similar, as seen in Figure 8.37. The rightmost figure in Figure 8.38 shows that each thrust law 0 solution also uses an engine number of 8, leading to similar total thrust levels for each thrust law 0 solution.

The reason for the convergence of the thrust law 0 cases' parameters and performance can be found in the optimum TW ratios obtained for the thrust law 0 case. This can be seen in Figure 8.39, where the optimum TW ratio for thrust law 0 is clearly within a small margin, leading to the small margin of necessary engine performance, and therefore engine parameters. Conversely, the minimum and maximum TW ratios for the baseline and thrust law 2 cases vary much more, and there is therefore less convergent behaviour for the engine parameters, and consequently also on performance. The result of a constant TW ratio for thrust law case 0 can be seen in the rightmost figure on Figure 8.39, as the dynamic pressure for thrust law 0 case is almost twice that of the baseline and thrust law 2 case at the start of the ascent. The higher TW ratios accelerate the vehicles to higher velocities that those using the linear and polynominal thrust laws.

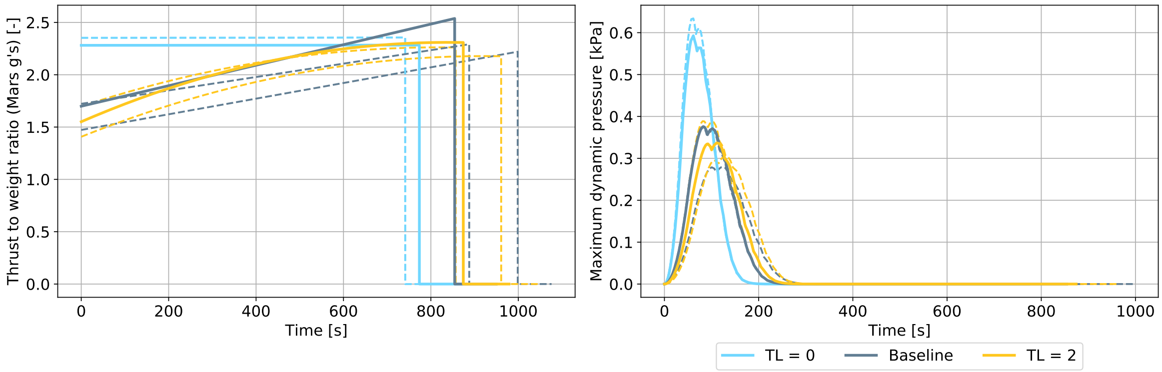

Figure 8.39: The TW ratio's (left) and the maximum dynamic pressure (right) for each thrust case

Figure 8.40 shows the ascent profiles for all three thrust law cases. The higher thrust values due to the higher TW ratio for thrust law case 0 leads to the vehicles gaining velocity at a much faster rate than the other two cases. In the leftmost graph, the ascent profile also shows the thrust law 0 case gaining altitude at a much faster pace, due to the higher velocity and different optimum pitch angles. Although the higher velocities induce a higher drag component, it reduces the time of flight which in turn decreases the gravity loss. As discussed in Section 8.1 for the baseline case, the reduction of gravity losses is prioritised, as this reduces the propellant mass. For all three cases, the optimum vehicle for its respective case is the vehicle that attains the target velocity the fastest, thereby supporting the observation that gravity losses are the main source of delta-V losses during the ascent.

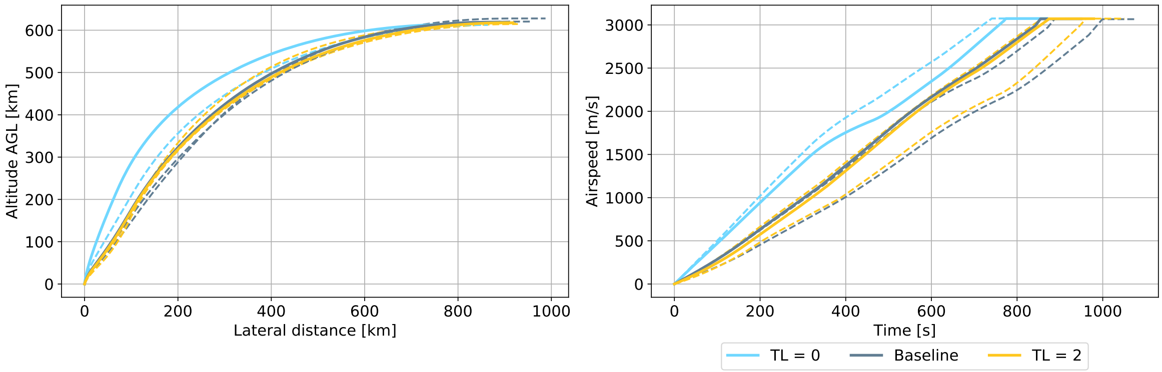

Figure 8.40: The ascent profile for each thrust case

Although the choice of thrust law has no effect on the descent of the vehicle, as the thrust law is only implemented during the ascent, the entry corridor of each case are shown in Figure 8.41 to show that for each case, again the optimum solution is the solution that has the lowest airspeed before the retroburn initiation.

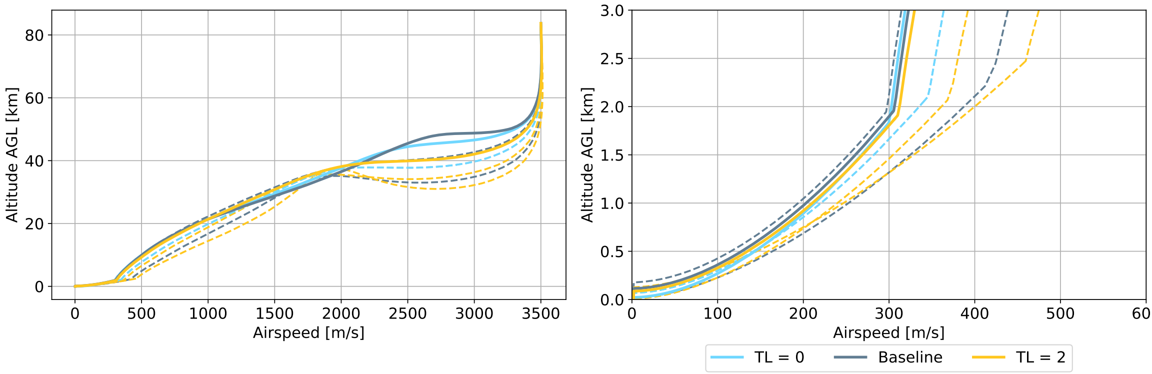

Figure 8.41: The entry corridor for each thrust case

The design variables, engine properties, and mass breakdown for the optimum solutions of each thrust law case is given in Table 8.7. The results of all seeds for both thrust laws 0 and 2 can be found in Appendix C.6. It is clear that the thrust law 0 case performs a much steeper ascent, with greater pitch angle values for both nodes 2 and 3 compared to the baseline and thrust law 2 cases. The thrust law 0 case also has a higher total thrust compared to the baseline case, and the thrust law 2 case has almost double that of the baseline case. Thrust law 0 requires a higher initial TW ratio and therefore higher initial thrust, however the higher thrust sized for the thrust case 2 may be an efficiency in the optimiser.

The inefficiencies in the optimiser may stem from the presence of a very high number of design variables. Although the optimiser is able to obtain solutions that are evidently optimised, it is inevitable that increasing the number of design variables exponentially increases the complexity and computation effort needed to optimise the problem. Although the thrust law 0 case may indeed be a more optimum thrust profile compared to the baseline and thrust law 2 case, it must not be forgotten that is utilises one less design variables, namely the minimum TW ratio. Therefore is it able to allot more computational effort to solving for the remaining design variables in the same amount of generations, compared to the baseline and thrust law 2 cases. This notion can also be applied therefore to the total designed thrust for thrust law 2.

Table 8.7: The optimum solutions for all three thrust law cases

Design Variables	**Baseline**	**Thrust Law 0**	**Thrust Law 2**
Optimum Trajectory Design Variables			
Node 1 [deg]	86.205	86.926	85.797
Node 2 [deg]	58.012	74.009	57.608
Node 3 [deg]	63.165	67.161	63.522
Node 4 [deg]	42.330	31.810	40.619
Node 5 [deg]	13.578	8.760	11.853
Node 6 [deg]	-8.522	-6.696	-8.026
Min TW [-]	1.701	1.665	1.552
Max TW [-]	2.525	2.284	2.305
Entry γ [deg]	-3.620	-3.775	-4.530
Entry δ [deg]	27.755	29.088	31.978
Entry τ [deg]	-9.011	-5.378	-0.937
Entry α [deg]	57.292	58.424	53.106
Retroburn altitude [m]	2125	2027	2063
Optimum Vehicle Design Variables			
Mass flow [kg/s]	51.974	53.626	103.021
Chamber pressure [Pa]	18110229	26680323	16729183
O/F ratio [-]	3.618	3.791	3.907
Engine number [-]	6	8	6
Ascent propellant [kg]	113905	111790	124446
Landing propellant [kg]	4754	7155	3509
Exhaust diameter [m]	0.902	1.158	0.813
Vehicle diameter [m]	7.469	8.220	8.301
Engine Properties			
Specific Impulse (vac) [s]	387.770	404.635	373.154
Engine thrust (vac) [kN]	186.575	200.878	355.883
Total thrust (vac) [kN]	1119.453	1607.027	2135.301
Mass Breakdown			
Dry mass [kg]	21941	23201	23248
Propellant mass [kg]	123084	123623	132625
Payload mass [kg]	1200	1200	1200
GTOW [kg]	**146226**	**148024**	**157073**

8.7. Summary of the Results

The results in this chapter present the optimum vehicle and trajectory designs for each scenario detailed by the research questions. The baseline scenario is the focus of the research, and also serves as a reference to which the results obtained for different scenarios may be compared. The baseline scenario is described by a Martian base location at 42.5° North and 25.5° East, with an altitude of -3700 m with respect to the Martian geoid. The vehicle is launched into a circular target orbit, at an altitude of 607.74 km, with an inclination of 44.96°, and a delta-V of 387.24 is taken into account for the rendezvous, docking, and de-orbit burns. The entry back to the base from the node orbit is simulated from an altitude 80 km, where the vehicle has a velocity of 3500 m/s and a heading angle of 45.04°. The vehicle transports a total payload mass of 1200 kg to and from the node, and utilises thrust law 1.

The optimum vehicle obtained for the baseline scenario has GTOW of 146.2 tonnes, of which 123.1 tonnes is propellant mass. The driving aspect of the design is the ascent phase, as it requires the greatest propellant mass, and therefore its optimisation may lead to the reductions in GTOW. The optimum GTOW of 146.2 obtained by the MDO is a siginficant decrease compared to the Charon vehicle by Gaffarel et. al. [22] that was designed for the same mission scenario, of which the GTOW is 168.1 tonnes. This indicates that the MDO is effective in optimising for a reduced vehicle GTOW and obtains solutions with efficient propellant usage.

The effect of the mission scenario is further investigated by comparing the baseline scenario to the mission scenario used for the Hercules vehicle by Komar et. al. [38] (an ascent to 108 km altitude orbit with inclination 43.9° and an eccentricity of 0.0178), and a direct ascent to the node's circular orbit at 500 km. Each scenario leads to very different GTOWs found, with the Hercules scenario allowing for much lower GTOWs than the other two scenarios. The Hercules scenario obtained an optimum GTOW of 103.0 tonnes, which is greatly reduced with respect to the GTOW of both the direct ascent (127.2 tonnes), and the baseline (146.2 tonnes). From this it is clear that although launching into a lower orbit means that a greater delta-V is needed to rendezvous with the node, this is still preferable over launching into a higher orbit. The target orbit altitude is therefore highly influential on the GTOW as it greatly affects the ascent propellant, much more so than the extra delta-V necessary to rendezvous with the orbital node.

The Martian base location is also investigated, as it can have an effect on the delta-V necessary to reach the desired orbit due to the different surface rotational velocities at each location. Latitudes 21.25° and 5° are chosen, for which the optimum GTOWs found are 141.1 and 146.0 tonnes, respectively. The 21.25° location results reflect the expectations- that a lower latitude results in a reduced delta-V and therefore a reduced GTOW. The 5° GTOW, on the other hand, is greater than the GTOW for the 21.25° case. This could be attributed to the number of seeds simulated, as there is always some element of randomness due to the seed used in the MDO. Further, the difference in rotational velocity between the baseline and 21.25° case is much higher than between the 21.25° and the 5° case. The change in GTOW is expected, therefore, to be much more apparent between the baseline and the 21.25° case, which is shown by the results.

The increase and decrease of 50% payload mass (therefore 600 kg and 1800 kg, respectively) leads to an increase and decrease in average GTOWs found, namely 158.5 tonnes and 176.2 tonnes, respectively. This is as expected, as the vehicle must expend more propellant during both the ascent, and during the EDL phase to land with a greater payload mass, and vice versa.

The absence of crew, investigated by lifting the maximum g-load from 4 g_{mars} to 10 g_{mars}, does not significantly impact the average GTOW, however the optimum baseline GTOW is found to be lower than the optimum GTOW for the 10 g case (146.2 compared to 156.5 tonnes for the baseline and 10 g case, respectively). The optimum baseline scenario design does not utilise a maximum TW ratio greater than 3, therefore a reduction in ascent propellant is not expected. However, although the propulsive landing may benefit from a higher allowable thrust as this reduces the propellant needed, the higher g-load limitation results in a greater number of allowable EDL trajectories (as more vehicle are able to land). The EDL trajectory is therefore less optimised, and no significant reduction in overall GTOW is obtained.

Changes in thrust law leads to different GTOWs found. Thrust law 2 does not significantly affect the average GTOW, however thrust law 0 does greatly impact the average GTOW found. All three GTOWs found for thrust law 0 are under 153 tonnes, whereas the average GTOW for the baseline case lies at approximately 163 tonnes. This reduction may be due to the higher TW ratio at the start of the ascent, such that the gravitational losses are reduced, however it could also be due to the fact that there is one less design variable that must be optimised for the thrust law 0. A greater number of design variables leads to a more complex system to be optimised and that may adversely impact the performance.

9

Sensitivity Analysis

To determine the behaviour of the optimum design, as well as the behaviour of the solutions found within the MDO, a sensitivity analysis is performed. A sensitivity analysis shows the effects of uncertainties and changes to the parameters on the model and on the design. This knowledge is of great importance as large effects due to small changes are relevant to the optimum design. In this chapter, sensitivity analyses are conducted on both the optimum design itself, and on the MDO as a whole.

9.1. Optimum Design Sensitivity

Knowledge about the impact of uncertainties on the performance of the optimum solution is highly necessary when conducting an optimisation. This section presents the sensitivity analysis conducted on the optimum baseline solution found in Section 8.1. This means that the effects of the uncertainty in certain parameters and conditions on whether the vehicle is able to reach the target orbit, as well as land in the correct location whilst adhering to the constraints, are determined. First the sensitivity analysis method is presented, followed by the results.

9.1.1. Sobol Analysis Methodology

There are many ways of approaching sensitivity analyses, some of the most common methods being the one-at-a-time approach (OAT), factorial design, Monte Carlo analysis, and variance-based methods. The method applied to the optimum solution found is the Sobol method, which is a variance-based method.

The Sobol method estimates the influence of a given input on the output variance, by assigning each uncertain parameter an index that indicates that parameter's relative influence on the output; in other words they quantify how much of the variance in the model output each uncertain parameter is responsible for. If a variable has a low Sobol index, changes of this variable results in comparatively small changes in the final model output. Conversely, if a parameter has a high Sobol index, a change in this parameter leads to a large change in the model output[1]. The advantage of the Sobol method is that it is able to combine the benefits of multiple sensitivity analyses into one method, as it determines the first-order effects (one-at-a-time approach) as well as the second-order effects (factorial), and total effects (Monte Carlo). The indices calculated are therefore categorised into first-order, second-order, and total order effects. It is custom, however, to only calculate the first and total order effects, which is also what is performed here, as it is unlikely that only two variables will be uncertain at any point in time.

The Sobol method relies on the decomposition on variance. Any system can be seen as a black box that is described by the function in 9.1. X denotes a set of input variables $X_1, X_2, ...X_d$, each having an uncertainty, and Y is a chosen univariate model output. Furthermore, the inputs are chosen independently and uniformly within the hypercube, i.e. $X_i \in [0,1]$ for $i = 1,2,...d$ [62].

---

[1] `https://uncertainpy.readthedocs.io/en/latest/theory/sa.html`

$$Y = f(X) \tag{9.1}$$

The variance may then be decomposed as shown in Equation 9.2, where f_0 is a constant and f_i is a function of X_i, f_{ij} a function of X_i and X_j, and so on. A condition of the decomposition is shown in Equation 9.3, meaning that all terms must be orthogonal [62].

$$Y = f_0 + \sum_{i=0}^{d} f_i(X_i) + \sum_{i<j}^{d} f_{ij}(X_i, X_j) + ... + f_{1,2...d}(X_1, X_2, ...X_d) \tag{9.2}$$

$$\int_0^1 f_{i_1 i_2 ... i_s}(X_{i_1}, X_{i,2}, ..., X_{i_d}) dX_k = 0 \quad \text{for} \quad k_i = i_s ... i_k \tag{9.3}$$

This leads to the definitions of the terms within the decomposition, as a function of conditional expected values. These are shown in 9.4. From this, it can be seen that f_0 is the expected value, f_i is the effect of varying only X_i, and f_{ij} is the effect of varying X_i and X_j simultaneously, additional to the effect of their individual variations. This is known as second-order interaction [62].

$$\begin{aligned} f_0 &= E(Y) \\ f_i(X_i) &= E(Y|X_i) - f_0 \\ f_{ij}(X_i, X_j) &= E(Y|X_i, X_j) - f_0 - f_i - f_j \end{aligned} \tag{9.4}$$

Next, the functional decomposition can be squared and integrated, as given in Equation 9.5, where $f(\mathbf{X})$ denotes the square integral [62].

$$\int f^2(\mathbf{X}) d\mathbf{X} - f_0^2 = \sum_{s=1}^{d} \sum_{i_1<i_2...<i_s}^{d} \int f_{i_1,...i_s}^2 dX_{i_1} ... dX_{i_s} \tag{9.5}$$

The left-hand side of 9.5 is now equal to the variance of Y, and the terms on the right-hand side are the variance terms, now decomposed with respect to X_i. It can therefore be rewritten as Equation 9.6, where V_i and V_{ij} are given in 9.7. The $\sim i$ notation indicates the set of variables except X_i. The decomposition therefore shows how the variance of the model output can be quantified and attributed specifically to each output, and interactions thereof [62].

$$\mathrm{Var}(Y) = \sum_{i=1}^{d} V_i + \sum_{i<j}^{d} V_{ij} + ... + V_{12...d} \tag{9.6}$$

$$\begin{aligned} V_i &= \mathrm{Var}_{X_i}(E_{x\sim i}(Y|X_i)) \\ V_{ij} &= \mathrm{Var}_{X_{ij}}(E_{x\sim ij}(Y|X_i, X_j)) - V_i - V_j \end{aligned} \tag{9.7}$$

The indices with respect to the first-order effects, meaning the effect of changing only variable X_i, can then be calculated using Equation 9.8, where S_i denotes the first-order Sobol index [62]. If no higher-order effects are present, the total sum of the first-order indices equals 1, and the greater the deviation from 1, the greater the higher-order effects are.

$$S_i = \frac{V_i}{\mathrm{Var}(Y)} \tag{9.8}$$

The indices with respect to the total effects, meaning the effect of X_i including the effects of all other variables, can then be calculated using Equation 9.9, where S_{Ti} denotes the first-order Sobol index [62].

$$S_{Ti} = 1 - \frac{\mathrm{Var}_{\mathbf{X}_{\sim i}}(E_{X_i}(Y|\mathbf{X}_{\sim i})}{\mathrm{Var}(Y)} \tag{9.9}$$

To calculate the indices, the generation of the input dataset (X) is needed, and for this, the Monte Carlo method is used. The Monte Carlo method generates a sequence of randomly distributed points inside the hypercube (this therefore satisfies condition 9.3). However, it is customary to use quasi-random sampling sequences such as the Sobol sequence, Saltelli sequence, or the Latin Hypercube, as this improves the efficiency of the estimators. To determine the values, $N(d+1)$ runs are needed, where N denotes the number of user-determined runs, and d the number of uncertain variables (variables that are allowed to vary between bounds). This, of course, leads to high computational expenses if the number of runs and/or number of uncertain variables are high, which is a drawback of the Sobol method, especially if the computational time of a single run is high.

The methodology implemented to calculate the indices in this research is shown in Figure 9.1. The calculation of the quasi-random Monte Carlo inputs is done by using the Python Library SALib[2]. This library is a publicly available and widely-used tool to determine Sobol indices, as well as the Morris and FAST methods. The inputs generated by the SALib library are then used as inputs to run the ascent and the descent trajectories in Tudat, of which the outputs are saved. SALib then uses these outputs to determine the Sobol indices.

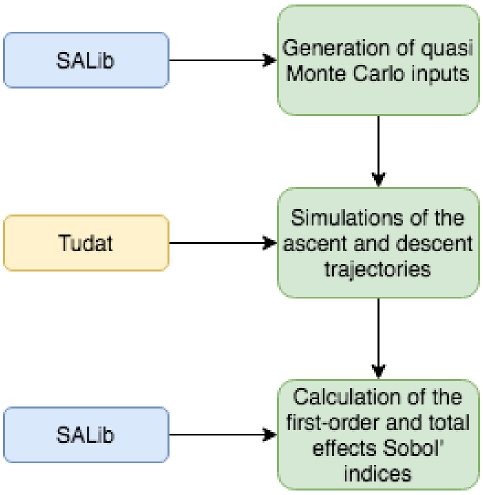

Figure 9.1: The methodology implemented to calculate the Sobol indices

9.1.2. Uncertain Variables, Bounds, and Settings

The uncertain variables must first be identified, as well as their bounds. As the optimum solution is investigated, it is pertinent to know whether the vehicle is still able to reach its target orbit, as well as land, with the inclusion of uncertainties in variables. The uncertain variables that are identified can be found in Tables 9.1 and 9.2 for the ascent and EDL phases, respectively.

---

[2] `https://salib.readthedocs.io/en/latest/`

Table 9.1: The uncertain variables and their respective bounds for the ascent Sobol analysis

Ascent Variable	Bound
Node 1 [deg]	± 1
Node 2 [deg]	± 1
Node 3 [deg]	± 1
Node 4 [deg]	± 1
Node 5 [deg]	± 1
Node 6 [deg]	± 1
Mass flow [kg/s]	± 2
Chamber pressure [Pa]	± 100
O/F ratio [-]	± 0.05
TW min [-]	± 0.05
TW max [-]	± 0.3

Table 9.2: The uncertain variables and their respective bounds for the EDL Sobol analysis

EDL Variable	Bound
Entry latitude [deg]	± 0.000245
Entry longitude [deg]	± 0.00183
Entry altitude [m]	± 2.6025
Entry speed [m/s]	± 0.2
Entry heading [deg]	± 1
Entry flight path angle [deg]	± 1
Angle of attack [deg]	± 1
Mass flow [kg/s]	± 2
Chamber pressure [Pa]	± 100
O/F ratio [-]	± 0.05
Retroburn altitude [m]	± 100

The variables for the ascent are identified due to their influence on the trajectory, and possible uncertainty. All parameters chosen are design variables, with no other initial conditions used. This is because it is highly unlikely that there is an uncertainty in the launch conditions, such as location or velocity. Further, other design variables such as exhaust diameter and vehicle diameter are also not chosen. This is due to the fact that for the diameters, manufacturing errors are negligible. The pitch node bounds are taken as 1 degree, as Haex [23] found that the nodes are allowed to vary between 0.4° and 0.8° to reach the target orbit. The TW_{min} is taken as 0.05 as there may be some differences in desired and actual thrust produced by the engines. TW_{max} is greater, at 0.3, as there is a difference between the TW_{max} in the simulation and TW_{max} set by the design variables due to the difference in estimated and actual ascent burn times (see Subsection 6.4.3). Mass flow is chosen as there may be a difference between the desired and actual mass flow, as well as chamber pressure and mixture ratio.

The variables for the EDL phase, however, do include all the EDL initial conditions, as there is an uncertainty of 100 m in the propagation. The entry latitude, longitude, and altitude are therefore calculated such that at their maximum values, the vehicle deviates no more than 100 m from its original initial position. The entry speed bound is taken from the uncertainty determined by Gaffarel et. al. [22] for the Charon vehicle. The other orientation angles' bounds are also set to 1 degree as per the ascent phase, and the engine variable bounds are set equal to those of the ascent. Lastly, the retroburn altitude bound is also set to 100 m due to the propagation uncertainty.

As stated in Subsection 9.1.1, the number of quasi-random Monte Carlo runs necessary is $N(d+1)$, where d denotes the number of uncertain variables, and N the user-set number of runs. The SALib library uses a Saltelli sequence to generate the inputs, for which the value of N must be 2 to the power of something. Therefore, N is set to 16384, or 2^{14}, as this is still manageable in terms of computational effort.

9.1.3. Results

The sensitivity analysis of the optimum solution concerns its performance. For the ascent phase, the vehicle's ability to reach the target orbit is evaluated, by assessing the final orbit's pericentre, eccentricity, and inclination, as these are also the constraints in the MDO. A variable's effect on the parameter in question is also taken with respect to the parameter's margin. For example, a pericentre altitude difference of 1 km would lead to a pericentre output of 1/10 (as the pericentre margin is 10 km), as opposed to 1/607. This ensures that the effect is scaled to the margins, and not the absolute value of the target parameter. Figure 9.2 presents the Sobol indices for the first-order effects (S_i), where θ_1 - θ_6 denote the pitch angle nodes, $\dot{m}$ the engine mass flow, P the engine chamber pressure, O/F the mixture ratio, TW_{min} the minimum thrust to weight ratio, and TW_{max} the maximum thrust to weight ratio. The indices are sorted highest to lowest. In Appendix D.1 all first-order indices can be found.

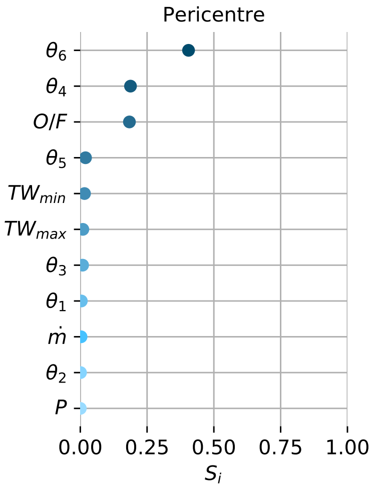

Figure 9.2: The Sobol indices for the first-order effects for the ascent phase (note that the colour has no significance)

From Figure 9.2 it can be seen that the final pitch node, θ_6, has the largest effect on both the pericentre and the eccentricity of the orbit. The final node, of course, determines the final attitude of the vehicle and therefore it clear to see how it has the largest effect on the both parameters. For both parameters, the fourth node has the second greatest influence, meaning that these are the nodes that have the largest role in determining the altitude and shape of the orbit, however, the pericentre is much more sensitive to node 4 than the eccentricity is.

The pericentre is also sensitive to the mixture ratio, which evidently has an influence on the engine properties. It is also interesting to see that for all three parameters the minimum TW ratio is always placed above the maximum TW ratio. Although the minimum TW ratio's uncertainty is more constrained, changes in the initial TW ratio affect the entire ascent trajectory, unlike the maximum thrust to weight ratio, and it therefore has a greater impact on the final orbit.

For the inclination, however, the first node, θ_1, has by far the largest effect, with all other variables having comparatively little to no effect on the inclination. It is clear the see that most variables, however, when varied alone, do not have a significant impact on the final orbit, and the sum of the indices equates to 0.9991, meaning the total order effects are almost negligible.

Although it is interesting to evaluate the individual effects of each variable on the final orbit, the total effects paint arguably a more valuable picture, as there is only a small chance that in reality only one variable will deviate from its designed value. Figure 9.3 presents the total effect indices for the ascent phase (in Appendix D.2 all total indices can be found).

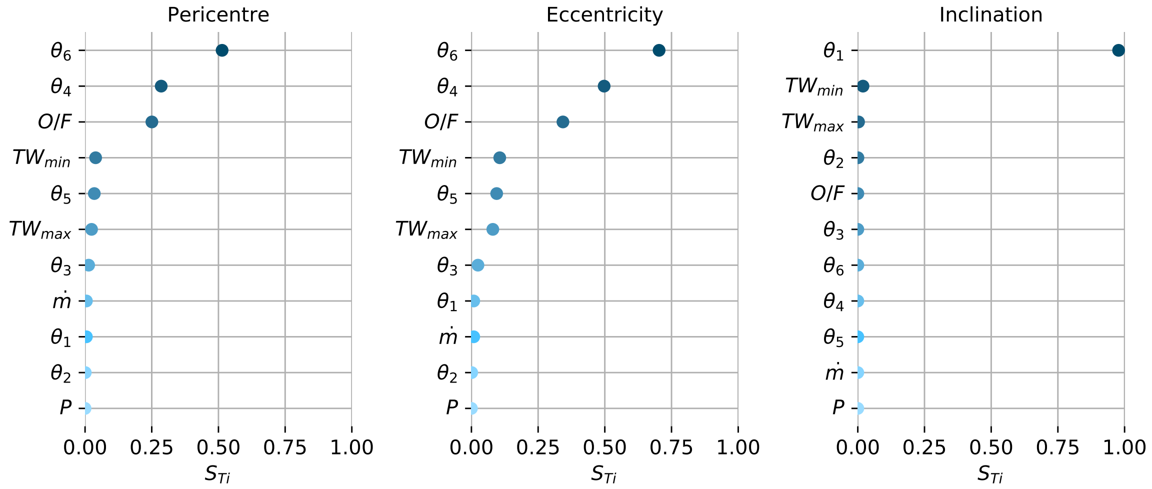

Figure 9.3: The Sobol indices for the total effects for the ascent phase (note that the colour has no significance)

As can be seen from Figure 9.3, there is a significant difference between the first-order and total effects of the variables with respect to the eccentricity, and a little with respect to the pericentre. The magnitudes of the indices are much greater for the total effects of the eccentricity, showing the final eccentricity is highly sensitive to changes when they occur for multiple variables simultaneously. The pericentre is also more susceptible to changes when multiple variables are varied. However, interestingly, while the rankings of the variables remain largely the same for both parameters as for the first-order effects, they now occur in exactly the same order as each other. Although the eccentricity of the final orbit is more sensitive to the uncertain variables than the pericentre altitude, the hierarchy of the variables' influence is the same. This due to the both variables being influenced by each other, as varying the eccentricity of an orbit can affect the pericentre altitude, and vice versa.

For both cases, node 6 evidently holds the greatest influence, with node 4 remaining second, and the first three nodes ranked among the least impactful. The orbital injection of the vehicle is therefore determined predominantly by the latter portion of the ascent compared to the start, most likely due to the closer proximity to the injection point, as well as the higher velocities at which the vehicle travels at the end of the ascent.

The total effects with respect to the inclination, however, remain almost identical to the first-order effects, as predicted by the summed value of the first-order effects. The first node is the driving variable, and evidently holds by far the greatest influence over the inclination with and without higher order effects. Although the order of the other variables have changed slightly, their effects are comparatively so small that they can be considered insignificant when compared to the effect of the first node.

For the EDL phase, the landing coordinates, the vehicle's velocity, and pitch angle at touchdown are evaluated. Although the landing altitude is also constraint within the tool, this was necessary to remove any ambiguity in the exact landing location. In this case, the vehicles all landed at the correct altitude. Figure 9.4 presents the Sobol indices for the first-order effects (S_i), where δ_0 denotes the initial latitude, τ_0 the initial longitude, h_0 the initial altitude, V_0 the initial velocity, χ_0 the initial heading angle, γ_0 the initial flight path angle, α_0 the angle of attack, and h_{rb} the retroburn altitude. The indices are sorted highest to lowest. In Appendix D.1 the all the first-order indices can be found.

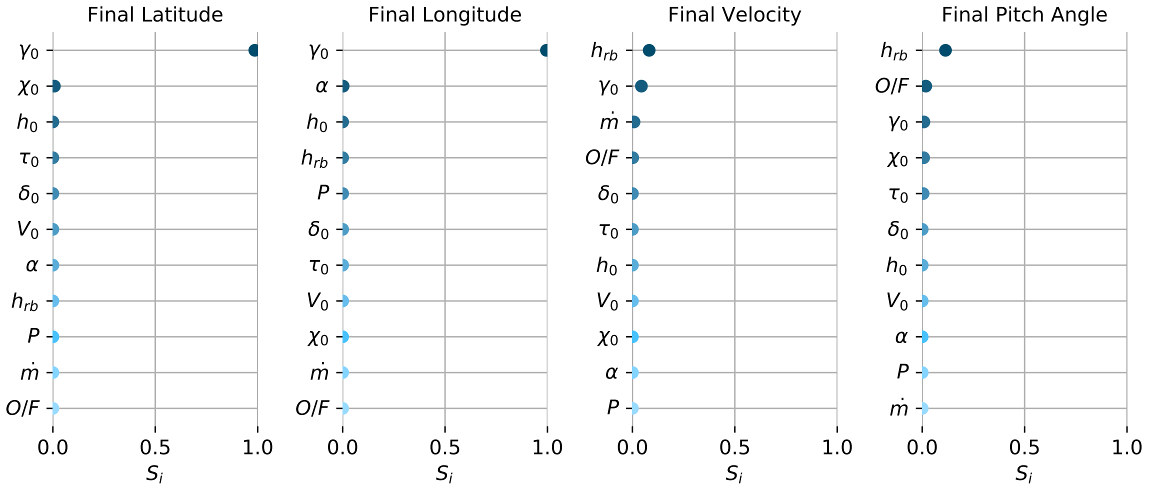

Figure 9.4: The Sobol indices for the first-order effects for the EDL phase (note that the colour has no significance)

As seen in Figure 9.4, the initial flight path angle by by far the most dominant variable in the vehicle's landing latitude and longitude. Although the other parameters may have an effect, they have outstandingly less influence than the initial flight path angle. The initial flight path angle, of course, dictates in great part the aerodynamic forces, which in turn affect the time of flight and velocity of the vehicle throughout the trajectory. It is therefore unsurprising to see that it has by far the greatest effect on the landing location. The summed values of the first-order indices are 0.993 and 0.998, indicating very little to no higher-order effects.

Although the other variables have very little to no effect on the landing location, it is interesting to see that the second greatest effect on the final latitude is produced by the initial heading angle. Although bearing angle guidance implemented in the simulation to steer the vehicle toward the correct landing location, this is only initiated at an altitude of 50 km due to the low atmospheric density above 50 km. The change in initial heading is therefore still influential. The second greatest parameter for the longitude, on the other hand, is the angle of attack. The angle of attack determines the lift, and therefore also the time of flight, and consequently also the longitude of the landing location.

The final velocity and final pitch angles are not influenced as predominantly by just one variable as the final latitude and final longitude. It is also notable that neither parameter are as influenced by the varying of one single parameter as the final landing location. Both parameters are, however, most affected by the retroburn altitude, which is to be expected, as this greatly determines the both the velocity at which the retroburn is initiated, and the time available for the vehicle to decelerate and to turn to a vertical attitude (as all other variables are kept equal for first-order analyses). For both the final pitch and velocity, the flight path angle is also an influential variable at second and third place, respectively, as this greatly determines the trajectory as a whole and so also the velocity at which the retroburn is initiated. The mixture ratio evidently is also an influential factor, affecting the engine performance and consequently also the propulsive landing.

Again, it is interesting to isolate the individual effects of each variable, however, in reality multiple uncertainties will always be present and therefore the total order effects are highly valuable. Figure 9.5 presents the total effect indices for the EDL phase (Appendix D the all the total indices can be found).

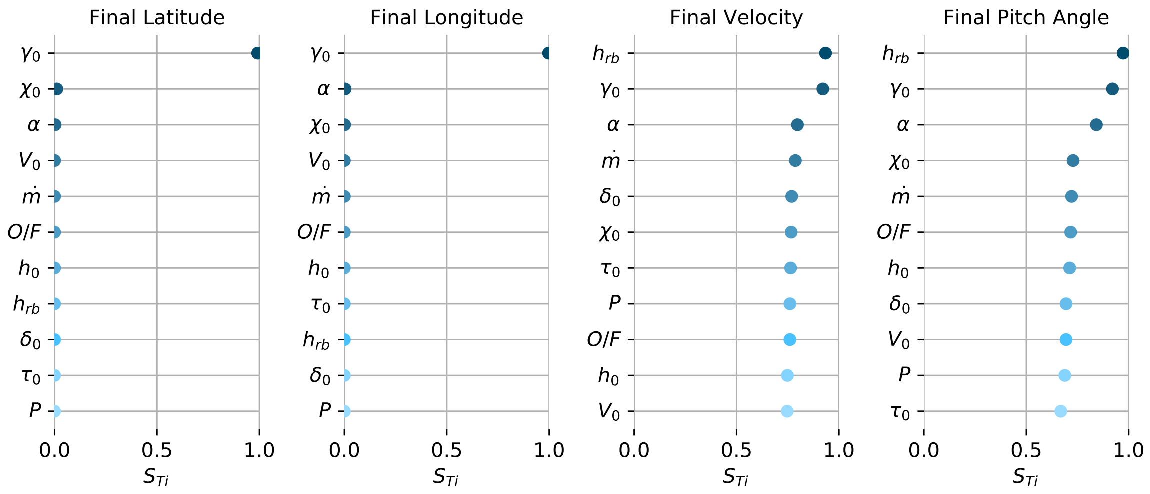

Figure 9.5: The Sobol indices for the total effects for the EDL phase

It is immediately clear from Figure 9.5 that while the magnitudes of the indices pertaining to the latitude and longitude have remained almost identical, as predicted by the summed values of the first-order indices, the indices pertaining to the final velocity and final pitch angle have increased dramatically. While the final latitude and longitude are affected almost solely by the initial flight path angle and are comparatively insensitive to all other variables, the final velocity and final pitch angle are highly sensitive to all variables when varied simultaneously. Although there is a hierarchy in the influence of the variables, it is evident that a propulsive landing is a very sensitive manoeuvre, and that it is very volatile to changes within any variable. The rankings of the variables, when compared to the first-order effects, have changed, with the exception of the retroburn altitude and initial flight path angle, which remain the most influential two variables. The angle of attack, however, has a much greater effect when varied simultaneously with other variables than when its varied alone. Although the retroburn altitude can be considered the most influential variable for a safe landing, it is clear that all aspects of the landing must be carefully controlled for the landing to be executed as desired.

In conclusion, it is clear that there are certain variables that affect the performance of the vehicle to a much higher degree than others. For the ascent, this is pitch nodes 6, 4, and 1, with interaction effects impacting the final pericentre and final eccentricity the greatest. These sensitivities are expected, however should a high-fidelity model be implemented, a greater focus is necessary for the simulation of the vehicle's orientation and trajectory than the performance of the engine in order to determine the vehicle's ability to reach the desired orbit. For the EDL phase, the initial flight path angle is the dominant variable for both first-order and total effects with respect to the landing location. This indicates, again, that the orientation of the vehicle throughout the trajectory is highly instrumental to its performance. The execution of the retroburn, on the other hand, is highly affected by interactive affects, indicating that is requires high precision and accuracy of the variables as it is a volatile manoeuvre that requires a high focus.

9.2. MDO Sensitivity

Not only should the sensitivity of the optimum design be addressed, but also the sensitivity of the model as a whole. The aerodynamic coefficients and the propulsion system efficiency are two factors that are necessary to model the vehicle and its trajectory, and may greatly influence the optimum design. The sensitivity of the model to these are therefore investigated.

9.2.1. Aerodynamics

The aerodynamic coefficient data for the optimisation is generated by Missile DATCOM, a powerful tool that, as discussed in Chapter 5, is shown to be applicable for a Martian atmosphere if certain conditions are accounted for. However, the validation of the drag coefficients is not possible for angles of attack below 40°, as well as both lift and drag coefficients at any velocities lower than Mach 2. This is very unfortunate, as the coefficients in these regions may be highly influential to the optimum design of the vehicle due to their usage during the ascent which is known to be the bottleneck of the design. The sensitivity of the MDO is therefore investigated by altering the coefficients by +15%, +5%, -15%, and -5%, as 15% is approximately the maximum deviation of the Missile DATCOM data from the Martian validation data (see Section 5.3). Again, three seeds are used to optimise each case and obtain three solutions. The GTOWs and mass breakdown for each case's optimum can be found in Figure 9.6

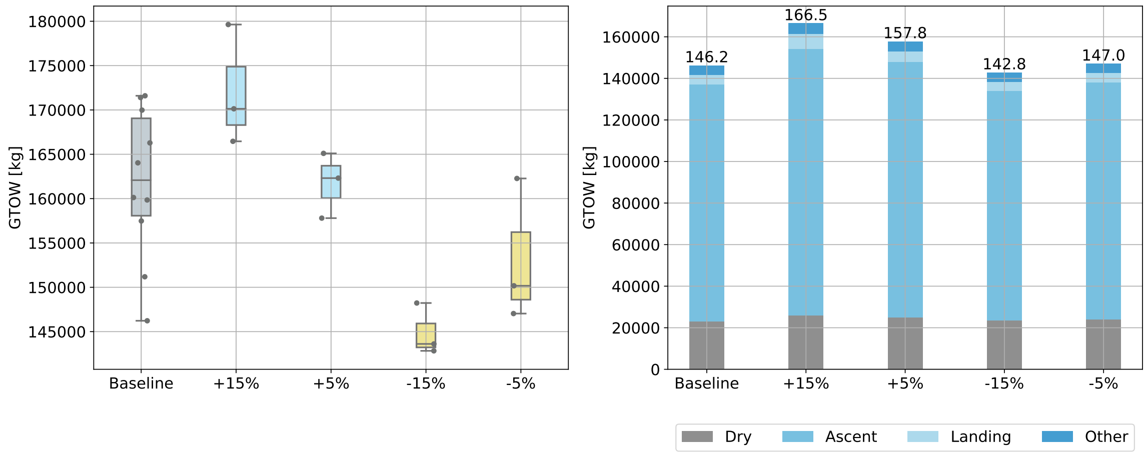

Figure 9.6: The GTOW of all the vehicles for each aerodynamics case (left) and the GTOW breakdown of each optimum vehicle's mass (right). The values above each seed's breakdown in the rightmost figure indicates the GTOW in tonnes

As can be clearly seen from Figure 9.6, the aerodynamics have a significant effect on the GTOW of the solutions found. As is expected, the greater the aerodynamic coefficients, the greater the GTOW, as this increases the drag forces on the vehicle, which is unwanted during the ascent. The -15% case obtains the solution with the lowest GTOW, at 142.8 tonnes, and the +15% the highest, at 166.5 tonnes. Although the -5% case does not obtain a GTOW solution that is less than the baseline, its average is much lower than the baseline's, and its optimum solution is only marginally larger than the baseline's. From the mass breakdowns in the rightmost figure in Figure 9.6, it is clear that the differences in GTOW are again mostly due to reductions in ascent propellant, but differences in landing propellant masses can also be seen. To investigate this, the ascent and landing propellant masses for all solutions are shown in Figure 9.7.

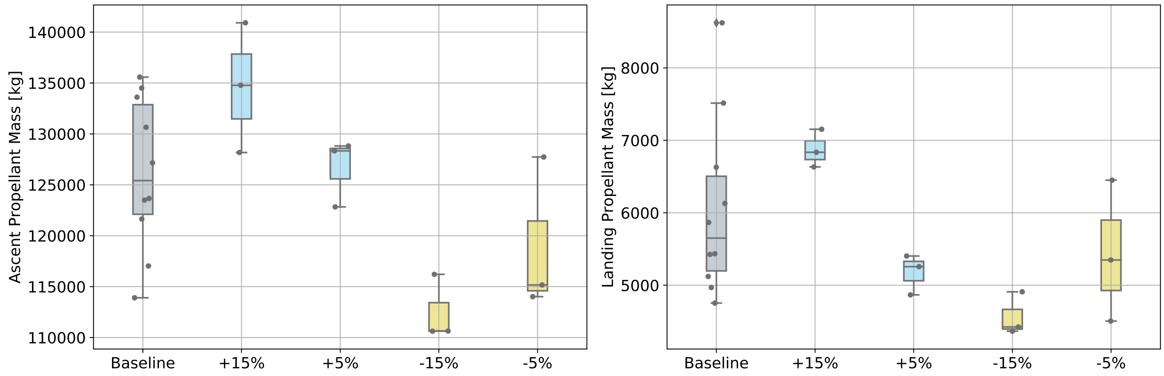

Figure 9.7: The ascent and landing propellant masses for all aerodynamics cases

From Figure 9.7 the effects of the aerodynamic data on not only the ascent propellant masses, but the also on the landing propellant masses, are clearly observed. The ascent propellant masses are affected by greater modelled drag forces on the vehicle, however the landing masses are also adversely affected by increased modelled aerodynamic forces, and the dry masses of the increased coefficient solutions are also greater, due to the greater propellant mass. The effects of the aerodynamic data on the EDL trajectories are shown in Figure 9.8. From the figure, it is clear to see that the solutions with decreased coefficients are less affected by drag and therefore have a much longer time of flight. They also experience skipping flight, indicated by the peak in altitude, due to the increased lift. This skipping effect, combined with a lighter dry mass, is what allows for the decreased coefficient solutions to obtain a lighter GTOW than the increased coefficients. The effects on the engine properties is further seen in Figure 9.9.

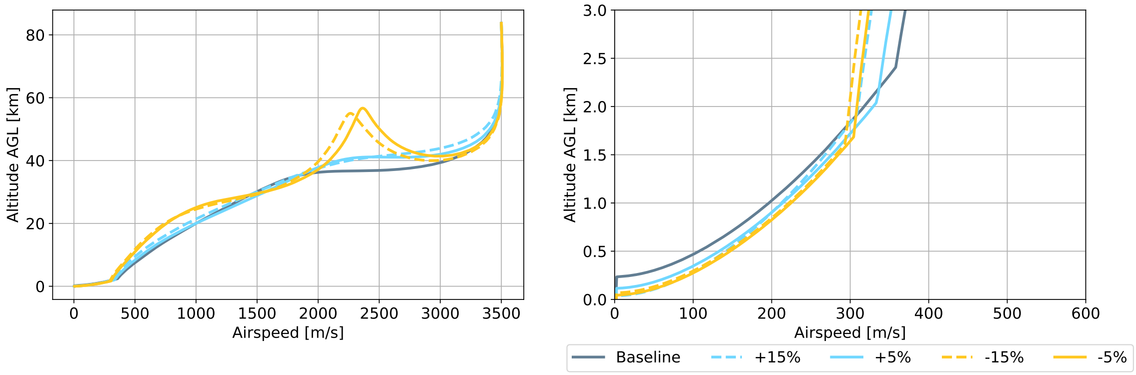

Figure 9.8: The EDL profiles for all aerodynamics cases

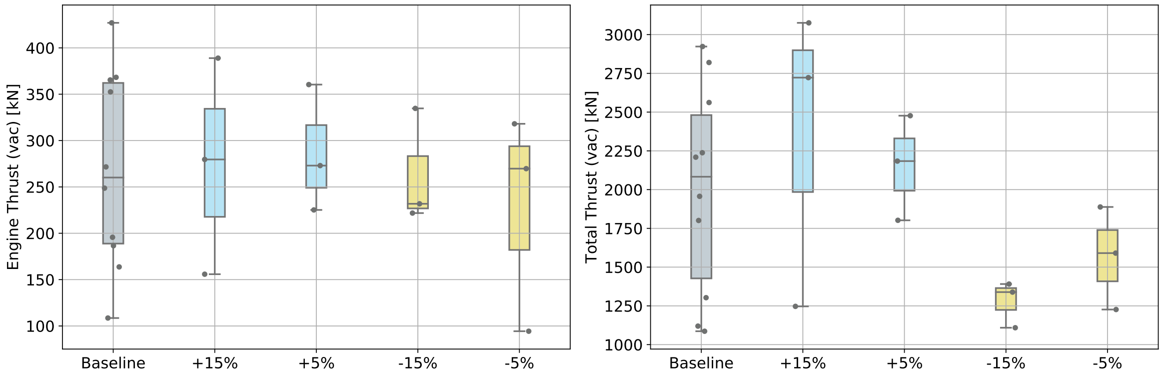

Figure 9.9: The engine and total thrust delivered for all aerodynamics cases

From Figure 9.9, the engine thrust is not seen to be greatly affected by the change in aerodynamics. The total vehicle thrust, however, is seen to increase with increasing aerodynamic coefficients, to overcome to the additional aerodynamic forces induced by the greater coefficients. Likewise, less thrust is necessary if the aerodynamic coefficients are decreased, as less aerodynamic forces are present. Lastly, the results of all seeds for can be found in Appendix E.1. Overall, it is clear from the results that the aerodynamic coefficients have a significant effect on the solutions obtained.

9.2.2. Propulsion System

As seen in Section 4.1, the properties of the propulsion system are modelled using Ideal Rocket Theory. The overestimation of the engine performance due to the assumptions is compensated for by applying a quality factor over both the thrust and the specific impulse values. These factors, named the thrust quality factor and the propellant consumption quality factor, respectively, are obtained by calculating the factors for 4 existing engines by comparing their performance to their modelled performance, and taking the mean average. This, of course, leads to uncertainties in the model, as this places a high dependence on the 4 engines chosen. To investigate the effects of the uncertainties in these factors, they are simultaneously increased and decreased by 2.5% and 5%. Again, three seeds are used to optimise each case and obtain three solutions. The GTOWs and mass breakdown for each case's optimum can be found in Figure 9.10.

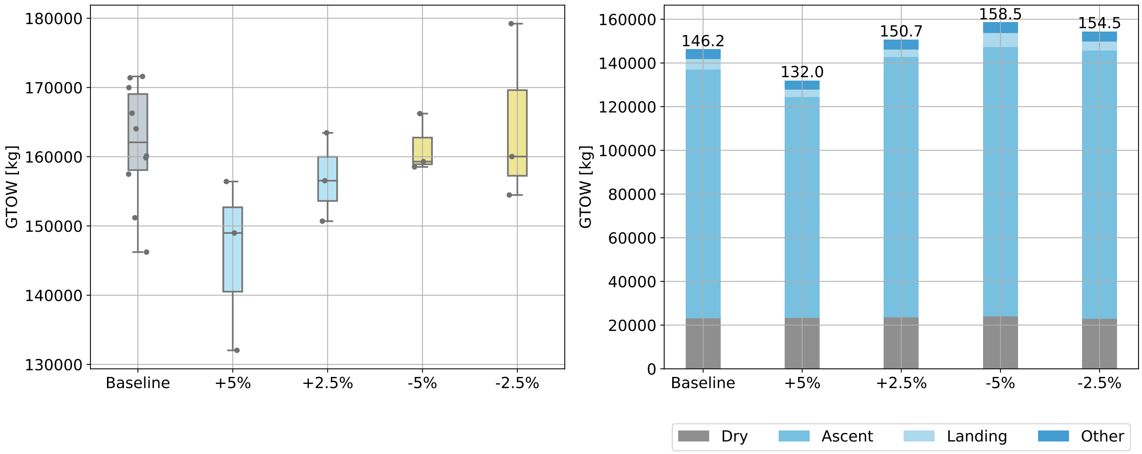

Figure 9.10: The GTOW of all the vehicles for each propulsion system efficiency case (left) and the GTOW breakdown of each optimum vehicle's mass (right). The values above each seed's breakdown in the rightmost figure indicates the GTOW in tonnes

As can be seen from Figure 9.10, there is a slight effect on the GTOW that is caused by the change in the factors. The greater the propulsion system's efficiency due to a higher factor, the less ascent propellant is necessary, leading to a lower GTOW. The optima of all the cases fall within the expectations, with the most efficiency propulsion system case, +5%, obtaining a significantly lower optimum GTOW than the baseline with 132.0 tonnes. The least efficient propulsion system case, -5%, obtains the greatest GTOW, at 158.5 tonnes. The greatest GTOW of all the seeds is obtained by the -2.5% case, however this deviation from expectations may be caused by the small number of seeds run per case. The average GTOW value for the +5% case is, for example, higher than the baseline case. To clearly observe the effects on the propellant masses, Figure 9.11 shows the ascent and landing propellant masses for all cases.

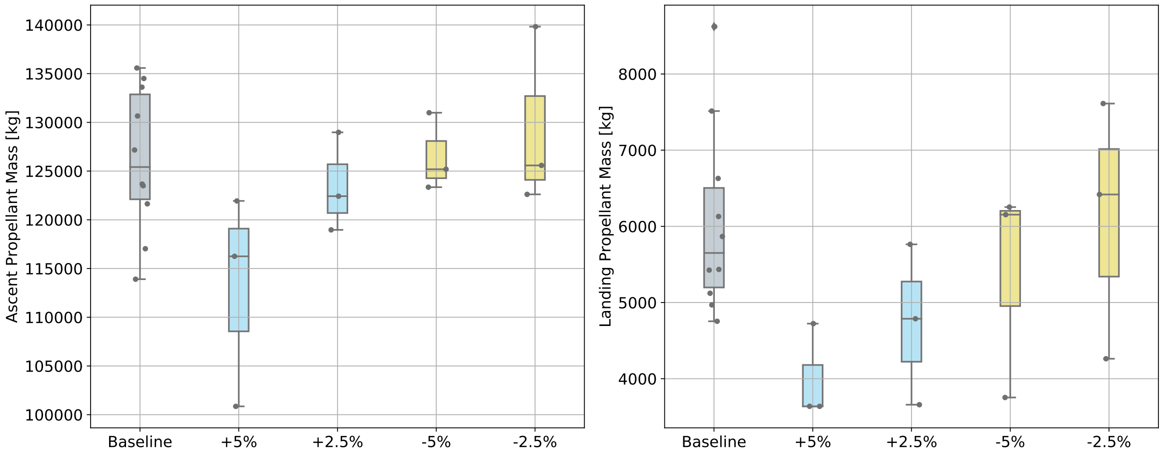

Figure 9.11: The ascent and landing propellant masses for all propulsion system efficiency cases

As can be seen in Figure 9.11, there is a clear relationship between the both ascent and landing propellant masses, and the propulsion system efficiency. In increase in the factors allows for less propellant to be consumed to deliver the same thrust and therefore less propellant is needed. This is also evident from the landing propellant masses, as high thrust must be delivered to perform the retroburn, and therefore a higher efficiency delivers a higher thrust. The engine and total thrust for all cases is given in Figure 9.12.

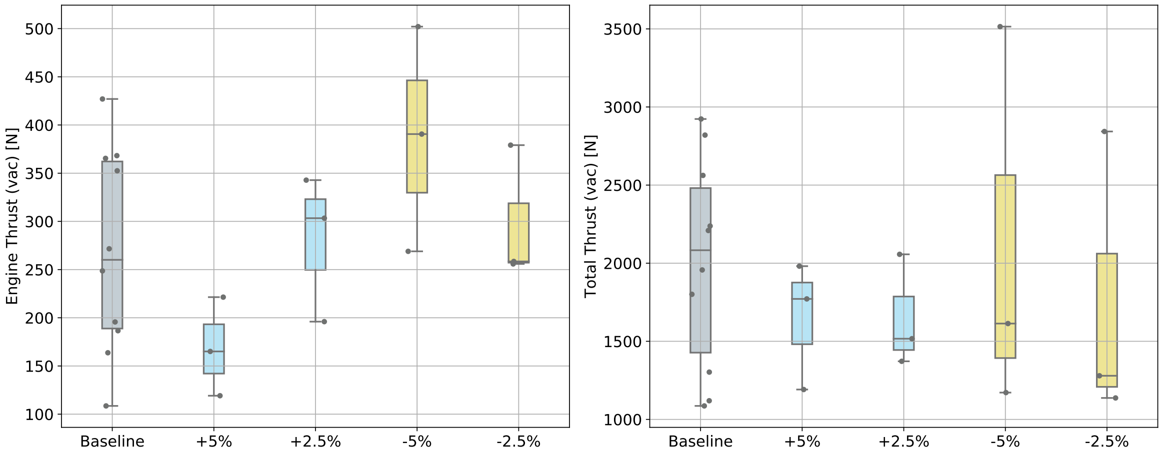

Figure 9.12: The engine and total thrust for all propulsion system efficiency cases

From Figure 9.12, interestingly however, it is observed that the less efficient cases, -5% and -2.5%, have a higher engine thrust level than the higher efficiency cases, +5% and +2.5%. This is contradictory to the expected results, however these solutions may arise from the design needing to compensate for a lower thrust level. The total thrust levels show the opposite relationship, namely that the total thrust of the -5% and -2.5% cases show average total thrust levels that are less than the +5% and +2.5% cases. The relationship between the total thrust and propulsion efficiency, however, is not as distinct as for the engine thrust levels. Overall, however, from the results it is clear that a higher propulsion efficiency results in lower GTOW values. The design variables, engine properties, and mass breakdown for each solution per case can be found in Appendix E.2.

10

Conclusions and Recommendations

Throughout this report the context of the research, its methodology, and the obtained results are presented. In this chapter, the conclusions of the results and the recommendations for future work are given. the conclusions are first presented with respect to the original research questions and the sensitivity analyses in Section 10.1, and the recommendations discussed in Section 10.2.

10.1. Conclusions

As the frontier of human space exploration is pushed ever further, sights have been set on Mars as the next stepping stone for human space exploration. Beyond a first crewed Martian landing, the desire to establish a permanent and self-sustaining settlement on Mars presents space agencies and private companies alike with the challenge of how to best approach such a goal. Over the decades many concepts have been proposed, and in 2017, NASA's ISRU-to-the-wall campaign presented a mission plan that determined the transport between the two planets to be managed by interplanetary vehicles journeying between orbital nodes [4]. The orbital nodes are placed in orbits about both Earth and Mars and act as portals for the crew and cargo before they embark on either the interplanetary journey, or the descent to its respective planet's surface. As a means of movement between such a node and the surface is required, the need for reusable space transportation therefore on Mars becomes clear.

Concepts for a shuttle vehicle that fulfils this need have been proposed by Komar et. al. [38] and Gaffarel et. al. [22], however as of yet no global optimisation scheme has been applied to obtain designs for the vehicle and its trajectories. For this, a Multidisciplinary Design Optimisation (MDO) scheme is chosen, as it has been shown to be highly successful for complex and non-linear design problems, such as the design of launch vehicles. The Gross Take Off Weight (GTOW) is identified as the objective function for the optimisation. Typically, the reduction of the costs is usually the driving factor, however a cost estimate for the shuttle vehicle is exceedingly difficult. Not only is its realisation still decades away, meaning technology and their costs will most likely evolve, but the estimation of the shuttle's transport to Mars, its operational costs, and maintenance costs are also extremely difficult to estimate. The GTOW of a vehicle, however, is highly influential to its cost, and therefore can serve as a proxy.

The results of this research may aid the allocation of the design and engineering efforts to the dominant factors that affect the vehicle and trajectory design. The vehicle design may further provide a preliminary vehicle concept from which further research may take cues, and the performance of the chosen meta-heuristic optimisation method may also be of value as such a method has not yet been applied to a reusable launch vehicle on Mars. This thesis has presented an answer to the original research question, stated below:

Research Question:

What is the optimal design of a crewed reusable Martian single-stage-to-orbit shuttle vehicle and its trajectory in terms of its gross take off weight?

To determine the optimal design of the shuttle vehicle, the mission scenario is first identified. The vehicle must transport a mass of 1200 kg, including 6 crew, to and from an orbital node placed in a circular orbit at an altitude of 500 km. The orbital node is placed in the same orbit as in the mission scenarios for the Hercules and Charon vehicle concepts, designed by Komar et. al. [38] and Gaffarel et. al. [22], respectively. The Martian base is set to the same location as in the mission scenario of the Charon vehicle, at 42.5° North and 25.5° East. The phasing orbit to which the vehicle ascends prior to docking is a circular orbit at 44.96° inclination and 607.74 km altitude, the same as the Charon vehicle. The rendezvous and docking stages of the mission are not simulated in the optimisation, however the necessary propellant to execute the manoeuvres is taken into account in the vehicle GTOW. The Entry, Descent, and Landing (EDL) phase is initiated using the same conditions as the Charon vehicle, at an altitude of 80 km and at a velocity of 3500 m/s. The total mission scenario is therefore same as the Charon vehicle's, and the design obtained by the MDO scheme can be compared.

The MDO optimisation is run for 10 seeds, and therefore 10 optimum baseline solutions are found, of which the GTOW values range from 146.2 tonnes to 171.4 tonnes. As the Charon vehicle's GTOW value is 168.1 tonnes, this indicates that the application of an MDO scheme to the design of the shuttle vehicle yields significant mass reductions. With the 10 simulated seeds, mass reductions of more than 20 tonnes are observed, which could possibly be more if more seeds are simulated. The application of the MDO is therefore successful in exploring the design space, and performs well in obtaining designs that are preferable to those obtained through sequential design. It also shows promise for single-stage-to-orbit launch vehicle related applications, and could potentially be applied to higher-level designs. The design variables for the optimum vehicle and associated trajectory are given in Tables 10.1 and 10.2, and the final engine performance and mass breakdown of the vehicle is given in 10.3.

Table 10.1: The trajectory design variables found for the baseline scenario

Trajectory Design	**Value**
Node 1 [deg]	86.205
Node 2 [deg]	58.012
Node 3 [deg]	63.165
Node 4 [deg]	42.330
Node 5 [deg]	13.578
Node 6 [deg]	0.075
Min TW [-]	1.701
Max TW [-]	2.525
Entry γ [deg]	-3.620
Entry δ [deg]	27.755
Entry τ [deg]	-9.011
Entry α [deg]	57.292
Retroburn altitude [m]	2125

Table 10.2: The uncertain variables and their respective bounds for the EDL Sobol' analysis

Vehicle Design	**Value**
Mass flow [kg/s]	51.974
Chamber pressure [Pa]	18110229
O/F ratio [-]	3.618
Engine number [-]	6
Ascent propellant mass [kg]	113905
Landing propellant mass [kg]	4754
Engine exhaust diameter [m]	0.902
Vehicle diameter [m]	7.469

Table 10.3: The engine performance and mass breakdown of the optimum solution found for the baseline scenario

Final Design	**Value**
Specific impulse (vac) [s]	387.770
Engine thrust (vac) [kN]	186.575
Totalthrust (vac) [kN]	1119.453
Dry mass [kg]	23141
Total propellant mass [kg]	123084
GTOW [kg]	146226

The differences in GTOW values between the 10 obtained baseline solutions stem predominantly from differences in ascent propellant mass, which is also the reason the GTOW value of the optimum MDO vehicle is less than the Charon's GTOW. This can be attributed to differences in the ascent thrust profile, as well as in the ascent strategy and engine design. Both vehicles' thrust profiles are a linear increase from a minimum to a maximum Thrust to Weight (TW) ratio. Though both vehicle's minimum TW ratios lie around 1.5, the Charon vehicle's maximum TW ratio is 4, whereas those found by the MDO all lie below 2.6, indicating that a high TW ratio introduces inefficiencies with respect to the propellant consumption. These inefficiencies could also be influenced by the thermodynamic properties of the propellants, as the Charon mixture ratio is significantly lower than those of the MDO solutions', comparing 3.12 to on average 3.6, respectively. The mixture ratio influences the thrust produced by the propulsion system due to the stoichiometric properties it determines, and therefore also influences the vehicle mass. The Charon ascent strategy is further comprised of a gravity turn, followed by a coast and an attitude correction once the target orbit is reached. However, the vehicles in the MDO are all injected directly into the orbit, eliminating the need for an attitude correction. These factors all contribute to the reduced ascent propellant mass of the MDO solutions compared to the Charon vehicle's.

The EDL profiles of the MDO solutions show a great variance, indicating that the EDL phase is not as constrained as the ascent, as well as not as influential to the GTOW as the ascent is. The landing propellant of the Charon vehicle is actually less than those found by the MDO scheme. This is due to the different landing constraints placed upon the trajectory, as the Charon vehicle lands with a velocity of 6.1 m/s, and the MDO vehicles land with a maximum velocity of 2.5 m/s, leading to a higher propellant mass for the MDO solutions. Nonetheless, the gains in landing propellant mass are less than the reduction in ascent propellant mass, as the GTOW is still less for the solutions found by the MDO scheme.

These solutions serve as the baseline scenario, to which the other solutions found can be compared, and the effects of the changes in conditions observed. The research question is broken down into three further subquestions, answered individually below.

Subquestion 1: *How does the mission scenario affect the GTOW?*

The mission scenario can be separated into two factors, namely the target orbit, and the Martian base location. They are both assessed individually below.

Target Orbit

The target orbit has a very large influence on a vehicle's design, affecting not only the delta-V necessary to reach the orbit itself, but also the delta-V necessary to rendezvous with the node. To investigate the effect of the target orbit, two other mission scenarios are evaluated, namely the scenario determined by Komar et. al. for the Hercules vehicle [39], and a direct ascent scenario to the node. Although a direct ascent is considered too high-risk to ever be implemented in practice, it is an interesting hypothetical scenario to which other solutions can be compared. The Hercules target orbit is an elliptical orbit with an eccentricity of 0.0178, a pericentre altitude of 108 km, and an inclination of 43.9°. The EDL phase is initiated at an altitude of 132 km with a velocity of 3200 m/s. In the direct ascent scenario, the vehicle is injected directly into a circular orbit of 500 km altitude at an inclination of 44.96° (the same as the baseline). The same EDL initial conditions are taken for the direct ascent, as for the baseline. As the Hercules scenario may be compared to the Hercules vehicle designed by Komar et. al. [38], 10 seeds are used to obtain 10 solutions. For the direct ascent 3 solutions are found using 3 different seeds.

The results indicate that the Hercules mission scenario is easily the most GTOW-optimal strategy of the three explored. Where the most optimum design for the baseline is found to have a GTOW of 146.2 tonnes, the optimum for the Hercules case is only 103.0 tonnes. The direct ascent also indicates a mass benefit of launching to a lower target orbit, as its optimum GTOW is found to be 127.2 tonnes. Evidently, though more delta-V is needed for the Hercules vehicle to transfer from its phasing orbit to the orbital node, the total ascent still requires less propellant than ascending directly to the orbital node, as well as to a higher phasing orbit. The gravity losses introduced with increasing target orbit altitude evidently greatly affect the GTOW of the vehicle, as the differences in GTOW stem from ascent propellant mass reduction.

The target orbit and rendezvous strategy also have a clear effect on the design of the propulsion system. The minimum and maximum TW ratios for the Hercules vehicle are higher than for both the baseline and direct ascent cases, at 2.3 and 3.8 for the Hercules, respectively. The orbital velocity at 108 km (Hercules scenario) is higher than the orbital velocities at 607 km (baseline scenario) and 500 km (direct scenario), and in order to propel the vehicle to the required velocity in only 108 km vertical distance, higher TW ratios are required. The total thrust delivered by the propulsion system for the Hercules case is therefore almost double that of both the baseline and the direct ascent cases. The EDL initial condition differences, although affecting the trajectory, have a much less significant effect on the GTOW. The ascent is evidently the most influential component of the mission scenario.

The results found by the MDO for the Hercules case may also be compared to the designed vehicle by Komar et. al. [38]. As stated, the optimum GTOW found using the MDO is 103.0 tonnes, which is value much smaller than the Hercules vehicle, that has a GTOW values of 162.8 tonnes. This difference of almost 60,000 kg is a considerable mass reduction, however the Hercules vehicle transports a payload mas of 5750 kg to orbit, and the MDO vehicle a payload of 1200 kg. The payload mass of almost 5 times the MDO vehicle's amount undoubtedly greatly influences the propellant mass necessary for every stage of the mission. Therefore the performance of the MDO scheme cannot be directly quantified through the comparison, as the payload masses differ. However, the two vehicle designs are very similar in terms of engine performance, with the greatest differences in design being the propellant masses.

Martian Base Location

The latitude of the Martian base dictates the minimum inclination attainable by a launch vehicle without the launch vehicle executing additional manoeuvres, and it also in part determines the delta-V required to reach an orbit. The closer a launch location is to the planet's equator, the more it can exploit the planet's rotational velocity at that location. A location that is closer to the equator is, therefore in theory, preferable. To investigate this, two other latitude locations are investigated, namely the midway point between the original latitude and the equator, 21.25°, and one very close to the equator, 5°. For both new locations three solutions are obtained using 3 different seeds.

Both the lower latitude locations obtain lower optimum GTOWs and average GTOWs than the baseline case, with the 21.25° case obtaining an optimum GTOW of 141.1 tonnes, and the 5° case a GTOW of 146.0 tonnes (200 kg less than the baseline of 146.2 tonnes). Evidently, although the 5° optimum is lighter than the baseline, it is only marginally so, as well as it being heavier than the optimum GTOW of the 21.25° case. This could be due to a number of factors. Firstly, the number of seeds run for both cases may not allow for a representative behaviour to be observed. The 5° case may, therefore have many lighter solutions, and conversely, the 21.25° case's optimum of 141.1 tonnes may be an outlier. Furthermore, the difference in rotational velocity between the 21.25° location and the baseline is 3 times the difference in rotational velocity between the 21.25° and the 5° case. Therefore, this means that the 21.25° case's solutions are much more similar to the 5° solutions than to the baseline. This is reflected in the results, as the average GTOWs of the 5° and 21.25° cases are very close. This, in combination with the number of seeds run, may be the underlying cause of the unexpected greater GTOW for the 5° case compared to the 21.25° case.

Subquestion 2: *How do the mission constraints affect the GTOW?*

The mission scenario can be separated into two factors, namely the payload capacity, and the fact that the mission is crewed. They are both assessed individually below.

Payload Capacity

The payload capacity is influential to the performance of a vehicle as it must be injected into orbit, and then decelerated upon landing. A higher payload mass therefore instinctively should require a greater propellant consumption for both the ascent and the EDL phases. Two different payload masses than the baseline mass are explored, namely a +50% case and a -50% case, leading to payload masses of 1800 kg en 600 kg, respectively. For each case, three solutions using 3 different seeds are obtained.

The expected effect of the payload mass on the GTOW value is reflected in the results. The +50% payload case yields an optimum solution with a GTOW of 162.7 tonnes. The optimum solution of the -50% case has a GTOW of 149.7 tonnes, which is in fact greater than the baseline optimum of 146.2 tonnes, however, the average GTOW of the three -50% payload case is less than the baseline case. The average of the -50% case lies at 156 tonnes, whereas the average of the baseline case lies at 162 tonnes. Therefore, although the lowest GTOW of all payload cases is in fact the baseline, the general trend of the payload mass is that with decreasing mass, the GTOW also decreases. The fact that the optimum baseline case has a lower GTOW than the optimum -50% payload case could also be due to the higher number of seeds run, as 10 solutions are found for the baseline case, compared to 3 for the -50% payload case. The change in payload mass also has a direct effect on the propulsion system, namely on the total vehicle thrust. The -50% payload case is designed for a total thrust of 836 kN, where as the baseline case is designed for 1119 kN, and the +50% case is designed for 1156 kN, indicating that a higher thrust is needed to transport greater masses.

The Presence of Crew

The presence of crew on the vehicle imposes stricter limitations on the maximum load the vehicle may experience throughout the mission. When crew are transported, this limit is set to 4 g_{mars}, thereby constraining the maximum acceleration during both the ascent and the propulsive landing. It is valuable to explore what effect this limitation has on the optimum design of the shuttle vehicle, and the maximum load is therefore increased to 10 g_{mars}. Three solutions are found using three different seeds.

The increase of the maximum load constraint has no remarkable effect on the GTOW values. The optimum solution for the 10 g load case is found to have a GTOW value of 156.5 tonnes, which is 10,000 kg heavier than the optimum baseline solution. However, the range of the GTOW values for the 10 g load case are within those of the baseline case, and therefore lead to similar GTOW values with no significant relative increase or decrease. As observed in the baseline scenario, the ascent propellant is the dominant contributor to the GTOW, and as the optimum solutions' maximum TW ratios do not exceed 2.6, lifting the maximum load from 4 g to 10 g does not offer any advantage for the ascent.

Although no changes in GTOW are seen, other differences in design do arise from increasing the maximum load, namely in the EDL phase of the mission. The the 10 g limit allows for the 10 g solutions to reduce their retroburn altitude as their deceleration capabilities are increased. The efficiency of a propulsive landing with respect to propellant usage is also increased by increasing the thrust during the landing. However, contrary to expectations, the landing propellant consumption is not reduced, but rather increased. This can most likely be attributed to the functioning of the optimiser. As the ascent is the aspect of the design where most GTOW reductions are possible, this is the focus of the optimiser. The 10 g limit facilitates widening the margins between which the vehicle is capable of landing. The landing is therefore not optimised as much as the baseline case, leading to a higher landing propellant consumption.

Subquestion 3: *How do different ascent thrust profiles affect the GTOW?*

As the ascent propellant mass is the main contributor to the vehicle's GTOW, and its reduction is the focus of the optimisation. Optimising the ascent includes the thrust profile. As the thrust is constrained by a maximum load, the thrust profiles are expressed in TW ratios. The baseline case implements a linear TW relationship between a minimum and a maximum, however two other profiles are investigated, namely a constant TW ratio, and a quadratic thrust law.

From the results, it is interesting to see that the convergence toward an optimum GTOW value is much higher for the thrust law 0 case than for the baseline and thrust law 2 cases. Although the baseline case still has the lowest GTOW value of 146.2 tonnes, compared to 148.0 tonnes for thrust law 0, and 157.1 tonnes for thrust law 2, the average GTOW lies much lower for the thrust law 0 case, at 151 tonnes compared to 162 tonnes for the baseline. All three GTOW values found for the thrust law 0 case are within 4 tonnes of each other, whereas the baseline case's GTOWs are spread over more than 20 tonnes.

This convergence is reflected in the design of the three thrust law 0 case's vehicles and trajectories. The thrust law 0 thrust ascent profile is determined solely by its maximum TW ratio, therefore it is much more constrained. The values for the engine mass flow, chamber pressure, and engine number all show a much higher convergence than the other two thrust laws, resulting in very small ranges for the engine thrust and total thrust values. The thrust law 0 case even obtains a result for the ascent propellant consumption that is lower than the baseline case, however due to it higher landing propellant mass, its overall GTOW mass is still higher than that of the baseline case.

Although the thrust law 0 shows very high performance in terms of GTOW, this convergence of the design may also be due to the more constrained nature of the problem. Although a high number of variables allows for a great breadth of vehicle and trajectory designs to be explored, it also exponentially increases the complexity and therefore computational power necessary to obtain solutions. As the thrust law 0 case is run for the same number of generations, however utilises one less design variable, namely the minimum TW ratio, it is more constrained and more efficient in its optimisation. It is still unclear whether the convergence of the design is due to the thrust law itself, or due to the optimisation, however these influences must be kept in mind.

Sensitivity Analysis

The sensitivity of the obtained results, as well as the MDO as a whole, is very valuable. It determines the aspects of the design that are most influential, as well as highlighting the effects of the uncertainties. A sensitivity analysis is performed on the optimum vehicle found for the baseline scenario, as well as the MDO as a whole.

Sensitivity of the Optimum Design

The sensitivity of the optimum design to uncertainties in the design variables and other influential variables such as initial conditions is quantified by applying a variance-based global sensitivity analysis, namely a Sobol' analysis [62]. This method determines the relative influence of a variable on the outcome with respect to the other uncertain variables, in terms of first-order effects (one at a time) and total effects (all variables varied). The vehicle's ability to reach the target orbit (in terms of pericentre, eccentricity, inclination) and to land within the constraints (with respect to latitude, longitude, landing velocity, and landing pitch angle) is evaluated.

The sensitivity of the pericentre and the eccentricity to changes in design variables are very similar, with both parameters being the most sensitive to the final pitch node value, followed by the fourth pitch node value, and the mixture ratio for both the first-order and total effects. The total order effects are greater than the first-order effects, indicating that there is interference between the variables. The inclination, however, is sensitive to almost only the first pitch angle node, with all other variables having comparatively little to no influence. For all three parameters, however, the minimum TW ratio has a greater influence than the maximum TW ratio.

The sensitivity of the EDL phase is evaluated with respect to design variables, as well as all the initial conditions. As the simulation has a positional uncertainty of 100 m this is needed, and in reality there will also always be a margin or uncertainty. The landing location is shown to be highly sensitive to the initial flight path angle, with both the first order and total effects dominated by the flight path angle effects. The final velocity and final pitch angle are shown to be most affected by the retroburn altitude, however both parameters are not greatly sensitive with respect to first order effects. On the other hand, both parameters are highly sensitive to all uncertain variables with respect to total order effects, indicating high interference between all the variables. The propulsive landing is therefore an extremely volatile manoeuvre that necessitates extremely high accuracy of variables for safe execution.

Sensitivity of the MDO scheme

There are, of course, also uncertainties and assumptions made in the MDO scheme models. The Missile DATCOM software, although sufficient for the research presented here, is not fully validated for the range of Mach numbers and drag coefficients it is utilised for. This leaves a great uncertainty with respect to the accuracy of the calculated coefficients. The thrust efficiency and the propellant efficiency are also aspects of the model that is determined by averaging the model's performance with respect to just 4 other engines. The presence of uncertainties in these variables is therefore also evident. The MDO's sensitivity to these two variables is therefore investigated.

The model's sensitivity to the aerodynamic coefficients is tested by varying the coefficients by +15%, +5%, -15%, and -5%, and the results show a clear influence of the aerodynamics on the GTOW obtained. The GTOWs found for the increased coefficients are greater than the baseline, and equally, the decreased GTOWs values are lower, with the lowest found for the -15% case and the highest found for the +15% case. Greater coefficients induce a higher drag force on the vehicle, and as the ascent is the bottleneck of the design, this increases the ascent propellant, resulting in higher GTOWs. However, interestingly, the landing propellant masses for the increased coefficients also increases. This, however, was due to the solutions found for the decreased coefficients experiencing skipping due to the higher lift forces. The skipping entry decreases the velocity before retroburn, and the dry masses of the vehicles are also less due to the smaller propellant masses, leading to lower landing propellant masses. The engine thrust is not seen to be greatly affected by the aerodynamic coefficients, however the total engine thrust is seen to be affected in the same way as the GTOW. The vehicle thrust increases with increasing aerodynamic coefficients, to overcome to additional aerodynamic forces.

The model's sensitivity to the propulsion efficiency factors, namely the thrust quality factor and the propellant consumption quality factor, is tested by varying the factors by +5%, +2.5%, -5%, and -2.5%. It is clear from the results obtained that there is a relationship between the quality factors and the GTOW, as a higher quality factor, meaning a higher propulsion efficiency, results in a lower GTOW. A higher efficiency allows for less propellant to be necessary to deliver the same thrust level, and therefore results in less ascent propellant as well as significantly less landing propellant. The optimum engine thrust is seen to have the inverse relationship to what is expected, namely that the engine thrust increases with decreasing efficiency, perhaps to compensate for the lower efficiency. The total vehicle thrust, however, is less affected by the change in quality factors than the engine thrust, however the effect is the opposite to the engine thrust, such that greater propulsion efficiency results in higher total thrust.

All the research questions posed have been effectively answered, with clear conclusions drawn for all questions, with the exception of the Martian base location, where a more robust investigation should be performed to solidify the reasoning behind the results. Is is evident from the baseline solution that the MDO scheme is successful in obtaining designs for the vehicle and trajectories, and that it is an effective method to apply to a design problem such as a launch vehicle on Mars.

10.2. Recommendations

The design process throughout this research, as well as the results, shed light on interesting topics worthy of further investigation, as well as drawbacks of the methods used. This section identifies these topics, and discusses the model's the weaknesses and their potential solutions or improvements. They are listed below, categorised into their various topics.

Vehicle Design

The design of the vehicle in this research is performed on a very conceptual level, with little to no attention given to potentially influential geometric factors, such as the nose cone shape. Though Missile DATCOM is a powerful tool to determine the aerodynamic coefficients, it has drawbacks in terms of the available blunt nose cone shapes, and therefore this aspect remains uninvestigated. Although for the conceptual nature of this research it may be left unoptimised, it is necessary to understand the influence of the nose geometry on the trajectory, and on the vehicle performance.

Further, the research performed in this study concerns no moment control, and therefore the addition of lifting surfaces, reaction control systems, or 6 Degrees Of Freedom (6DOF) control algorithms is unnecessary. This study shows promising results for the feasibility of such a shuttle vehicle, however it is necessary for this topic to be investigated further by including a 6DOF simulation and research. Such a simulation would also open up possibilities for geometrical and reaction control system optimisation, such as fins and thrusters.

As the mission scenario of the vehicle is the same as that of the Charon vehicle, many masses of the Charon vehicle are taken for various subsystems and structures. As this is research is conducted in a very conceptual level, this is possible, however for continued research, these masses must be determined with greater accuracy.

Aerodynamic Modelling

As discussed in Chapter 5, Missile DATCOM can be used to obtain aerodynamic coefficient data for Martian atmospheres for certain ranges of angle of attack and Mach numbers. However, no appropriate data is available to validate the Missile DATCOM drag coefficient calculation for angles of attack below 40°, as well both lift and drag coefficients at any velocities lower than Mach 2. This leaves a knowledge gap for a highly influential range of drag coefficients as these are dominant during the ascent, and as well as no information regarding the accuracy of the coefficients around the transsonic regime. It is known that the Missile DATCOM version used in this research overestimates the wave drag around the transsonic regime, however this cannot be tested or quantified for Martian conditions. As most of the mass reductions are due to reductions in ascent propellant, the gap in this knowledge could lead to inaccurate estimations of the GTOW, which is supported by the aerodynamics model sensitivity analysis. Therefore a different method of determining the aerodynamic coefficients should be applied, or a newer version of Missile DATCOM should be utilised in future.

Trajectory Design

The optimisation method applied the trajectories has shown to be powerful enough to obtain solutions that minimise the GTOWs effectively. However, as mentioned in the vehicle recommendations, the simulations do not concern any moment control, and therefore no sizing of the reaction control systems is performed, and the moments that are necessary to change and maintain the vehicle's attitude are not calculated. Should the research be continued, a simulation that includes 6DOF is necessary to understand the feasibility of the trajectories designed.

Further, the design of the ascent and the EDL phases is kept simple to reduce the number of design variables. 6 pitch angle nodes is used for the ascent, however this is less than the numbers of nodes used by Haex [23] and Rozemeijer [58]. A higher number of nodes increases the accuracy of the trajectory, and therefore increasing the number of nodes also increases the optimisation possibilities. This is therefore an area where greater optimisation may be possible. Further, the angle of attack is not modulated throughout the gliding entry. Its control could therefore lead to more optimum solutions.

Optimisation Scheme

For an optimisation, there is always a trade-off between the design detail and computational effort. A higher number of design variables leads to a more detailed design and thus a greater search space. However, with each added design variable, the optimisation complexity and subsequently also the computational effort, is increased. Although the search space is broadened when including a high number of design variables, this may affect the optimisation adversely, due to the increased scope of the optimisation.

As seen in the baseline scenario, there is little convergence of the design variables. There are, of course, many different possibilities for the design, however the lack of convergence may indicate that the global optimum is not yet reached. This may be due to the number of design variables present in the optimisation. For thrust case 0, the number of design variables were reduced, and the results converged to much more similar values, as well as the GTOW average being reduced. The identification of the most influential design variables should be considered, such that only the variables with the greatest influence are optimised for.

Result Analysis

In order to understand the effect of different parameters on the behaviour of the results, three seeds are run in each new case. This, however, may not accurately represent the actual behaviour, or influence. Comparing the behaviour of the results of 10 baseline seeds to the behaviour of 3 seeds may not be representative. This is perhaps seen when comparing the latitude locations' results. This choice is made to reduce the time necessary to obtain the results, however this affects the analysis that is possible. This is an aspect that must be taken into consideration when comparing any optimisations that require seeds and multiple runs to determine their convergence.

A

Martian Atmospheric Model Development

The MCD is commercially available online[1], from which various atmospheric properties can be gathered for altitudes ranging from 0 to 250 km. Tudat allows custom atmospheric models as input in table form, for which the available dependent variables are the local density, pressure, temperature, gas constant, molar mass, and specific heat ratio. The local density, pressure, and temperature as a function of altitude are directly available from the MCD.

The local gas constant, molar mass, and specific heat ratio have to be calculated using other available properties. The mass ratios of each gas present, namely CO_2, Ar, N_2, CO, and O_3, are calculated using each gas' mass column data given by the MCD using Equation A.1, where m_g denotes the mass of the respective gas, and m_T the total mass, given in kg/m^2.

$$\frac{m_g}{m_T} = \frac{m_g}{m_{CO_2} + m_{Ar} + m_{N_2} + m_{CO} + m_{O_3}} \tag{A.1}$$

Using the gas' mass ratios, the atmosphere's molar mass can be found using the known molar mass of each gas. This is done using Equation A.2, where each gas' molar mass is given in Table A.1 as calculated using the chemical composition calculator on WebQC[2]. M_{tot} denotes the molar mass of the gas composition at each specific altitude.

$$M_{tot} = \frac{m_{CO_2}}{m_T} M_{CO_2} + \frac{m_{Ar}}{m_T} M_{Ar} + \frac{m_{N_2}}{m_T} M_{N_2} + \frac{m_{CO}}{m_T} M_{CO} + \frac{m_{O_3}}{m_T} M_{O_3} \tag{A.2}$$

Table A.1: The molar masses of each element present in the Martian atmosphere

Gas	**Molar Mass [g/mol]**
CO_2	44.01
Ar	39.95
N_2	28.01
CO	28.01
O_3	48.00

The specific gas constant of each gas can then be found using Equation A.3, where R denotes the universal gas constant and $R_{s,g}$ the specific gas constant for the gas with molar mass M_g. The specific gas constant for the atmosphere at each altitude is then found using mass fractions, as seen in Equation A.4.

---

[1] `http://www-mars.lmd.jussieu.fr/mars/access.html`

[2] `https://www.webqc.org/mmcalc.php`

$$R_{s,g} = \frac{R}{M_g} \tag{A.3}$$

$$R_s = \frac{m_{CO_2}}{m_T} R_{s,CO_2} + \frac{m_{Ar}}{m_T} R_{s,Ar} + \frac{m_{N_2}}{m_T} R_{s,N_2} + \frac{m_{CO}}{m_T} R_{s,CO} + \frac{m_{O_3}}{m_T} R_{s,O_3} \tag{A.4}$$

The ratio of specific heats for each altitude (R_s) can then be found using the local specific gas constant, and the molar heat capacity as constant pressure, c_p. The molar heat capacity as constant volume, c_v, is found first using Equation A.5, from which the ratio of specific heats (γ), given in Equation A.6, can then be determined. The (shortened) atmosphere model used for the simulations can be found in Table A.2.

$$c_v = R_s - c_p \tag{A.5}$$

$$\gamma = \frac{c_p}{c_v} \tag{A.6}$$

Table A.2: The atmospheric model implemented in Tudat using the MCD

Altitude [m]	**Density [kg/m^3]**	**Pressure [Pa]**	**Temp. [K]**	**Specific gas constant [J/kg/K]**	**Specific heat ratio** [-]	**Molar mass [mol/kg]**
0.00	2.255420e-02	8.217790e+02	185.866	189.905622	1.352862	0.043782
7352.94	1.061770e-02	4.105170e+02	203.197	189.905622	1.338705	0.043782
14705.90	5.470160e-03	1.983090e+02	190.172	189.905622	1.349167	0.043782
22058.80	2.707680e-03	9.082060e+01	176.003	189.905622	1.361878	0.043782
29411.80	1.249290e-03	3.939870e+01	165.454	189.905622	1.372435	0.043782
36764.70	5.458150e-04	1.632430e+01	157.017	189.905622	1.381675	0.043782
44117.60	2.275750e-04	6.510500e+00	150.189	189.905622	1.389745	0.043782
51470.60	9.045730e-05	2.520760e+00	146.424	189.905622	1.394437	0.043782
58823.50	3.438900e-05	9.777780e-01	149.738	189.905622	1.390256	0.043782
66176.50	1.349450e-05	3.871780e-01	150.764	189.905622	1.388959	0.043782
73529.40	5.371580e-06	1.544170e-01	151.186	189.905622	1.388326	0.043782
80882.40	2.172940e-06	6.167060e-02	148.671	189.905622	1.391083	0.043782
88235.30	8.999500e-07	2.383620e-02	138.719	189.905622	1.403262	0.043782
95588.20	3.420380e-07	8.712080e-03	132.630	189.905622	1.410073	0.043782
102941.00	1.258120e-07	3.114360e-03	127.843	189.905622	1.413990	0.043782
110294.00	4.504050e-08	1.080300e-03	122.002	189.905622	1.416237	0.043782
117647.00	1.518590e-08	3.747360e-04	123.293	189.905622	1.404916	0.043782
125000.00	5.194570e-09	1.424050e-04	134.871	189.905622	1.380121	0.043782
132353.00	1.967840e-09	5.997580e-05	145.925	189.905622	1.358387	0.043782
139706.00	8.265560e-10	2.742140e-05	153.423	189.905622	1.340816	0.043782
147059.00	3.759140e-10	1.334940e-05	157.811	189.905622	1.325299	0.043782
154412.00	1.813330e-10	6.843950e-06	160.232	189.905622	1.310249	0.043782
161765.00	9.168990e-11	3.676790e-06	161.558	189.905622	1.295056	0.043782
169118.00	4.825720e-11	2.063320e-06	162.299	189.905622	1.279796	0.043782
176471.00	2.624170e-11	1.204050e-06	162.726	189.905622	1.264733	0.043782
183824.00	1.489570e-11	7.331420e-07	162.957	189.905622	1.250363	0.043782
191176.00	8.899830e-12	4.669890e-07	163.085	189.905622	1.237658	0.043782
198529.00	5.372810e-12	3.040850e-07	163.177	189.905622	1.225744	0.043782
205882.00	3.430190e-12	2.061040e-07	163.223	189.905622	1.216002	0.043782
213235.00	2.219530e-12	1.425610e-07	163.258	189.905622	1.207378	0.043782
220588.00	1.491290e-12	1.012980e-07	163.277	189.905622	1.200438	0.043782
227941.00	1.012440e-12	7.321150e-08	163.291	189.905622	1.194375	0.043782
235294.00	7.162620e-13	5.438950e-08	163.299	189.905622	1.190038	0.043782
242647.00	4.974180e-13	4.044860e-08	163.307	189.905622	1.185445	0.043782
250000.00	3.704430e-13	3.126550e-08	163.311	189.905622	1.183108	0.043782

B

Repeat Orbit Calculation

Repeat orbits can be calculated in various ways, however the method prescribed by Wertz is addressed here [68]. To find the semi-major axis of an orbit that must repeat x times a day, an initial semi-major axis $a0$ is first calculated by Equation B.3 for the orbit. Using this initial guess, the subsequent orbital perturbations caused by J_2 on the right ascension of the ascending node ($\dot{\Omega}$), argument of periapsis ($\dot{\omega}$), and mean anomaly ($\dot{M}$) are calculated, using Equations B.4, B.5 and B.6. The mean angular motion (n) is then further calculated using Equation B.7, and from this value, another value for the a can be found. μ_m denotes the gravitational parameter of Mars, T_m the sidereal rotational period of Mars, R_m the mean Martian radius, $J2$ the J2 constant for Mars, j the number of orbits before repeat, k the number of days before repeat, and $\dot{L}$ the rotational rate of Mars.

$$k_1 = \mu_m^{1/3} \frac{2\pi}{T_m}^{-2/3} \tag{B.1}$$

$$k_2 = 0.75 J_2 \sqrt{\mu_m} R_m^2 \tag{B.2}$$

$$a0 = k_1 \frac{j}{k}^{-2/3} \tag{B.3}$$

$$\dot{\Omega} = -2 k_2 a^{-7/2} \cos i (1 - e^2)^{-2} \tag{B.4}$$

$$\dot{\omega} = k_2 a^{-7/2} (5 \cos i^2 - 1)(1 - e^2)^{-2} \tag{B.5}$$

$$\dot{M} = k_2 a^{-7/2} (3 \cos i^2 - 1)(1 - e^2)^{-2} \tag{B.6}$$

$$n = \frac{j}{k}(\dot{L} - \dot{\Omega}) - (\dot{\omega} + \dot{M}) \tag{B.7}$$

$$a = \left[\frac{\mu_m}{\left(\frac{n}{T_m} \frac{\pi}{180} \right)^2} \right]^{1/3} \tag{B.8}$$

By knowing that the orbit node lies at 500 km altitude, the semi-major axis must therefore be 500 km added to the Martian radius. The value for the number of repeats per day was found using trial and error, by testing which value would output the correct semi-major axis (varying j as input, k equal to 1). This is 11.7 repeats per day. An accuracy setting of 1 m is implemented for the iterations (1 decimal place more than the given values), meaning that if the difference between a and $a0$ is larger than 1 m, then the a calculated from n is be used to recalculate, starting from Equation B.4, until difference is less than 1 m.

C

MDO Results

This appendix presents all the results found using the MDO scheme for all scenarios investigated.

C.1. Baseline Results

Table C.1 and C.2 present the design variables, engine properties, and mass breakdown for the optimum solutions found for the baseline scenario for seeds 100-500 and 600-1000 , respectively.

Table C.1: The design variables for the optimum solutions found for seed 100-500 for the baseline case

Baseline	**Seed 100**	**Seed 200**	**Seed 300**	**Seed 400**	**Seed 500**
Optimum Trajectory Design Variables					
Node 1 [deg]	86.221	85.002	86.205	86.407	85.133
Node 2 [deg]	57.734	52.248	58.012	61.169	72.649
Node 3 [deg]	57.873	56.564	63.165	69.198	67.816
Node 4 [deg]	41.617	49.630	42.330	40.139	40.184
Node 5 [deg]	11.550	14.220	13.578	11.172	13.361
Node 6 [deg]	-0.002	-6.316	0.075	-0.023	-0.016
Min TW [-]	1.724	1.413	1.701	1.854	1.643
Max TW [-]	2.280	2.232	2.525	2.394	2.162
Entry γ [deg]	-4.514	-4.555	-3.620	-4.864	-4.626
Entry δ [deg]	31.852	32.056	27.755	32.546	32.057
Entry τ [deg]	0.380	2.321	-9.011	1.101	0.953
Entry α [deg]	57.104	61.130	57.292	56.768	59.002
Retroburn altitude [m]	2107	2183	2125	2418	2254
Optimum Vehicle Design Variables					
Mass flow [kg/s]	45.635	99.304	51.974	102.663	68.395
Chamber pressure [Pa]	10406822	20194043	18110229	25179520	22199001
O/F ratio [-]	3.458	3.500	3.618	3.751	3.610
Engine number [-]	11	8	6	8	9
Ascent propellant [kg]	117031	135581	113904	133611	123497
Landing propellant [kg]	5121	4969	4753	6629	6129
Exhaust diameter [m]	0.974	0.945	0.902	0.986	1.153
Vehicle diameter [m]	8.372	7.950	7.469	7.001	6.939
Engine Properties					
Specific Impulse (vac) [s]	387.518	383.454	387.770	384.455	392.721
Engine thrust (vac) [kN]	163.714	352.510	186.575	365.387	248.658
Total thrust (vac) [kN]	1800.860	2820.086	1119.453	2923.100	2237.924

Mass Breakdown					
Dry mass [kg]	23185	24621	21941	24928	24125
Propellant mass [kg]	126801	145577	123084	145469	134520
Payload mass [kg]	1200	1200	1200	1200	1200
GTOW [kg]	**151186**	**171398**	**146225**	**171597**	**159846**

Table C.2: The design variables for the optimum solutions found for seed 600-1000 for the baseline case

Baseline	**Seed 600**	**Seed 700**	**Seed 800**	**Seed 900**	**Seed 1000**
Optimum Trajectory Design Variables					
Node 1 [deg]	86.132	85.021	86.134	85.704	85.124
Node 2 [deg]	50.351	56.101	62.752	59.119	56.285
Node 3 [deg]	67.832	65.503	62.283	69.078	58.515
Node 4 [deg]	47.785	46.820	41.716	41.399	47.679
Node 5 [deg]	14.938	12.629	11.853	12.512	13.790
Node 6 [deg]	-0.016	-0.020	0.025	0.028	-0.016
Min TW [-]	1.616	1.464	1.726	1.652	1.474
Max TW [-]	2.843	2.045	2.384	2.178	2.196
Entry γ [deg]	-3.870	-2.958	-4.403	-4.840	-5.599
Entry δ [deg]	29.617	19.655	31.521	32.457	34.008
Entry τ [deg]	-15.730	-22.195	0.556	-2.980	-0.149
Entry α [deg]	37.628	61.635	60.628	52.280	40.520
Retroburn altitude [m]	2504	2038	2137	2476	2467
Optimum Vehicle Design Variables					
Mass flow [kg/s]	103.259	29.125	123.216	75.100	52.570
Chamber pressure [Pa]	21429336	19216191	17442427	19592789	27609085
O/F ratio [-]	3.688	3.393	3.646	3.747	3.560
Engine number [-]	6	12	6	4	10
Ascent propellant [kg]	134502	123664	130653	127164	121641
Landing propellant [kg]	5425	7513	5434	8621	5866
Exhaust diameter [m]	1.289	0.950	0.989	1.127	1.171
Vehicle diameter [m]	6.873	7.734	7.094	5.658	7.265
Engine Properties					
Specific impulse (vac) [s]	385.189	402.672	374.332	390.647	402.069
Engine thrust (vac)[kN]	368.210	108.568	426.989	271.593	195.674
Total thrust (vac) [kN]	2209.262	1302.818	2561.937	1086.372	1956.742
Mass Breakdown					
Dry mass [kg]	23885	22920	23956	22048	24023
Propellant mass [kg]	144894	136003	141129	140784	132257
Payload mass [kg]	1200	1200	1200	1200	1200
GTOW [kg]	**169979**	**160123**	**166285**	**164033**	**157480**

C.2. Change in Target Orbit Results

Table C.3 and C.4 present the design variables, engine properties, and mass breakdown for the optimum solutions found for the Hercules scenario for seeds 100-500 and 600-1000, respectively.

Table C.3: The design variables for the optimum solutions found for seed 100-500 for the Hercules case

Hercules	**Seed 100**	**Seed 200**	**Seed 300**	**Seed 400**	**Seed 500**
Optimum Trajectory Design Variables					
Node 1 [deg]	85.154	85.194	85.267	85.003	85.259
Node 2 [deg]	77.032	69.781	64.336	67.568	63.179
Node 3 [deg]	47.687	30.292	43.851	47.539	41.411
Node 4 [deg]	26.494	13.786	15.530	24.232	31.172
Node 5 [deg]	7.490	5.068	6.502	1.692	5.666
Node 6 [deg]	-4.883	-2.490	-7.614	0.245	-3.566
Min TW [-]	2.209	2.083	2.225	2.104	2.163
Max TW [-]	3.542	3.200	3.579	3.388	3.895
Entry γ [deg]	-5.050	-4.183	-3.137	-4.192	-5.241
Entry δ [deg]	30.639	28.256	25.734	28.486	31.107
Entry τ [deg]	-5.595	-13.233	-26.621	-10.555	-6.754
Entry α [deg]	57.096	35.738	41.158	55.669	51.424
Retroburn altitude [m]	2323	2895	2594	2111	2530
Optimum Vehicle Design Variables					
Mass flow [kg/s]	46.939	110.398	82.223	95.740	95.329
Chamber pressure [Pa]	23910114	18267983	16703147	15418056	18201988
O/F ratio [-]	3.499	3.475	3.361	3.365	3.878
Engine number [-]	8	8	8	5	6
Ascent propellant [kg]	70648	73411	71095	77951	72390
Landing propellant [kg]	5184	4514	4003	6309	4318
Exhaust diameter [m]	1.034	0.845	1.040	1.112	1.210
Vehicle diameter [m]	7.238	7.709	6.904	8.420	6.712
Engine Properties					
Specific impulse (vac) [s]	401.420	375.618	383.682	382.209	391.206
Engine thrust (vac) [kN]	174.433	383.885	292.050	338.754	345.241
Total thrust (vac) [kN]	1395.467	3071.083	2336.404	1693.774	2071.450
Mass Breakdown					
Dry mass [kg]	22327	24240	23358	22418	22940
Propellant mass [kg]	79676	82152	79072	88473	80623
Payload mass [kg]	1200	1200	1200	1200	1200
GTOW [kg]	**103204**	**107593**	**103630**	**112091**	**104764**

Table C.4: The design variables for the optimum solutions found for seed 600-1000 for the Hercules case

Hercules	**Seed 600**	**Seed 700**	**Seed 800**	**Seed 900**	**Seed 1000**
Optimum Trajectory Design Variables					
Node 1 [deg]	85.994	85.008	85.125	85.147	85.429
Node 2 [deg]	60.774	69.651	68.965	70.383	54.778
Node 3 [deg]	37.484	32.014	46.868	36.494	36.708
Node 4 [deg]	15.219	15.801	26.533	11.992	16.890
Node 5 [deg]	5.329	1.624	5.859	4.500	8.479
Node 6 [deg]	-4.123	-0.190	-5.218	-2.859	-7.053
Min TW [-]	2.515	2.230	2.631	2.333	1.538
Max TW [-]	3.750	3.798	3.677	3.872	2.964
Entry γ [deg]	-4.614	-3.686	-4.518	-3.023	-2.707
Entry δ [deg]	29.993	27.082	29.549	24.309	22.322
Entry τ [deg]	-12.766	-16.433	-12.844	-20.835	-23.402
Entry α [deg]	43.616	47.979	50.180	58.766	62.763
Retroburn altitude [m]	2791	2255	2873	2041	2412

		Optimum Vehicle Design Variables			
Mass flow [kg/s]	41.272	73.678	83.405	153.821	107.683
Chamber pressure [Pa]	8053256	6556962	21553978	13179391	9601640
O/F ratio [-]	3.391	3.188	3.294	3.614	3.393
Engine number [-]	13	4	6	4	4
Ascent propellant [kg]	74701	73542	84595	70229	80720
Landing propellant [kg]	6845	4888	5149	4744	6851
Exhaust diameter [m]	0.773	0.909	0.814	1.257	0.984
Vehicle diameter [m]	6.641	8.646	5.468	8.105	7.717
		Engine Properties			
Specific impulse (vac) [s]	375.730	354.524	364.177	374.982	369.382
Engine thrust (vac) [kN]	143.555	241.812	281.187	533.972	368.228
Total thrust (vac) [kN]	1866.225	967.251	1687.126	2135.889	1472.915
		Mass Breakdown			
Dry mass [kg]	22772	21134	22455	22733	21798
Propellant mass [kg]	85887	82530	94059	79026	91920
Payload mass [kg]	1200	1200	1200	1200	1200
GTOW [kg]	**109860**	**104865**	**117715**	**102960**	**114918**

Table C.5 presents the design variables, engine properties, and mass breakdown for the optimum solutions found for the direct ascent scenario.

Table C.5: The design variables for the optimum solutions found for the direct ascent case

Direct Ascent	**Seed 100**	**Seed 200**	**Seed 300**
	Optimum Trajectory Design Variables		
Node 1 [deg]	85.579	86.457	86.737
Node 2 [deg]	58.260	56.639	52.063
Node 3 [deg]	60.869	67.227	61.821
Node 4 [deg]	46.025	36.467	36.146
Node 5 [deg]	11.401	5.301	9.339
Node 6 [deg]	-7.126	-3.475	-8.390
Min TW [-]	1.422	1.769	1.778
Max TW [-]	2.947	2.433	2.643
Entry γ [deg]	-5.697	-4.908	-4.956
Entry δ [deg]	34.342	32.716	33.065
Entry τ [deg]	4.947	-5.283	-7.626
Entry α [deg]	55.123	44.597	44.213
Retroburn altitude [m]	1965	2593	2579
	Optimum Vehicle Design Variables		
Mass flow [kg/s]	64.167	66.481	53.006
Chamber pressure [Pa]	27230721	21243358	31613598
O/F ratio [-]	3.498	3.476	3.172
Engine number [-]	7	6	5
Ascent propellant [kg]	117215	105278	95364
Landing propellant [kg]	6657	6562	4517
Exhaust diameter [m]	0.873	1.194	1.238
Vehicle diameter [m]	8.186	6.147	5.141
	Engine Properties		
Specific impulse (vac) [s]	392.663	398.787	398.471
Engine thrust (vac) [kN]	233.250	245.433	195.529

Total thrust (vac) [kN]	1632.756	1472.598	977.645
Mass Breakdown			
Dry mass [kg]	22965	22588	21954
Propellant mass [kg]	128629	116367	104003
Payload mass [kg]	1200	1200	1200
GTOW [kg]	**152795**	**140156**	**127157**

C.3. Change in Martian Base Location Results

Tables C.6 and C.7 present the design variables, engine properties, and mass breakdown for the optimum solutions found for the latitude locations of 0° and 21.25°, respectively.

Table C.6: The design variables for the optimum solutions found for the 0° latitude location

Latitude = 5°	**Seed 100**	**Seed 200**	**Seed 300**
Optimum Trajectory Design Variables			
Node 1 [deg]	85.000	85.000	85.000
Node 2 [deg]	53.979	58.882	52.754
Node 3 [deg]	69.183	68.565	61.726
Node 4 [deg]	52.766	42.381	41.929
Node 5 [deg]	13.900	12.728	12.046
Node 6 [deg]	-5.480	-7.837	-7.677
Min TW [-]	1.407	1.876	1.759
Max TW [-]	2.235	2.661	2.336
Entry γ [deg]	-4.033	-6.286	-5.991
Entry δ [deg]	-2.485	-1.692	-1.504
Entry τ [deg]	-23.845	1.746	-15.415
Entry α [deg]	52.906	38.865	37.419
Retroburn altitude [m]	1381	1500	1617
Optimum Vehicle Design Variables			
Mass flow [kg/s]	69.128	36.281	64.684
Chamber pressure [Pa]	23949106	12345648	23016838
O/F ratio [-]	3.326	3.081	3.793
Engine number [-]	7	10	8
Ascent propellant [kg]	126279	121679	112649
Landing propellant [kg]	3663	6178	4546
Exhaust diameter [m]	0.920	0.815	0.830
Vehicle diameter [m]	7.402	8.208	7.052
Engine Properties			
Specific impulse (vac) [s]	381.544	386.499	389.759
Engine thrust (vac) [kN]	244.168	126.568	233.392
Total thrust (vac) [kN]	1709.178	1265.687	1867.139
Mass Breakdown			
Dry mass [kg]	23065	22450	23137
Propellant mass [kg]	134553	132600	121706
GTOW [kg]	**158818**	**156251**	**146043**

Table C.7: The design variables for the optimum solutions found for the 21.25° latitude location

Latitude = 21.25°	**Seed 100**	**Seed 200**	**Seed 300**
Optimum Trajectory Design Variables			
Node 1 [deg]	85.001	85.001	89.016
Node 2 [deg]	53.484	51.927	67.792
Node 3 [deg]	59.644	58.872	65.342
Node 4 [deg]	47.250	39.332	53.935
Node 5 [deg]	14.518	12.173	17.342
Node 6 [deg]	-7.634	-8.437	-7.455
Min TW [-]	1.510	1.735	1.296
Max TW [-]	2.475	2.236	2.653
Entry γ [deg]	-4.761	-5.360	-6.162
Entry δ [deg]	19.143	18.796	20.275
Entry τ [deg]	-4.151	3.473	3.415
Entry α [deg]	49.569	56.324	40.923
Retroburn altitude [m]	2318	2247	2210
Optimum Vehicle Design Variables			
Mass flow [kg/s]	38.404	43.174	45.920
Chamber pressure [Pa]	22038930	11604034	16286940
O/F ratio [-]	3.330	3.505	3.081
Engine number [-]	9	8	9
Ascent propellant [kg]	130387	108928	122758
Landing propellant [kg]	7979	4581	3614
Exhaust diameter [m]	0.976	0.836	1.107
Vehicle diameter [m]	6.639	6.858	7.259
Engine Properties			
Specific impulse (vac) [s]	389.531	385.092	392.716
Engine thrust (vac) [kN]	138.486	153.914	166.946
Total thrust (vac) [kN]	1246.380	1231.312	1502.515
Mass Breakdown			
Dry mass [kg]	22731	22043	22915
Propellant mass [kg]	143412	117898	130829
Payload mass [kg]	1200	1200	1200
GTOW [kg]	**167344**	**141142**	**154944**

C.4. Payload Change Results

Tables C.8 and C.9 present the design variables, engine properties, and mass breakdown for the optimum solutions found for the -50% and +50% payload scenario, respectively.

Table C.8: The design variables for the optimum solutions found for the -50% payload case

-50% Payload	**Seed 100**	**Seed 200**	**Seed 300**
Optimum Trajectory Design Variables			
Node 1 [deg]	85.008	85.247	85.263
Node 2 [deg]	54.150	52.285	53.928
Node 3 [deg]	61.622	62.077	66.310
Node 4 [deg]	47.855	50.763	43.857
Node 5 [deg]	14.625	16.371	13.136
Node 6 [deg]	-6.899	-7.911	-6.384
Min TW [-]	1.431	1.414	1.522
Max TW [-]	2.270	2.641	2.089

Entry γ [deg]	-5.515	-4.598	-5.697
Entry δ [deg]	33.697	31.916	34.327
Entry τ [deg]	-2.193	-2.286	-1.176
Entry α [deg]	35.682	50.441	44.835
Retroburn altitude [m]	2749	2225	2397
Optimum Vehicle Design Variables			
Mass flow [kg/s]	25.206	90.291	39.059
Chamber pressure [Pa]	16326220	13059102	5584328
O/F ratio [-]	3.607	3.497	3.300
Engine number [-]	9	5	8
Ascent propellant [kg]	115706	129721	146033
Landing propellant [kg]	6947	5862	7450
Exhaust diameter [m]	1.071	1.162	0.764
Vehicle diameter [m]	6.457	8.041	6.096
Engine Properties			
Specific impulse (vac) [s]	403.098	396.789	387.149
Engine thrust (vac) [kN]	94.061	322.249	235.597
Total thrust (vac) [kN]	846.553	1288.998	1413.587
Mass Breakdown			
Dry mass [kg]	21928	22378	22786
Propellant mass [kg]	127152	132255	147227
Payload mass [kg]	600	600	600
GTOW [kg]	**149681**	**155233**	**170613**

Table C.9: The design variables for the optimum solutions found for the +50% payload case

+50% Payload	**Seed 100**	**Seed 200**	**Seed 300**
Optimum Trajectory Design Variables			
Node 1 [deg]	85.826	85.938	85.309
Node 2 [deg]	61.354	54.988	53.671
Node 3 [deg]	62.076	66.954	68.056
Node 4 [deg]	44.268	45.075	43.871
Node 5 [deg]	13.815	13.179	13.341
Node 6 [deg]	-7.925	-7.073	-6.403
Min TW [-]	1.613	1.638	1.532
Max TW [-]	2.508	2.444	2.117
Entry γ [deg]	-5.081	-4.248	-4.028
Entry δ [deg]	33.048	30.899	30.406
Entry τ [deg]	-0.953	-1.859	-15.875
Entry α [deg]	48.499	59.290	42.796
Retroburn altitude [m]	2479	2380	2631
Optimum Vehicle Design Variables			
Mass flow [kg/s]	95.981	121.360	35.711
Chamber pressure [Pa]	26879423	16152611	7220104
O/F ratio [-]	3.669	3.381	3.643
Engine number [-]	5	5	9
Ascent propellant [kg]	135405	154941	127096
Landing propellant [kg]	7249	7779	6580
Exhaust diameter [m]	0.966	0.765	1.244
Vehicle diameter [m]	7.308	6.505	5.978
Engine Properties			
Specific impulse (vac) [s]	382.275	366.343	388.565
Engine thrust (vac) [kN]	339.665	411.582	128.455

Total thrust (vac) [kN]	1698.329	2057.914	1156.099
Mass Breakdown			
Dry mass [kg]	23006	23359	22301
Propellant mass [kg]	147840	168384	138557
Payload mass [kg]	1800	1800	1800
GTOW [kg]	**172646**	**193544**	**162659**

C.5. 10 g Maximum Load Results

Table C.10 presents the design variables, engine properties, and mass breakdown for the optimum solutions found for the 10 g$_{mars}$ load case.

Table C.10: The design variables for the optimum solutions found for the 10 g load case

10 g	**Seed 100**	**Seed 200**	**Seed 300**
Optimum Trajectory Design Variables			
Node 1 [deg]	85.718	85.827	85.339
Node 2 [deg]	57.421	51.975	54.002
Node 3 [deg]	68.343	46.783	65.589
Node 4 [deg]	44.472	45.035	45.567
Node 5 [deg]	13.496	13.722	12.855
Node 6 [deg]	-7.072	-8.366	-5.943
Min TW [-]	1.613	1.544	1.520
Max TW [-]	2.371	2.346	2.129
Entry γ [deg]	-5.488	-6.132	-3.055
Entry δ [deg]	34.055	34.820	19.126
Entry τ [deg]	-3.873	2.388	-27.897
Entry α [deg]	39.458	43.378	55.401
Retroburn altitude [m]	1085	1131	1100
Optimum Vehicle Design Variables			
Mass flow [kg/s]	60.313	62.683	97.661
Chamber pressure [Pa]	14813268	24640826	13568528
O/F ratio [-]	3.850	3.375	3.330
Engine number [-]	9	7	3
Ascent propellant [kg]	121891	128602	134444
Landing propellant [kg]	5312	8552	7025
Exhaust diameter [m]	1.063	1.136	1.121
Vehicle diameter [m]	6.185	7.255	8.319
Engine Properties			
Specific impulse (vac) [s]	391.403	397.146	375.213
Engine thrust (vac) [kN]	218.538	230.459	339.228
Total thrust (vac) [kN]	1966.850	1613.218	1017.684
Mass Breakdown			
Dry mass [kg]	23427	23171	21749
Propellant mass [kg]	131918	142227	146467
Payload mass [kg]	1200	1200	1200
GTOW [kg]	**156546**	**166598**	**169416**

C.6. Thrust Law 0 and 2 Results

Tables C.11 and C.12 present the design variables, engine properties, and mass breakdown for the optimum solutions found for thrust laws 0 and 2, respectively.

Table C.11: The design variables for the optimum solutions found for thrust law 0

Thrust Law 0	**Seed 100**	**Seed 200**	**Seed 300**
Optimum Trajectory Design Variables			
Node 1 [deg]	86.926	87.448	87.448
Node 2 [deg]	74.009	63.080	63.080
Node 3 [deg]	67.161	61.822	61.822
Node 4 [deg]	31.810	31.462	31.462
Node 5 [deg]	8.760	8.621	8.621
Node 6 [deg]	-6.696	-8.403	-8.403
Min TW [-]	1.665	1.516	1.516
Max TW [-]	2.284	2.355	2.355
Entry γ [deg]	-3.775	-4.822	-4.822
Entry δ [deg]	29.088	32.501	32.501
Entry τ [deg]	-5.378	-0.264	-0.264
Entry α [deg]	58.424	53.172	53.172
Retroburn altitude [m]	2026	2235	2235
Optimum Vehicle Design Variables			
Mass flow [kg/s]	53.626	66.159	66.159
Chamber pressure [Pa]	26680323	28640504	28640504
O/F ratio [-]	3.791	3.692	3.692
Engine number [-]	8	8	8
Ascent propellant [kg]	111789	116167	116167
Landing propellant [kg]	7154	5545	5545
Exhaust diameter [m]	1.158	0.896	0.896
Vehicle diameter [m]	8.220	7.367	7.367
Engine Properties			
Specific impulse (vac) [s]	404.635	385.827	385.827
Engine thrust (vac) [kN]	200.878	236.305	236.305
Total thrust (vac) [kN]	1607.027	1890.441	1890.441
Mass Breakdown			
Dry mass [kg]	23201	23406	23406
Propellant mass [kg]	123622	126442	126442
Dry mass [kg]	1200	1200	1200
GTOW [kg]	**148024**	**151049**	**151049**

Table C.12: The design variables for the optimum solutions found for thrust law 2

Thrust Law 2	**Seed 100**	**Seed 200**	**Seed 300**
Optimum Trajectory Design Variables			
Node 1 [deg]	85.052	85.797	86.316
Node 2 [deg]	51.867	57.608	54.281
Node 3 [deg]	69.379	63.522	63.819
Node 4 [deg]	45.981	40.619	38.036
Node 5 [deg]	10.570	11.853	11.188
Node 6 [deg]	-5.355	-8.026	-8.063
Min TW [-]	1.408	1.552	1.699
Max TW [-]	2.174	2.305	2.259

Entry γ [deg]	-6.110	-4.530	-5.625
Entry δ [deg]	35.109	31.978	34.149
Entry τ [deg]	-2.045	-0.937	1.414
Entry α [deg]	40.183	53.106	45.963
Retroburn altitude [m]	2476	2062	2270
Optimum Vehicle Design Variables			
Mass flow [kg/s]	79.401	103.021	61.852
Chamber pressure [Pa]	19205793	16729183	14562901
O/F ratio [-]	3.476	3.907	3.787
Engine number [-]	4	6	8
Ascent propellant [kg]	127321	124445	126631
Landing propellant [kg]	5338	3509	6325
Exhaust diameter [m]	0.811	0.813	0.792
Vehicle diameter [m]	5.458	8.301	7.513
Engine Properties			
Specific impulse (vac) [s]	381.344	373.154	380.420
Engine thrust (vac) [kN]	280.307	355.883	217.827
Total thrust (vac) [kN]	1121.229	2135.301	1742.618
Mass Breakdown			
Dry mass [kg]	21973	23247	22896
Propellant mass [kg]	137352	132625	137877
Payload mass [kg]	1200	1200	1200
GTOW [kg]	**160526**	**157072**	**161974**

D

Sobol′ Analysis Results

This appendix presents all the Sobol' indices. The indices with respect to first-order effects are given in Section D.1, and the indices with respect to total effects are given in Section D.2.

D.1. First-Order Effects

Tables D.1 and D.2 present the first-order effects Sobol' indices for the ascent and EDL phases, respectively.

Table D.1: The first-order effects Sobol' indices for the ascent phase

Uncertain Variable	Pericentre	Eccentricity	Inclination
θ_1	0.00385760	0.00053335	0.97674866
θ_2	0.00081410	0.00012311	0.00051484
θ_3	0.00859547	0.00130045	0.00008799
θ_4	0.18792706	0.02402952	0.00000791
θ_5	0.01953845	0.01404525	0.00000506
θ_6	0.40520073	0.14687446	0.00008379
TW_{min}	0.01578405	0.00345097	0.01865126
TW_{max}	0.00954944	0.00000000	0.00276525
P	0.00001101	0.00004664	0.00000016
$\dot{m}$	0.00276740	0.00000000	0.00000639
O/F	0.18390094	0.01108132	0.00018336

Table D.2: The first-order effects Sobol' indices for the EDL phase

Uncertain Variable	Final Latitude	Final Longitude	Final Velocity	Final Pitch Angle
δ_0	0.00000115	0.00000000	0.00000000	0.00000000
τ_0	0.00000348	0.00000000	0.00000000	0.00447446
h_0	0.00001045	0.00001400	0.00000000	0.00000000
V_0	0.00000000	0.00000000	0.00000000	0.00000000
γ_0	0.98597263	0.99511828	0.04387433	0.00834362
χ_0	0.00747260	0.00000000	0.00000000	0.00696312
α	0.00000000	0.00241128	0.00000000	0.00000000
h_{rb}	0.00000000	0.00000052	0.08173057	0.11385024
P	0.00000000	0.00000019	0.00000000	0.00000000
$\dot{m}$	0.00000000	0.00000000	0.00782040	0.00000000

O/F	0.00000000	0.00000000	0.00144489	0.01748996

D.2. Total Effects

Tables D.3 and D.4 present the total effects Sobol' indices for the ascent and EDL phases, respectively.

Table D.3: The total effects Sobol' indices for the ascent phase

Uncertain Variable	**Pericentre**	**Eccentricity**	**Inclination**
θ_1	0.00501553	0.00866615	0.97762975
θ_2	0.00081152	0.00102714	0.00055806
θ_3	0.01345814	0.02445978	0.00009042
θ_4	0.28542231	0.49746779	0.00000809
θ_5	0.03467616	0.09461037	0.00000467
θ_6	0.51367218	0.70347047	0.00008692
TW_{min}	0.03965994	0.10616325	0.01947365
TW_{max}	0.02439271	0.08020251	0.00282914
P	0.00000253	0.00000985	0.00000000
$\dot{m}$	0.00506920	0.00864089	0.00000400
O/F	0.25049002	0.34300408	0.00022990

Table D.4: The total effects Sobol' indices for the EDL phase

Uncertain Variable	**Final Latitude**	**Final Longitude**	**Final Velocity**	**Final Pitch Angle**
δ_0	0.00000016	0.00000001	0.76928727	0.69421966
τ_0	0.00000016	0.00000001	0.76407417	0.66853836
h_0	0.00000055	0.00000030	0.74840903	0.71174001
V_0	0.00008077	0.00002995	0.74752294	0.69407111
γ_0	0.99149906	0.99718421	0.92133887	0.92075370
χ_0	0.01102210	0.00117108	0.76681713	0.72824982
α	0.00257089	0.00361799	0.79744734	0.84222832
h_{rb}	0.00000027	0.00000001	0.93458310	0.97270194
P	0.00000015	0.00000000	0.76080632	0.68809828
$\dot{m}$	0.00003421	0.00001126	0.78723329	0.72104099
O/F	0.00001717	0.00000586	0.76042021	0.71669831

E

Model Sensitivity Analysis Results

This appendix presents all all the results found using the MDO scheme for all the model sensitivity analysis cases.

E.1. Aerodynamics Sensitivity

Table E.1, E.2, E.3, and E.4 present the design variables, engine properties, and mass breakdown for the solutions found for the +15%, +5%, -15%, and -5% cases, respectively.

Table E.1: The design variables for the optimum solutions found for the +15% aerodynamics coefficients case

+15% Aerodynamics	**Seed 100**	**Seed 200**	**Seed 300**
Optimum Trajectory Design Variables			
Node 1 [deg]	85.120	87.013	85.134
Node 2 [deg]	56.555	61.994	51.118
Node 3 [deg]	41.375	64.354	68.572
Node 4 [deg]	50.814	37.501	49.217
Node 5 [deg]	15.884	10.948	13.318
Node 6 [deg]	-8.065	-8.246	-5.718
Min TW [-]	1.401	2.059	1.473
Max TW [-]	2.468	2.648	2.278
Entry γ [deg]	-4.408	-3.917	-4.115
Entry δ [deg]	31.402	29.588	30.675
Entry τ [deg]	-2.164	-12.638	-1.480
Entry α [deg]	53.631	38.758	60.282
Retroburn altitude [m]	2121	2522	2104
Optimum Vehicle Design Variables			
Mass flow [kg/s]	43.477	107.236	76.898
Chamber pressure [Pa]	15209535	25369835	28026810
O/F ratio [-]	3.910	3.946	3.875
Engine number [-]	8	7	11
Ascent propellant [kg]	134775	128172	140912
Landing propellant [kg]	6835	7152	6633
Exhaust diameter [m]	0.818	1.296	0.946
Vehicle diameter [m]	7.877	7.336	7.267
Engine Properties			
Specific impulse (vac) [s]	387.212	391.779	392.786
Engine thrust (vac) [kN]	155.847	388.931	279.615

Total thrust (vac) [kN]	1246.777	2722.520	3075.775
Mass Breakdown			
Dry mass [kg]	22379	24790	25587
Propellant mass [kg]	146550	140470	152844
Payload mass [kg]	1200	1200	1200
GTOW [kg]	**170130**	**166461**	**179631**

Table E.2: The design variables for the optimum solutions found for the +5% aerodynamics coefficients case

+5% Aerodynamics	**Seed 100**	**Seed 200**	**Seed 300**
Optimum Trajectory Design Variables			
Node 1 [deg]	85.067	85.665	85.190
Node 2 [deg]	56.204	55.164	59.582
Node 3 [deg]	50.396	65.323	66.784
Node 4 [deg]	46.431	43.046	43.424
Node 5 [deg]	15.445	13.841	14.280
Node 6 [deg]	-8.081	-7.572	-7.190
Min TW [-]	1.416	1.585	1.536
Max TW [-]	2.259	2.256	2.137
Entry γ [deg]	-5.095	-4.412	-4.042
Entry δ [deg]	33.287	31.385	30.000
Entry τ [deg]	-4.780	-4.228	-7.955
Entry α [deg]	43.874	48.954	50.352
Retroburn altitude [m]	2308	2165	2177
Optimum Vehicle Design Variables			
Mass flow [kg/s]	97.561	71.961	59.612
Chamber pressure [Pa]	25094387	16955080	26706596
O/F ratio [-]	3.235	3.554	3.701
Engine number [-]	5	8	11
Ascent propellant [kg]	128331	122830	128815
Landing propellant [kg]	4867	5256	5403
Exhaust diameter [m]	0.982	1.113	0.985
Vehicle diameter [m]	6.175	7.799	7.281
Engine Properties			
Specific impulse (vac) [s]	380.033	390.286	388.591
Engine thrust (vac) [kN]	360.393	272.998	225.168
Total thrust (vac) [kN]	1801.969	2183.991	2476.850
Mass Breakdown			
Dry mass [kg]	23118	23749	24713
Propellant mass [kg]	137993	132851	139189
Payload mass [kg]	1200	1200	1200
GTOW [kg]	**162312**	**157800**	**165102**

Table E.3: The design variables for the optimum solutions found for the -15% aerodynamics coefficients case

-15% Aerodynamics	**Seed 100**	**Seed 200**	**Seed 300**
Optimum Trajectory Design Variables			
Node 1 [deg]	85.265	85.688	85.642
Node 2 [deg]	66.596	50.233	70.966
Node 3 [deg]	59.360	54.679	54.886

Node 4 [deg]	41.434	45.098	42.167
Node 5 [deg]	14.264	13.390	12.035
Node 6 [deg]	-8.310	-7.260	-7.380
Min TW [-]	1.563	1.536	1.684
Max TW [-]	2.167	2.248	2.297
Entry γ [deg]	-5.091	-5.412	-6.126
Entry δ [deg]	33.795	34.889	35.869
Entry τ [deg]	-22.176	-17.564	-11.975
Entry α [deg]	48.804	54.546	54.143
Retroburn altitude [m]	1751	1885	1717
Optimum Vehicle Design Variables			
Mass flow [kg/s]	92.394	62.841	65.478
Chamber pressure [Pa]	26455216	23290107	26636130
O/F ratio [-]	3.606	3.487	3.873
Engine number [-]	4	6	4
Ascent propellant [kg]	110625	110639	101395
Landing propellant [kg]	4366	4909	3268
Exhaust diameter [m]	1.140	1.094	0.849
Vehicle diameter [m]	8.114	6.789	8.326
Engine Properties			
Specific impulse (vac) [s]	391.325	398.462	397.655
Engine thrust (vac) [kN]	334.712	231.806	221.787
Total thrust (vac) [kN]	1338.848	1390.836	1108.936
Mass Breakdown			
Dry mass [kg]	22285	22480	22050
Propellant mass [kg]	119348	119932	124977
Payload mass [kg]	1200	1200	1200
GTOW [kg]	**142833**	**143613**	**148227**

Table E.4: The design variables for the optimum solutions found for the -5% aerodynamics coefficients case

-5% Aerodynamics	**Seed 100**	**Seed 200**	**Seed 300**
Optimum Trajectory Design Variables			
Node 1 [deg]	85.050	85.751	85.402
Node 2 [deg]	55.394	60.924	53.617
Node 3 [deg]	41.966	58.601	56.015
Node 4 [deg]	48.474	41.310	46.565
Node 5 [deg]	14.088	13.319	15.379
Node 6 [deg]	-6.855	-8.105	-8.295
Min TW [-]	1.443	1.615	1.455
Max TW [-]	2.105	2.232	2.419
Entry γ [deg]	-5.746	-6.637	-5.766
Entry δ [deg]	33.652	37.416	35.921
Entry τ [deg]	-13.552	-6.366	-13.187
Entry α [deg]	63.480	45.385	50.535
Retroburn altitude [m]	1776	2031	2064
Optimum Vehicle Design Variables			
Mass flow [kg/s]	82.969	25.653	86.361
Chamber pressure [Pa]	24477164	11420472	32403106
O/F ratio [-]	3.095	3.184	3.862
Engine number [-]	11	13	5
Ascent propellant [kg]	146461	115166	114015
Landing propellant [kg]	6811	6450	4505

Exhaust diameter [m]	0.852	1.138	1.130
Vehicle diameter [m]	8.532	7.115	5.731
Engine Properties			
Specific impulse (vac) [s]	381.600	397.258	397.852
Engine thrust (vac) [kN]	269.712	94.342	318.076
Total thrust (vac) [kN]	1887.986	1226.456	1590.380
Mass Breakdown			
Dry mass [kg]	23155	22713	22891
Propellant mass [kg]	137917	126258	122946
Payload mass [kg]	1200	1200	1200
GTOW [kg]	**162272**	**150171**	**147038**

E.2. Propulsion Sensitivity

Table E.5, E.6, E.7, and E.8 present the design variables, engine properties, and mass breakdown for the solutions found for the +5%, +2.5%, -5%, and -2.5% cases, respectively.

Table E.5: The design variables for the optimum solutions found for the +5% propulsion system quality factors case

+5% Propulsion Efficiency	**Seed 100**	**Seed 200**	**Seed 300**
Optimum Trajectory Design Variables			
Node 1 [deg]	85.073	85.871	85.494
Node 2 [deg]	63.904	69.569	51.479
Node 3 [deg]	64.652	61.786	55.821
Node 4 [deg]	46.276	41.390	44.165
Node 5 [deg]	14.759	10.746	14.027
Node 6 [deg]	-7.426	-6.316	-7.691
Min TW [-]	1.492	1.735	1.509
Max TW [-]	2.375	2.287	2.182
Entry γ [deg]	-3.697	-3.924	-4.548
Entry δ [deg]	28.441	29.797	31.928
Entry τ [deg]	-18.320	-3.637	1.115
Entry α [deg]	47.509	60.958	60.883
Retroburn altitude [m]	2399	2370	2295
Optimum Vehicle Design Variables			
Mass flow [kg/s]	45.470	32.404	61.746
Chamber pressure [Pa]	16732468	11912893	31604364
O/F ratio [-]	3.683	3.480	3.230
Engine number [-]	12	10	8
Ascent propellant [kg]	121937	100855	116252
Landing propellant [kg]	4723	3637	3637
Exhaust diameter [m]	1.115	1.032	0.960
Vehicle diameter [m]	6.165	5.571	6.114
Engine Properties			
Specific impulse (vac) [s]	392.187	397.143	387.360
Engine thrust (vac) [kN]	165.084	119.133	221.419
Total thrust (vac) [kN]	1981.015	1191.336	1771.356
Mass Breakdown			
Dry mass [kg]	23867	22222	23402
Propellant mass [kg]	131350	108612	124383
Payload mass [kg]	1200	1200	1200
GTOW [kg]	**156418**	**132035**	**148986**

Table E.6: The design variables for the optimum solutions found for the +2.5% propulsion system quality factors case

+2.5% Propulsion Efficiency	**Seed 100**	**Seed 200**	**Seed 300**
Optimum Trajectory Design Variables			
Node 1 [deg]	85.386	85.027	86.328
Node 2 [deg]	55.430	59.327	58.786
Node 3 [deg]	62.620	62.362	58.854
Node 4 [deg]	51.030	50.377	38.804
Node 5 [deg]	15.887	15.965	12.144
Node 6 [deg]	-7.733	-7.518	-8.363
Min TW [-]	1.450	1.402	1.758
Max TW [-]	2.734	2.590	2.279
Entry γ [deg]	-4.329	-5.650	-4.853
Entry δ [deg]	31.370	34.065	32.695
Entry τ [deg]	-11.813	3.926	2.326
Entry α [deg]	42.426	56.742	57.621
Retroburn altitude [m]	2439	2473	2173
Optimum Vehicle Design Variables			
Mass flow [kg/s]	53.119	84.495	96.243
Chamber pressure [Pa]	11856104	17988124	21216810
O/F ratio [-]	3.160	3.174	3.182
Engine number [-]	7	5	6
Ascent propellant [kg]	118967	128977	122425
Landing propellant [kg]	3658	5763	4787
Exhaust diameter [m]	1.170	1.166	0.893
Vehicle diameter [m]	5.857	5.972	7.818
Engine Properties			
Specific impulse (vac) [s]	388.858	387.774	375.368
Engine thrust (vac) [kN]	196.001	303.321	342.803
Total thrust (vac) [kN]	1372.007	1516.608	2056.821
Mass Breakdown			
Dry mass [kg]	22463	22718	23332
Propellant mass [kg]	127027	139530	132005
Payload mass [kg]	1200	1200	1200
GTOW [kg]	**150690**	**163448**	**156538**

Table E.7: The design variables for the optimum solutions found for the -5% propulsion system quality factors case

-5% Propulsion Efficiency	**Seed 100**	**Seed 200**	**Seed 300**
Optimum Trajectory Design Variables			
Node 1 [deg]	86.208	85.401	85.491
Node 2 [deg]	60.305	71.226	70.045
Node 3 [deg]	68.727	63.405	59.222
Node 4 [deg]	41.139	45.172	43.006
Node 5 [deg]	13.184	11.442	12.362
Node 6 [deg]	-7.971	-5.845	-7.042
Min TW [-]	1.741	1.633	1.634
Max TW [-]	2.496	2.351	2.288
Entry γ [deg]	-3.994	-4.281	-5.094
Entry δ [deg]	29.962	30.907	33.160
Entry τ [deg]	-12.264	-5.649	-3.349

Entry α [deg]	43.943	49.557	41.976
Retroburn altitude [m]	2296	2286	2184
Optimum Vehicle Design Variables			
Mass flow [kg/s]	114.148	74.913	145.308
Chamber pressure [Pa]	26724435	25186072	16160972
O/F ratio [-]	3.699	3.996	3.986
Engine number [-]	3	6	7
Ascent propellant [kg]	125189	123347	130988
Landing propellant [kg]	6153	6253	3753
Exhaust diameter [m]	1.009	1.069	1.122
Vehicle diameter [m]	7.110	7.540	7.114
Engine Properties			
Specific impulse (vac) [s]	379.091	387.801	373.226
Engine thrust (vac) [kN]	390.578	268.940	502.058
Total thrust (vac) [kN]	1171.734	1613.643	3514.412
Mass Breakdown			
Dry mass [kg]	21965	22918	25275
Propellant mass [kg]	136129	134413	139754
Payload mass [kg]	1200	1200	1200
GTOW [kg]	**159294**	**158531**	**166230**

Table E.8: The design variables for the optimum solutions found for the -2.5% propulsion system quality factors case

-2.5% Propulsion Efficiency	**Seed 100**	**Seed 200**	**Seed 300**
Optimum Trajectory Design Variables			
Node 1 [deg]	85.513	85.703	85.729
Node 2 [deg]	69.407	53.071	58.379
Node 3 [deg]	60.188	69.877	62.431
Node 4 [deg]	42.031	43.703	45.514
Node 5 [deg]	11.477	13.031	12.877
Node 6 [deg]	-6.521	-6.616	-6.888
Min TW [-]	1.658	1.608	1.597
Max TW [-]	2.175	2.248	2.435
Entry γ [deg]	-5.680	-5.250	-4.629
Entry δ [deg]	34.188	33.319	32.257
Entry τ [deg]	0.825	-2.794	-3.378
Entry α [deg]	46.602	38.360	46.510
Retroburn altitude [m]	2369	2770	2008
Optimum Vehicle Design Variables			
Mass flow [kg/s]	73.726	71.589	110.115
Chamber pressure [Pa]	7898691	25205980	22695944
O/F ratio [-]	3.849	3.572	3.343
Engine number [-]	5	11	3
Ascent propellant [kg]	125581	139822	122612
Landing propellant [kg]	6418	7611	4262
Exhaust diameter [m]	1.002	0.944	0.858
Vehicle diameter [m]	6.852	7.227	8.026
Engine Properties			
Specific impulse (vac) [s]	374.901	390.010	371.897
Engine thrust (vac) [kN]	255.875	258.471	379.106
Total thrust (vac) [kN]	1279.378	2843.185	1137.319
Mass Breakdown			

Dry mass [kg]	21964	25202	21817
Propellant mass [kg]	136861	152817	131454
Payload mass [kg]	1200	1200	1200
GTOW [kg]	**160025**	**179220**	**154472**

Bibliography

[1] Nasa's space launch system: Progress toward launch. *Accelerating Space Commerce, Exploration, and New Discovery Conference, ASCEND 2020*, pages 6–13, 2020. doi: 10.2514/6.2020-4037.

[2] E. Adler, E. Howell, T. McClure, J. Nichols, T. Aiken, N. Bartel, C. Byrd, R. Weibrecht, and M. Zheng. Subscale demonstration and validation of the hercules ascent, descent, and entry vehicle. *AIAA Scitech 2020 Forum*, 1 PartF(January):1–33, 2020. doi: 10.2514/6.2020-2015.

[3] D. Akin. Mass estimating relationships. ENAE 791 Launch and Entry Vehicle Design University of Maryland, 2016. `https://spacecraft.ssl.umd.edu/academics/791S16/791S16L08.MERsx.pdf`.

[4] D. C. Arney, C. A. Jones, J. J. Klovstad, D. R. Komar, K. Earle, R. Moses, and H. R. Shyface. Sustaining human presence on Mars using ISRU and a reusable Lander. *AIAA SPACE 2015 Conference and Exposition*, (April 2019), 2015. doi: 10.2514/6.2015-4479.

[5] S. H. Bae, H. Jung, and J. S. Kim. A Preliminary Configuration Design of Methane/Oxygen Bipropellant Small-Rocket-Engine through Theoretical Performance Analysis. *Journal of the Korean Society of Propulsion Engineers*, 19(3):47–53, 2015. ISSN 1226-6027. doi: 10.6108/kspe.2015.19.3.047.

[6] M. Balesdent, N. Bérend, P. Dépincé, and A. Chriette. A survey of multidisciplinary design optimization methods in launch vehicle design. *Structural and Multidisciplinary Optimization*, 45(5):619–642, 2012. ISSN 1615147X. doi: 10.1007/s00158-011-0701-4.

[7] J. Benito and B. J. Johnson. Trajectory optimization for a mars ascent vehicle. *AIAA/AAS Astrodynamics Specialist Conference, 2016*, (September):1–11, 2016. doi: 10.2514/6.2016-5441.

[8] J. T. Betts. Survey of numerical methods for trajectory optimization. *Journal of Guidance, Control, and Dynamics*, 21(2):193–207, 1998. doi: 10.2514/2.4231. URL `https://doi.org/10.2514/2.4231`.

[9] W. B. Blake. User's Manual -1997 Fortran 90 Revision Final Report for Period April 1993-December 1997 Air Vehicles Directorate. (December 1997), 1998.

[10] M. Boere. Optimisation of Descent Trajectories for a Lunar Base Settlement. Master's thesis, TU Delft, The Netherlands, 2010.

[11] F. Castellini. *Multidisciplinary Design Optimization For Expendable Launch Vehicles*. PhD thesis, Politecnico Do Milano, 2012. URL `https://www.politesi.polimi.it/handle/10589/56841`.

[12] C. J. Cerimele, E. A. Robertson, R. R. Sostaric, C. H. Campbell, P. Robinson, D. A. Matz, B. J. Johnson, S. J. Stachowiak, J. A. Garcia, J. V. Bowles, D. J. Kinney, and J. E. Theisinger. A rigid mid-lift-to-drag ratio approach to human mars entry, descent, and landing. *AIAA Guidance, Navigation, and Control Conference, 2017*, 3:1–22, 2017. doi: 10.2514/6.2017-1898.

[13] V. Clark. Modelling of Propellant Management Systems in Early-Phase Launcher Development. *European Conference for Aerospace Sciences*, 2015.

[14] S. Contant. Design and Optimization of a Small Reusable Launch Vehicle Using Vertical Landing Techniques. Master's thesis, TU Delft, The Netherlands, 2019.

[15] D. Curry. Space shuttle orbiter thermal protection system design and flight experience. 1993.

[16] P. N. Desai, R. D. Braun, W. C. Engelund, F. M. Cheatwood, and J. A. Kangas. Mars ascent vehicle flight analysis. *7th AIAA/ASME Joint Thermophysics and Heat Transfer Conference*, 1998. doi: 10.2514/6.1998-2850.

[17] A. Deshpande and M. Kumar. *Artificial Intelligence for Big Data: Complete Guide to Automating Big Data Solutions Using Artificial Intelligence Techniques.* Packt Publishing, 2018. ISBN 1788472179.

[18] B. G. Drake. *Human Exploration of Mars Design Reference Architecture 5.0.* Number July. Rawlings, 2009. ISBN 3016210134.

[19] J. Dutheil. Highly reusable LOx/LCH4 ACE rocket engine designed for SpacePlane: Technical Maturation progress via key system demonstrators results. *7th EUROPEAN CONFERENCE FOR AERONAUTICS AND SPACE SCIENCE (EUCASS)*, pages 1–15, 2017. doi: 10.13009/EUCASS2017-552.

[20] J. Dutheil. Private Communication, November 2020. Email communication regarding the dimensions of the ACE-42R engine.

[21] R. R. L. Ernst. Liquid Rocket Analysis (LiRA): Development of a Liquid Bi-Propellant Rocket Engine Design, Analysis and Optimization Tool. Master's thesis, TU Delft, The Netherlands, 2014.

[22] J. Gaffarel, A. Kadhum, M. Fazaeli, D. Apostolidis, M. Berger, L. Ciunaitis, W. Helsdingen, L. Landergren, M. Lentner, J. Neeser, L. Trotta, and M. Naeije. From the martian surface to its low orbit in a reusable single-stage vehicle—charon. *Aerospace*, 8(6), 2021. ISSN 2226-4310. doi: 10.3390/aerospace8060153. URL `https://www.mdpi.com/2226-4310/8/6/153`.

[23] T. Haex. Aerospace Mk-III: An exploration of cost driven mission scenarios of a winged Two Stage to Orbit semi-Reusable Launch Vehicle integrated in the common airspace. Master's thesis, TU Delft, The Netherlands, 2020.

[24] W. E. Hammond. *Design methodologies for space transportation systems.* American Institute of Aeronautics and Astronautics, 2001.

[25] J. Head, J. Dickson, J. Mustard, R. Milliken, D. Scott, B. Johnson, D. Marchant, J. Levy, K. Kinch, C. Hvidberg, F. Forget, D. Boucher, J. Mikucki, J. Fastook, and K. Klaus. Mars Human Science Exploration and Resource Utilization: The Dichotomy Boundary Deuteronilus Mensae Exploration Zone. *First Landing Site/Exploration Zone Workshop for Human Missions to the Surface of Mars*, pages 1–2, 2015. doi: 10.1130/G24382A.1.3. URL `http://www.hou.usra.edu/meetings/explorationzone2015/pdf/1033.pdf`.

[26] B. Hendrickx and B. Vis. *Energiya—Buran: The Soviet Space Shuttle.* Springer, 01 2007. ISBN 978-0-387-69848-9. doi: 10.1007/978-0-387-73984-7.

[27] R. J. G. Hermsen. Cryogenic propellant tank pressurization: A Practical investigation on the tank collapse factor for small, high-pressure, cryogenic rocket propellant tanks. Master's thesis, TU Delft, The Netherlands, 2017.

[28] J. W. Hickman, A. Wilhite, D. Stanley, and D. R. Komar. Optimization of the Mars Ascent Vehicle for Human Space Exploration. *Journal of Spacecraft and Rockets*, 47(2):361–370, 2010. ISSN 00224650. doi: 10.2514/1.45101.

[29] S. J Hoffman and D Ph. The Mars Surface Reference Mission : A Description of Human and Robotic Surface Activities. *Science*, (December), 2001.

[30] B. Hufenbach, K. C. Laurini, J. C. Piedboeuf, B. Schade, K. Matsumoto, F. Spiero, and A. Lorenzoni. The global exploration roadmap. *62nd International Astronautical Congress 2011, IAC 2011*, 4(August):3266–3275, 2011.

[31] D. K. Huzel, D. H. Huang, H. Arbit, American Institute of Aeronautics, Astronautics., and Rockwell International. *Modern Engineering for Design of Liquid-Propellant Rocket Engines / Dieter K. Huzel and David H. Huang; Revised, Updated, and Enlarged by Harry Arbit ... [et Al.].* American Institute of Aeronautics and Astronautics Washington, 1992. ISBN 1563470136.

[32] E. M. Jones. Lunar Module Quick Reference Data. *Grumman.* ISSN 02613131.

[33] T. Kato, D. Terakado, H. Nanri, T. Morito, I. Masuda, H. Asakawa, H. Sakaguchi, Y. Ishikawa, T. Inoue, S. Ishihara, and M. Sasaki. Subscale Firing Test for Regenerative Cooling LOX/Methane Rocket Engine. *7th European Conference for Aeronautics and Space Sciences (EUCASS)*, pages 2–5, 2017. doi: 10.13009/EUCASS2017-381. URL `https://www.eucass.eu/doi/EUCASS2017-381.pdf`.

[34] M. Kesteren, B. T. C. Zandbergen, M. Naeije, and A. Kleef. Design and analysis of an airborne, solid propelled, nanosatellite launch vehicle using multidisciplinary design optimization. 06 2015.

[35] T. Khan and I. Qamar. Factors Affecting Characteristic Length of the Combustion Chamber of Liquid Propellant Rocket Engines. *Mehran University Research Journal of Engineering and Technology*, 38(3): 729–744, 2019. ISSN 02547821. doi: 10.22581/muet1982.1903.16.

[36] J. H. Kim, H. Jung, and J. S. Kim. Analysis of the Theoretical Performance Characteristics for Methane-fuel Bipropellant Rocket Engine. *Journal of the Korean Society of Propulsion Engineers*, 18(3):1–7, 2014. ISSN 1226-6027. doi: 10.6108/kspe.2014.18.3.001.

[37] I. A. Klepikov, B. I. Katorgin, and V. K. Chvanov. New generation of rocket engines, operating by ecologically safe propellant 'liquid oxygen and liquefied natural gas (methane)'. *Acta Astronautica*, 41(4-10): 209–217, 1997. ISSN 00945765. doi: 10.1016/S0094-5765(98)00076-9.

[38] D. R. Komar and R. Moses. Hercules single-stage reusable vehicle supporting a safe, affordable, and sustainable human lunar & mars campaign. *AIAA SPACE and Astronautics Forum and Exposition, SPACE 2017*, (203999):1–29, 2017. doi: 10.2514/6.2017-5288.

[39] D. R. Komar, P. Tartabini, and J. R Clark. Lunar and Mars Ascent and Descent / Entry Crew Abort Modes for the Hercules Single-Stage Reusable Vehicle. *IEEE Aerospace Conference*, (July), 2018.

[40] K. V. Kumar and W. T. Norfleet. Issues on Human Acceleration Tolerance After Long Duration Space Flights. *Nasa Technical Memorandum*, 1992.

[41] M. Leonardi and F. Nasuti. System Analysis of a LOX / Methane Expander Bleed Engine. *7th European Conference for Aeronautics and Space Sciences (EUCASS)*, (1):2016, 2016. doi: 10.13009/EUCASS2017-332. URL `https://www.eucass.eu/doi/EUCASS2017-332.pdf`.

[42] C. L. Marsh and R. D. Braun. Fully-propulsive mars atmospheric transit strategies for high-mass missions. *Journal of Spacecraft and Rockets*, 48(2):271–282, 2011. ISSN 15336794. doi: 10.2514/1.49394.

[43] E. Millour, F. Forget, A. Spiga, A. Colaitis, T. Navarro, J.-B. Madeleine, J.-Y. Chauffray, L. Montabone, M. A. Lopez-Valverde, F. Gonzalez-Galindo, F. Lefevre, F. Montmessin, S. R. Lewis, P. L. Read, M.-C. Desjean, and J.-P. Huot. Mars climate database version 5. In *European Planetary Science Congress*, September 2012. URL `http://oro.open.ac.uk/35431/`. EPSC Abstracts, Vol. 7 EPSC2012-302 2012, European Planetary Science Congress 2012.

[44] F. Mirande. Design optimization of ground and air-launched hybrid rockets. Master's thesis, TU Delft, The Netherlands, 2015.

[45] E. Mooij. The motion of a vehicle in a planetary atmosphere. *Delft University of Technology, Faculty of Aerospace Engineering, Report LR-768*, 01 1994.

[46] E. Mooij. Ae4870b - re-entry systems. Lecture Notes Re-entry Systems, 2017-2018.

[47] P. Moore and G. Hunter. *The Atlas of the Solar System, year = 1997.* Number July. ISBN 0517001926.

[48] J. A. Mulder, W.H.J.J. van Staveren, J.C. van der Vaart, E. de Weerdt, de Visser. C.C., A.C. in 't Veld, and E. Mooij. Flight dynamics lecture notes ae3202. Flight Dynamics Course Reader, 2013. TU Delft.

[49] E. Musk. [Twitter user `@elonmusk`]. "Raptor engine just reached 330 bar chamber pressure without exploding!". August 2018.

[50] NASA. Pioneering Space: NASA ' s Next Steps on the Path to Mars. pages 1–13, 2014. URL `https://www.nasa.gov/sites/default/files/files/Pioneering-space-final-052914b.pdf`.

[51] R. Noomen. ae4-878.integrators.v4-11. Lecture Slides Mission Geometry and Orbit Design, 2018.

[52] G. Petitpas. Simulation of boil-off losses during transfer at a lh2 based hydrogen refueling station. *International Journal of Hydrogen Energy*, 43(46):21451–21463, 2018. ISSN 0360-3199. doi: https://doi.org/10.1016/j.ijhydene.2018.09.132. URL `https://www.sciencedirect.com/science/article/pii/S0360319918330234`.

[53] G. Pezzella and A. Viviani. Aerodynamic analysis of a manned space vehicle for missions to mars. *Journal of Thermodynamics*, 2011, 01 2011. doi: 10.1155/2011/857061.

[54] T. P. Polsgrove, T. K. Percy, M. Rucker, and H. D. Thomas. Update to Mars Ascent Vehicle Design for Human Exploration. *IEEE Aerospace Conference Proceedings*, 2019-March:1–15, 2019. ISSN 1095323X. doi: 10.1109/AERO.2019.8741709.

[55] M. Popp, J. Hulka, V. Yang, and M. Habiballah. *Liquid Rocket Thrust Chambers: Aspects of Modeling, Analysis, and Design*. American Institute of Aeronautics and Astronautics, August 2004. ISBN 978-1-56347-223-7. doi: https://doi.org/10.2514/4.866760.

[56] O. Roeva, S. Fidanova, and M. Paprzycki. Influence of the population size on the genetic algorithm performance in case of cultivation process modelling. In *2013 Federated Conference on Computer Science and Information Systems*, pages 371–376, 2013.

[57] W. Rogers. Apollo experience report: Lunar module landing gear subsystem. 1972. NASA TN D-6850.

[58] M. Rozemeijer. Toroidal Staged Microlaunch Vehicles. Master's thesis, TU Delft, The Netherlands, 2020.

[59] H. Schlingloff. *Astronautical Engineering: An Introduction to the Technology of Spaceflight*. Schlingloff Publ., 2005. ISBN 9783000162893. URL `https://books.google.nl/books?id=p6h_AAAACAAJ`.

[60] E. Seedhouse. *Energiya—Buran: The Soviet Space Shuttle*. Springer, Cham, 2016. ISBN 978-3-319-26112-6. doi: https://doi.org/10.1007/978-3-319-26112-6.

[61] P. M. Sforza. Chapter 7 - launch mechanics. In P. M. Sforza, editor, *Manned Spacecraft Design Principles*, pages 199 – 302. Butterworth-Heinemann, Boston, 2016. ISBN 978-0-12-804425-4. doi: https://doi.org/10.1016/B978-0-12-804425-4.00007-6. URL `http://www.sciencedirect.com/science/article/pii/B9780128044254000076`.

[62] I.M Sobol'. Global sensitivity indices for nonlinear mathematical models and their monte carlo estimates. *Mathematics and Computers in Simulation*, 55(1):271–280, 2001. ISSN 0378-4754. doi: https://doi.org/10.1016/S0378-4754(00)00270-6. URL `https://www.sciencedirect.com/science/article/pii/S0378475400002706`. The Second IMACS Seminar on Monte Carlo Methods.

[63] SpaceX. Starship users guide, revision 1.0. `https://web.archive.org/web/20200402122214/https://www.spacex.com/sites/spacex/files/starship_users_guide_v1.pdf`. Accessed 28/08/2020.

[64] G. P. Sutton. *Rocket Propulsion Elements*. 2010. ISBN 1893912124.

[65] R. Varvill and A. Bond. The SKYLON Spaceplane. *Journal of the British Interplanetary Society*, 57:22–32, January 2004.

[66] K. F. Wakker. *Fundamentals of Astrodynamics*. Delft University of Technology, 2015.

[67] C. Weiland. *Aerodynamic Data of Space Vehicles*. Springer, 01 2014. doi: 10.1007/978-3-642-54168-1.

[68] J. R. Wertz. *Mission Geometry; Orbit and Constellation Design and Management*. Springer Netherlands, 2001.

[69] X. Xin Fang and C. Bing Shen. Study on atomization and combustion characteristics of LOX/methane pintle injectors. *Acta Astronautica*, 136(March):369–379, 2017. ISSN 00945765. doi: 10.1016/j.actaastro.2017.03.025. URL `http://dx.doi.org/10.1016/j.actaastro.2017.03.025`.

[70] B. T. C. Zandbergen. Thermal rocket propulsion (version 2.07). Thermal Rocket Propulsion Course Reader, 2018. TU Delft.

[71] H. Zheng, X. Zeng, J. Zhang, and H. Sun. *The Application of Carbon Fiber Composites in Cryotank*. 03 2018. ISBN 978-953-51-3905-8. doi: 10.5772/intechopen.73127.

[72] R. M. Zubrin. Mars and lunar direct: Maximizing the leverage of in-situ propellant production to develop a coherent architecture for the space exploration initiative. *AIAA Space Programs and Technologies Conference, 1992*, 1992. doi: 10.2514/6.1992-1669.